THE UNIVERSITY OF MANITOBA

CREEP CRACK GROWTH UNDER CYCLIC LOADING CONDITIONS - A CONTINUUM DAMAGE APPROACH

by

© Guoguang Chen

A Thesis

Submitted to the Faculty of Graduate Studies

in Partial Fulfillment of the Requirements for the Degree

of Doctor of Philosophy

Department of Mechanical Engineering

Winnipeg, Manitoba

June, 1988

ISBN 0-315-48125-0

CREEP CRACK GROWTH UNDER CYCLIC LOADING CONDITIONS

A CONTINUUM DAMAGE APPROACH

BY

GUOGUANG CHEN

A thesis submitted to the Faculty of Graduate Studies of
the University of Manitoba in partial fulfillment of the requirements
of the degree of

DOCTOR OF PHILOSOPHY

ABSTRACT

This thesis presents a new analytical model for analyzing creep crack initiation and propagation under static and cyclic loading conditions. This model combines the continuum damage constitutive relationships for creep deformation; the several yield surfaces coupled with Mroz's kinematic hardening rule for cyclic plastic response; the hybrid explicit-implicit integration scheme for creep stress analysis; the modified breakable element algorithm coupled with the damage criterion for simulating creep crack initiation and propagation; and the finite element method. This combined creep fracture model is capable of predicting static and cyclic creep crack growth.

Numerical studies by the proposed model indicate that plastic strains play an significant role in both static and cyclic creep fracture. For a cracked specimen subjected to static loadings, the instantaneous plastic strain may slow down the stress relaxation in the vicinity of the crack tip. The slower stress relaxation causes faster damage accumulation in the near tip region and slower damage evolution in the area away from the crack tip. Such confined damage results in an earlier crack initiation but slower crack propagation.

In the creep dominated fracture, unloading and reloading may interrupt the stress relaxation near the crack tip and cause a significant stress increase ahead of the crack tip and an expansion of the plastic zone. Consequently, the creep damage accumulation along the crack extension line is accelerated by the load cycling, resulting in an earlier crack initiation and faster crack growth.

ACKNOWLEDGMENTS

The author wishes to express his deepest gratitude to Dr. T. R. Hsu for the valuable advice and guidance throughout the course of the study. Sincere appreciation is also due to Dr. J. Shewchuk, Dr. A. H. Shah and Dr. A. S. Kobayashi for their valuable suggestions.

Thanks are also extended to his colleagues and friends, Messrs. G. Pizey, N. S. Sun and Z. L. Gong for their assistance and useful discussions.

A special acknowledgment is due to Messrs. L. Haberman and T. Cornell of the Industrial Technology Centre, Manitoba Research Council, for their support in the preparation of this thesis. The author is particularly grateful to Mr. K. Bornn and Mrs. E. Rieger for their patience in typing the manuscript.

The financial support by the Natural Science and Engineering Research Council of Canada and fellowships provided by the University of Manitoba and the Manitoba Hydro Ltd. are greatly acknowledged.

Above all, the author would like to thank his wife Yingzi for her patience during the long period of study and preparation of this dissertation. The author is indebted to his parents in China for their sincere support and encouragement.

CONTENTS

CHAPTER 1

INTRODUCTION

1.1 Introduction

The creep behavior of metals at high temperature is well known and documented. However, almost all design analyses against creep failure up to now is based on unnotched, uniaxial laboratory test data with an objective to ensure that the creep deformation is kept within acceptable limits and that the creep damage accumulation in the structure will not cause premature rupture during its service life.

Structures where failure is localized present a more difficult problem. The criterion employed for elevated temperature design has been that the time allowed for the crack initiation should exceed the design life. However, due to the complex geometries of most of these structures and the nature of the stress history during service, crack initiation is often difficult to predict. There are other shortcomings of this concept. First, small crack-like defects may exist in a machine component before it is put into service, in particular, such cracks may have been initiated in "heat-affected zones" during welding. Secondly, creep and fatigue damage processes may cause small cracks to appear very early in the component's life, and withdrawl from service at this point may be both uneconomical and unnecessary. These considerations have prompted the development of a fail-safe design philosophy, in which account is taken for both crack initiation and crack propagation.

The current interest in the study of creep crack propagation derives from the need for accurate design codes for nuclear power plant and aircraft jet engine, in which the requirements for safety and economy are obvious. A common service load type in these applications is a cycle which begins with an initial start-up followed by a long operating or hold period and then, finally, shut-down. Start-up and shut-down cause a cyclic stress history, whereas the hold period may involve creep deformation and stress redistribution. Cracks may therefore initiate and propagate under a combination of fatigue and creep conditions.

The fracture behavior of materials under combined creep-fatigue condition is strongly affected by frequency. Rapid cyclic loading is associated with fatigue cracking which is in a transgranular mode and slowly varying or static loading is associated with creep cracking which is in an intergranular fracture. Figure 1.1 is an example showing the dependence of the cracking mode on frequency[105], for A286 steel at 1100°F. The intergranular fracture occurs when frequency is less than 10 cpm. This frequency range is often encountered in engineering practice and hence, is of considerable interest in the study of the fatigue-creep interaction.

When frequency is very low, the fatigue damage can be neglected, and the crack growth is dominated by creep. It has been observed, however, that the creep crack growth could be accelerated by a cyclic loading in very low frequency. The reason for such an acceleration of crack growth is not clear at

this time. One possibility is that the cyclic plasticity associated with the unloading and reloading has some influences on the creep damage accumulation near the crack tip. The present study attempts to assess the effect of the plasticity on the creep crack initiation and propagation under static and cyclic loadings.

1.2 Objective of Thesis

This thesis describes a research effort leading to a creep fracture mechanics methodology designed to treat static and cyclic creep crack propagation in structures. Based on the theory of continuum damage mechanics, a finite element model for static and cyclic creep fracture is developed, which has the following unique features:

(1) the plastic hardening behavior of materials under cyclic conditions can be described;

(2) the creep crack initiation and extension can be predicted; and

(3) the inherent numerical instability associated with the damage approach can be avoided.

The objective of the thesis is to investigate the effect of the instantaneous plastic strain on the static and cyclic creep crack propagations by using this finite element model. For creep fracture problems, the instantaneous plasticity unavoidably occurs near the crack tip. However, it has been omitted in most creep fracture analyses. The role of the instantaneous plastic strain in the creep crack growth has not yet been well

understood. However, speculation is that plasticity plays an important role in cyclic creep fracture problems, as the stress redistribution at the crack tip may occur after unloading and reloading due to the kinematic hardening nature of materials. By applying the proposed finite element model to cracked panels, the present work investigates how the instantaneous plasticity affects the stress redistribution and the damage accumulation ahead of the crack tip and hence, affects the creep crack initiation and the subsequent propagation under both static and cyclic loadings.

1.3 Scope of Thesis

The thesis is divided into eight chapters:

Chapter 1 is an introduction, describing the objective and scope of the thesis;

Chapter 2 is a review of the basic mechanical behavior of creep and the corresponding mathematical formulation;

Chapter 3 describes the finite element formulation in elastic-plastic-creep stress analysis;

Chapter 4 is a general review on the development of creep fracture mechanics and cyclic creep fracture;

Chapter 5 presents a finite element model for cyclic creep fracture analysis using the continuum damage approach. Major ingredients of this model include the following items:

(1) a suitable plastic hardening model for cyclic loadings;

(2) a mixed explicit-implicit algorithm for high computational efficiency in creep stress analysis; and

(3) a modified breakable element algorithm for simulating creep crack initiation and propagation.

Chapter 6 presents the results of a case study for creep crack growth under static loadings;

Chapter 7 presents the results of the case study for creep crack growth under cyclic loadings;

Chapter 8 is the conclusion drawn from the present research and recommendations for further study.

A bibliography is presented at the conclusion of the thesis.

CHAPTER 2

CONTINUUM DAMAGE MECHANICS OF CREEP

2.1 Basic Mechanical Behavior of Creep [1][2][3][4]

Creep is a time-dependent deformation which occurs when a material is loaded for a prolonged period of time. Time dependence is the chief characteristic of creep deformation. Figure 2.1 is a typical creep curve which describes the development of strain with time in a solid under constant stress and temperature. At the time, t=0, the curve shows an instantaneous response ε_0, which, depending on the magnitude of the stress, could be elastic or elasto-plastic. Thereafter, the creep curve is divided into three parts: the first part with a decreasing creep strain rate called primary creep; the second part with an approximate constant creep strain rate called secondary or steady- state creep; and the final part with a rapidly increasing strain rate called tertiary creep. Creep rupture occurs at the end of the tertiary creep stage.

The creep curve shown in Figure 2.1 is strongly influenced by stress and temperature. The influence of stress at constant temperature is shown in Figure 2.2, while the influence of temperature at constant stress is shown in Figure 2.3. Note that both cases show thresholds below which no noticeable creep is observed.

The relationship of stress and time to rupture is also shown in Figure 2.2. It is seen that the time to rupture increases as stress decreases. Furthermore, as indicated in

Figure 2.3, the time to rupture decreases as the temperature increases.

If the stress is removed during the creep process, a phenomenon of creep recovery will take place, as shown in Figure 2.4. The instantaneous response is that the elastic strain $\varepsilon^E=\sigma/E$ is recovered. After that, there is a certain amount of strain recovery that becomes asymptotic and no more strain is recovered. In Figure 2.4, ε_R^C is the recovered creep strain and ε^P is the permanent strain that is made up of irrecoverable plastic strain (if any) and creep strain components.

Figure 2.5[5] is an example showing the material behavior upon reloading. Clearly, the time at rest (or dwell time) has an influence on the subsequent creep curve. If unloading and reloading are carried out rapidly, the material tends to ignore the effect of load change, as shown in Figure 2.5(a). However, as indicated in Figures 2.5(b) and (c), longer rest period at zero load results in a higher transient creep rate upon reloading.

2.2 Continuum Damage Mechanics of Creep

2.2.1 The state variable theory

The slow, time-dependent deformation in materials undergoing creep deformation is actually the macroscopic reflection of the kinetics of several different modes of microstructural rearrangement of the polycrystalline lattice. It is well understood that[6] the protracted initial period of

creeps is dominated by viscous modes such as dislocation glides and climbs, flow of grain boundaries and vacancy diffusion, while the rapid increase of the strain rate typifying the tertiary creep is directly traceable to the accelerated microvoids growth preceding their coalescence leading to the creep rupture. In order to be able to predict the material behavior under creep conditions, a rational theory must reflect the influence of the microstructural kinetics on the response. However, the irregularities in the lattice and the distribution of microdefects render such a theory unable to be used in the macroscopic sense[7]. A promising strategy is, therefore, to establish a macroscopic model which will broadly mirror the salient features of the microstructural mechanisms "with more or less distortion and blurring of detail"[8]. The state variable method is a widely used approach of this kind.

The basic assumptions of the state variable theory is that: (a) the response of the material depends only on the current state of the microstructural defects; and (b) the current state of the microstructural defects can be described by a finite set of internal variables. Based on these assumptions, the constitutive relations of materials can be expressed in terms of the state variables ω_j as[9]

$$\dot{\varepsilon} = f(\sigma, \omega_j, t) \qquad (2.1\ a)$$

and

$$\dot{\omega}_i = g_i(\sigma, \omega_j) \qquad i,j = 1,2,\ldots n \tag{2.1 b}$$

The number of the state variables, n, and the functions f and g_i are determined either on the basis of the theories of metal physics or on the results of appropriately chosen mechanical tests. Obviously, for the purpose of the practical engineering applications, the number of the state variables should be as small as possible and the forms of the functions f and g_i should be as simple as possible.

2.2.2 Uniaxial constitutive relations

The simplest form of the state variable theory to describe the uniaxial behavior of creep rupture is Kachanov's damage theory[10]. He proposed a scalar quantity, damage parameter ω, as the single state variable in the constitutive relation which can be shown as:

$$\dot{\varepsilon} = A\left(\frac{\sigma}{1-\omega}\right)^n \tag{2.2 a}$$

$$\dot{\omega} = B\left(\frac{\sigma}{1-\omega}\right)^{\phi} \tag{2.2 b}$$

where A, B, n and ϕ are material constants determined by mechanical testings. The damage parameter ω is the measure of material's deterioration during creep. When the material is undamaged, ω=0, then equation (2.2 a) reduces to the well known Norton's law

$$\dot{\varepsilon} = A\sigma^n \tag{2.3}$$

for the steady-state creep. On the other hand, rupture occurs when $\omega=1$. Integration of (2.2 b) using the above postulation will lead to a relation between the rupture time t_R and the applied stress σ as

$$t_R = \frac{1}{B(1+\phi)} \sigma^{-\phi} \tag{2.4}$$

The values of constants B and ϕ can therefore be obtained from the rupture curve, while A and n can be obtained from the steady state conditions as described in equation (2.3).

The Kachanov's damage equation (2.2) was extended by Odquist[11] and Rabotnov[12] to include the primary creep as shown below:

$$\dot{\varepsilon} = A\left(\frac{\sigma}{1-\omega}\right)^n t^m \tag{2.5 a}$$

$$\dot{\omega} = B\left(\frac{\sigma}{1-\omega}\right)^\phi \tag{2.5 b}$$

Thus, the entire creep process including primary, secondary and tertiary creeps can be described by the modified Kachanov's damage equation (2.5).

Note that the coefficient A in equation (2.5 a) is temperature-dependent. The temperature dependence of A is usually expressed as[13]

$$A = Ke^{-Q/RT} \tag{2.6}$$

where

Q = activation energy;

R = universal gas constant;

T = absolute temperature;

K = material constant

2.2.3 Multi-dimensional constitutive relations

A valid multi-dimensional constitutive theory for creep must satisfy the following requirements:

a) The multiaxial formulation must reduce to the correct uniaxial formulation when it is appropriate;

b) The model should express the constancy of volume that has been observed experimentally during the creep process;

c) The equations should embody the lack of influence of the hydrostatic state of stress that has been observed experimentally for creep;

d) For isotropic materials, the principal directions of stress and strain should coincide;

e) The model should reflect the dependence of the creep rupture on the multi-dimensional stress state that has been observed experimentally[14].

The multi-dimensional form of Kachanov's damage theory which satisfies the above requirements, has been proposed by Leckie and Hayhurst[15] as

$$\dot{\varepsilon}_{ij} = \frac{3}{2} A \left(\frac{\bar{\sigma}}{1-\omega} \right)^n \frac{S_{ij}}{\bar{\sigma}} t^m \qquad (2.7\ a)$$

$$\dot{\omega} = B\left[\frac{(1-\alpha)\bar{\sigma} + \alpha\sigma_I}{1 - \omega}\right]^{\phi} \qquad (2.7\ b)$$

where

ε_{ij} = creep strain components;

S_{ij} = deviatoric stress components;

$\bar{\sigma}$ = effective stress;

σ_I = maximum principal stress;

α = material constant $(0 \leq \alpha \leq 1)$

Equation (2.7 b) indicates that the damage evolution in creep materials is dependent on the linear combination of the effective stress and the maximum principal stress. As reported by Hayhurst[14], the rupture time for copper is dependent on the maximum principal stress so that $\alpha = 1$. For some precipitate-hardened materials such as aluminum alloys tested by Johnson[16], the rupture properties are dependent on the effective stress so that $\alpha = 0$. The α values for other materials vary between 0 and 1.

Leckie[17] compared the predictions of these formula with the experimental results of a variety of multiaxial stress states for copper, aluminum alloy and stainless steel and found the comparison to be satisfactory.

Murakami suggested a constant c in the strain rate equation (2.7 a) as:

$$\dot{\varepsilon}_{ij} = \frac{3}{2} A \left(\frac{\bar{\sigma}}{1-c\omega} \right)^n \frac{S_{ij}}{\bar{\sigma}} t^m \qquad (2.7\ c)$$

to allow for better correlating the test results[18].

It is worth noting that the constitutive equation (2.7) is valid for primary, secondary and tertiary creeps. The effect of the rest time on the creep behavior in repeated loading is not considered in the formulation. Generally speaking, equation (2.7) losses its validity for cyclic loading cases. However, since quick unloading and reloading does not influence the creep behavior, as described in the previous section, the continuum damage model (2.7) can still be used to predict the creep behavior of materials under repeated loading without rest time.

A number of sophisticated damage theory[19,20,21,22] and general constitutive models[23,24,25] have been developed to describe more complicated material behavior such as damage anisotropy, cyclic hardening and softening, creep-yield interaction, etc. These theories usually involve more state variables, more complicated function forms and more material constants to be determined experimentally. These complexities render these theories difficult to be used in engineering practice.

CHAPTER 3

ELASTIC-PLASTIC-CREEP STRESS ANALYSIS BY FINITE ELEMENT METHOD

3.1 Introduction

The complexity of the elastic-plastic-creep stress analysis is due to the fact that both plastic and creep deformations are highly non-linear. The time-dependent nature of creep further increases the difficulties in solving this type of problem. In most cases, a numerical approach, such as the finite element method, appears to be the only practical solution method for these problems. A unified finite element procedure dealing with plasticity and creep has been established[26,27] and will be reviewed in this chapter.

3.2 Basic Matrix Formulation of FEM

The basic idea of the finite element method is to discretize a continuum into a finite number of subdomains (elements) which are connected at their apexes or, in some cases, at selected points on the edges (nodes). The unique advantage of such a discretization is that the formulations need only to be applied to the individual elements of certain specified geometries rather than the entire solid of complex geometry.

The governing matrix formulations of the finite element analysis have been well documented[26,27]. The conventional displacement approach is used in this analysis and hence is briefly reviewed as follows:

Element Interpolation Function:

$$\{u\} = [N]\{u\}^e \tag{3.1}$$

where $\{u\}$ is the displacement vector for any point in an element;

$[N]$ is the matrix containing the interpolation function;

$\{u\}^e$ is the corresponding nodal displacement vector.

Strain-Displacement Relation:

$$\{\varepsilon\} = [B]\{u\} \tag{3.2}$$

where $\{\varepsilon\}$ is the strain vector;

$[B]$ is the strain-displacement transformation matrix.

Stress-Strain Relation:

$$\{\sigma\} = [D]\{\varepsilon\} \tag{3.3}$$

where $\{\sigma\}$ is the stress vector;

$[D]$ is the stress-strain constitutive matrix.

Element Stiffness:

$$[K]^e = \int_v [B]^T [D] [B] \, dv \tag{3.4}$$

where $[K]^e$ is the element stiffness matrix and v denotes the volume of the element.

The global stiffness matrix [K] is formed by summing up the stiffness matrices of each individual element in the finite

element mesh to give

$$[K] = \sum_{e=1}^{E} [K]^e \tag{3.5}$$

where E denotes the total number of elements in the structure. The equilibrium equations for the structure can then be obtained as

$$[K] \{u\}^e = \{F\} \tag{3.6}$$

in which $\{F\}$ is the nodal force vector.

Equations (3.6) can be used to solve for the unknown nodal displacement $\{u\}^e$. Strain and stress components for each element are calculated subsequently using equations (3.2) and (3.3).

3.3 Elastic-Plastic Stress Analysis

As the relationship between stresses and strains in elastic-plastic materials is non-linear, the stiffness of the material cannot be regarded as constant. There are basically two kinds of approaches in the finite element analysis to deal with the varying stiffness of materials, namely initial stress/strain and the incremental strain methods. The latter approach is adopted in this analysis for its relative simplicity in computations. The derivations presented here are based on the work of Hsu[27].

The incremental plasticity approach assumes a linear relationship between the incremental stresses and strains. This assumption implies that the entire non-linear loading process can be divided into many piecewise linear loading steps. Within each

loading step, the equilibrium equations can be expressed as

$$[K]_i \{\Delta u\}_i = \{\Delta F\}_i \tag{3.7}$$

where $[K]_i$ is the stiffness matrix;

$\{\Delta u\}_i$ is the incremental displacement vector; and

$\{\Delta F\}_i$ is the incremental nodal force vector for the i^{th} loading step.

After each load increment, the variable stiffness matrix $[K]_i$ must be updated to account for the change in the stress-strain relations due to the elastic-plastic effects. The formulation of the matrix [K] for the elastic-plastic analysis require the following information:

(1) A yield criterion to establish a yield surface in the stress space;

(2) A flow rule relating the plastic strain increments to the yield surface; and

(3) A hardening rule to describe the expanding, shrinking and shifting of the yield surfaces during the deformation process.

3.3.1 Yield criterion

The Von Mises yield criterion is widely acknowledged as an appropriate representation of the initial yield surface based both on the good correlation with testing data and on its mathematical simplicity. This criterion is derived from the distortion energy theory which states that plastic deformation

occurs when the distortion energy of the material reaches a certain critical value. For an isotropic material, the yield surface F, defined by the Von Mises criterion, is expressed as

$$F = J_2 - 1/3\ \sigma_y^2 \tag{3.8}$$

in which

$$J_2 = 1/2\ S_{ij}\ S_{ij} \tag{3.9}$$

is the second deviatoric stress invariant, S_{ij} is the deviatoric stress tensor, and σ_y denotes the initial yield strength of the material from a uniaxial tension test. Geometrically, equation (3.8) represents an ellipsoid in a three-dimensional stress space. The function F in equation (3.8) represents the yield function (or plastic potential function) which describes plastic yielding at current stress state during plastic deformation.

It is obvious that a plastic state is attained when $F = 0$, while the material is in the elastic region if $F < 0$.

3.3.2 Prandtl-Reuss flow rule

The Prandtl-Reuss flow rule assumes that the plastic strain increment is linearly related to the current stress and predicts that the plastic strain increment is normal to the associated yield surface at the stress point. Mathematically, the plastic flow rule using the von Mises yield criterion can be expressed as

$$d\varepsilon_{ij}^{p} = \frac{\partial F(\sigma_{ij})}{\partial \sigma_{ij}} d\lambda = S_{ij}\, d\lambda \qquad (3.10)$$

in which $d\varepsilon_{ij}^{p}$ is the components of the plastic strain increment and $d\lambda$ is a positive proportionality factor.

3.3.3 Kinematic hardening rule

When some materials are plastically deformed in tension, their compressive yield strength in the subsequent compression reduces by the same amount of the increment in the previous tensile loading. This behavior was first discovered by J. Bauschinger in 1881 and is called the Bauschinger effect. The result of this effect is a strain hysterisis observed after a complete tension-compression load cycle, as shown in Figure 3.1.

For the multiaxial loading situation, the Bauschinger effect is modelled by the translation of the yield surface in the stress space. A number of knematic hardening rules have been proposed to describe the translation of the yield surface.

Introducing the translated deviatoric stress tensor S'_{ij} as proposed by Hsu[27]:

$$S'_{ij} = (\sigma_{ij} - \alpha_{ij}) - 1/3\ (\sigma_{kk} - \alpha_{kk})\ \delta_{ij} \qquad (3.11)$$

in which α_{ij} is the tensor of the accumulated kinematic translation of the centre of the yield surface in the stress space, the Von Mises yield surface becomes:

$$F = 1/2\ S'_{ij}\ S'_{ij} - 1/3\ \sigma_{y}^{2} = 0 \qquad (3.12)$$

The translation tensor α_{ij} in equation (3.11) may be computed by Prager's hardening rule[28]. This rule assumes that the translation of the centre of the yield surface is in the direction of the plastic strain increment, i.e. normal to the yield surface. Mathematically, it can be shown as follows:

$$d\alpha_{ij} = d\mu_1 \, d\varepsilon^p_{ij} \tag{3.13}$$

This rule, in general, cannot be satisfied in case one of the stress components is zero[29]. Ziegler subsequently proposed a modification to overcome this deficiency. His hardening rule[29] assumes that the incremental translation of the yield surface is in the direction of the vector which connects the centre point of the current surface to the existing stress point, that is:

$$d\alpha_{ij} = d\mu_2 \, (\sigma_{ij} - \alpha_{ij}) \tag{3.14}$$

$d\mu_1$ and $d\mu_2$ in equations (3.13) and (3.14) are multipliers. Figure 3.2 shows a schematic representation of these two hardening rules.

As the current version of the TEPSAC Program[27] adopts the Ziegler's hardening rule, Ziegler's equation (3.14) will be used in the subsequent derivations.

3.3.4 Derivation of the elastic-plastic element equation

Assume that the total strain increment $d\varepsilon_{kl}$ can be decomposed into an elastic part $d\varepsilon^e_{kl}$ and a plastic part $d\varepsilon^p_{kl}$ as

$$d\varepsilon_{kl} = d\varepsilon^{e}_{kl} + d\varepsilon^{p}_{kl} \tag{3.15}$$

Thus, the incremental constitutive relationship can be defined by

$$d\sigma_{ij} = D^{e}_{ijkl}\, d\varepsilon^{e}_{kl} \tag{3.16}$$

where $d\sigma_{ij}$ is the incremental stress tensor, and D^{e}_{ijkl} is the elastic tensor expressed as

$$D^{e}_{ijkl} = \frac{E}{1+\nu}\left(\delta_{ik}\,\delta_{jl} + \frac{\nu}{1-2\nu}\,\delta_{ij}\,\delta_{kl}\right) \tag{3.17}$$

in which E is the Young's modulus, and ν the Poisson's ratio.

Now, if the projection of $d\sigma_{ij}$ on the outward normal to the yield surface at the stress point is $(C\cdot d\varepsilon^{p}_{ij})$, where C is a positive scalar to be determined later, then

$$(d\sigma_{ij} - C\cdot d\varepsilon^{p}_{ij})\,\frac{\partial F}{\partial \sigma_{ij}} = 0 \tag{3.18}$$

By substituting equation (3.10) into equation (3.18), one obtains

$$d\lambda = \frac{1}{C}\,\frac{(\partial F/\partial \sigma_{ij})\; d\sigma_{ij}}{(\partial F/\partial \sigma_{ij})(\partial F/\partial \sigma_{ij})} \tag{3.19}$$

By substitution of equations (3.15), (3.16) and (3.10) into equation (3.19), one obtains

$$d\lambda = \frac{1}{h}\,\frac{\partial F}{\partial \sigma_{ij}}\, D^{e}_{ijkl}\, d\varepsilon_{kl} \tag{3.20}$$

where

$$h = C \frac{\partial F}{\partial \sigma_{ij}} \frac{\partial F}{\partial \sigma_{ij}} + \frac{\partial F}{\partial \sigma_{ij}} D^{e}_{ijkl} \frac{\partial F}{\partial \sigma_{kl}} \tag{3.21}$$

Combining equations (3.20) and (3.21) with (3.10) and substitute the combined relation into equations (3.15) and (3.16), one obtains

$$d\sigma_{ij} = (D^{e}_{ijkl} - D^{p}_{ijkl})\, d\varepsilon_{kl} = D^{ep}_{ijkl}\, d\varepsilon_{kl} \tag{3.22}$$

where

$$D^{p}_{ijkl} = \frac{1}{h} D^{e}_{ijkl}\, S'_{ij}\, S'_{kl}\, D^{e}_{ijkl} \tag{3.23}$$

and

$$D^{ep}_{ijkl} = D^{e}_{ijkl} - \frac{1}{h} D^{e}_{ijkl}\, S'_{ij}\, S'_{kl}\, D^{e}_{ijkl} \tag{3.24}$$

The scalar C, defined by (3.18), is determined by relating equation (3.22) to the uniaxial state which leads to the following:

$$C = \frac{2}{3} \frac{d\sigma_{11}}{d\varepsilon^{p}_{11}} = \frac{2}{3} \frac{1}{1/E_t - 1/E} = \frac{2}{3} H' \tag{3.25}$$

where the hardening parameter H′ is defined to be the slope of the flow curve of a material in the plastic range and E_t is the slope of the uniaxial $\sigma - \varepsilon$ curve, as shown in Figure 3.3.

The multiplier $d\mu_2$ is determined by the condition that the stress point remains on the yield surface during the plastic flow. Thus, by employing equation (3.12), one obtains

$$dF = \frac{\partial F}{\partial \sigma_{ij}} (d\sigma_{ij} - d\alpha_{ij}) = 0 \tag{3.26}$$

Substituting equation (3.13) into (3.26) and by using the relationship $S'_{ij} = \partial F / \partial \sigma_{ij}$, one gets

$$d\mu_2 = \frac{S'_{ij}\, d\sigma_{ij}}{(\sigma_{ij} - \alpha_{ij})\, S'_{ij}} \tag{3.27}$$

In order to facilitate the subsequent finite element formulation, a translation of the above key equations into appropriate matrix forms is necessary. The results of such a translation are summarized as follows:

(1) Constitutive equation (3.22)

$$\{d\sigma\} = [D_{ep}]\, \{d\varepsilon\} \tag{3.28}$$

(2) Elastic-plastic matrix (3.24)

$$[D_{ep}] = [D_e] - (1/h)\, [D_e]\, \{S'\}\, \{S'\}^T\, [D_e] \tag{3.29}$$

where

$$h = C\, \{S'\}^T\, \{S'\} + \{S'\}^T\, [D_e]\, \{S'\} \tag{3.30}$$

(3) Proportionality factor (3.20)

$$d\lambda = (1/h)\ \{S'\}^T\ [D_e]\ \{d\varepsilon\} \tag{3.31}$$

(4) The Multiplier (3.27)

$$d\mu_2 = \frac{\{S'\}^T\ \{d\sigma\}}{(\{\sigma\} - \{\alpha\})^T\ \{S'\}} \tag{3.32}$$

(5) Translation of yield surface (3.14)

$$\{d\alpha\} = (\{\sigma\} - \{\alpha\})\ d\mu_2 \tag{3.33}$$

3.3.5 Determination of hardening parameter H'

In the current version of the TEPSAC Program, the elastic-plastic effective stress-strain curve suitable for multi-dimensional stress space is represented by a continuous function with no distinction between the elastic and plastice regimes as[30,31]

$$\bar{\sigma} = \frac{\bar{E}\ \bar{\varepsilon}}{\left\{1 + \left[\frac{\bar{E}\ \bar{\varepsilon}}{\left(1 - \frac{\bar{E}'}{\bar{E}}\right)\bar{\sigma}_k + \bar{E}'\ \bar{\varepsilon}}\right]^n\right\}^{1/n}} \tag{3.34}$$

where

$$\bar{E} = \frac{3E}{2(1+\nu)}, \quad \text{the effective modulus of elasticity}$$

$$\bar{E}' = \frac{3E'}{3 - \frac{(1-2\nu)E'}{E}}, \quad \text{the effective modulus of plasticity}$$

with E and E′ to be the respective moduli of elasticity and plasticity from a uniaxial stress-strain curve, and

$\bar{\sigma}_k$ = a stress level at which the elastic line intersects with the tangent of the plastic curve, as shown in Figure 3.4, and

n = a factor which determines the abruptness of the elastic-plastic transition.

By differentiating the stress in (3.34) with respect to the strain, one may obtain a tangent modulus E_t

$$E_t = \frac{d\bar{\sigma}}{d\bar{\varepsilon}} = \frac{\bar{E}\left\{1 + \left[\frac{\bar{E}\,\bar{\varepsilon}}{\left(1 - \frac{\bar{E}'}{\bar{E}}\right)\bar{\sigma}_k + \bar{E}'\bar{\varepsilon}}\right]^{n+1}\frac{\bar{E}'}{\bar{E}}\right\}}{\left\{1 + \left[\frac{\bar{E}\,\bar{\varepsilon}}{\left(1 - \frac{\bar{E}'}{\bar{E}}\right)\bar{\sigma}_k + \bar{E}'\bar{\varepsilon}}\right]^{n}\right\}^{\frac{n+1}{n}}} \qquad (3.35)$$

Then the hardening parameter H′ for isotropic hardening rule or C for kinematic hardening rule can be determined by equation (3.25).

The advantage of this function is that the entire stress-strain curve, including two straight lines in the elastic and work hardening regimes with a gradual elastic-plastic transition, can be described by a single expression. However, this function defines a one-to-one correspondence between the stress and strain. In cyclic loading case, the stress and strain are no longer one-to-one correspondent. Therefore, this approach is not applicable to cyclic loading cases.

3.4 Creep Stress Analysis by Finite Element Method

A basic assumption involved in creep stress analysis is that the total strain $\{\varepsilon\}$ can be partitioned into the elastic $\{\varepsilon_e\}$, plastic $\{\varepsilon_p\}$ and creep $\{\varepsilon_c\}$ components, so that the total strain increment can be expressed as[32]

$$\{\Delta\varepsilon\} = \{\Delta\varepsilon_e\} + \{\Delta\varepsilon_p\} + \{\Delta\varepsilon_c\} \tag{3.36}$$

The separation of plastic and creep strains is clearly an artificial device, since they are both related to the movement of dislocation. However, it has been shown by Onat[33] that this is a reasonable and convenient assumption if $\{\Delta\varepsilon_p\}$ is associated with high rates of loading.

Recall the relationship between the stress increment and the elastic and plastic strain increments, i.e. equation (3.28):

$$\{\Delta\sigma\} = [D_{ep}]\ (\{\Delta\varepsilon_e\} + \{\Delta\varepsilon_p\}) \tag{3.37}$$

Substituting equation (3.36) into equation (3.37), the stress increment can be expressed as

$$\{\Delta\sigma\} = [D_{ep}] (\{\Delta\varepsilon\} - \{\Delta\varepsilon_c\}) \tag{3.38}$$

Introducing the strain-displacement relation, equation (3.2), equation (3.38) becomes

$$\{\Delta\sigma\} = [D_{ep}] ([B] \{\Delta u\} - \{\Delta\varepsilon_c\}) \tag{3.39}$$

where $\{\Delta u\}$ is the incremental displacement vector.

The equation of equilibrium to be satisfied at any time t take the form

$$\int_v [B]^T \{\Delta\sigma\} dv = \{\Delta F\} \tag{3.40}$$

where $\{\Delta F\}$ is the vector of equivalent nodal load increment due to surface traction and body force, and v is the element volume. By combining equations (3.39) and (3.40), the equilibrium equation becomes

$$\int_v [B]^T [D_{ep}] ([B] \{\Delta v\} - \{\Delta\varepsilon_c\}) dv = \{\Delta F\} \tag{3.41}$$

3.5 Time Integration Scheme

Since creep is a time-dependent deformation, the creep stress analysis is in fact a transient problem. The major difficulty involved in creep stress analysis is that the creep constitutive equations are highly non-linear and the resulting equations are stiff in nature. The stability and accuracy of the finite element solution critically depend on the selection of a proper size of time steps associated with an appropriate integration scheme.

Generally speaking, there are two common classes of one-step integration schemes for creep analysis, i.e. explicit and implicit. The advantages of the explicit scheme suggested by Zieckiewicz and Cormeau[34] and Cormeau[35] is that it is concise and simply coded. But the stability condition is rather stringent and very small time steps are required. The implicit scheme was proposed by Hughes and Taylor[36] and was lately modified by Kanchi et al[37]. It allows the use of larger time step sizes but requires more operation in every time step. This drawback has made the implicit scheme computationally uneconomical, especially for large scale problems where a large number of elements are involved. The formulations of the explicit and implicit algorithms are briefly reviewed as follows:

The multi-dimensional form of the general constitutive relation for creep, i.e. equation (2.1), can be stated as

$$\{\dot{\varepsilon}^c\} = f_1 (\{\sigma\}, \{\omega\}, t) \qquad (3.42\ a)$$

$$\{\dot{\omega}\} = f_2 (\{\sigma\}, \{\omega\}) \qquad (3.42\ b)$$

3.5.1 Explicit algorithm

$$\{\Delta\varepsilon^c\} = \{\dot{\varepsilon}^c_n\}\ \Delta t \qquad (3.43)$$

$$\{\Delta\omega\} = \{\dot{\omega}_n\}\ \Delta t \qquad (3.44)$$

where the subscript n denotes the n^{th} time step.

The stress increment can be expressed by substituting equation (3.43) into equation (3.39) as shown below:

$$\{\Delta\sigma\} = [D_{ep}]\ ([B]\ \{\Delta u\} - \{\dot{\varepsilon}_n^c\}\ \Delta t) \tag{3.45}$$

The governing equation (3.40) now becomes

$$(\int_v [B]^T[D_{ep}][B]\ dv)\{\Delta u\} = \int_v [B]^T[D_{ep}]\{\dot{\varepsilon}_n^c\}\ \Delta t\ dv + \{\Delta F\} \tag{3.46}$$

Cormeau has performed a stability analysis and derived the explicit stability conditions for some constitutive relations[35]. For the steady-state creep obeying Norton's law (2.3), the stability condition requires that

$$\Delta t < \Delta t_{critical} = \frac{4(1+\nu)}{3nE} \cdot \frac{1}{A(\bar{\sigma}_{max})^{n-1}} \tag{3.47}$$

where $\bar{\sigma}_{max}$ is the maximum effective stress in the structure. In the creep fracture problems $\bar{\sigma}_{max}$ is very high due to a high stress concentration at the crack tip. The value of the stress index of the creep law, n, ranges from 5 to 10 for most metals. A typical allowable time step size determined by equation (3.47) in creep fracture analyses in the order of 10^{-5}hr., as reported by Hsu et al[103] and Ehlers et al[112].

3.5.2 Implicit algorithm

The increments of creep strain and state variables occurring in a time increment Δt are assumed to take the form

$$\{\Delta\varepsilon^c\} = [(1 - \gamma)\{\dot{\varepsilon}_n^c\} + \gamma\{\dot{\varepsilon}_{n+1}^c\}]\ \Delta t \tag{3.48}$$

and

$$\{\Delta\omega\} = [(1 - \gamma)\{\dot{\omega}_n\} + \gamma\{\dot{\omega}_{n+1}\}]\ \Delta t \tag{3.49}$$

with $0 \leq \gamma \leq 1$. It is readily seen that the explicit scheme is actually a special case of the above equation with $\gamma = 0$. On the other hand, the case of $\gamma = 1$ represents a fully implicit scheme. The case with $\gamma = 1/2$ denotes the implicit trapezoidal scheme which is generally known as the Crank-Nicolson rule of integration.

The incremental creep strain $\{\dot{\varepsilon}_{n+1}\}$ and the state variable $\{\dot{\omega}_{n+1}\}$ in equation (3.48) and (3.49) can be approximated by a limited Taylor series expansion as

$$\{\dot{\varepsilon}^c_{n+1}\} = \{\dot{\varepsilon}^c_n\} + [H_1]\{\Delta\sigma\} + [H_2]\{\Delta\omega\} + \{H_3\}\ dt \tag{3.50}$$

and

$$\{\dot{\omega}_{n+1}\} = \{\dot{\omega}_n\} + [G_1]\{\Delta\sigma\} + [G_2]\{\Delta\omega\} \tag{3.51}$$

in which

$$[H_1] = \frac{\partial\{\dot{\varepsilon}^c\}}{\partial\{\sigma\}}, \quad [H_2] = \frac{\partial\{\dot{\varepsilon}^c\}}{\partial\{\omega\}}, \quad \{H_3\} = \frac{\partial\{\dot{\varepsilon}^c\}}{\partial t} \tag{3.52}$$

$$[G_1] = \frac{\partial\{\dot{\omega}\}}{\partial\{\sigma\}}, \quad [G_2] = \frac{\partial\{\dot{\omega}\}}{\partial\{\omega\}} \tag{3.53}$$

By substituting equation (3.51) into (3.49), one gets

$$\{\Delta\omega\} = [g]\ (\{\dot{\omega}_n\} + \gamma[G_1]\{\Delta\sigma\})\ \Delta t \tag{3.54}$$

in which

$$[g] = ([I] - \gamma[G_2]\ \Delta t)^{-1} \tag{3.55}$$

where [I] is the identity matrix.

Now, if one substitutes equations (3.48), (3.50) and (3.54) into (3.38) and rearranges the terms, the stress increments can be expressed by the following equation:

$$\{\Delta\sigma\} = [D^*_{ep}]\ ([B]\{\Delta u\} - \{\dot{\varepsilon}^c_n\}\Delta t - ([H_2][g]\{\dot{\omega}_n\} + \{H_3\})\ \gamma\Delta t^2) \tag{3.56}$$

where

$$[D^*_{ep}] = ([I] + \gamma\Delta t[D_{ep}]\ ([H_1] + \gamma[H_2][g][G_1]\Delta t))^{-1}[D_{ep}] \tag{3.57}$$

The governing equation can thus be derived by substituting equation (3.56) into equation (3.40). The final form of the equation is given as

$$(\int_V [B]^T[D^*_{ep}][B]dv)\{\Delta u\} =$$

$$\int_V [B]^T[D^*_{ep}]\ (\{\dot{\varepsilon}^c_n\}\Delta t + ([H_2][g]\{\dot{\omega}_n\} + \{H_3\})\ \gamma\Delta t^2)\ dv + \{\Delta F\} \tag{3.58}$$

Although the implicit integration scheme is not unconditionally stable, computational experiences have shown that it is much more stable than the explicit scheme with larger time steps. However, since the stiffness matrix used in this method is a function of element stresses, reformulation and inversion of

the stiffness matrix is necessary in every time step of computations. As a result, the implicit scheme requires substantially more computer time in every time step. For large problems involving a great many elements, this drawback makes the implicit integration scheme uneconomical.

CHAPTER 4

CREEP CRACK PROPAGATION

4.1 Introduction

Recognition of the fact that failure of high temperature components can occur by the propagation of a single crack which can nucleates from pre-existing flaws, weld defects or creep-fatigue damage processes, has led to a significant increase in creep crack growth study during the past 15 years. Most of the research in this area tends to be on finding a proper representative parameter which would correlate measured crack propagation rates in as universal a manner as possible. A number of parameters have been developed with different degree of success. This chapter reviews some promising approaches with an emphasis on their applicabilities and limitations in characterizing creep crack growth in engineering materials.

4.2 Stress Intensity Factor K

Systematic research into creep crack growth began with the application of linear elastic fracture mechanic techniques to high temperature components. Siverns and Price[38], in a study of 2 1/4 Cr 1 Mo ferric steel, suggested that the creep crack growth rate could be expressed as a power function of the elastic stress intensity factor K as

$$\frac{da}{dt} = A\ K^n \qquad (4.1)$$

where a is the crack length, and A and n are constants. This was supported by Neat and Siverns[39], Floreen[40] and James[41].

It has been found that the correlation between da/dt and K can only be observed in creep-brittle materials for a very small range of K[42]. It has been pointed out by Gouch, Haigh and King[43] that specimen geometry, initial notch depth and applied load all affect correlations. The variations observed experimentally between correlations of crack growth rate and stress intensity factor obtained under different loading conditions and, with varying specimen geometry, have been rationalized in an analysis by Pilkington and Smith[44].

The reason why the stress intensity factor K can not be expected to characterize the creep crack growth for a wide range of conditions is quite understandable. The non-linear nature of the creep deformation makes the extent of applicability of the linear elastic fracture parameter K in high temperature fractures to be very limited. K correlation is only valid for creep-brittle material with low value of creep index and high crack velocities[45].

4.3 Net Section Stress σ_{net}

The second widely used method for studying creep crack growth is to correlate the crack growth rate with the net section stress. The net section stress is defined as the applied load divided by the area of the uncracked ligament. The correlations of creep crack growth rate with σ_{net}, first made by Harrison and

Sander[46], is of a form analogous to those with K (equation (4.1)):

$$\frac{da}{dt} = A\ \sigma_{net}^{n} \qquad (4.2)$$

where A and n are material constants, though different from those in equation (4.1).

Although net section stress method was supported by other researchers[47,48,49,50], correlations of creep crack growth with σ_{net} have been neither more nor less successful than those with stress intensity factor K in embracing data obtained from a variety of testing conditions. Actually, the stress intensity factor and the net section stress describe two extremes of stress distribution in a specimen, whereas the true stress distribution in most specimens probably lies between these two extremes. In materials in which little stress relaxation can occur before a crack extends by rupture of the material ahead of the crack tip, the crack growth rate may correlate with a stress level related to that modeled by the elastic stress intensity factor. In materials in which more extensive stress relaxation can take place before localized rupture occurs, the stresses may relax to a value close to the nominal value of σ_{net}. In such cases, the crack growth rates may correlate with σ_{net}. This argument supports the notion that K is only applicable in "creep brittle" material, whilst σ_{net} is only applicable in "creep ductile" material such as put forward by Ellison and Neate[50] and Neate[51].

4.4 Contour Integration C^*

4.4.1 The J-integral concept in elastic-plastic fracture mechanics

The path independent integral J, proposed by Rice[52], is defined as

$$J = \int_{\Gamma} (W\, dy - T_i \frac{\partial u_i}{\partial x} ds) \tag{4.3}$$

where W is the strain energy density given by

$$W = \int \sigma_{ij}\, d\varepsilon_{ij} \tag{4.4}$$

with T_i and u_i to be the components of the respective surface traction and displacement vectors, x and y the coordinates and s are length along a contour Γ surrounding a crack tip, as shown in Figure 4.1. The J-integral has been proven to be path independent if the material obeys the following constitutive relation:

$$\varepsilon = c\sigma^p \tag{4.5}$$

where c and p are material constants. Note that the constitutive relation (4.5) requires a one-to-one correspondence between the strain and stress. If unloading occurs, the relation between strain and stress will no longer be one-to-one correspondent. Therefore, unloading violates the path-independence of the J-integral. Strictly speaking, J-integral is valid for non-linear elastic material.

Further, it has been shown that[53] J may also be expressed as

$$J = -\frac{1}{B}\frac{dU}{da} \tag{4.6}$$

where U is the potential energy functional and B is the thickness of the plane. By equation (4.6), J-integral may be interpreted as the potential energy difference between two identically loaded bodies of incrementally differing crack lengths.

It has also been shown by Rice[52] that for linear elastic materials, the J-integral is identical to G, the energy release rate per unit crack extension. Therefore

$$J = G_I = \frac{K_I^2}{E'}$$

where K_I is the mode I stress intensity factor, and

$$E' = E \qquad \text{for plane stress}$$

$$E' = \frac{E}{1-\nu^2} \qquad \text{for plane strain}$$

The path-independent nature of the J-integral presents a unique advantage that it is possible to evaluate this integral along any region enclosing the crack tip. The paths of integration can be chosen to include the region where the stress and strain fields can be determined with sufficient accuracy.

Hutchinson[54] and Rice and Rosengren[55] have proven that for materials following a power law hardening stress-strain

relation such as shown in equation (4.5), the stress and strain field near the crack tip can be characterized by the J-integral as

$$\sigma_{ij} \propto (J/r)^{1/(p+1)} \qquad (4.7\ a)$$

$$\varepsilon_{ij} \propto (J/r)^{p/(p+1)} \qquad (4.7\ b)$$

where r is the distance from the crack tip. Equation (4.7) is known as "the HRR singularity" in the literature.

Begley and Landes[56] suggested the J-integral to be the fracture criterion in elastic-plastic situation. The measurement techniques for J_{IC}, the critical value of the J-integral for crack initiation, have been proposed by Landes and Begley[57] and Rice, Paris and Merkle[58]. These techniques have been documented in ASTM standard E813-81[59].

Although the path-independency of the J-integral is based on the deformation theory of plasticity (equation (4.5)), experimentation and computation have shown[60], despite lack of proof, that J concept can be extended to situation involving incremental plasticity behavior.

4.4.2 C^* parameter

(1) Definition of the C^* integral

Consider a material which deforms in steady-state creep according to the Norton's creep law (equation (2.3)):

$$\dot{\varepsilon} = A\ \sigma^n \qquad (4.8)$$

Comparison of equations (4.5) and (4.8) shows that the two equations have a similar form, with the strain of (4.5) being replaced by strain rate. By analogy, Turner and Webster[61] and Landes and Begley[62] suggested an expression for C^* integral as

$$C^* = \int_\Gamma W^* \, dy - T_i \frac{\partial \dot{u}_i}{\partial x} \, ds \qquad (4.9)$$

where W^* is strain energy rate density given by

$$W^* = \int \sigma_{ij} \, d\dot{\varepsilon}_{ij} \qquad (4.10)$$

and $\dot{u}_i$ is the displacement rate vector.

By analogy with equation (4.6), C^* can also be expressed as

$$C^* = -\frac{1}{B} \frac{d\dot{U}}{da} \qquad (4.11)$$

where $\dot{U}$ is the potential power and is analogous to the potential energy U in equation (4.6).

(2) Near-tip stress field

Goldman and Hutchinson[63] have shown that the near-tip stress and strain rate distribution in a cracked body undergoing purely steady-state creep deformation are characterized by C^*:

$$\sigma_{ij} \propto (C^*/r)^{1/(n+1)} \qquad (4.12\ a)$$

$$\dot{\varepsilon}_{ij} \propto (C^*/r)^{n/(n+1)} \qquad (4.12\ a)$$

For the case involving elastic and power law creep strains, Riedel and Rice[64] have analyzed the asymptotic solutions and shown that the stress singularity near the crack tip is of the order of $r^{-1/n+1}$ in comparison to the inverse square root singularity for an initial elastic stress field. From the analysis, the creep zone size r_c is given by

$$r_c = \frac{1}{2\pi}\left(\frac{K_i}{E}\right)\left[\frac{(n+1)^2\, E^n\, At}{2n\alpha_n^{n-1}}\right]^{2/(n-1)} F_{cr}(\theta) \qquad (4.13)$$

where K_i is the initial stress intensity factor, E is Young's modulus, A and n are defined in equation (4.8) and α_n^{n-1} is approximately equal to unity. $F_{cr}(\theta)$ is a function of angle (θ) measured from the plane of the crack in the anticlockwise direction and is given in Reference [64]. Riedel and Rice have also defined a characteristic time for the transition from small scale creep to extensive creep of the whole specimen given by

$$t_i = \frac{K^2\,(1-\nu^2)}{E\,(n+1)\,C^*} \qquad (4.14)$$

where ν is Poisson's ratio.

While the above analysis pertains to stationary cracks, some progress has been made in analyzing the near-tip stress field for a moving crack. Hui and Riedel[65] and Hui[66] have analyzed the steady state asymptotic fields around a crack propagating at constant velocity in a power law creeping solid. They concluded that the stress singularity depends on the value

of the creep exponent n. For $n < 3$, inverse square root singularity exists, while for $n > 3$, stress-strain singularity is of the form of $r^{-1/(n-1)}$ and depends only on crack growth rate and not on applied load. The implication is that for crack growth rates greater than some minimum value, the rates are proportional to K^n for small scale creep and for the growth rates less than the minimum, no stable steady-state growth is possible. Hart's observations are similar[67,68]. However, these analyses were based on a small scale creep assumption while neglecting the influence of crack tip stress relaxation.

(3) Determination of C^*

The experimental data reduction scheme employed by Landes and Begley[62] is analogous to that previously employed[57] in determining J. The test procedure is summarized in Figure 4.2. The data are collected as load and crack length versus time for a constant displacement rate, Step 1. These data are then used to determine load as a function of displacement rate for various crack lengths, Step 2, and crack growth rate versus crack length, Step 5. The power or energy rate input, $\dot{U}$, is measured as the area under the curves in Step 2. $\dot{U}$ is plotted versus crack length in Step 3. The slope of the curves in Step 3 is C^* as defined in equation (4.11). C^* can be plotted as a function of displacement rate, Step 4. Combining the curves from Step 4 and Step 5 gives the desired result of crack growth rate versus C^*,

Step 6. This method involves 6 steps and requires data from many tests.

Several approximate expressions of the C^* integral have been developed to simplify the test procedure for the determination of C^*. These approximate expressions were derived based on the definition of C^*, equation (4.11), in conjunction with the Norton's creep law, equation (4.8). The limit load analysis technique[72] was used to give the following approximate expressions of C^* for different specimen geometries:

Nikbin, Webster and Turner[69]

$$C^* = \frac{1}{B} \cdot \frac{P}{n+1} \cdot \frac{d\dot{\Delta}}{da} \quad \text{(for Double Cantilever Beam specimen)} \tag{4.15}$$

Harper and Ellison[70]

$$C^* = -\frac{n}{n+1} \cdot \frac{P\dot{\Delta}}{BW} \left[\frac{1}{m} \cdot \frac{dm}{d(a/W)}\right] \tag{4.16}$$

(the term $\left[\frac{1}{m} \cdot \frac{dm}{d(a/W)}\right]$ for commonly used specimen geometries can be found in Reference [71,72])

Koterazawa and Mori[73]

$$C^* = \frac{P\dot{\Delta}}{B(W-2a)} \quad \text{(for Double Edge Notch specimen)} \tag{4.17}$$

$$C^* = \frac{2P\dot{\Delta}}{B(W-a)} \quad \text{(for Compact Tension Specimen)} \tag{4.18}$$

Ohji, Ognia and Kubo[74]

$$C^* = \frac{n-1}{n+1} \sigma_{net} \dot{\delta} \quad \text{(for Centre Notched specimen)} \tag{4.19}$$

$$C^* = \frac{2n-1}{2n+1} \sigma_{net} \dot{\delta} \quad \text{(for Round Notched Bar specimen)} \tag{4.20}$$

where

P = applied load;

W = width of the specimen;

$\dot{\Delta}$ = displacement rate at the load point; and

$\dot{\delta}$ = crack opening displacement rate.

These expressions allow C^* parameter to be experimentally determined by using single specimen.

(4) Relevance of C^* to creep crack propagation

It appears that C^*-parameter correlates the crack growth rate better for a broader range of conditions than other parameters such as K and σ_{net} and hence received more attention than the other parameters[75,76,77]. However, C^*-parameter, like K and σ_{net}, has its limitations. The conceptual difficulty of C^*-parameter results from the fact that the analogy between C^* and J is mathematical, not physical. Although the potential energy U in equation (4.6) has definite physical significance in elastic analysis, there is no corresponding interpolation of the identical function $\dot{U}$ in the creep analysis. The quantity which does have physical significance in the rate problem is the

creep energy dissipation rate which is equal to the power applied to the specimen at loading points. The approximate expressions (4.16 to 4.18) established the relationships between C^* and the creep energy dissipation rate $P\dot{\Delta}$. Therefore, C* may approximately be defined as the rate of change of creep energy dissipation rate with crack length. However, it must be stressed that this cannot immediately be related to the energy release with crack growth. Furthermore, expressions (4.16) to (4.18) have indicated that in different specimen geometries, the proportion of the power input which will be expended in crack growth will differ. This fact implies that the C^* correlation may be affected by specimen geometries and initial crack lengths[78]. Despite extensive work using this parameter, it remains to be proven that there exists a unique $da/dt - C^*$ relation for a wide range of conditions.

It must be emphasize that the path-independency of the C^* integral requires the strain components other than the secondary creep to be excluded in the analysis. Strictly speaking, C^* is only applicable to secondary creep. Neglecting the tertiary creep implies that C^* approach is valid only if the damage accumulation is largely confined to the immediate crack tip area. In other words, C^*-parameter is valid under small scale damage conditions. For materials that exhibit pronounced tertiary creep, the widespread creep damage growth ahead of the crack will invalidate the characterization property of C^*.

Ignoring the plastic strain limits C^* to be valid only under small scale yielding conditions. An instance reported by

Sexana et al[80] clearly shows the need to include plasticity in the creep fracture analysis. They illustrated that for the 316 stainless steel at 594°C, plastic strain dominated the creep propagation process. To remedy this, Liu and Hsu[81] proposed the C_g^* integral which modified the C^* expression by including a plastic energy rate integral term. They claimed that this parameter can uniquely characterize creep crack growth behavior from the small scale yielding to extensive yielding. However,the creep law used in C_g^* is still the Norton's steady-state creep law.

4.5 Continuum Damage Mechanics Approach

It is clear from the above review, that the correlations between the various proposed parameters and the creep crack growth rate are basically empirical. None of these theories has been justified by consideration of the physical mechanisms of creep fracture. This is the principal deficiency of these techniques since the purpose of developing such theories is to extrapolate short-term laboratory data, obtained from small specimens, to large structural components which are expected to operate for thousands of hours. The only characteristic that can be used to justify such extrapolation is that the same physical mechanisms operate in the short term in the laboratory, as operate in the long term in the real structure. It is imperative, therefore, that further developments of these theories be related to the governing physical mechanisms.

The continuum damage mechanics approach was first introduced by Hayhurst et al[82]. In this approach, a constitutive equation of the continuum damage mechanics, equation (2.7), was used to describe the entire creep and damage processes under multiaxial states of stress. The boundary value problem for cracked specimens is solved by using the finite element method. The method allows creep damage to grow and the local failure occurs when the damage parameter in an element reaches the value of unity. After element failure takes place, the boundary value problem is redefined. In this way, the advancement of a zone of damage or a crack may be modeled. The unique advantage of the continuum damage mechanics approach is that it is consistent, to some extent, with the physical mechanisms that cause creep crack growth, as described by Hayhurst[82,83].

Hayhurst et al[82] studied crack growth in externally and internally cracked tension members under steady load in various materials of aluminum alloy, copper and in 316 stainless steel. The following major conclusions were drawn from his studies:

(1) The principal effect of continuum damage is to weaken the strength of the singular stress fields and eventually to nullify them. The near-tip stresses are overestimated by the C^* approach, which omits the growth of continuum damage as a field quantity; and

(2) The orientation of a growing crack propagation is dependent on the multiaxial stress rupture criterion of the material, the geometry of the cracked body and the loading

conditions. This behavior can not be modeled by other theories.

Although Hayhurst's continuum damage model appears to offer a great promise in creep fracture research, there are certain shortcomings in his approach. First, the instantaneous plastic strain was omitted in his model. It would be expected that the instantaneous plastic strain near the crack tip will give rise to a pronounced crack blunting before creep crack growth takes place and the blunt crack will cause widespread damage. Therefore, it is important to consider the influence of the plastic strain on the damage evolution and crack propagation.

Secondly, the Hayhurst's method necessitates the use of the finite element analysis to solve the boundary value problem. Due to the highly non-linear constitutive equations involved in the description of the creep strain and damage evolutions, the numerical time-integration can present difficulties.

Thirdly, this model assumes that the fracture of an element occurs when the damage parameter ω in the element approaches the value of unity. It is clear from equation (2.7) that both creep strain rate and damage rate approach infinity as $\omega \to 1$. This gives rise to a very serious numerical stability problem in the computations.

Finally, Hayhurst modeled the fracture process of the cracked specimen in an element-by-element manner. The fracture behavior predicted is, therefore, dependent on the shape and size of the elements. At this stage, the continuum damage mechanics method appears to be capable of predicting the rupture time of a

cracked body rather than the crack initiation and the subsequent growth.

4.6 Cyclic Creep Fracture

Many components operating at elevated temperatures are subjected to combined monotonic and cyclic loading which can lead to creep-fatigue interaction. The interaction of fatigue and creep or the effect of hold-times in low-cycle high-strain fatigue testing has been the subject of several reviews[84,85] and some predictive techniques, such as linear damage summation method, frequency-modified strain range method and strain range partitioning method have been developed[86,87,88]. In general, no single method is inherently more accurate than the other, although the linear damage summation method is the method most widely incorporated into design procedures due to its relative ease of application to a wide range of relevant creep-fatigue situations. The linear damage summation method is based on time and cycle fractions using a linear cumulative law equated to unity at failure, but it is often found that the combined effect of creep and fatigue was more damaging than the above model suggested. These models for creep rupture under cyclic stress conditions have been derived for uniform sections and the effects of stress concentrations due to the presence of cracks have not been taken into account.

Experimental work on crack propagation under cyclic creep conditions is very limited. The test results on 1 Cr-Mo-V steel by Ellison and Walton[89] and on 0.5 Cr-Mo-V steel by Smith and

Webster[90] showed that for the creep dominated fracture, the crack growth rate can be accelerated by the increase of loading frequency. One typical example is given in Figure 4.3[90]. Another interesting phenomenon is that the transient stress redistribution ahead of the crack tip is faster in cyclic tests than in static tests. These observations were supported by Harpner[91,92].

The linear damage summation method has been applied to cyclic creep crack propagation by Ellison and Walton[89]. They attempted to predict the cyclic creep crack growth rate by the linear summation of the independently assessed contributions from creep and fatigue as

$$(da/dt)_{c-f} = (da/dt)_c + da/dn \cdot dn/dt \qquad (4.21)$$

They found, however, the crack propagation rate predicted by this model was much lower than the test results. Attempts to correlate the cyclic creep crack growth rate with C^*-parameter have also been made[92,93,94]. So far, there is no firm evidence of a unique relationship between C^* and the cyclic creep crack growth rate. It is doubtful that the C^* approach could be used in cyclic creep fracture, as frequently large unloadings in cyclic conditions seriously violate the requirements of the path-independency of the C^* integral.

The reason why load cycling accelerates the creep crack propagation has not yet been explored. One possibility is that, as suggested by Ellison[75] and Webster[93], the stress levels are 'rejuvenated' after each cycle, which implies a more damaging

situation than in the static load case. However, this speculation has not been verified. The present work will investigate the stress redistribution and damage evolution near the crack tip under cyclic loading situations and assess the effect of the loading frequency on the creep crack growth.

CHAPTER 5

FINITE ELEMENT MODEL FOR CYCLIC CREEP FRACTURE BY CONTINUUM DAMAGE MECHANICS APPROACH

5.1 Introduction

The foregoing literature survey has revealed that all the proposed creep fracture parameters are subjected to some restrictions from the material ductility, specimen geometry, initial crack length and loading conditions. There is no single parameter which is capable of correlating the creep crack growth rate for a wide range of materials and test conditions. There is no theoretical evidence so far that these parameters can be used in cyclic creep fracture situations.

The continuum damage mechanics method has successfully been applied to creep crack propagation problems. The attractive feature of the approach is that the creep crack growth is predicted by evaluating the local damage evolution near the crack tip. Obviously, this method can be applied to the cyclic creep fracture if the local stress-strain-damage states near the crack tip can be determined in cyclic loading cases.

As described in Chapter 4, the major difficulties involved in the continuum damage approach are: (a) the absence of plastic strains; (b) numerical instability as $\omega \to 1$; and (c) mesh dependence of results. To extend the continuum damage mechanics method to cycle creep crack growth problems, these obstacles have to be eliminated.

This chapter presents a finite element model for cyclic creep fracture, which includes:

(1) a cyclic plasticity model for the determination of the stress-strain variation during plastic loading, unloading, reversed loading and reloading;

(2) a mixed explicit-implicit integration scheme for higher computational efficiency;

(3) a modified breakable element model for simulating the creep crack initiation and propagation. This technique can also eliminate the numerical instability associated with the damage criterion and reduce the mesh dependence of the results.

5.2 Cyclic Plasticity Constitutive Model

5.2.1 Theory of several yield surfaces and Mroz's hardening rule

As described in section 3.3.5, the Hsu-Bertels plasticity constitutive model (3.34), which is adopted in the current version of TEPSAC program, defines a one-to-one correspondence between stress and strain. Under cyclic loadings, the relationship between stress and strain is no longer one-to-one correspondent. A suitable plasticity hardening model for the determination of the stress-strain variation during plastic loading, unloading, reversed loading and reloading is essential for prediction of the material damage due to load cycling.

In this study, the plasticity model is based on the combined translations of several yield surfaces in the stress space[95]. Each yield surface is defined by the Von Mises criterion and it relates one of the piecewise linear segments

idealizing the uniaxial stress-strain material curve to the multiaxial stress state, as shown in Figure 5.1. Each yield surface is allowed to translate in the stress space up to its bounding yield surface to which it remains connected until the unloading stage. The translation rate is governed by the Mroz's hardening rule[96]. As shown in Figure 5.2, the Mroz's hardening rule assumes that the incremental translation of the current yield surface f_1 is in the direction of the vector which connects the stress point p on the current yield surface to the corresponding stress point R on the bounding yield surface f_{1+1}. The stress point R is defined by a vector $\overline{O_{1+1}R}$ which is parallel to the vector $\overline{O_1P}$.

The reason why the Mroz's hardening rule is adopted in the present study is that the Ziegler's hardening rule[29] is inconsistent with the theory of several yield surfaces in complex loading cases involving unloading and subsequent loading along a different stress path. Consider a two-yield surface system in two-dimensional stress field, as shown in Figure 5.3. As the material is initially isotropic, the yield surfaces f_1 and f_2 are similar and initially concentric, enclosing the origin 0. When a uniaxial stress σ_2 is applied, the stress point moves from 0 along the vertical axis. By increasing the load, it reaches the ellipse f_1 and makes f_1 moves along this axis until it contacts the ellipse f_2 at A. Now the specimen is partially unloaded to a point B inside f_1. Next a horizontal stress σ_1 is applied and the stress point moves parallel to the horizontal axis, reaching the ellipse f_1 at C. According to the Ziegler's hardening rule,

the instantaneous translation of f_1 will occur along O_1C. It is impossible in this case, because moving in this direction will not allow the point C to make contact with the ellipse f_2 without intersecting this ellipse. Mroz argued that C must move to a point D on f_2 since these two points correspond to the same direction of outward normal. The instantaneous translation of f_1 will thus occur along CD. Mathematically, the translation of the yield surfaces can be described as

$$d\alpha_{ij}^{(n)} = d\mu^{(n)} \, (\sigma_{ij}^{(n+1)} - \sigma_{ij}^{(n)}) \tag{5.1}$$

where $\alpha_{ij}^{(n)}$ is the tensor of the accumulated kinematic translation of the n^{th} yield surface and $\sigma_{ij}^{(n+1)}$ is the stress of the bounding yield surface with the same outward vector as the stress of the inner yield surface, $\sigma_{ij}^{(n)}$. This requires that

$$\sigma_{ij}^{(n+1)} = \alpha_{ij}^{(n+1)} + \frac{\sigma_y^{(n+1)}}{\sigma_y^{(n)}} \, (\sigma_{ij}^{(n)} - \alpha_{ij}^{(n)}) \tag{5.2}$$

where $\sigma_y^{(n+1)}$ and $\sigma_y^{(n)}$ are the material uniaxial stresses at the end of the $(n+1)^{th}$ and n^{th} linear segment of the linearized uniaxial stress-strain curve and $d\mu$ is a multiplier.

The employment of the concept of the combination of several yield surfaces enables both inclusion of the Bauschinger effect during reversed plasticity and description of the non-linear uniaxial material curve by several piecewise linear segments. The present model assumes that the material is of the Massing

type[109], namely, the stress-strain curves associated with one-dimensional symmetrical closed hysteresis loops should be of the same form as the initial loading curve except for an enlargement by a factor of two. Most of the engineering materials obey the Massing description[110]. Also, it is assumed that the material preserves in its memory the maximum stress values from the last plastic loading stage.

5.2.2 Formulations of the cyclic plasticity model

According to the several yield surfaces theory, the n^{th} yield surface, $f^{(n)}$, is defined by the Von Mises criterion as

$$f^{(n)} = \frac{1}{2} S'_{ij} \cdot S'_{ij} - \frac{1}{3} \sigma_y^{(n)2} = 0 \qquad (5.3)$$

in which S'_{ij} is the translated deviatoric stress tensor defined by

$$S'_{ij} = (\sigma_{ij} - \alpha_{ij}^{(n)}) - \frac{1}{3} \delta_{ij} (\sigma_{mm} - \alpha_{mm}^{(n)}) \qquad (5.4)$$

The plastic flow is now defined by the normality condition of the plastic strain increment to the associated n^{th} yield surface at the stress point:

$$d\varepsilon_{ij}^{p} = d\lambda^{(n)} \frac{\partial f^{(n)}}{\partial \sigma_{ij}} \qquad (5.5)$$

where $d\lambda^{(n)}$ is a positive scalar associated with the n^{th} yield surface.

Projecting $d\sigma_{ij}$ to the outward normal of the n^{th} yield surface leads to:

$$(d\sigma_{ij} - C^{(n)}\, d\varepsilon^{p}_{ij}) \cdot \frac{\partial f^{(n)}}{\partial \sigma_{ij}} = 0 \qquad (5.6)$$

where $C^{(n)}$ is a positive scalar to be determined.

By substitution of equation (5.5) into equation (5.6), one obtains

$$d\lambda^{(n)} = \frac{1}{C^{(n)}} \cdot \frac{(\partial f^{(n)}/\partial \sigma_{ij})\, d\sigma_{ij}}{(\partial f^{(n)}/\partial \sigma_{ij})(\partial f^{(n)}/\partial \sigma_{ij})} \qquad (5.7)$$

During the plastic loading $d\lambda^{(n)} \geq 0$, unloading begins when $d\lambda^{(n)} < 0$.

By substituting equations (3.15, 3.16 and 5.5) into equation (5.7), one gets

$$d\lambda^{(n)} = \frac{1}{h^{(n)}} \cdot \frac{\partial f^{(n)}}{\partial \sigma_{ij}} D^{e}_{ijkl}\, d\varepsilon_{kl} \qquad (5.8)$$

where

$$h^{(n)} = C^{(n)} \frac{\partial f^{(n)}}{\partial \sigma_{ij}} \cdot \frac{\partial f^{(n)}}{\partial \sigma_{ij}} + \frac{\partial f^{(n)}}{\partial \sigma_{ij}} D^{e}_{ijkl} \frac{\partial f^{(n)}}{\partial \sigma_{kl}} \qquad (5.9)$$

By combining equations (5.8) and (5.9) with (5.5), and substituting into equations (3.15) and (3.16), one obtains

$$d\sigma_{ij} = (D^{e}_{ijkl} - D^{p}_{ijkl})\, d\varepsilon_{kl} = D^{ep}_{ijkl}\, d\varepsilon_{kl} \qquad (5.10)$$

where

$$D^{p}_{ijkl} = \frac{1}{h^{(n)}} D^{e}_{ijkl} S'_{ij} S'_{kl} D^{e}_{ijkl} \tag{5.11}$$

and

$$D^{ep}_{ijkl} = D^{e}_{ijkl} - \frac{1}{h^{(n)}} D^{e}_{ijkl} S'_{ij} S'_{kl} D^{e}_{ijkl} \tag{5.12}$$

The scalar $C^{(n)}$ in equation (5.9) physically means the stiffness of the material during the plastic deformation. As the stress ($\bar{\sigma}$) versus strain ($\bar{\varepsilon}$) curve becomes anisotropic due to the postulated shift of the yield surfaces, the stiffness of the material varies from one direction to another. Taking into account of such an anisotropy, Hsu suggested that the value of $C^{(n)}$ can be determined as follows[27]:

$$\frac{1}{C^{(n)}} = \frac{1}{H_{ij}} \left(\frac{\sigma_{ij}}{\sigma_w}\right)^2 \tag{5.13}$$

where $2\sigma_w^2 = B_{ij} (\sigma_{ij})^2 + \delta_{ij} (\sigma_{ij})^2$ (sum over i,j = 1,2,3)

$B_{ij} = 1$

H_{ij} = weighted $H^{(n)}$

with $H^{(n)}$ defined by

$$H^{(n)} = \frac{1}{\frac{1}{E_t^{(n)}} - \frac{1}{E}} = \frac{E \cdot E_t^{(n)}}{E - E_t^{(n)}}$$

where $E_t^{(n)}$ is the slope of the $(n+1)^{th}$ linear segment of the uniaxial material stress-strain curve.

Now, in order to complete the mathematical formulation, the translation of the yield surface, $d\alpha_{ij}^{(n)}$ defined by the Mroz's hardening rule equation (5.1), should be determined. The scalar $d\mu^{(n)}$ in equation (5.1) is determined by the condition that the stress point remains on the yield surface during the plastic flow

$$df^{(n)} = \frac{\partial f^{(n)}}{\partial \sigma_{ij}} (d\sigma_{ij} - d\alpha_{ij}^{(n)}) = 0 \tag{5.14}$$

substituting equation (5.1) into equation (5.14), one obtains

$$d\mu^{(n)} = \frac{S'_{ij} \cdot d\sigma_{ij}}{(\sigma_{ij}^{(n+1)} - \sigma_{ij}^{(n)}) S'_{ij}} \tag{5.15}$$

Translating the above equations into appropriate matrix forms facilitates the finite element formulations which are summarized as follows:

(1) Constitutive equation (5.10)

$$\{d\sigma\} = [D_{ep}] \{d\varepsilon\} \tag{5.16}$$

(2) Elastic-plastic matrix

$$[D_{ep}] = [D_e] - \frac{1}{h^{(n)}} [D_e] \{S'\} \{S'\}^T [D_e] \tag{5.17}$$

where

$$h^{(n)} = C^{(n)} \{S'\}^T \{S'\} + \{S'\}^T [D_e] \{S'\} \quad \text{(multiaxial)} \tag{5.18}$$

with $C^{(n)}$ defined by the expression (5.13).

(3) Proportionality factor (5.8)

$$d\lambda^{(n)} = \frac{1}{h^{(n)}} \cdot \{S'\}^T [D_e] \{d\varepsilon\} \tag{5.19}$$

(4) Multiplier (5.15)

$$d\mu^{(n)} = \frac{\{S'\}^T \{d\sigma\}}{(\{\sigma^{(n+1)}\} - \{\sigma\})^T \{S'\}} \tag{5.20}$$

where

$$\{\sigma^{(n+1)}\} = \{\alpha^{(n+1)}\} + \frac{\sigma_y^{(n+1)}}{\sigma_y^{(n)}} (\{\sigma\} - \{\alpha^{(n)}\}) \tag{5.21}$$

(5) Translation of yield surfaces (5.1)

$$\{d\alpha^{(n)}\} = d\mu^{(n)} (\{\sigma^{(n+1)}\} - \{\sigma^{(n)}\}) \tag{5.22}$$

Note that the translated deviatoric stress tensor $\{S'\}$ defined by equation (5.4) and quantities $h^{(n)}$, $d\lambda^{(n)}$ and $d\mu^{(n)}$ are all related to the n^{th} yield surface. Therefore, after completing the stress calculation for every load step, it is necessary to check which yield surface the current stress state is associated with. This cyclic plasticity model has been implemented into the TEPSAC program.

5.3 Mixed Explicit-Implicit Algorithm for Creep Stress Analysis

Proper selection of time-integration scheme is a very important step in the creep stress analysis of solids. Both explicit and implicit algorithms are widely used for such purposes. As described in section 3.5.1, the explicit scheme is much more expedient in computations than the implicit scheme. Unfortunately, this scheme usually results in an unstable situation and extremely small time increments have to be used. The implicit scheme is more stable, but requires substantially more computational effort in every step of calculations.

The stability condition associated with the explicit scheme of Norton's law creep, i.e. equation (3.47), reveals that the critical time step size ensuring stability is controlled by the element where the highest stress or highest creep strain rate occurs. For the portion of the structure at a lower stress or lower creep strain rate, much larger time steps can be used without causing instability. According to equation (3.47), for those elements in which the value of the effective stress is 0.6 of the maximum effective stress in the structure, the time step could be 7.7 to 99.2 times the critical one, depending on the value of the creep exponent n which ranges from 5 to 10 for most metals. For creep fracture problems, high stress concentration occurs at the crack tip, while stress levels in the remaining portions of the specimen are relatively low. Selecting time step sizes according to the crack tip stress or strain rates is obviously not economical and unnecessary. A desirable situation, however, is to develop a computational model which includes both

these algorithms with the implicit algorithm being used for those elements near the crack tip and the explicit algorithm for the remaining part of the specimen.

5.3.1 Formulations of the mixed explicit-implicit algorithm

We consider a finite element model in which elements are partitioned into two groups: the explicit elements and the implicit elements. The integration schemes corresponding to these two element groups, which have been given in Section 3.5, are summarized as follows:

(1) Explicit elements

$$\{\Delta\varepsilon^t\} = \{\dot{\varepsilon}^c_n\}\ \Delta t \tag{5.23}$$

$$\Delta\omega = \dot{\omega}_n\ \Delta t \tag{5.24}$$

$$\{\Delta\sigma\} = [D_{ep}]\ ([B]\{\Delta u\} - \{\dot{\varepsilon}^c_n\}\ \Delta t) \tag{5.25}$$

$$\left(\int_v [B]^T[D][B]dv\right)\ \{\Delta u\} = \int_v [B]^T[D_{ep}]\{\dot{\varepsilon}^c_n\}\Delta t\ dv + \{\Delta F\} \tag{5.26}$$

(2) Implicit Elements

$$\{\Delta\varepsilon^c\} = [(1-\gamma)\{\dot{\varepsilon}^c_n\} + \gamma\{\dot{\varepsilon}^c_{n+1}\}]\ \Delta t\ , \quad 0\leq\gamma\leq 1 \tag{5.27}$$

$$\Delta\omega = [(1-\gamma)\dot{\omega}_n + \gamma\dot{\omega}_{n+1}]\ \Delta t \tag{5.28}$$

$$\{\dot{\varepsilon}^c_{n+1}\} = \{\dot{\varepsilon}^c_n\} + [H_1]\ \{\Delta\sigma\} + \{H_2\}\ \Delta\omega + \{H_3\}\ \Delta t \tag{5.29}$$

$$\dot{\omega}_{n+1} = \dot{\omega}_n + [G_1]\{\Delta\sigma\} + G_2\ \Delta\omega \tag{5.30}$$

in which

$$[H_1] = \frac{\partial\{\dot{\varepsilon}^c\}}{\partial\{\sigma\}}, \quad \{H_2\} = \frac{\partial\{\dot{\varepsilon}^c\}}{\partial\omega}, \quad \{H_3\} = \frac{\partial\{\dot{\varepsilon}^c\}}{dt} \tag{5.31}$$

$$[G_1] = \frac{\partial\dot{\omega}}{\partial\{\sigma\}}, \quad G_2 = \frac{\partial\dot{\omega}}{\partial\omega} \tag{5.32}$$

then

$$\{\Delta\sigma\} = [D^*_{ep}]\ ([B]\{\Delta u\} - \{\dot{\varepsilon}^c_n\}\ \Delta t - (g\{H_2\}\dot{\omega}_n + \{H_3\})\ \gamma\Delta t^2) \tag{5.33}$$

where

$$[D^*_{ep}] = \{[I] + \gamma\Delta t[D_{ep}]\ ([H_1] + \gamma g\{H_2\}[G_1]\Delta t)\}^{-1}\ [D_{ep}] \tag{5.34}$$

$$g = \frac{1}{1 - \gamma\ G_2\ \Delta t} \tag{5.35}$$

$$\left(\int_v [B]^T[D^*_{ep}][B]dv\right)\{\Delta u\} = \int_v [B]^T[D^*_{ep}]\ (\{\dot{\varepsilon}^c_n\}\Delta t + (g\dot{\omega}_n\{H_2\} + \{H_3\})\gamma\Delta t^2)\ dv + \{\Delta F\} \tag{5.36}$$

Recall the constitutive equation (2.7):

$$\{\dot{\varepsilon}^c\} = \frac{3}{2} A \left(\frac{\bar{\sigma}}{1-c\omega}\right)^n \cdot \frac{\{S\}}{\bar{\sigma}}\ t^m \tag{5.37 a}$$

$$\dot{\omega} = B \left[\frac{(1-\alpha)\bar{\sigma} + \alpha\sigma_I}{1 - \omega}\right]^\phi \tag{5.37 b}$$

For this constitutive model which will be used in the analysis of the cyclic creep crack growth in this study, the matrices in (5.31) and (5.32) can be expressed explicitly as

$$[H_1] = \frac{3}{2} A\, t^m \left(\frac{\bar{\sigma}}{1-c\omega}\right)^n \frac{1}{\bar{\sigma}} \left(\frac{3(n-1)}{2\bar{\sigma}^2} ([Q]\{\sigma\})\,([Q]\{\sigma\})^T + [Q]\right) \tag{5.38}$$

$$\{H_2\} = \frac{cn}{1-c\omega} \{\dot{\varepsilon}_n^c\}\,, \qquad \{H_3\} = \frac{m}{t} \{\dot{\varepsilon}_n^c\} \tag{5.39}$$

$$[G_1] = \frac{\phi\dot{\omega}}{[(1-\alpha)\bar{\sigma} + \alpha\sigma_I]} \left[\alpha \frac{\partial \sigma_I}{\partial\{\sigma\}} + (1-\sigma)\frac{\partial\bar{\sigma}}{\partial\{\sigma\}}\right] \tag{5.40}$$

For plane case[97]

$$\sigma_I = \frac{\sigma_x + \sigma_y}{2} + \sqrt{\left(\frac{\sigma_x - \sigma_y}{2}\right)^2 + \tau_{xy}^2} \tag{5.41}$$

Hence

$$\frac{\partial\sigma_I}{\partial\{\sigma\}} = \left[\frac{1}{2} + \frac{\sigma_x - \sigma_y}{4\sqrt{\left(\frac{\sigma_x-\sigma_y}{2}\right)^2 + \tau_{xy}^2}} \quad \frac{1}{2} - \frac{\sigma_x - \sigma_y}{4\sqrt{\left(\frac{\sigma_x-\sigma_y}{2}\right)^2 + \tau_{xy}^2}} \quad \frac{\tau_{xy}}{\sqrt{\left(\frac{\sigma_x-\sigma_y}{2}\right)^2 + \tau_{xy}^2}}\right] \tag{5.42 a}$$

$$\frac{\partial\bar{\sigma}}{\partial\{\sigma\}} = \frac{3}{2\bar{\sigma}} \{S\}^T \tag{5.42 b}$$

The matrix [Q] in equation (5.38) is defined by the relation $[S] = [Q]\{\sigma\}$. These explicit expressions simplify calculation and reduce the storage requirement during the computations.

5.3.2 Self-adjusting element partition of the mixed explicit-implicit scheme

The unique feature of the present mixed explicit-implicit scheme is that the partition of two element groups is self-adjusting based on the rates of creep strain and damage in these elements. Before every computation step, the definition of explicit and implicit element groups is carried out according to the following criteria:

$$(\dot{\bar{\varepsilon}}^c)_e \geq (\dot{\bar{\varepsilon}}^c)_s \qquad (5.43\ a)$$

$$(\dot{\omega})_e \geq (\dot{\omega})_s \qquad (5.43\ b)$$

in which the subscripts e and s denote the current values in the element and the respective specified values. If either of these conditions is satisfied in a particular element, that element will be treated as an implicit element. The contrary, of course, would be treated as explicit elements. If the parameters $(\dot{\bar{\varepsilon}}^c)_s$ and $(\dot{\omega})_s$ are properly chosen, implicit elements would take up a relatively large area in the specimen in the early stage due to high strain rates in the material during primary creep stage. The number of the implicit elements will be automatically reduced with time as the creep deformation proceeds beyond the primary stage and the creep strain rate reduces. During such time, only a small number of elements near the crack tip remains to be treated as implicit. Since implicit elements require many more operations than explicit elements, this self-adjusting element

partition algorithm results in a significant saving in the computational effort.

In order to make the mixed explicit-implicit scheme effective, the parameters $(\dot{\varepsilon}^c)_s$ and $(\dot{\omega})_s$ have to be properly selected. If the values of these two parameters specified are too small, the implicit element group would be too large, resulting in low computational efficiency. On the other hand, if these two values are too large, the implicit element group would be so small that the allowable time step sizes would have to remain very small. From the author's experiences, the values between 0.01% ~ 0.1% hr^{-1} for $(\dot{\bar{\varepsilon}}^c)_s$ and between 0.05 ~ 0.1 hr^{-1} for $(\dot{\bar{\omega}})_s$ were found realistic for creep fracture problems.

5.3.3 Automatic time step control

Both constant and variable time increments are allowed in the present mixed explicit-implicit algorithm. For the variable time step scheme, the selection of the time increment is based on the following two considerations:

(1) Restriction on the increase in creep strain. It is suggested that the magnitude of the time step be related to the ratio of incremental effective creep strain to the total effective strain. This ratio is limited by an input parameter τ_1, which can be used to evaluate an allowable time step size by the following expression:

$$\Delta t_1 = \tau_1 \frac{\bar{\varepsilon}}{\sqrt{2/3 \{\dot{\varepsilon}^c\}^T \{\dot{\varepsilon}^c\}}} \tag{5.44}$$

The value of τ_1 used by the author in the creep fracture analyses has been between 0.5 and 1.0 with no indication of instability.

(2) Restriction on the increase in the damage parameter. The following relation is employed:

$$\Delta t_2 = \tau_2 \frac{1}{\dot{\omega}} \tag{5.45}$$

where τ_2 is an input parameter controlling the time steps on the basis of the changes of the damage. The value of τ_2 may be selected from the range 0.05 to 0.1, according to our computational experiences.

Conditions (5.44) and (5.45) are applied to all elements of the structure. Then the time increment for the next step of calculations can be selected by

$$\Delta t = \text{Min}[\Delta t_1, \Delta t_2] \tag{5.46}$$

Since oscillations may result from abrupt changes of the time step, a limit of time step change to one half of the previous step was adopted.

The present mixed explicit-implicit algorithm has been implemented into the TEPSAC program. The details of the computer implementations and numerical examples showing a high computational efficiency of this algorithm can be found in the author's recent paper[98] attached to this thesis as an Appendix. This algorithm has also been applied to creep fracture problems to provide a more realistic approach[99].

5.4 'Breakable Element' Algorithm

The 'breakable element' algorithm was first proposed by Hsu and Bertels to model crack growth in an elastic-plastic fracture analysis[100]. The concept of the 'breakable element' is based on the successive reduction of the stiffness matrix of elements containing crack tip during crack growth. Hsu and Kim[101,102] further improved the computational accuracy by creating a pseudo nodal point in the element. This pseudo nodal point moves through the breakable element as the crack tip extends, producing a smooth crack growth. This numerical technique in conjunction with the rupture strain criterion has recently been applied to a creep crack propagation problem by Hsu and Zhai[103].

In this analysis, a modification in the 'breakable element' model has been made to incorporate the damage criterion of the continuum damage mechanics as described in Section 4.5. The local remesh of the element containing crack tip is introduced to avoid the deterioration of the crack tip element, which may take place when the crack tip nodes approach the nodes of the adjacent element during crack growth. The procedure of the 'breakable element' technique employed in this analysis is outlined as follows:

Step 1 A number of 'breakable elements' are positioned along the expected crack path as shown in Figure 5.4(a). Upon completion of the stress analysis at any time step, the values of the damage parameter ω in breakable elements are extrapolated as a smooth curve toward the crack tip using a least squares curve fitting

technique. Usually, the damage ω changes significantly at the first four element immediately adjacent to the crack tip. Therefore, the damage ω at the crack tip is extrapolated based on the values at the centroids of these elements, as shown in Figure 5.4(b). The distribution of the damage ω ahead of the crack tip is thus expressed as

$$\omega(x) = a_1 x^3 + a_2 x^2 + a_3 x + a_4 \tag{5.47}$$

where x denotes the distance from the crack tip along the crack path and a_1, a_2, a_3 and a_4 are constants derived from the least square analysis of the average strains at the element centroids (x_1, x_2, x_3, x_4). The extrapolated damage at the crack tip can be expressed as $\omega_{ext} = \omega(0)$. No crack extension is considered to occur if $\omega_{ext} \leq 0.99$. The computation may proceed further until $\omega_{ext} > 0.99$.

Step 2 At the time $\omega_{ext} > 0.99$ in any portion of a breakable element, crack growth process begins and the amount of crack extension, Δx, is evaluated by solving for the value of x in equation (5.47) at which $\omega(x) = 0.99$.

Step 3 The original nodal points at the crack tip are shifted by the amount Δx shown in Figure 5.4(b) to the positions of the pseudo nodal points, which specify the current location of the crack tip. Figure 5.5(b) illustrates schematically the shifting of the crack tip nodes. The value of the damage ω in the new

crack tip element is updated by using equation (5.47), based on the location of the element centroid.

Step 4 The $[K]^e$ matrices of the elements surrounding the crack tip are re-evaluated for the next time step. As shown in Figure 5.5(b), the nodal point shift changes the geometries of elements surrounding the crack tip. The geometry change in these elements causes a change in the [B] matrix, which in turn changes the [K] matrix in equation (3.4). Thus, after the crack tip nodes shift, the $[K]^e$ matrices of the corresponding elements are evaluated according to

$$[K']^e = \int_{v'} [B']^T [D] [B'] \, dv' \tag{5.48}$$

where $[K']^e$ is the re-evaluated $[K]^e$ matrix;

$[B']$ is the [B] matrix after the nodal point shift; and

v' is the changed volume of the elements surrounding the crack tip.

Step 5 The shifting to the new pseudo nodal points at each time step continues so long as ω_{ext} exceeds 0.99. If the crack tip reaches the middle point of the original crack tip element, this point becomes the new crack tip and the topology is locally modified as shown in Figure 5.5(c). The element is then considered to have fractured and incapable of carrying any load. Consequently, the nodal forces carried by this element before it breaks have to be released and the equivalent stress field near

the crack tip has to be redistributed to the entire structure, with those elements immediately adjacent to the new crack surfaces taking most of it. This force release is simulated by the following nodal force relaxation step.

Step 6 The stiffness matrix of the broken element is set to be zero so it will not carry any load in the further analysis.

Since relaxation occurs in the direction normal to the path of crack growth, the equivalent forces are applied to the structure as illustrated in Figure 5.6. These forces applied to each node can be calculated by

$$F_1 = F_2 = \sigma_{yy} \cdot L/4 \tag{5.49}$$

in which σ_{yy} is the stress component normal to the crack line before the element breaks and L is the original length of the breakable element. In order to maintain a smooth computation, small load increments have to be used. The equivalent forces are, therefore, applied to the specimen over 10 equal incremental loading steps. A stress analysis on the entire structure is performed with these nodal forces, while the external load remains constant during this process. The increments of displacements and stresses so derived are added to the accumulated displacements and stresses of the structure.

The 'breakable element' technique described above can effectively overcome the instability problems associated with the creep crack growth analyzed by the continuum damage approach.

Although the extrapolated damage in the portion of the element near the crack tip exceed 0.99 when the crack extends, the value of the damage at the centroid of the crack tip element which is used in the computations is still well below this critical value. Consequently, relatively large time steps can still be used without losing stability even when the crack starts to grow. Furthermore, by using this numerical model, the onset of the creep crack growth can readily be predicted and the amount of the crack extensions can also be determined. Therefore, this model is capable of simulating the entire process of creep crack propagation.

5.5 Computer Code 'TEPSAC'

A finite element computer code TEPSAC[27] (Thermal Elastic-Plastic Stress Analysis with Creep) has been employed in this investigation for the numerical modeling of cyclic creep crack growth. The TEPSAC code was originally developed by Hsu and his associates[104] to analyze thermal elastic-plastic stress problems. The code, although limited to two-dimensional plane, or three-dimensional axisymmetric structures, can handle large classes of thermomechanical problems using a simplex element algorithm. The fracture mechanics module has been implemented by Kim[102] to simulate stable crack growth. As described in this chapter, this crack growth model has been modified and a cyclic plasticity theory and a mixed explicit-implicit integration scheme have been implemented. With these modifications, the TEPSAC code now becomes a powerful computer program dealing with cyclic creep crack propagation problems.

CHAPTER 6

CREEP CRACK GROWTH UNDER STATIC LOADINGS

6.1 Introduction

The finite element computer program TEPSAC with the numerical modeling technique presented in Chapter 5 is employed in a study of the creep fracture behavior of a 316 stainless steel panel subjected to static loadings. The main concern of this study is the role of the instantaneous plasticity in the creep fracture. To the author's knowledge, since the plastic strain is usually neglected in most of creep fracture analysis, its effects on the creep fracture behavior of materials are not clear yet. Two cases, one with and the other without plastic strains, are analyzed. The influence of the plastic strain on the stress redistribution ahead of the crack tip, on the damage evolution, and on the crack initiation and subsequent growth are discussed.

6.2 Description of the Problem

A centre-notched panel with the dimensions defined in Figure 6.1 is subjected to a boundary stress σ_0 = 70 MPa. This plate is assumed to be in plane stress condition.

The material of this plate is assumed to be 316 stainless steel at 650°C. The uniaxial tension stress-strain curve of this material at 650°C, which is tested in the thermomechanics lab at the University of Manitoba, is shown in Figure 6.2. This curve is idealized by three piecewise linear segments depicted by dotted lines. The corresponding elastic- plastic properties taken from this figure are given in Table 1.

TABLE 1

ELASTIC-PLASTIC PROPERTIES OF 316 STAINLESS STEEL AT 650°C

Modulus of Elasticity	E_i	130,000 MPa
Plastic Tangent Moduli	$E_t^{(1)}$	5,000 MPa
	$E_t^{(2)}$	2,667 MPa
Yield Strength	$\sigma_{ys}^{(1)}$	120 MPa
	$\sigma_{ys}^{(2)}$	165 MPa

TABLE 2

CREEP PROPERTIES OF 316 STAINLESS STEEL AT 650°C

A	1.14×10^{-15}
n	5.51
m	-0.47
C	0.7
B	2.64×10^{-13}
ϕ	4.23
α	0.7

(units in megapascals, absolute creep strain and hours)

The uniaxial creep tests for this material were also carried out in the thermomechanics lab. The uniaxial creep data, as shown in Figure 6.3, were used to determine the material constants involved in the creep constitutive equation (5.37). The parameter α, which determines the damage evolution under a multi-dimensional stress state, was taken from Hayhurst et al[82]. The creep properties were determined by fitting the curves in Figure 6.3. Table 2 summarizes the creep properties used in the analysis.

A finite element model of the specimen is shown in Figure 6.4(a), with the details of the refined mesh surrounding the crack tip given in Figure 6.4(b). Due to the symmetry in geometry and boundary conditions, only one quarter of the plate needed to be considered. A total of 312 elements were used together with 273 nodes representing 506 degrees of freedom. In order to minimize the possible discretization effects on crack growth, elements of relatively small size were distributed uniformly in the vicinity of the crack tip. A layer of identical quadrilateral elements representing the breakable elements was placed along the projected crack path. The height of each breakable element was 0.05mm, that is, 1/200 of the original crack length.

By using this finite element model, two cases of creep crack growth are studied. Case 1 is a fully elastic-plastic-creep analysis. In case 2, plasticity is excluded by setting a artificially high value of the yield strength for the material.

6.3 Predictions of Crack Initiation and Crack Growth

The creep crack growth histories of the specimen for the cases with and without plastic strains are depicted in Figure 6.5. The predicted crack initiation time for the case with plastic strains is 182 hours, while the same time for the case without plastic strains is 276 hours. The incubation time in the later case is about 50% longer than that in the former case. On the other hand, as indicated in Figure 6.5, the crack grows much slower in the case with plastic strains.

A direct correlation of the numerical predictions to test data is not available in the present stage. However, Figure 6.6 shows a comparison of the present study with experimental results presented in [79]. Mass and Pineau carried out the creep fracture test for 316 stainless steel at 600°C and correlated the crack growth rate to the C^* parameter. In the present study, the crack growth rates, $\dot{a}$, were directly obtained from Figure 6.5 and the corresponding values of C^* were calculated by using equation (4.19). It can be seen from Figure 6.6 that the crack growth rates predicted in the case with plastic strains agree with the test results very well. The predicted crack growth rate for the case without plastic strains appear too high in comparison to the test results. Note that the test temperature is not exactly the same as used in our study. However, since the relationship between the crack growth rate $\dot{a}$ and the C^* parameter is temperature independent as pointed out by Taira and Ohtani[106], these comparisons are still useful.

Taira and Ohtani[106] tested 304 stainless steel at 650°C. Figure 6.7 shows the correlation between the crack growth rate and the net section stress. As the chemical compositions and the creep properties for 304 SS and 316 SS are quite close, it is possible to compare our numerical results with their test data. Figure 6.7 shows that the crack growth rate prediction for the case with plastic strains is in good agreement with the test results. It seems that the case without plastic strains predicts too high crack growth rate.

The fact that these comparisons are all in favour of the case with plastic strains suggests that the instantaneous plasticity should be included in the creep fracture analysis to obtain a realistic prediction of the creep crack initiation and propagation. More experimental verifications of the analytical results are necessary to confirm this point.

6.4 Plastic Zone

In finite element computations, plasticity is defined by the value of $d\lambda$, determined by equation (5.19). Areas in which this value is greater or equal to zero are denoted in Figure 6.8 as the plastic zone for various stages of creep in the specimen. The initial plastic zone right after loading is relatively large. As indicated in Figure 6.8, the plastic zone shrinks very rapidly. After 1 hour of creep, the plastic zone diminishes to a small region near the crack tip. After 10 hours, it is confined to only a few elements away from the crack tip. It is interesting to note that at that time, the crack tip element is

no longer plastic and the plastic zone moves away from the crack tip. The plastic zone vanishes before the crack propagation begins. In the crack propagation stage, the entire region of the specimen is actually in an elastic state.

The rapid diminishing of the plastic zone is due to a fast stress relaxation in the plastic zone. The high stress level in the plastic zone causes fast creep deformation which is constrained by surrounding elastic region where the creep strain is much lower. Consequently, unloading in the plastic zone occurs and the plastic zone shrinks.

The short duration of the plastic strains in the specimen does not mean that the influence of the instantaneous plasticity is insignificant. On the contrary, the instantaneous plasticity significantly affects the entire creep fracture process. It has been shown in the previous section that the presence of plastic strains leads to a prediction of considerably earlier crack initiation and slower crack propagation. Its effects on the stress distribution and the damage evolution ahead of the crack tip will be discussed in the next section.

6.5 Stress Distribution and Damage Evolution Ahead of Crack Tip

In the present study, a crack extension is assumed to occur when the value of the extrapolated damage at the crack tip exceeds 0.99. The creep fracture behavior of the material is, therefore, controlled by the damage evolution and distribution ahead of the crack tip. According to the theory of the continuum damage mechanics, the rate of the damage is determined by the

linear combination of the effective stress and the maximum principal stress (equation (2.7 b)). As a consequence, the redistribution of the effective stress and the maximum principal stress ahead of the crack tip plays an important role in the creep crack growth.

6.5.1 Stationary crack

The histories of the effective stress and the maximum principal stress at the centroid of the element immediately ahead of the crack tip for both cases, with and and without plastic strains, are presented in Figure 6.9 and 6.10 respectively. The maximum principal stress coincides with the normal stress to the crack sufaces, i.e. σ_{yy}. The effective stress and the maximum stress decrease with time very rapidly for both cases. As described in Chapter 4, C^* approach suggests that after an initial transient period, the near tip stress field reaches a stable state characterized by C^*. Figures 6.9 and 6.10 show that no such stable state can be found when the damage in the material was taken into account.

It can be seen from Figures 6.9 and 6.10 that the initial stresses in the crack tip element for the case without plastic strains were much higher than that for the case with plastic strains. The initial elastic stresses in the former case relaxed very rapidly. Consequently, after a very short time of creep, the crack tip stresses in the former case became lower than that in the latter case. This situation lasted for about 130 hours.

The higher crack tip stresses for the plasticity case resulted in a faster damage rate in the crack tip element, as shown in Figure 6.11. The higher damage rate in turn caused faster damage accumulation, as depicted in Figure 6.12. As a result, the crack initiation in the case with plastic strains was considerably earlier than in the case without plastic strains.

The distributions of the effective stress ahead of the crack tip at various times before the crack initiation are presented in Figures 6.13, 6.14 and 6.15. At t = 0, the initial elastic stress distribution shows much higher stress gradient near the crack tip than the elastic-plastic stress distribution. However, at t = 10 hours, due to a faster stress relaxation occurring in the case without plastic strains, the stress gradient ahead of the crack tip in this case became lower than that in the case with plastic strain, as illustrated in Figure 6.14. Figure 6.15 indicates that this phenomenon is more pronounced at t = 100 hours. Figures 6.16, 6.17 and 6.18 plot the distributions of the maximum principal stress ahead of the crack tip at various times, showing the same features.

The higher stress gradient near the crack tip in the case with plastic strains causes the higher gradient of the damage rate. Figure 6.19 shows the distribution of the damage rate at t = 100 hours for both cases. The distributions of the damage parameter ahead of the crack tip at t = 100 hours for both cases are depicted in Figure 6.20. In the first two elements adjacent to the crack tip, the values of the damage parameter for the case considering plasticity are higher than that for the case omitting

plasticity. This is the reason why the crack starts to propagate earlier in the former case. Figure 6.20 also indicated that in the subsequent elements, the values of the damage parameters for the former case are considerably lower. It would be expected, therefore, that after the first two elements broke, it might take longer for the extrapolated damage at the crack tip to grow up from a lower level to a critical value to cause crack extension in the former case. This can probably be used to explain the reason why the creep crack propagates slower in the case with plastic strains than that without plastic strains.

6.5.2 Growing crack

The distributions of the effective stress and the maximum principal stress at various crack growth stage are plotted in Figures 6.21 through 6.25 and Figures 6.26 through 6.30 respectively. It is observed from these figures that the crack tip stress is quite low and the peak stress occurs at a location away from the crack tip. The C^* theory suggests that there is a stress singularity at the crack tip, characterized by the C^* parameter. The present study indicates that this is not true.

These figures also show that the peak stress decreases with crack propagation. This implies that there is no stable stress distribution ahead of the moving crack tip which was suggested by the C^* theory.

A comparison of the stress distributions for the cases with and without plastic strains indicates that after the first two elements broke, the effective stress and the maximum principal

stress for the latter case are higher along the crack extension line.

Figures 6.31 through 6.35 illustrate the distributions of the damage rate ahead of the moving crack tip. It can be seen from these figures that the damage along the crack extension line for the case without plastic strains accumulates faster. This is obviously due to the higher effective stress and maximum principal stress for this case in the creep crack propagation process.

The damage distributions ahead of the moving crack tip are illustrated in Figures 6.36 through 6.40. These figures indicated that the case omitting plastic strains is more damaging than the case considering plastic strains. This is why the creep crack growth rate in the former case is faster.

6.6 Crack Profile

Figure 6.41 shows the crack profiles for both cases at the crack initiation times. The crack is sharper in the case neglecting plastic strains. The reason is that the material becomes less ductile in the absence of plastic strains.

Figures 6.42 through 6.45 illustrate the crack profiles at various stages of the crack growth. Comparing these figures with Figure 6.42, one may observe that the growing crack is sharper than the stationary crack. These results confirm the observations made by Taira et al[107]. and Hsu et al[103].

These figures also show that both COA (crack opening angle) and CTOA (crack tip opening angle) are not constant, no matter whether plasticity is included in the analysis or not. For a

given crack length, CTOA for the case omitting plastic strains is smaller.

6.7 Brief Summary

Numerical results obtained by using the proposed algorithm agreed well with limited available experimental results presented by other researchers. The case studies presented in this chapter have revealed the significance of the instantaneous plasticity in the creep crack propagation under static loadings. For a cracked panel subjected to static loadings, the role of the plastic strains is to slow down the stress relaxation at the vicinity of the crack tip. The slower stress relaxation causes the damage to accumulate faster in the near tip region and slower in the area away from the crack tip. Such a confined damage results in an earlier crack initiation and slower crack propagation. If the instantaneous plasticity is neglected in the creep fracture analysis, both the crack initiation time and the creep crack growth rate may be overestimated.

Numerical results have revealed no stress singularity near the crack tip. As well, no stable stress distribution ahead of the growing crack. These discoveries contradict the prediction by the popular C^* parametric studies.

CHAPTER 7

CREEP CRACK GROWTH UNDER CYCLIC LOADINGS

7.1 Introduction

The significance of the plasticity in the creep crack growth under static loadings has been discussed in Chapter 6. It would be expected that the plasticity plays an even more important role in the cyclic loading case. In the absence of plastic strains, a linear unloading and reloading would not change the local stress state at the crack tip. However, in the presence of the plastic strains, a reverse yielding associated with unloading would cause an instantaneous elastic-plastic stress distribution to be superimposed upon reloading. The stress change near the crack tip would influence the damage evolution and hence the creep fracture behavior of the material. This chapter will investigate the effects of the plasticity on the cyclic creep crack growth.

7.2 Description of the Problem

The major factors affecting the creep crack propagation under cyclic conditions involve the frequency, the shape and amplitude of the loading cycles and the operating temperature. Since the purpose of the present study is to investigate the role of the plasticity associated with unloading and reloading in the creep dominated crack growth, a constant temperature is assumed in the analysis. For the sake of simplicity, the loading pattern considered here is repeated loadings without a rest period, as

shown in Figure 7.1. The unloading-reloading is assumed to be done so quickly that no creep recovery would take place in that period. As explained in Chapter 2, the continuum damage constitutive model, i.e. equation (2.7), can be used to describe the creep and damage processes in the material for this loading pattern.

The computational model including the geometry and dimensions of the panel structure and the material properties are those presented in Chapter 6. Three loading cases have been analyzed. In the first case, a static boundary stress $\sigma_0 = 70$ MPa is applied. The other two cases consider the repeated loadings with the maximum boundary stress of 70 MPa and the minimum boundary stress of 5 MPa. Unloading and reloading are executed every 50 hours in case 2 and every 20 hours in case 3. The results of the first case have been described in Chapter 6 and will be used to compare with that of the other two cases.

7.3 Predictions of Crack Initiation and Crack Growth

Figure 7.2 shows the predicted crack growth histories for all three loading cases. For the static loading case, the crack initiation time is 182 hours, while for the two cyclic loading cases, the crack onset is predicted to occur at 154 hours and 135 hours respectively. This result indicated that for the creep dominated fracture, load cycling can shorten the crack incubation time and a higher loading frequency can result in an earlier creep crack initiation and rupture.

Figure 7.2 also indicates that case 3, in which unloading and reloading were done every 20 hours, predicted fastest creep crack propagation and hence shortest life time, while case 1, the static loading case, predicted lowest crack growth rate and longest life time of all three cases. These results are consistent with the experimental observations reported by Ellison and Watson[89] and Smith and Webster[90] showing that the crack growth rate can be accelerated with an increase in loading frequency.

7.4 Plastic Zone

It has been described in Section 6.4 that for the static loading case, the plastic zone shrank very rapidly and vanished before the crack propagation began. This is due to a fast stress relaxation resulting from high stress concentration in the near tip region. The variations of the plastic zone for the two cyclic loading cases are depicted in Figures 7.3 and 7.4 respectively. It can be seen from Figure 7.3 that at the time before the first unloading, the plastic zone has diminished to a very small region. Upon unloading, reversed yielding occurs around the crack tip. After reloading, a considerably expanded plastic zone surrounding the crack tip developed. The expansion of the plastic zone after unloading and reloading is due to the stress redistribution associated with the cyclic hardening property of the material. As will be shown in the next section, a process of unloading, reverse yielding and reloading raises the stresses ahead of the crack tip, resulting in a larger yielding

area around the crack tip. The plastic zone size increases with the load cycling, as illustrated in Figure 7.3. Figure 7.4 shows a similar feature of the plastic zones for case 3. Comparing Figure 7.4 with Figure 7.3 reveals that a higher frequency gives rise to a faster expansion of the plastic zone, indicating more influence of plastic strains in case 3.

The shapes of the plastic zone for various stages of crack growth in case 3 are plotted in Figure 7.5. As the crack grows, the plastic zone spreads over a continually larger area, finally reaching a state of gross plasticity. The same trend for case 2, although to a lesser extent, can be found in Figure 7.3.

7.5 Stress Redistribution Ahead of Crack Tip Due to Unloading and Reloading

The variation of the maximum principal stress at the centroid of element 1 in the first loading cycle for case 2 is illustrated in Figure 7.6. Point A denotes the initial maximum principal stress at the centroid of the element immediately adjacent to the crack tip. After 50 hours of creep, the stress reduces to point B due to the stress relaxation; then unloading takes place. When the applied stress drops to approximately two thirds of the original value, reverse yielding in this element occurs. The stress continues to drop until it reaches point D, when reloading begins. Upon reloading, the element yields again at point E. The stress increases with the load until the load cycle completes at point F. The maximum principal stress in element 1 increases from point B to point F. Figure 7.7 shows

the variation of the maximum principal stress in element 1 in the first load cycle for case 3. Unloading starts at point B′ which is higher than B due to less time for creep relaxation in case 3. After unloading and reloading, the stress increases from B′ to F′. Although the net stress increase, F′B′, in case 3 is a little less than FB in case 2, the resultant stress F′ is still higher than F, owing to a higher unloading point B′. Figures 7.6 and 7.7 clearly indicate that the stress variation associated with load cycling is closely related to the kinematic hardening properties of the material, the loading level and the extent of the creep stress relaxation.

Figures 7.8 and 7.9 illustrate the redistributions of the effective stress and the maximum principal stress ahead of the crack tip due to unloading and reloading at t = 50 hours in case 2. Both figures show an obvious stress increase along the crack extension line. Consequently, a significant expansion of the plastic zone occurs upon reloading.

7.6 Stress Distributions and Damage Evolutions Ahead of the Crack Tip in Cyclic Loading Cases

7.6.1 Stationary crack

The histories of the effective stress and the maximum principal stress at the centroid of the element immediately ahead of the crack tip for all three cases are presented in Figures 7.10 and 7.11 respectively. It can be seen from these figures that in the static loading case, the crack tip stresses

continually decrease due to creep stress relaxation. In the cyclic loading cases, however, the stress relaxation at the vicinity of the crack tip is frequently interrupted by unloading and reloading. After every time of unloading and reloading, crack tip stress increases significantly and then the stress relaxation re-starts from a new stress level. As a consequence, the crack tip stresses in the cyclic loading cases are always higher than that under static loading. Figures 7.10 and 7.11 also indicate that the near tip stresses in case 3 are higher than that in case 2, as the unloading and reloading were done more frequently in case 3.

According to equation (2.7 b), the damage rate is proportional to the ϕ^{th} power of the linear combination of the effective stress and the maximum principal stress (ϕ = 4.22 for this material, see Table 2). Hence, an increase in the effective stress and the maximum principal stress after unloading and reloading will result in a considerably higher rate of damage accumulation in the crack tip element. Figure 7.12 illustrates the variations of the damage rate in the element immediately ahead of the crack tip for all three cases. After every time of unloading and reloading, the damage rate increased significantly in the two cyclic loading cases. Figure 7.12 also shows that case 3 is more damaging than case 2, since the load change in case 3 is more frequent.

Higher damage rates in the crack tip element for cyclic loading cases resulted in faster damage accumulation near the crack tip. The damage evolutions of the crack tip element for

the three cases are presented in Figure 7.13. It is observed that the damage evolution in the crack tip accelerates with the loading frequency. This is the reason why load cycling shortens the crack incubation time and causes earlier crack initiation in creep dominated fractures.

The distributions of the effective stress ahead of the crack tip at various times before the crack initiation are presented in Figures 7.14, 7.15 and 7.16. Along the crack extension line, effective stress increases with the frequency. Figures 7.17, 7.18 and 7.19 plot the distributions of the maximum principal stress ahead of the crack tip at various times, showing a similar trend.

It is worth noting that for all static and cyclic loading cases considered here, the peak stress does not occur in the crack tip element. The fact that the stress in the crack tip element is lower than the peak stress which takes place away from the tip implies that there is no stress singularity at the crack tip for both static and cyclic loading cases. In other words, for creep dominated fracture, load cycling does not change the characteristic of the stress distribution ahead of the crack tip, although it does influence the values of the stresses near the tip.

The higher stresses ahead of the crack tip in cyclic loading cases produce higher damage rates in these cases. Figures 7.20, 7.21 and 7.22 illustrate the distributions of the damage rate along the extension line at t = 40, 80 and 120 hours for all three cases. The distributions of the damage ahead of

the crack tip for the three cases at various times are presented in Figures 7.23, 7.24 and 7.25. These figures clearly show that the cyclic loading cases are more damaging than the static loading case and the case with higher frequency, case 3, is more damaging than the case with lower frequency, case 2.

7.6.2 Growing crack

The distributions of the effective stress and the maximum principal stress at various crack growth stages are plotted in Figures 7.26 through 7.29 and Figures 7.30 through 7.33 respectively. A common feature of these stress curves is that the crack tip stress is quite low and the peak stress occurs away from the crack tip. This fact reveals that for a growing crack, the load cycling does not change the characteristic of the stress distribution ahead of the crack tip.

Comparing the stress distributions among three cases indicates that the stresses along the crack extension line in the static loading case is always lower than that in the two cyclic loading cases. Between the two cyclic loading cases, stresses in case 3 are obviously higher than in case 2. As the crack advances, the differences in the stresses among these three cases appear to become more pronounced.

Figures 7.34 through 7.37 present the distributions of the damage rate ahead of the moving crack tip. In the static load case, the damage along the crack growth path accumulates considerably slower than in the cyclic cases. This is clearly due to the lower effective stress and the maximum principal

stress in the static case in the creep crack propagation stage. These figures also show that the differences in the damage rates among the three cases become larger as the crack propagates.

The damage distributions ahead of the growing crack tip are illustrated in Figures 7.38 through 7.41. These figures indicate that the damage evolution ahead of the moving crack accelerates with the loading frequency in the creep dominated crack growth. This is the reason why case 3 predicts fastest creep crack propagation and hence shortest life time, while case 1, the static case, predicts lowest crack growth and longest life time among the three cases considered here.

7.7 Brief Summary

The three cases studied in this chapter have demonstrated the importance of the cyclic plasticity in the cyclic creep crack growth. For a cracked panel subjected to repeated loadings, unloading and reloading may interrupt the stress relaxation near the crack tip and cause a significant stress increase ahead of the crack tip and an expansion of the plastic region. As a consequence, the creep damage accumulation along the crack extension line is accelerated by load cycling, resulting in an earlier crack initiation and faster crack propagation than the static case. Unloading and reloading more frequently, therefore, may cause shorter crack incubation time, higher crack growth rate and hence, shorter life time of the structure. It is clear that the cyclic plasticity hardening plays an important role in the analysis. It would not be possible to analyze the effects of

loading cycles on the cyclic creep crack propagation without a suitable cyclic plasticity hardening model.

CHAPTER 8

CONCLUSIONS AND RECOMMENDATIONS

8.1 Conclusions

An analytical procedure for prediction of creep crack initiation and crack propagation under static and cyclic loading conditions has been presented. This procedure includes the following major elements: continuum damage constitutive equations for creep deformations; the von Mises yield surfaces concept coupled with Mroz's kinematic hardening rule for cyclic plasticity response; the mixed explicit-implicit algorithm for creep stress analysis; the modified breakable element technique coupled with the damage criterion for creep crack initiation; and propagation and the finite element numerical method. This combined procedure enables the following features:

(1) Inclusion of all creep stages, i.e. primary, secondary and tertiary creeps, in the creep fracture analysis;

(2) Prediction of creep crack initiation and subsequent growth based on the damage accumulation in the vicinity of the crack tip;

(3) Inclusion of repeated loading conditions which leads to a combined creep-cyclic plasticity effect on the creep dominated fracture; and

(4) High computational efficiency.

Significant observations were made on the creep-fracture behavior of material through case studies performed on a centre notched plate structure subjected to a static load to study. A

number of these observations have never been reported before in open literature. The role of the instantaneous plasticity in the creep crack growth was also investigated. The following conclusions can be drawn from the present research:

(1) The inherent plasticity slows down the stress relaxation in the vicinity of the crack tip;

(2) The slower stress relaxation causes faster damage accumulation in the near tip region and slower damage evolution in the areas away from the crack tip;

(3) Such confined damage at the crack tip results in an earlier crack initiation but slower subsequent crack propagation; and

(4) Neglecting the instantaneous plasticity in creep fracture analysis may lead to over-estimations of both the crack initiation time and the crack growth rate.

The creep crack growth in a centre-cracked panel subjected to cyclic loadings was analyzed using the proposed finite element model. The results of the analysis reveal that:

(1) Unloading and reloading may interrupt the stress relaxation near the crack tip and cause a significant stress increase ahead of the crack tip and an expansion of the plastic zone;

(2) Cyclic loading accelerates the damage accumulation ahead of the crack tip and hence, results in an earlier crack initiation and faster crack propagation than static loadings; and

(3) In creep dominated fracture, more frequent unloading and reloading may cause shorter crack initiation time, higher crack growth rate and hence, shorter life time of components.

It is also important to note that the present investigation indicated that no stress singularity existed near the tip of the crack. As well, there was no evidence that the stress distribution showed sign of being stable. Both of these observations are in contradiction to the results derived by the popular C^* approach.

8.2 Recommendations

The present study has extended the continuum damage mechanics method to cyclic creep fracture analysis. The results from this study has demonstrated the unique advantages of the present approach over many existing methods. This approach provides a good potential for further research in the area of the combined creep-fatigue crack growth. The following recommendations with regard to further work in this area are in order.

(1) Experimental verification of the analytical results produced by the present method is necessary.

(2) Although quite complicated and expensive, it would be desirable to implement a finite strain algorithm given in [27] into the present finite element model, which would permit more precise computation of the near tip strain field.

(3) It has been reported that creep rupture may occur when the value of the damage parameter is less than unity[111]. An in-depth study on the critical value of the damage parameter for creep rupture would provide more reliable predictions of creep crack initiation and propagation.

(4) The creep constitutive equation employed in the present approach is valid only for simply cyclic loadings, i.e. repeated loading without rest. In order to analyze creep crack growth under more general cyclic loadings, development of creep constitutive equations capable of describing more complicated material behavior, such as cyclic creep hardening and softening and rest time effects, is warranted.

(5) To the author's knowledge, the mixed mode creep fracture has not been studied so far. The dependence of the damage evolution on the multiaxial stress state permits the determination of the orientation of creep crack growth in mixed mode fractures[82]. A step-by-step interactive analysis using the nodal grafting technique[113] combined with the multiaxial stress rupture criterion would provide a viable approach for mixed mode creep fracture.

REFERENCES

[1] I. Finnie and W. R. Heller, "Creep of Engineering Materials", McGraw-Hill Book Co., Inc., New York, (1959).

[2] F. Garofalo, "Fundamentals of Creep and Creep Rupture in Metals", Macmillan Co., New York, (1965).

[3] H. Kraus, "Creep Analysis", John Wiley & Sons, Inc., New York, (1980).

[4] J. T. Boyle and J. Spence, "Stress Analysis for Creep", Butterworth & Co. (Publishers) Ltd., (1983).

[5] T. T. Wang and E. E. Onat, "Nonlinear Mechanical Behavior of 1100 Aluminum at 300°F", Acta Mech., 5, pp. 54-70, (1968).

[6] J. Gittus, "Creep, Viscoelasticity and Creep Fracture in Solids", Applied Science Publ., (1975).

[7] E. Kroner, "Dislocation: A New Concept in the Continuum Theory of Plasticity", Journal Mathematics and Physics, 42, pp. 27-37, (1962).

[8] R. Hill, "The Essential Structure of Constitutive Laws for Metal Composites and Polycrystals", J. of Mech. Phys. Solids, 15, pp. 79-95, (1967).

[9] F. A. Leckie and A. R. S. Ponter, "On the State Variable Description of Creeping Materials", Ingenieur-Archives, 43, pp. 158-167, (1974).

[10] L. M. Kachanov, "On the Creep Fracture Time", Izu, AN SSR, Otd. Tekhn. Nauk, 8, pp. 26-31, (1958). (in Russian)

[11] F. K. G. Odquist, "Mathematical Theory of Creep and Creep Rupture", Oxford University Press, (1966).

[12] Y. N. Rabotonov, "Creep Problems in Structural Members", (1966) in Russian, English Translation by F. A. Leckie, North-Holland Publ., (1969).

[13] J. E. Dorn, "Some Fundamental Experiments on High Temperature Creep", J. Mech. Phys. Solids, 3, pp. 85-116, (1955).

[14] D. R. Hayhurst, "Creep Rupture under Multiaxial State of Stress", J. Mech. Phys. Solids, 20, pp. 381-390, (1972).

[15] F. A. Leckie and D. R. Hayhurst, "Creep Rupture of Structure", Proc. R. Soc. Lond., A340, pp. 323-347, (1974).

[16] A. E. Johnson, J. Henderson and B. Khan, "Complex-stress Creep Relaxation and Fracture of Metallic Alloys", Her Majesty's Stationary Office, Edinburgh, (1962).

[17] F. A. Leckie, "The Constitutive Equations of Continuum Creep Damage Mechanics", Proc. R. Soc. Lond., A288, pp. 27-47, (1978).

[18] S. Murakami and N. Ohno, "A Continuum Theory of Creep and Creep Damage", Creep in Structures, Proc. IUTAM Symp., Leicester, A.R.S. Ponter and D. R. Hayhurst (Eds.), pp. 422-443, (1980).

[19] J. L. Chaboche, "Description Thermodynamique et Phenomenologique de la Viscoplasticite Cyclique avec Endommagement", ONERA Publ., No. 1978-3, (1978).

[20] L. M. Kachanov, "Creep and Fracture at Complex Loading", Problem Prochnosti, No. 6, pp. 3-5, (1977) (in Russian).

[21] D. Kjacinovic, "Constitutive Equations for Damaging Materials", J. Appl. Mech., **50**, pp. 355-360, (1983).

[22] D. Krajcinovic and S. Selvaraj, "Creep Rupture of Metals-An Analytical Model", J. Eng. Mater. Tech., **106**, pp. 405-409, (1984).

[23] E. W. Hart, "Constitutive Relations for the Non-elastic Deformation of Metals", J. Eng. Mater. Tech., **98**, pp. 193-202, (1976).

[24] A. K. Miller, "An Inelastic Constitutive Model for Monotonic Cyclic and Creep Deformation", J. Eng. Mater. Tech., **98**, pp. 97-105, (1976).

[25] D. N. Robinson, "A Unified Creep-Plasticity Model for Structural Metals at High Temperatures", Report ORNL/TM-5969, Oak Ridge Nat'l Lab., (1978).

[26] O. C. Zieckiewicz, "The Finite Element Method", McGraw-Hill, 3rd edition, (1977).

[27] T. R. Hsu, "The Finite Element Method in Thermomechanics", Allen & Unwin (Publishers), (1986).

[28] W. Prager, "The Theory of Plasticity: A Survey of Recent Achievements", James Clayton Lecture, Proc. Instit. Mech. Eng. London, **169**, pp. 41-50, (1955).

[29] H. Ziegler, "A Modification of Prager's Hardening Rule", Quat. Appl. Math. **18(1)**, pp. 55-65, (1959).

[30] T. R. Hsu and A. W. M. Bertels, "An Improved Approximation of Constitutive Elasto-plastic Stress-strain Relationship for Finite Element Analysis", AIAA J., **12(10)**, pp. 1450-1452, (1974).

[31] S. Y. Cheng and T. R. Hsu, "On Elastic-plastic Stress-strain Relationship for Multiaxial Stress State", Int. J. Num. Meth. Eng., **12**, pp. 1617-1622, (1978).

[32] F. A. Leckie, "Advances in Creep Mechanics", Creep in Structures, Proc. IUTAM Symp., Leicester, A.R.S. Ponter and D. R. Hayhurst (Eds.), pp. 13-47, (1980).

[33] E. T. Onat and F. Fardshisheh, "Representation of Creep of Metals", Oak Ridge Nat'l Lab., Report ORNL-4783, (1972).

[34] O. C. Zieckiewicz and I. C. Cormeau, "Visco-plasticity-Plasticity and Creep in Elastic Soldis-A Unified Numerical Solution Approach", Int. J. Num. Meth. Eng., **8**, pp. 821-845, (1974).

[35] I. C. Cormeau, "Numerical Stability in Quasi-static Elasto/Visco-plasticity", Int. J. Num. Meth. Eng., **9**, pp. 109-127, (1975).

[36] T. J. R. Hughes and R. L. Taylor, "Unconditionally Stable Algorithms for Quasi-static Elasto/Visco-plastic Finite Element Analysis", Comp. Struct., **8**, pp. 169-173, (1978).

[37] M. B. Kanchi, O. C. Zieckiewicz and D. R. J. Owen, "The Visco-plastic Approach to Problems of Plasticity and Creep Involving Geometric Non-linear Effects", Int. J. Num. Meth. Eng., **12**, pp. 169-181, (1978).

[38] M. J. Siverns and A. T. Price, "Crack Propagation and Creep Conditions in a Quenched 2 1/4 Chromium 1 Molybdenum Steel", Int. J. Fracture, **9**, p. 199, (1973).

[39] G. J. Neate and M. J. Siverns, "The Application of Fracture Mechanics to Creep Crack Growth", Proc. Int. Conf. on Creep and Fatigue in Elev. Temp. Appl., Sheffield, Paper C234/74, Inst. Mech. Eng., (1974).

[40] S. Floreen, "The Creep Fracture of Wrought Nickel-Based Alloys by a Fracture Mechanics Approach", Metallurg, Trans., **6A**, p. 1741, (1975).

[41] L. A. James, "Some Preliminary Observations on the Extension of Cracks under Creep Condition in Quenched 2 1/4 Cr-Mo Steel", Int. J. Fracture, **9(2)**, pp. 199-207, (1973).

[42] E. G. Ellison and M. P. Harper, "Creep Behavior of Components Containing Cracks-A Critical Review", J. Strain Analysis, **13(1)**, pp. 35-51, (1978).

[43] D. J. Gooch, J. R. Haigh and B. L. King, "Relationship Between Engineering Metallurgical Factors in Creep Crack Growth", Met. Sci., **11**, p. 545, (1977).

[44] R. Pilkington and E. Smith, "Creep Crack Growth under LEFM Condition", J. Eng. Mater. Tech., **102**, p. 347, (1980).

[45] R. A. Ainsworth, "Some Observations on Creep Crack Growth", Int. J. Fracture, **18**, p. 26, (1982).

[46] C. B. Harrison and G. N. Sandor, "High Temperature Crack Growth in Law-cycle Fatigue", Eng. Fracture Mech., 3, p. 403, (1971).

[47] R. D. Nickolson and C. L. Formby, "The Validity of Various Fracture Mechanics Methods in Creep Temperature", Int. J. Fracture, **11**, p. 595, (1975).

[48] S. Taira, R. Ohtani and A. Nitta, "Creep Crack Initiation and Propagation in an 18 Cr 8 Ni Stainless Steel", Proc. 1973 Symp. on Mech. Behavior of Materials, **211**, (1974).

[49] P. L. Jones and A. S. Tetelman, "Characterization of the Elevated Temperature Static Load Crack Extension Behavior of Type 304 Stainless Steel", Eng. Fracture Mech., 12, pp. 79-97, (1979).

[50] E. G. Ellison and G. J. Neate, "Life Predictions Methods for Cracked Components Operating in the Creep Range", Conf. on Failure of Components Operating in Creep Range, Inst. Mech. Eng., p. 39, (1976).

[51] G. J. Neate, "Creep Crack Growth in 1/2% Cr-1/2% Mo-1/4% V Steel at 565°C", Eng. Fracture Mech., p. 297, (1977).

[52] J. R. Rice, "A Path Independent Integral and the Approxiamte Analysis of Strain Concentrations by Notches and Cracks", J. Appl. Mech., **35**, pp. 379-386, (1968).

[53] J. R. Rice, "Mathematical Analysis in the Mechanics of Fracture", Fracture—An Advanced Treatise, Ed. H. Liebowicz, Academic Press, New York, (1968).

[54] J. W. Hutchinson, "Singular Behavior at the End of a Tensile Crack in a Hardening Material", J. Mech. Phys. Solids, **16**, pp. 13-31, (1968).

[55] J. R. Rice and G. F. Rosengren, "Plane Strain Deformation Near a Crack Tip in a Power Law Hardening Material", J. Mech. Phys. Solids, **16**, pp. 1-12, (1968).

[56] J. A. Begley and J. D. Landes, "The J-integral as a Fracture Criterion", ASTM STP 514, pp. 1-20, (1972).

[57] J. D. Landes and J. A. Begley, "The Effect of Specimen Geometry on J_{IC}", ASTM STP 514, pp. 24-39, (1972).

[58] J. R. Rice, P. C. Paris and J. G. Merkle, "Some Further Results of J-integral Analysis and Estimates", ASTM STP 536, pp. 231-245, (1973).

[59] Test Standard for the Measurement of the Fracture Toughness J_{IC}, ASTM E813-81, (1981).

[60] A. S. Kobayashi, S. T. Chiu and R. Beenorkes, "A Numerical and Experimental Investigation of the Use of the J-integral", Eng. Fracture Mech., 5, pp. 293-305, (1973).

[61] C. E. Turner and G. A. Webster, "Application of Fracture Mechanics to Creep Crack Growth", Int. J. Fracture, 10, pp. 455-458, (1974).

[62] J. D. Landes and J. A. Begley, "A Fracture Mechanics Approach to Creep Crack Growth", ASTM STP 590, pp. 128-148, (1976).

[63] N. L. Goldman and J. W. Hutchinson, "Fully Plastic Crack Problems: The Center Crack Strip under Plane Strain", Int. J. Solids and Struct., 11(5), pp. 575-591, (1975).

[64] H. Riedel and J. R. Rice, "Tensile Cracks in Creeping Solids", ASTM STP 700, pp. 112-130, (1980).

[65] C. Y. Hui and H. Riedel, "The Asymptotic Stress and Strain Field Near the Tip of a Growing Crack under Creep Conditions", Int. J. Fracture, 17, pp. 409-425, (1981).

[66] C. Y. Hui and K. C. Wu, "The Mechanics of a Constantly Growing Crack in an Elastic Power-Law Creeping Material", Int. J. Fract., 31, pp. 3-16, (1986).

[67] E. W. Hart, "A Theory for Stable Crack Extension Rates in Ductile Materials", Int. J. Solids Struct., 16, p. 807, (1980).

[68] E. W. Hart, ASTM STP 803, p. 521, (1983).

[69] K. B. Nikbin, G. A. Webster and C. E. Turner, "Relevance of Non-linear Fracture Mechanics to Creep Cracking", ASTM STP 601, p. 47, (1976).

[70] M. P. Harper and E. G. Ellison, "The Use of the C^* Parameter in Predicting Creep Crack Propagation Rates", J. Strain Analysis, 12(3), pp. 167-179, (1977).

[71] D. J. F. Ewing and C. E. Richard, "The Yield Point Loads of Singly-notched Pin-loaded Tensile Strips", J. Mech. Phys. Solids, 22(1), pp. 27-36, (1974).

[72] J. R. Haigh and C. E. Richard, "Yield Point Loads and Compliance Functions of Fracture Mechanics Specimen", C.E.G.B. Report RD/L/M461, (1974).

[73] R. Koterazawa and T. Mori, "Applicability of Fracture Creep Conditions", J. Eng. Mater. Tech., **99**, pp. 298-305, (1977).

[74] K. Ohji, K. Ogura and S. Kubo, "Estimates of J-integral in the General Yielding Range and its Application to Creep Crack Problems", Trans. JSME, **44(382)**, pp. 1831-1838, (1978).

[75] E. G. Ellison and M. P. Harper, "Creep Behavior of Components Containing Cracks—A Critical Review", J. Strain Analysis, **13(1)**, pp. 35-51, (1978).

[76] R. Pilkington, "Creep Crack Growth in Low-alloy Steels", Metal Science, pp. 555-564, Oct. (1979).

[77] K. Sadananda and P. Shahinian, "Review of the Fracture Mechanics Approach to Creep Crack Growth in Structural Alloys", Eng. Fracture Mech., **15(3-4)**, pp. 327-342, (1981).

[78] I. Curbishley, R. Pilkington and G. J. Lloyd, "Macroscopic Creep Crack Growth in Type 316 Stainless Steel. III. Application of Linear and Nonlinear Elastic Fracture Mechanics", Eng. Fracture Mech., **23(2)**, pp. 401-422, (1986).

[79] E. Mass and A. Pineau, "Creep Crack Growth Behavior of Type 316 L Steel", Eng. Fracture Mech., **22(2)**, pp. 307-325, (1985).

[80] A. Sexena, H. A. Ernst and J. D. Landes, "Creep Crack Growth Behavior in 316 Stainless Steel at 594°C", Int. J. Fracture, **23**, pp. 245-257, (1983).

[81] Y. J. Liu and T. R. Hsu, "A General Treatment of Creep Crack Growth", Eng. Fracture Mech., **21(3)**, pp. 437-452, (1985).

[82] D. R. Hayhurst, P. R. Brown and C. J. Morrison, "The Role of Continuum Damage in Creep Crack Growth", Phil. Trans. R. Soc. London, **A311**, pp. 131-158, (1984).

[83] D. R. Hayhurst, P. R. Dimmer and C. J. Morrison, "Development of Continuum Damage in the Creep Rupture of Notched Bar", Phil. Trans. R. Soc. London, **A311**, pp. 103-129, (1984).

[84] E. Kremple, "Cyclic Creep—An Interpretative Literature Survey", W.R.C. Bulletin 195, pp. 63-123, (1974).

[85] E. G. Ellison and E. M. Smith, "Prediction Service Life in a Fatigue-Creep Environment", Fatigue at Elevated Temperatures, ASTM STP 520, pp. 575-612, (1973).

[86] L. F. Coffin, "High Temperature Fatigue Prediction and Interpretation", Int. Conf. on Creep and Fatigue in Elevated Temperature Application, Inst. Mech. Eng., pp. 103-127, (1973).

[87] S. S. Manson, "The Challenge to Unify Treatment of High Temperature Fatigue—A Partisan Approach Based on Strain Range Partitioning", Fatigue at Elevated Temperatures, ASTM STP 520, pp. 744-774, (1973).

[88] A. D. Batte, "Creep-fatigue Life Prediction", Fatigue at High Temperature, R. P. Skelton (Ed.), Applied Science Publishers, London, pp. 365-401, (1983).

[89] E. G. Ellison and D. Walton, "Fatigue, Creep and Cyclic Creep Crack Propagation in a 1 Cr-Mo-V Steel", Int. Conf. on Creep and Fatigue in Elevated Temperature Application, Inst. Mech. Eng., Paper No. C173/73, (1973).

[90] D. J. Smith and G. A. Webster, "Influence of Cyclic Loading on Crack Growth of a 1/2 Cr-Mo-V Steel", 4th Int. Conf. on Mech. Behavior Mater., Stockholm, (1983).

[91] M. P. Harper, "Creep, Cyclic Creep and Fatigue Fracture in a Low Alloy Steel", Ph.D. Thesis, University of Bristol, (1976).

[92] E. G. Ellison and A. J. F. Paterson, "Behavior of a 1 Cr-Mo-V Steel Subject to Combinations of Fatigue and Creep under Strain Control", Proc. Inst. Mech. Engrs., 190, p. 333, (1976).

[93] G. A. Webster, "Crack Growth at High Temperature", Engineering Approaches to High Temperature Design, Vol. 2, Recent Advances in Creep and Fracture of Engineering Materials and Structures, B. Wilshile and D. Owen (Eds.), pp. 1-55, (1983).

[94] S. Taira, R. Ohtani and T. Komatsu, "Application of J-integral to High Temperature Crack Propagation, Part II, Fatigue Crack Propagation", J. Eng. Mater. Tech., 101, pp. 162-167, (1979).

[95] W. O. Iwan, "On a Class of Models for the Yielding Behavior of Continuous and Composite Systems", J. Appl. Mech., 34, pp. 612-617, (1967).

[96] Z. Mroz, "On the Description of Anistropic Workhardening", J. Mech. Phys. Solids, 15, pp. 163-175, (1967).

[97] S. Timoshenko and J. N. Goodier, "Theory of Elasticity", McGraw-Hill, New York, (1970).

[98] G. G. Chen and T. R. Hsu, "A Mixed Explicit-Implicit (EI) Algorithm for Creep Stress Analysis", Int. J. Num. Meth. Eng., 26, pp. 511-524, (1988).

[99] G. G. Chen and T. R. Hsu, "A Finite Element Model for Creep Fracture Analysis Using Continuum Damage Approach", Proc. 4th Int. Conf. on Num. Meth. Fract. Mech., A. R. Luxmoore, D. R. J. Owen, Y. P. S. Rajapakse and M. F. Kanninen (Eds.), pp. 401-410, (1987).

[100] T. R. Hsu and A. W. M. Bertels, "Propagation and Opening of a Through Crack in a Pipe Subjected to Combined Cyclic Thermomechanical Loading", J. Press. Vess. Tech., ASME Trans. 98, pp. 17-25, (1976).

[101] T. R. Hsu and Y. J. Kim, "On Slow Crack Growth in Fuel Cladding by Finite Element Analysis", 5th Int. Conf. on Struct. Mech. in Reactor Tech., C3/12, (1979).

[102] Y. J. Kim and T. R. Hsu, "A Numerical Analysis on Stable Crack Growth Under Increasing Load", Int. J. Fracture, 20, pp. 17-32, (1982).

[103] T. R. Hsu and Z. H. Zhai, "A Finite Element Algorithm for Creep Crack Growth", Eng. Fract. Mech., 20, pp. 521-533, (1984).

[104] T. R. Hsu, A. W. M. Bertels, S. Banerjee and W. C. Harrison, "Theoretical Basis for a Transient Thermal Elasto-plastic Stress Analysis of Nuclear Reactor Fuel Element", Atomic Energy of Canada Ltd., Report AECL-5233, (1976).

[105] H. D. Solomon and L. F. Coffin Jr., "Effect of Frequency and Environment on Fatigue Crack Growth in A286 at 1100°F", Fatigue at Elevated Temperature, ASTM STP 520, pp. 112-122, (1973).

[106] S. Taira, R. Ohtani and T. Kitamura, "Application of J-integral to High-temperature Crack Propagatioin, Part I, Creep Crack Propagation", J. Eng. Mater. Tech., 101, pp. 154-161, (1979).

[107] S. Taira, R. Ohtani, "Crack Propagation in Creep", Proc. of 2nd Int. Conf. on Mech. Behav. Met., Boston, pp. 465-509, (1976).

[108] W. C. Chen, "A Literature Review of Fatigue and Creep Interaction", National Aeronautics and Space Administration, Report NGR 33-022-172, (1976).

[109] G. Massing, "Eigenspannungen und Verfestigung beim Messing", Proc. Second Int. Congress of Appl. Mech., pp. 332-335, (1926).

[110] H. R. Jhansale and T. H. Topper, "Engineering Analysis of the Inelastic Stress Response of a Structure Metal Under Variable Cyclic Strains", Cyclic Stress-strain Behavior Analysis, Experimentation and Failure Predictions, ASTM STP 519, pp. 246-270, (1973).

[111] Jean Lemaitre, "Local Approach of Fracture", Eng. Fract. Mech., 25, pp. 523-537, (1986).

[112] R. Ehlers and M. Riedel, "A Finite Element Analysis of Creep Deformation in a Specimen Containing a Macroscopic Crack", Advance in Fracture Research, Vol. 2, (Edited by D. Francois), Fifth Int. Conf. on Fracture, Cannes, pp. 691-698, (1981).

[113] A. R. Ingraftea, "Interactive Computer Simulation of Fracture Processes", Proc. 4th Int. Conf. on Num. Mech. Fract. Mech., A. R. Luxmoore, D. R. J. Owen, Y. P. S. Rajapakse and M. F. Kanninen (Eds.), pp. 677-699, (1987).

APPENDIX

INTERNATIONAL JOURNAL FOR NUMERICAL METHODS IN ENGINEERING, VOL. 26, 511–524 (1988)

A MIXED EXPLICIT–IMPLICIT (EI) ALGORITHM FOR CREEP STRESS ANALYSIS

G. G. CHEN AND T. R. HSU

Department of Mechanical Engineering, University of Manitoba, Winnipeg, Manitoba, Canada

SUMMARY

A mixed explicit–implicit numerical integration algorithm for creep stress analysis is presented in this paper. This method allows simultaneously use of, and thus benefit from, both these integration schemes. The continuum damage constitutive model is also implemented in this algorithm. The present method is suitable for the prediction of creep crack growth in solids using the continuum damage approach.

Numerical examples using different constitutive equations have been included to demonstrate the high efficiency of the proposed algorithm.

INTRODUCTION

Creep stress analysis has received increasing attention in engineering design in recent years owing to its practical importance in applications such as electric power generation, aerospace and petrochemical equipment. Generally, creep problems are more difficult to handle than elastic–plastic analyses as the constitutive equations employed in the creep analysis of solids at elevated temperature are usually very complicated. The finite element method appears to be the only practical solution to this type of problem. One major difficulty of using this method, however, is that the resulting equations are highly non-linear and stiff in nature. The stability and accuracy of the finite element solution critically depend on the selection of a suitable size of time steps associated with an appropriate integration scheme. This situation has motivated vigorous research in this area.

Generally speaking there are two common classes of one-step integration schemes for creep analysis, i.e. explicit and implicit. The explicit scheme, as suggested by Zienkiewitz and Cormeau[1] and Cormeau,[2] has been applied with success to a variety of engineering problems. The advantages of this method are that it is concise and simply coded. The stiffness matrix in this case is constant and may be factored once and for all. Unfortunately, this scheme is only conditionally stable and the stability condition is rather stringent. For structures subjected to slowly varying loads, or when equilibrium response is of prime interest, stability of solution requires much smaller time steps than those necessary for accuracy. Cormeau has performed a stability analysis and derived the explicit stability conditions for some simple constitutive relations.[2] For the steady-state creep obeying Norton's law, he presented a simple relationship between the critical time increment Δt_c and the effective stress as

$$\Delta t_c \propto \frac{1}{\bar{\sigma}_{\max}^{n-1}}$$

where $\bar{\sigma}_{\max}$ is the maximum effective stress in the region, n is the stress index of the creep law and its

0029–5981/88/020511–14$07.00

Received 27 January 1987
Revised 8 June 1987

value ranges from 5 to 10 for most metals. This expression indicates that the critical time step size ensuring the stability is controlled by the element where the highest stress or highest creep strain rate occurs. For the part of the structure at a lower stress or lower creep strain rate, much larger time steps can be used without causing instability. For instance, for those elements in which the value of the effective stress is 0·6 of the maximum effective stress, the time step could be 7·7 to 99·2 times the critical one, depending on the value of the material constant n. Since high stresses are often limited in a small portion of the structure for many engineering problems, especially in creep fracture mechanics, selecting time step sizes according to the maximum effective stresses or highest creep strain rate is both uneconomic and unnecessary. On the other hand, Hughes and Taylor proposed an implicit scheme,[3] which has been shown to be unconditionally stable if the scheme parameter $\gamma \geqslant 1/2$. Although stability of solution does not depend on the size of time step used in the computation, this method requires the use of an iteration procedure. The computational efficiency thus depends on the convergence of the iterations. Kanchi *et al.*[4] presented an alternative implicit scheme by incorporating a linear extrapolation of the creep strain rate tensor within each time interval. A Taylor series expansion technique was introduced in lieu of iteration. Although Kanchi's method is not unconditionally stable, computational experiences have shown that it is much more stable than the explicit scheme with larger time increments. However, since the stiffness matrix used in this method is a function of element stresses, reformulation and inversion of this matrix are necessary for every time step. As a result, all implicit schemes require more computation time. For large scale engineering problems where a great many elements are involved, this shortcoming becomes a serious drawback for the implicit method.

The mixed explicit–implicit algorithm (or EI scheme) can simultaneously achieve the attributes of both classes of schemes. It can circumvent these difficulties and lead to significant computational advantages. The mixed integration algorithm which was first proposed by Belytschko and Mullen[5] and Hughes and Liu[6] for structure dynamics, has been successfully applied to various engineering disciplines such as fluid mechanics and fluid–structure interaction problems,[7] and has recently been extended to linear and non-linear thermal analysis.[8, 9] The purpose of this paper is to apply this concept to creep analysis.

We begin by describing the formulations and the implementations of the EI scheme in the content of the general forms of creep constitutional models. For the implicit element group, formulations of Kanchi's method are modified to include the state variables appearing in the constitutive equations. We will then discuss solutions derived from simple test problems, with emphasis given to the behaviour of material following three different circumstances: von Mises viscoplastic deformation, power law creep and creep deformation described by the continuum damage theory.[10]

THEORETICAL FORMULATIONS

A. *Equilibrium equations*

A basic assumption involved in creep stress analysis is that the total strain $\boldsymbol{\varepsilon}$ can be partitioned into the elastic $\boldsymbol{\varepsilon}^e$, plastic $\boldsymbol{\varepsilon}^p$ and creep $\boldsymbol{\varepsilon}^c$ components, so that the total strain increment can be expressed as[11]

$$\Delta\boldsymbol{\varepsilon} = \Delta\boldsymbol{\varepsilon}^e + \Delta\boldsymbol{\varepsilon}^p + \Delta\boldsymbol{\varepsilon}^c \tag{1}$$

The stress increment is related to the elastic and plastic strain increments through the elasto-plasticity matrix $\mathbf{D}$ by

$$\Delta\boldsymbol{\sigma} = \mathbf{D}(\Delta\boldsymbol{\varepsilon}^e + \Delta\boldsymbol{\varepsilon}^p) \tag{2}$$

In general, **D** is a function of stresses, but in the absence of plastic strain, it reduces to a matrix of elastic constants.

The stress increment can be expressed in terms of the incremental displacement vector $\Delta\mathbf{u}$ as follows:

$$\Delta\boldsymbol{\sigma}=\mathbf{D}(\mathbf{B}\Delta\mathbf{u}-\Delta\boldsymbol{\varepsilon}^{c}) \tag{3}$$

in which **B** is the strain matrix.

The equation of equilibrium to be satisfied at any time t takes the form

$$\int_{v}\mathbf{B}^{T}\Delta\boldsymbol{\sigma}\,dv=\Delta\mathbf{R} \tag{4}$$

where $\Delta\mathbf{R}$ is the vector of the equivalent nodal load increment due to surface tractions and body forces, and v is the element volume. By combining equations (3) and (4) the equilibrium equations becomes

$$\int_{v}\mathbf{B}^{T}\mathbf{D}(\mathbf{B}\Delta\mathbf{u}-\Delta\boldsymbol{\varepsilon}^{c})\,dv=\Delta\mathbf{R} \tag{5}$$

B. *Constitutive Equations*

The state variable description[12] is a widely used method for the prediction of creep behaviour of materials subjected to general loadings. This method assumes that the creep strain rate is determined by the stress and certain well defined state variables such as $\boldsymbol{\omega}$. Mathematically, it can be expressed as follows:

$$\dot{\boldsymbol{\varepsilon}}^{c}=f_{1}(\boldsymbol{\sigma},\,\boldsymbol{\omega},\,t) \tag{6a}$$

These state variables can completely characterize the current deformation state of the material. The evolution of these state variables is governed by equations of the following form:

$$\dot{\boldsymbol{\omega}}=f_{2}(\sigma,\,\boldsymbol{\omega}) \tag{6b}$$

The number of state variables and the functions f_1 and f_2 are determined either by the theories of metal physics or on the results of appropriately chosen mechanical tests. One of the commonly used constitutive models is the continuum damage theory as proposed by Leckie and Hayhurst:[10]

$$\dot{\boldsymbol{\varepsilon}}^{c}=\frac{3}{2}A\left(\frac{\bar{\sigma}}{1-\omega}\right)^{n}t^{m}\frac{\mathbf{S}}{\bar{\sigma}} \tag{7a}$$

$$\dot{\omega}=B\left(\frac{\bar{\sigma}}{1-\omega}\right)^{p} \tag{7b}$$

in which **S** is the stress deviator vector and A, B, n, m and p are experimentally determined constants. The state variable ω is, in some sense, a measure of damage in the material induced by creep. The value $\omega=0$ represents an undamaged state of the material whereas rupture occurs when $\omega=1$. This constitutive model is considered to be capable of describing all three creep stages, i.e. primary, secondary and tertiary creep, in the material.[10] When $m=B=0$, equation (7) reduces to the well known Norton's equation which represents the steady-state creep behaviour, in the following form:

$$\dot{\boldsymbol{\varepsilon}}=\tfrac{3}{2}A\bar{\sigma}^{n-1}\mathbf{S} \tag{8}$$

C. *Mixed explicit–implicit algorithm (EI scheme)*

We consider a finite element model in which elements are partitioned into two groups: the explicit elements and the implicit elements. The integration schemes corresponding to these two element groups are given as follows.

(1) Explicit elements.

The increments of creep strain $\Delta\varepsilon^c$ and state variables $\Delta\omega$ occurring in a time interval $\Delta t = t_{n+1} - t_n$ are defined as

$$\Delta\varepsilon^c = \dot{\varepsilon}_n^c \Delta t \tag{9}$$

and

$$\Delta\omega = \dot{\omega}_n \Delta t \tag{10}$$

where $n \in [0, 1, \ldots, N]$ denotes the number of the time step. The stress increment can be expressed by substituting equation (9) into equation (3) as shown below:

$$\Delta\sigma = \mathbf{D}(\mathbf{B}\Delta\mathbf{u} - \dot{\varepsilon}_n^c \Delta t) \tag{11}$$

The element equation in equation (5) now becomes

$$\left(\int_v \mathbf{B}^T\mathbf{D}\mathbf{B}\,dv\right)\Delta\mathbf{U} = \int_v \mathbf{B}^T\mathbf{D}\dot{\varepsilon}_n^c \Delta t\,dv + \Delta\mathbf{R} \tag{12}$$

(2) Implicit elements:

The increments of creep strain and state variables occurring in a time increment Δt are assumed to take the form

$$\Delta\varepsilon^c = [(1-\gamma)\dot{\varepsilon}_n^c + \gamma\dot{\varepsilon}_{n+1}^c]\Delta t \tag{13}$$

and

$$\Delta\omega = [(1-\gamma)\dot{\omega}_n + \gamma\dot{\omega}_{n+1}]\Delta t \tag{14}$$

It is readily seen that the explicit scheme is a special case of the above equations with $\gamma = 0$. On the other hand, the case of $\gamma = 1$ represents a fully implicit scheme. The case with $\gamma = 1/2$ denotes the implicit trapezoidal scheme which is generally known also as the Crank–Nicolson rule of integration.

The state variables $\dot{\varepsilon}_{n+1}$ and $\dot{\omega}_{n+1}$ in equations (13) and (14) can be expressed in a limited Taylor series expansion[4] as follows:

$$\dot{\varepsilon}_{n+1}^c = \dot{\varepsilon}_n^c + \mathbf{H}_1\Delta\sigma + \mathbf{H}_2\Delta\omega + \mathbf{H}_3\Delta t \tag{15}$$

and

$$\dot{\omega}_{n+1} = \dot{\omega}_n + \mathbf{G}_1\Delta\sigma + \mathbf{G}_2\Delta\omega \tag{16}$$

in which

$$\mathbf{H}_1 = \frac{\partial\dot{\varepsilon}^c}{\partial\sigma}, \quad \mathbf{H}_2 = \frac{\partial\dot{\varepsilon}^c}{\partial\omega}, \quad \mathbf{H}_3 = \frac{\partial\dot{\varepsilon}^c}{\partial t} \tag{17}$$

$$\mathbf{G}_1 = \frac{\partial\dot{\omega}^c}{\partial\sigma}, \quad \mathbf{G}_2 = \frac{\partial\dot{\omega}}{\partial\omega} \tag{18}$$

All these matrices are evaluated at time $t = t_n$. For the constitutive model given in equations (7a) and (7b), these matrices can be expressed explicitly as

$$\mathbf{H}_1 = \frac{3}{2}At_n^m\left(\frac{\bar{\sigma}}{1-\omega_n}\right)^n\frac{1}{\bar{\sigma}}\left[\frac{3(n-1)}{2\bar{\sigma}^2}(\mathbf{Q}\sigma)(\mathbf{Q}\sigma)^T + \mathbf{Q}\right] \tag{19}$$

$$\mathbf{H}_2 = \frac{n}{1-\omega_n}\dot{\varepsilon}_n^c \tag{20}$$

$$\mathbf{H}_3 = \frac{m}{t_n}\dot{\varepsilon}_n^c \tag{21}$$

$$\mathbf{G}_1 = \frac{3}{2}p\dot{\omega}_n\frac{1}{\bar{\sigma}^2}\mathbf{S} \tag{22}$$

$$\mathbf{G}_2 = \frac{p\dot{\omega}_n}{1-\omega_n} \tag{23}$$

The matrix $\mathbf{Q}$ in equation (19) is defined by the relation $\mathbf{S}=\mathbf{Q}\boldsymbol{\sigma}$. These expressions simplify calculations and reduce the storage requirement during the computation.

Thus, by substituting equation (16) into (14), one gets

$$\Delta\boldsymbol{\omega} = \mathbf{g}(\dot{\boldsymbol{\omega}}_n + \gamma\mathbf{G}_1\Delta\boldsymbol{\sigma})\Delta t \tag{24}$$

in which

$$\mathbf{g} = (\mathbf{I}-\gamma\mathbf{G}_2\Delta t)^{-1} \tag{25}$$

where $\mathbf{I}$ is the identity matrix.

Now, if one substitutes equations (13), (15) and (24) into (3) and rearranges the terms, the stress increments can be expressed by the following equation:

$$\Delta\boldsymbol{\sigma} = \mathbf{D}^*[\mathbf{B}\Delta\mathbf{u} - \dot{\boldsymbol{\varepsilon}}_n^c\Delta t - (\mathbf{H}_2\mathbf{g}\dot{\boldsymbol{\omega}}_n + \mathbf{H}_3)\gamma\Delta t^2] \tag{26}$$

where

$$\mathbf{D}^* = [\mathbf{I} + \gamma\Delta t\mathbf{D}(\mathbf{H}_1 + \gamma\mathbf{H}_2\mathbf{g}\mathbf{G}_1\Delta t)]^{-1}\mathbf{D} \tag{27}$$

The element equation can thus be derived by substituting equation (26) into equation (4). The final form of this equation is shown below:

$$\left(\int_v \mathbf{B}^T\mathbf{D}^*\mathbf{B}\,dv\right)\Delta\mathbf{u} = \int_v \mathbf{B}^T\mathbf{D}^*[\dot{\boldsymbol{\varepsilon}}_n^c\Delta t + (\mathbf{H}_2\mathbf{g}\dot{\boldsymbol{\omega}}_n + \mathbf{H}_3)\gamma\Delta t^2]\,dv + \Delta\mathbf{R} \tag{28}$$

IMPLEMENTATION

The implementation of the mixed explicit–implicit algorithm into the base TEPSA code[1] is straightforward, as illustrated in the Appendix. The formations of stiffness matrix $\mathbf{K}$ and load vector $\Delta\mathbf{F}_{n+1}$ may be carried out in the usual element-by-element procedure. In the case when the $\mathbf{D}$ matrix is held constant, it is necessary only to form $\mathbf{K}^e$ once. After the displacements and stresses are updated, a Newton iteration method is employed to evaluate $\boldsymbol{\omega}_{n+1}$ in the implicit element group, as described in step 10 in the Appendix. If $\boldsymbol{\omega}_{n+1}^0 = \boldsymbol{\omega}_n + \dot{\boldsymbol{\omega}}\Delta t$ is taken as the initial value, the convergence is so fast that satisfactory results can be given by only several iterations.

Both constant and variable time increments are allowed in the present mixed explicit–implicit algorithm. For the variable time step scheme, the selection of time increment is based on the following two considerations.

(1) Restriction on the increase in creep strain. It is suggested that the size of the time step be related to the ratio of incremental effective creep strain to the total elastic strain in explicit elements. This ratio is limited by an input parameter τ_1, which can be used to evaluate an allowable time step

size by the following expression:

$$\Delta t_1 = \tau_1 \frac{\bar{\sigma}/E}{\sqrt{\frac{2}{3}\dot{\varepsilon}^c \dot{\varepsilon}^c}} \tag{29}$$

where **E** is the elastic modulus of the material. The time increment determined in equation (29) is applied to every explicit element. For the case of steady-state creep described by Norton's law and with $\gamma = 0$ (fully explicit) and $\tau_1 = 2/n$ are taken, equation (29) reduces to Cormeau's stability criterion.[2]

(2) Restriction on the increase in state variables. The following relation is used:

$$\Delta t_2 = \tau_2 \frac{1}{\|\dot{\omega}\|_\infty} \tag{30}$$

where τ_2 is an input parameter controlling the time steps on the basis of the changes of state variables. When dealing with creep damage constitutive equations such as equations (7a) and (7b), the value of τ_2 may be chosen between 0·05 and 0·1. Equation (30) is applied to all elements of the structure. Then the time increment for next step of computations can be selected by

$$\Delta t = \text{Min}[\Delta t_1, \Delta t_2] \tag{31}$$

NUMERICAL EXAMPLE

The EI scheme described in the foregoing sections has been implemented into the basic TEPSAC code[11] and a numerical example is presented to illustrate the computational advantages of using this approach. This example involves the creep deformation of a thick wall cylinder subject to an instantaneously applied internal pressure. The geometry and finite element idealization of the cylinder are illustrated in Figure 1. Of the ten quadrilateral simplex elements used, the two elements near the inner wall were designated as 'implicit' elements whereas the remaining elements were treated as 'explicit'. Three distinct constitutive equations were considered in the computation.

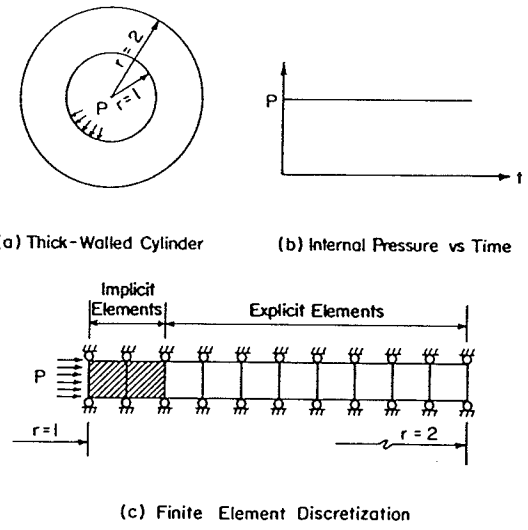

Figure 1. Finite element idealization of a thick wall cylinder

These were:

Case (1): The von Mises elasto-viscoplastic yield function;
Case (2): Norton's law for steady-state creep;
Case (3): The continuum damage theory.

Case (1): von Mises elasto-viscoplastic material

The constitutive relation used in this case as defined in Reference 13 takes the following form:

$$\dot{\varepsilon}^c = a\langle\phi\rangle \mathbf{S} \tag{32}$$

in which

$$\langle\phi\rangle = \begin{cases} 0 & \text{for } \phi \leqslant 0 \\ \phi & \text{for } \phi > 0 \end{cases}$$

and

$$\phi = \operatorname{sgn} F|F|,\ F = \bar{\sigma}/\sigma_y^2 - 1.$$

In the above expressions, a and σ_y are material constants. Equation (32) is a specific form of the general constitutive equations in (6a) and (6b) with the absence of any state variables. By taking $B=m=0$, $n=2$ in equation (7) and also replacing $\bar{\sigma}$ by $(\bar{\sigma}\sigma_y)/\sigma_y^2$, the following expression is obtained:

$$\dot{\varepsilon}^c = \frac{3}{2}A\left(\frac{\bar{\sigma}-\sigma_y^2}{\sigma_y^2}\right)\mathbf{S}$$

The above expression has an identical form to that shown in Equation (32). The computational procedure described in the Appendix can be directly applied by skipping steps relating to ω.

Parameters used in this case are given as follows:

$$\text{Internal pressure } P = 21\,000$$

$$\text{Elastic modulus } E = 3\times 10^6$$

$$\text{Poisson's ratio } \nu = 0{\cdot}3$$

$$A = 2\times 10^{-2}$$

$$\sigma_y = 3\times 10^4$$

Computations were performed by using the fully explicit scheme (all elements are explicit) and the mixed EI scheme with $\gamma = 1/2$ and 1 respectively. Time steps sizes of $\Delta t = 0{\cdot}5$, 1·0, 2·0 and 5·0 were used. Results of effective stress variations in the cylinder using these three integration schemes are shown in Figure 2. One may observe that the case using the explicit algorithm was accurate and stable, with $\Delta t = 0{\cdot}5$; but became less accurate at larger Δt's. Numerical overflow occurred on the tenth time step using $\Delta t = 5{\cdot}0$. On the other hand, all cases using mixed EI schemes gave stable results. It appeared that the results associated with $\gamma = 1$ are better than that with $\gamma = 0{\cdot}5$.

No significant difference in results was detected between the radial, circumferential and axial stress components calculated by the mixed EI scheme and those computed from the exact elastic perfect plastic solutions.[14]

Case (2): Norton's law for steady-state creep

This case study involves the deformation of the same thick walled cylinder under the steady-state creep obeying Norton's constitutive equation

$$\dot{\varepsilon}^c = \frac{3}{2}A\bar{\sigma}^{n-1}\mathbf{S}$$

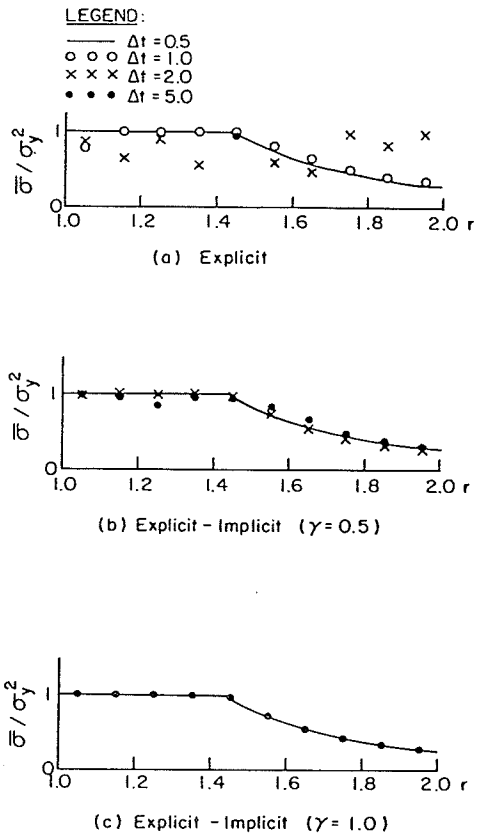

Figure 2. Distribution of effective stress in a thick wall cylinder using von Mises elasto-viscoplastic yield function

The following parameters were used in the computations

Internal pressure,	$P=10000$
Elastic modulus,	$E=5\times10^{6}$
Poisson's ratio,	$\nu=0{\cdot}3$
Material constants,	$A=2\times10^{-21}$
	$n=5$

Figure 3 shows the variations of the radial displacement of the inner surface of the cylinder using the fully explicit algorithm with different time step sizes. Results were stable and accurate with a small time increment, e.g. 0·02.

Increasingly deviations of results from the exact values occurred with time increments greater than 0·02. Instability finally occurred at $\Delta t=0{\cdot}12$. A similar trend can be observed on the variation of effective stress as shown in Figure 4 with the exact solution derived from Reference 12.

The displacements of the inner surface computed by using the mixed EI algorithms are presented in Figure 5 with time steps ranging from 0·02 to 0·3. The results are stable and accurate with the

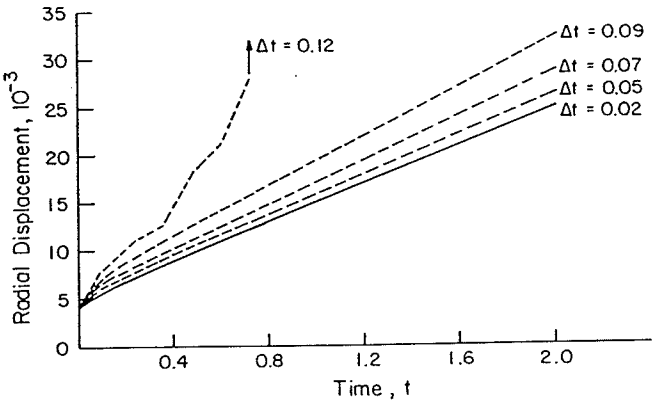

Figure 3. Creep radial displacement at inner surface using Norton's law and explicit scheme

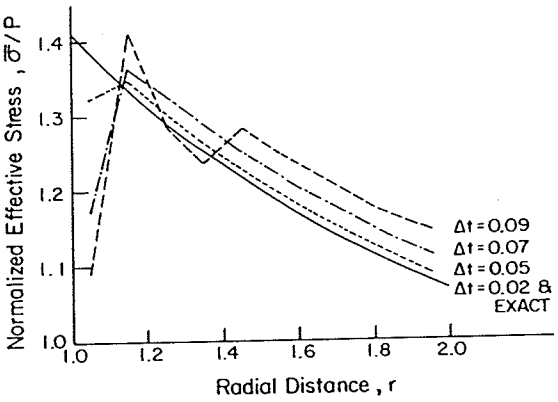

Figure 4. Creep effective stress distribution at $t=2{\cdot}0$ using Norton's law and explicit scheme

time increment $\Delta t \leqslant 0{\cdot}2$ for both values of γ. However, although the solutions remain stable, they become increasingly inaccurate with $\Delta t > 0{\cdot}2$. The distributions of circumferential, radial, axial and effective stress at steady state showed excellent correlations with those obtained from the exact solution.

Case (3): The continuum damage theory

The continuum damage constitutive model given in equations (7a) and (7b) was used to analyse the creep deformation of the thick wall cylinder. The damage parameter ω in these equations was taken as a single state variable and the constant m was set to be zero. The set of equation (7) can thus be used to describe the secondary and tertiary creeps. The following material properties were used in the computation: $B=3\times10^{-18}$, $p=4$ and all other parameters remained the same as in the Case (2) study. Since the analytical solution for this problem is not available, the numerical results calculated by the fully explicit scheme with a very small time increment $\Delta t=0{\cdot}01$ was used as the reference solution. For such a small time increment the explicit scheme and the mixed EI algorithms with $\gamma=1/2$ and 1 gave virtually identical results.

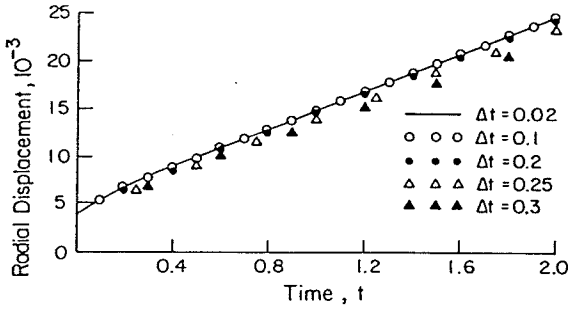

(a) Mixed Explicit - Implicit Scheme with $\tau = 1/2$

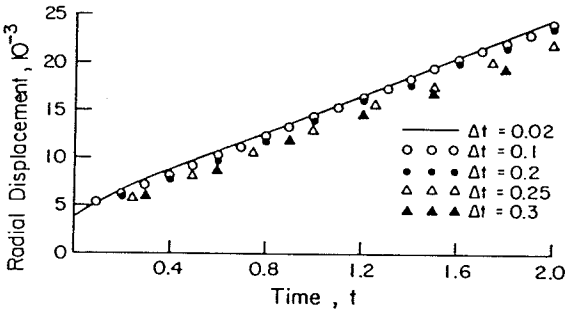

(b) Mixed Explicit - Implicit Scheme with $\tau = 1$

Figure 5. Creep radial displacement at inner surface using Norton's law and EI scheme

The radial displacement of the inner surface and the damage parameter at the element next to the inner surface are plotted in Figure 6 and Figure 7. The mixed EI algorithms with $\gamma = 1/2$ and 1 gave accurate results with large time increments up to $\Delta t = 0{\cdot}1$, whereas the results by the explicit scheme became unstable.

Figure 8 shows the distribution of the damage parameter ω along the radial direction. It is observed that the numerical results predicted by the mixed EI schemes for large time steps are very close to the reference solution, whereas the explicit scheme for $\Delta t = 0{\cdot}1$ is clearly erroneous.

The stress distribution at $t = 2{\cdot}0$ are presented in Figure 9. For $\Delta t = 0{\cdot}1$, the mixed EI solutions correlates well with the reference solution. Again, the explicit solution is unacceptable due to wild scattering of results.

Figure 10 shows the distribution of the effective stress at various instants. These results were calculated by the mixed EI scheme with $\gamma = 1/2$ and $\Delta t = 0{\cdot}1$. The solid line for $t = 0$ corresponds to the initial elastic stress distribution. It is interesting to note that stress near the inner surface decreases very rapidly due to the high value of the damage parameter ω and high creep strain rate. At $t = 2{\cdot}0$, the lowest effective stress takes place at the inner surface, and the peak stress occurs at about $r = 1{\cdot}2$.

CONCLUSIONS

A mixed EI scheme for creep stress analysis has been developed and presented in the paper. This method can use both explicit and implicit schemes simultaneously in different part of the structure

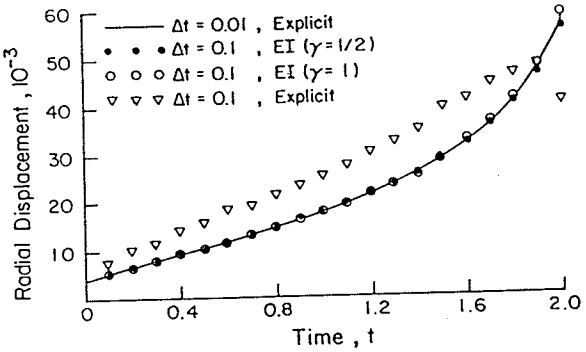

Figure 6. Creep radial displacement at inner surface using continuum damage theory and EI scheme

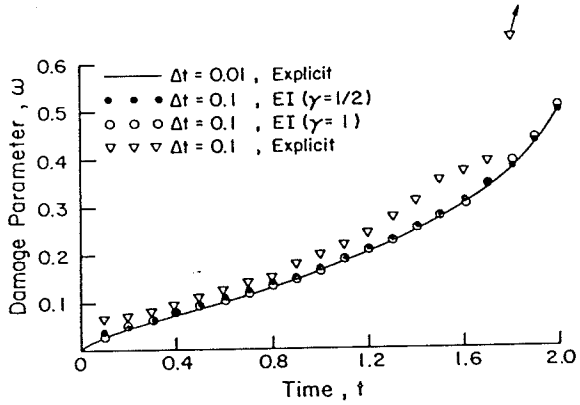

Figure 7. Variation of creep damage parameter at inner surface

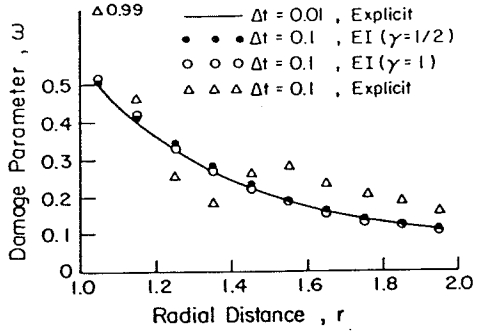

Figure 8. Distribution of creep damage parameter at $t = 2{\cdot}0$

and achieve a significant economy in computations. The numerical examples presented in this paper have demonstrated that significant improvements in the stability and accuracy of results are obtainable by using as little as two implicit elements. With this mixed EI scheme, much larger time step sizes can be employed with only slightly more computational effort than for the explicit scheme.

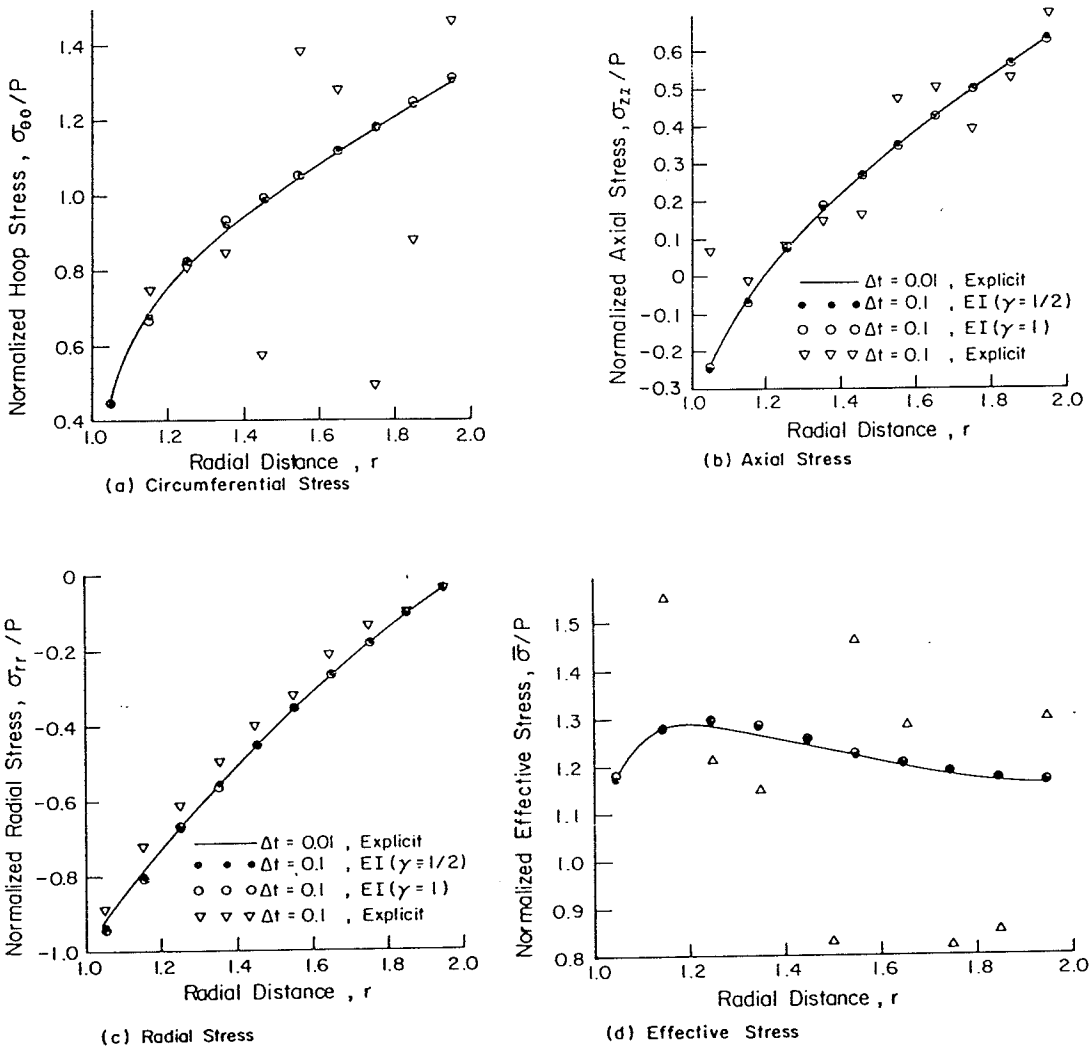

Figure 9. Distribution of creep stresses in cylinder at $t = 2{\cdot}0$ using continuum damage theory

The advantage of the proposed method over the fully implicit method is obvious. As described in the Appendix, the computational procedure of using the implicit elements is much more complicated and time consuming than that for the explicit elements. Furthermore, the element of the stiffness matrix associated with the explicit elements need only to be performed once and for all. Therefore, a considerable cost saving can be realized by treating most elements in the structure as explicit elements with the mixed explicit implicit method. For large scale problems where a great many elements are involved, this advantage is even more pronounced.

This scheme is especially attractive for creep fracture analysis, in which high concentrations of creep strains exist near the crack tip. In order to achieve accurate and stable results, an implicit scheme is desirable for the near tip region and the more economical explicit scheme is usually used in the remaining part of the structure. A mixed EI scheme such as that presented here can be applied with considerable flexibility and efficiency.

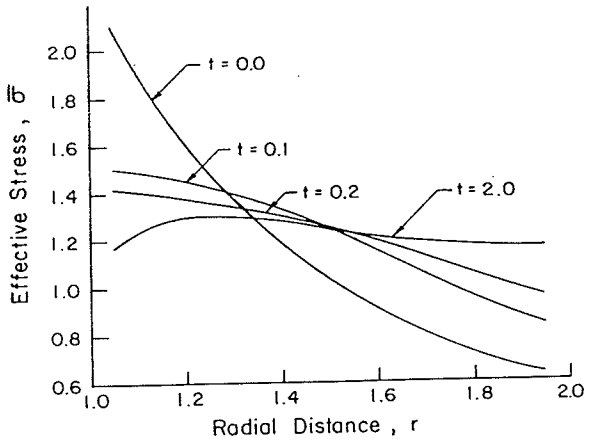

Figure 10. Distribution of effective stress using EI scheme ($\gamma=0{\cdot}5$, $\Delta t=0{\cdot}1$) using continuum damage theory

Recently, the continuum damage constitutive model has been employed in creep crack propagation problems.[15] The proposed scheme has been incorporated into this model to provide a more realistic approach to the study of creep crack growth.[16]

APPENDIX

Procedure of implementation of mixed EI scheme

1. Initialization: Set $n=0$ and $\boldsymbol{\varepsilon}_0^c=\mathbf{0}$, $\boldsymbol{\omega}_0=\mathbf{0}$, form $\mathbf{K}$ and $\mathbf{F}_0$, compute $\mathbf{U}_0=\mathbf{K}^{-1}\mathbf{F}_0$ and $\boldsymbol{\sigma}_0=\mathbf{DBU}_0$
2. Compute $\dot{\boldsymbol{\varepsilon}}_n^c=f_1(\boldsymbol{\sigma}_n, \boldsymbol{\omega}_n, t_n)$, $\dot{\boldsymbol{\omega}}_n=f_2(\boldsymbol{\sigma}_n, \boldsymbol{\omega}_n)$
3. Select Δt
4. Perform stiffness matrix:
   Explicit elements: $\mathbf{K}^e=\int_{v^e}\mathbf{B}^T\mathbf{DB}dv$
   Implicit elements: (1) form $\mathbf{H}_1$, $\mathbf{H}_2$, $\mathbf{H}_3$, $\mathbf{G}$, $\mathbf{G}_2$, $\mathbf{g}$
   (2) $\mathbf{D}_{n+1}^*=[\mathbf{I}+\gamma\Delta t\mathbf{D}(\mathbf{H}_1+\mathbf{H}_2\mathbf{g}\mathbf{G}_1\Delta t]^{-1}\mathbf{D}$
   (3) $\mathbf{K}_{n+1}^I=\int_{v^I}\mathbf{B}^T\mathbf{D}_{n+1}^*\mathbf{B}dv$
5. Equivalent load vector:
   Explicit elements: $\Delta\mathbf{F}_{n+1}^e=\int_{v^e}\mathbf{B}^T\mathbf{D}\dot{\boldsymbol{\varepsilon}}_n^c\Delta t\,dv$
   Implicit elements: $\Delta\mathbf{F}_{n+1}^I=\int_{v^I}\mathbf{B}^T\mathbf{D}_{n+1}^*[\dot{\boldsymbol{\varepsilon}}_n^c\Delta t+(\mathbf{H}_2\mathbf{g}\dot{\boldsymbol{\omega}}_n+\mathbf{H}_3)\gamma\Delta t^2]dv$
6. Assembling:
   $\mathbf{K}_{n+1}=\mathbf{K}^e+\mathbf{K}_{n+1}^I$
   $\Delta\mathbf{F}_{n+1}=\Delta\mathbf{F}_{n+1}^e+\Delta\mathbf{F}_{n+1}^I+\Delta\mathbf{R}_{n+1}$
7. Solve: $\mathbf{K}_{n+1}\Delta\mathbf{U}_{n+1}=\Delta\mathbf{F}_{n+1}$
8. Stress increment:
   Explicit elements: $\Delta\boldsymbol{\sigma}_{n+1}=\mathbf{D}(\mathbf{B}\Delta\mathbf{u}_{n+1}-\dot{\boldsymbol{\varepsilon}}_n^c\Delta t)$
   Implicit elements: $\Delta\boldsymbol{\sigma}_{n+1}=\mathbf{D}_{n+1}^*[\mathbf{B}\Delta\mathbf{u}_{n+1}-\dot{\boldsymbol{\varepsilon}}_n^c\Delta t-(\mathbf{H}_2\mathbf{g}\dot{\boldsymbol{\omega}}_n+\mathbf{H}_3)\gamma\Delta t^2]$
9. Update: $\mathbf{u}_{n+1}=\mathbf{u}_n+\Delta\mathbf{u}_{n+1}$, $\boldsymbol{\sigma}_{n+1}=\boldsymbol{\sigma}_n+\Delta\boldsymbol{\sigma}_{n+1}$

10. Evaluate ω_{n+1}:

    Explicit elements: $\omega_{n+1}=\omega_n+\dot{\omega}_n\Delta t$

    Implicit elements:

    (A) $i=0$, $\omega^0_{n+1}=\omega_n+\dot{\omega}_n\Delta t$

    (B) $\dot{\omega}^i_{n+1}=f_2(\sigma_{n+1},\ \omega)$

    (C) $\omega^{i+1}_{n+1}=\omega^i_{n+1}-(\mathbf{I}-\gamma\mathbf{G}_2\Delta t)^{-1}\{\omega^i_{n+1}-\omega_n-[(1-\gamma)\dot{\omega}_n+\gamma\omega^i_{n+1}]\Delta t\}$

    (D) If $\|\omega^{i+1}_{n+1}-\omega^i_{n+1}\|<\varepsilon$, $\omega_{n+1}\leftarrow\omega^{i+1}_{n+1}$; otherwise $i\leftarrow i+1$, go to (B)

11. $n\leftarrow n+1$, if $\sum_{i=1}^{n}\Delta t_i<T$, go to step 2; otherwise stop.

REFERENCES

1. O. C. Zienkiewicz and I. C. Cormeau, 'Visco-plasticity—plasticity and creep in elastic solids—a unified numerical solution approach', *Int. j. numer. methods eng.*, **8**, 821–845 (1974).
2. I. C. Cormeau, 'Numerical stability in quasi-static elasto/visco-plasticity', *Int. j. numer. methods eng.*, **9**, 109–127 (1975).
3. T. J. R. Hughes and R. L. Taylor, 'Unconditionally stable algorithms for quasi-static elasto/visco-plastic finite element analysis', *Comp. Struct.*, **8**, 169–173 (1978).
4. M. B. Kanchi, O. C. Zienkiewicz and D. R. J. Owen, 'The visco-plastic approach to problems of plasticity and creep involving geometric non-linear effects', *Int. j. numer. methods eng.*, **12**, 169–181 (1978).
5. T. Belytschko and R. Mullen, 'Stability of explicit–implicit mesh partition in time integration', *Int. j. numer. methods eng.*, **12**, 1575–1586 (1978).
6. T. J. R. Hughes and W. K. Liu, 'Implicit–explicit elements in transient analysis', *J. Appl. Mech. ASME*, **45**, 371–378 (1978).
7. W. K. Liu, 'Development of finite element procedures for fluid-structure interactions', *Report No. EERL 80-06*, California Institute of Technology, Pasadena, Calif., Aug. 1980.
8. W. K. Liu, 'Development of mixed time partition procedures for thermal analysis of structures', *Int. j. numer. methods eng.*, **19**, 125–140 (1983).
9. W. K. Liu, Y. F. Zhang and T. Belytschko, 'Implementation of mixed-time partition algorithms for non-linear thermal analysis of structures', *Comp. Methods Appl. Mech. Eng.*, **48**, 245–263 (1985).
10. F. A. Leckie and D. R. Hayhurst, 'Constitutive equations for creep rupture', *Acta Metall.*, **25**, 1059–1070 (1977).
11. T. R. Hsu, *The Finite Element Method in Thermomechanics*, George Allen Unwin, London, 1986.
12. J. T. Boyle and J. Spence, *Stress Analysis of Creep*, Butterworths, London, 1983.
13. D. R. J. Owen and E. Hinton, *Finite Elements in Plasticity: Theory and Practice*, Pineridge Press, Swanred. 1980.
14. W. Prager and P. G. Hodge, Jr., *Theory of Perfectly Plastic Solids*, Dover, New York, 1968.
15. D. R. Hayhurst, P. R. Brown and C. J. Morrison, 'The role of continuum damage in creep crack growth', *Phil. Trans. R. Soc. London A* **311**, 131–158 (1984).
16. G. G. Chen and T. R. Hsu, 'A Finite Element Model for Creep Fracture Analysis Using Continuum Damage Approach', *Fourth Int. Conf. On Numerical Methods in Fracture Mechanics* San Antonio, Texas, 22–26 March 1987.

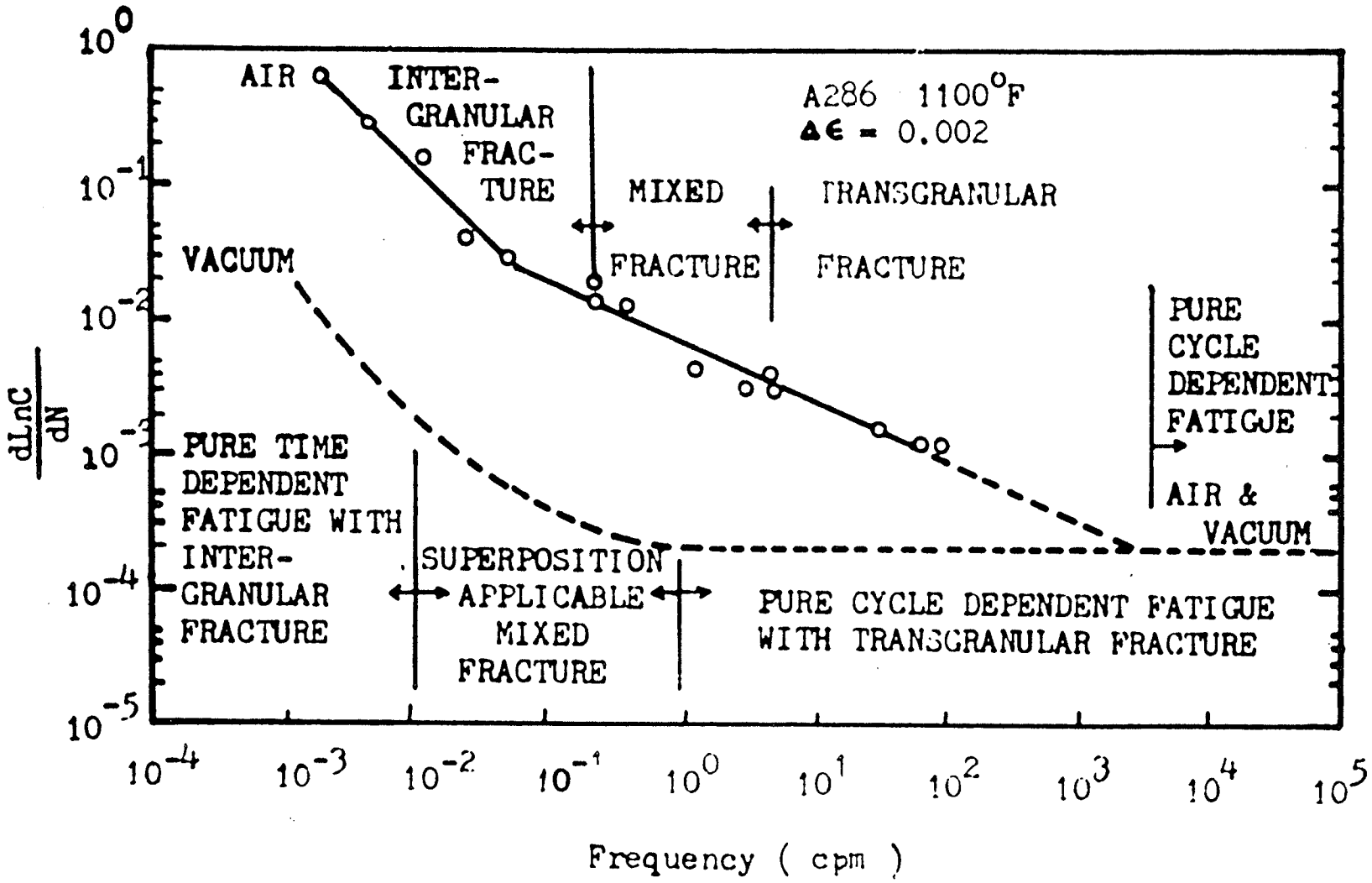

Figure 1.1 Effect of frequency on fatigue crack growth rate in A286, 1100°F [105]

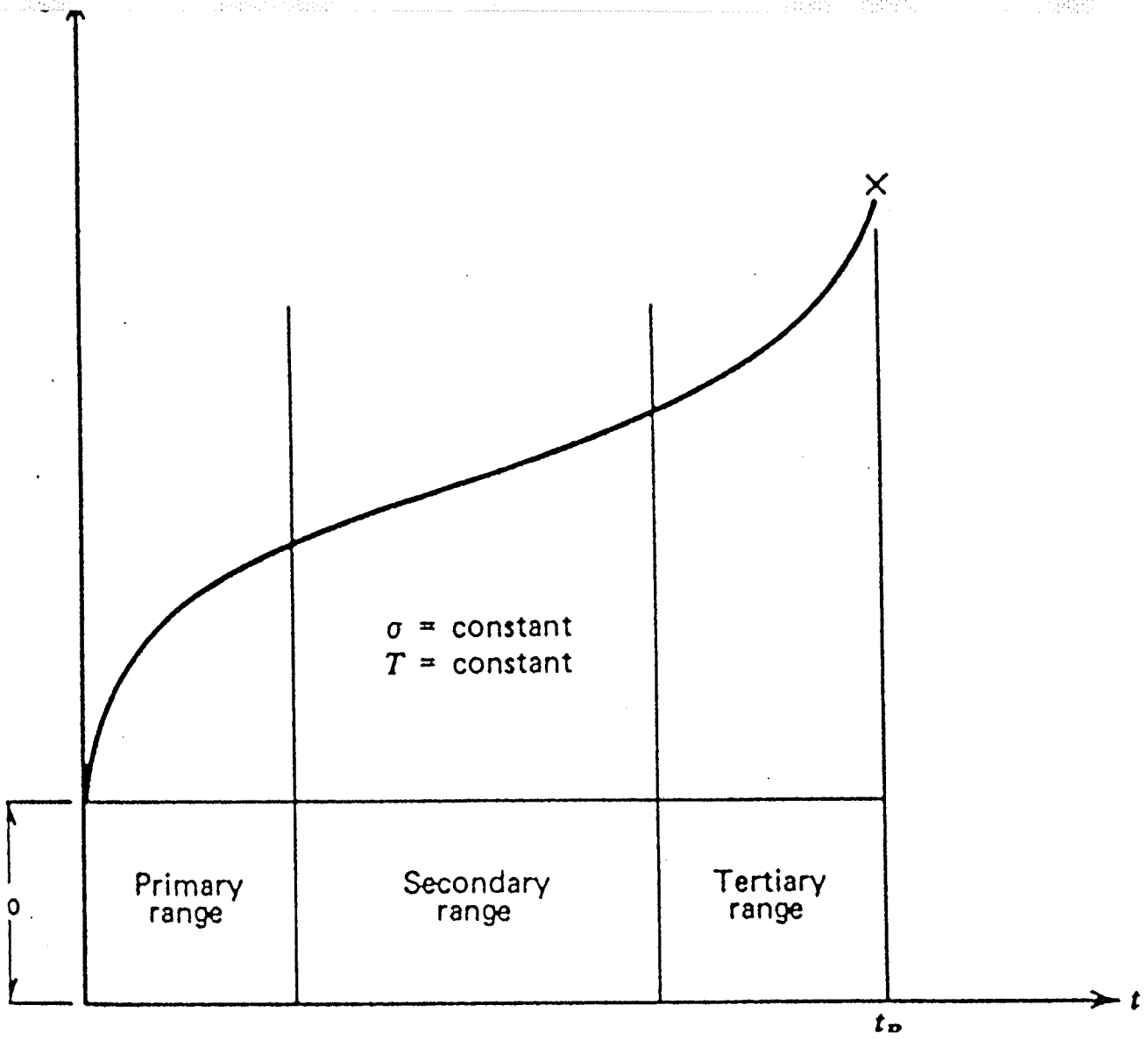

Figure 2.1 A typical creep strain history

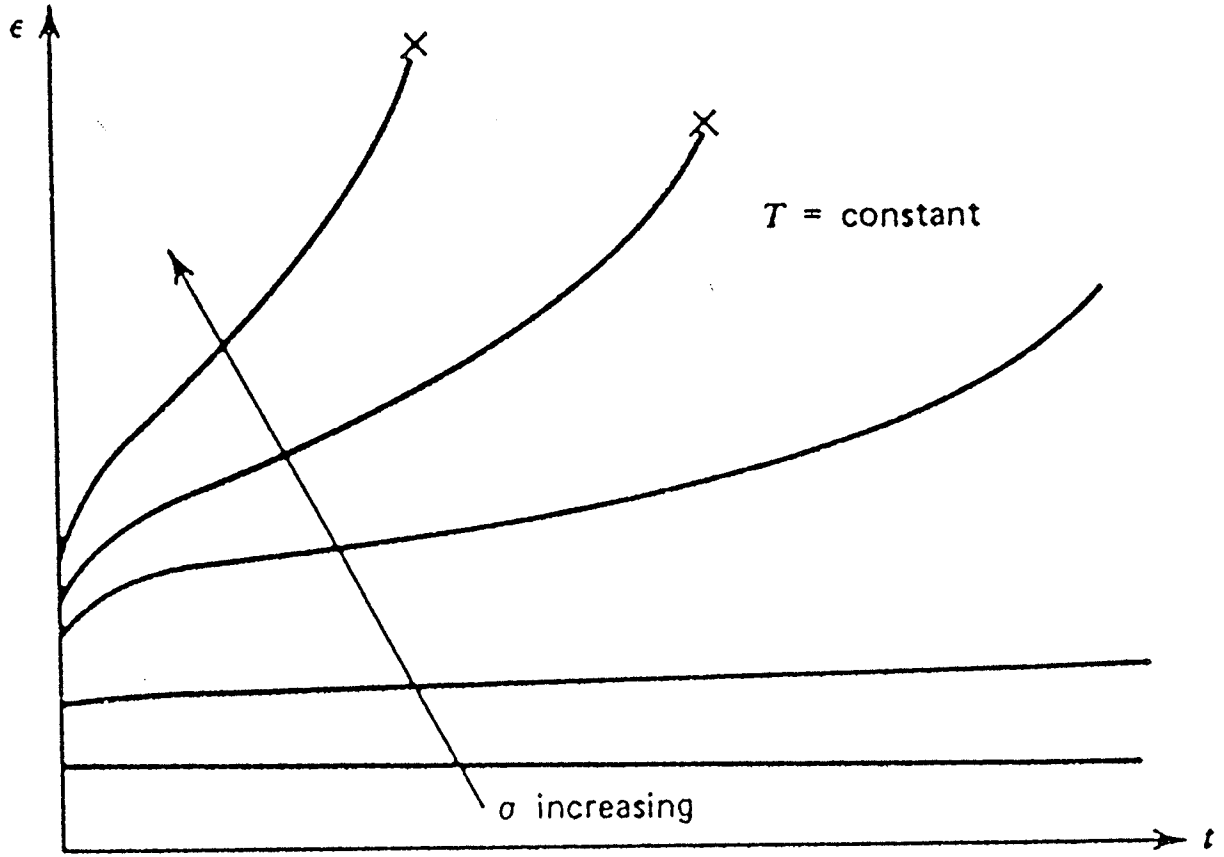

Figure 2.2 Effect of Stress on the creep curve at constant temperature

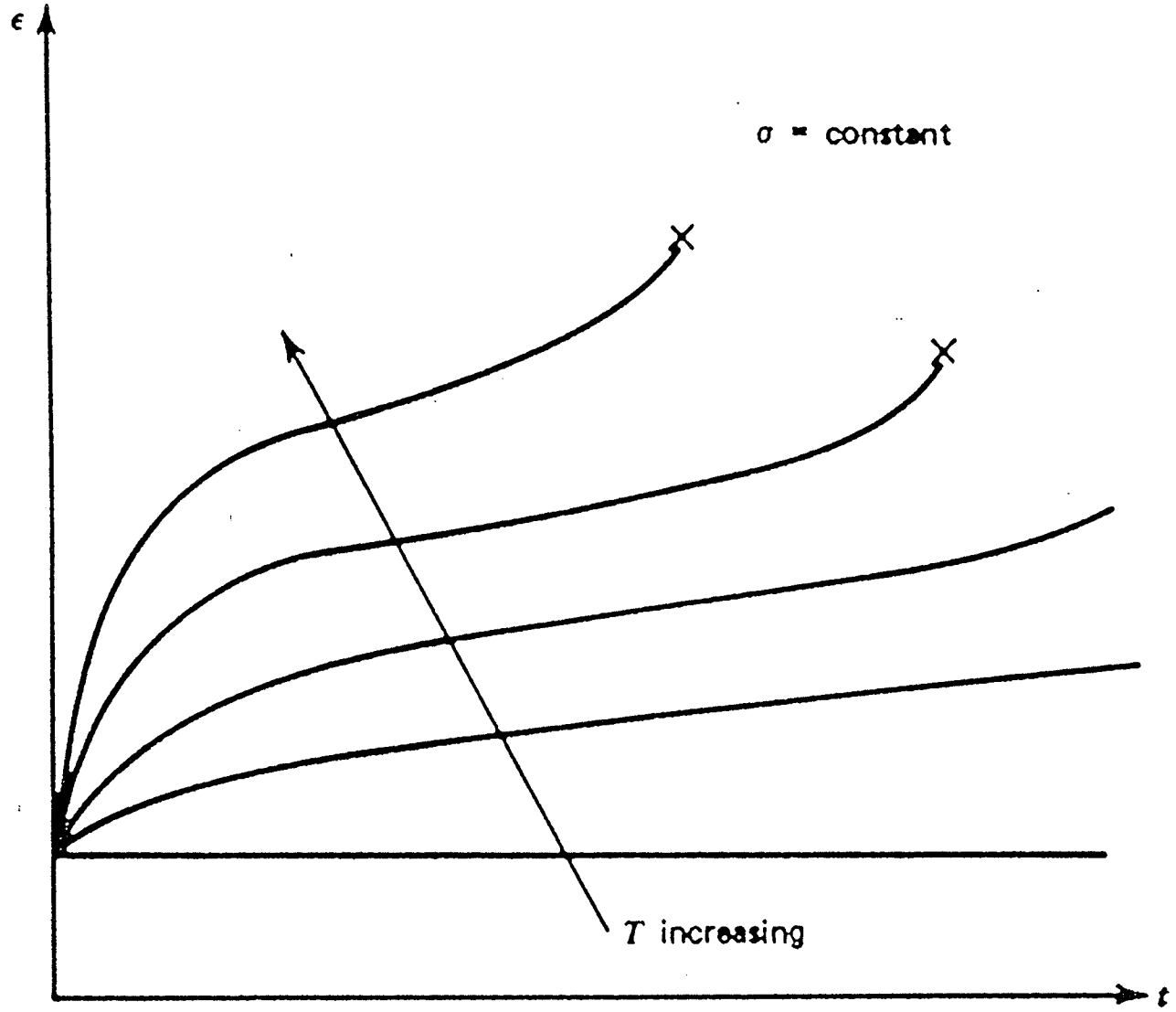

Figure 2.3 Effect of temperature on the creep curve at constant stress

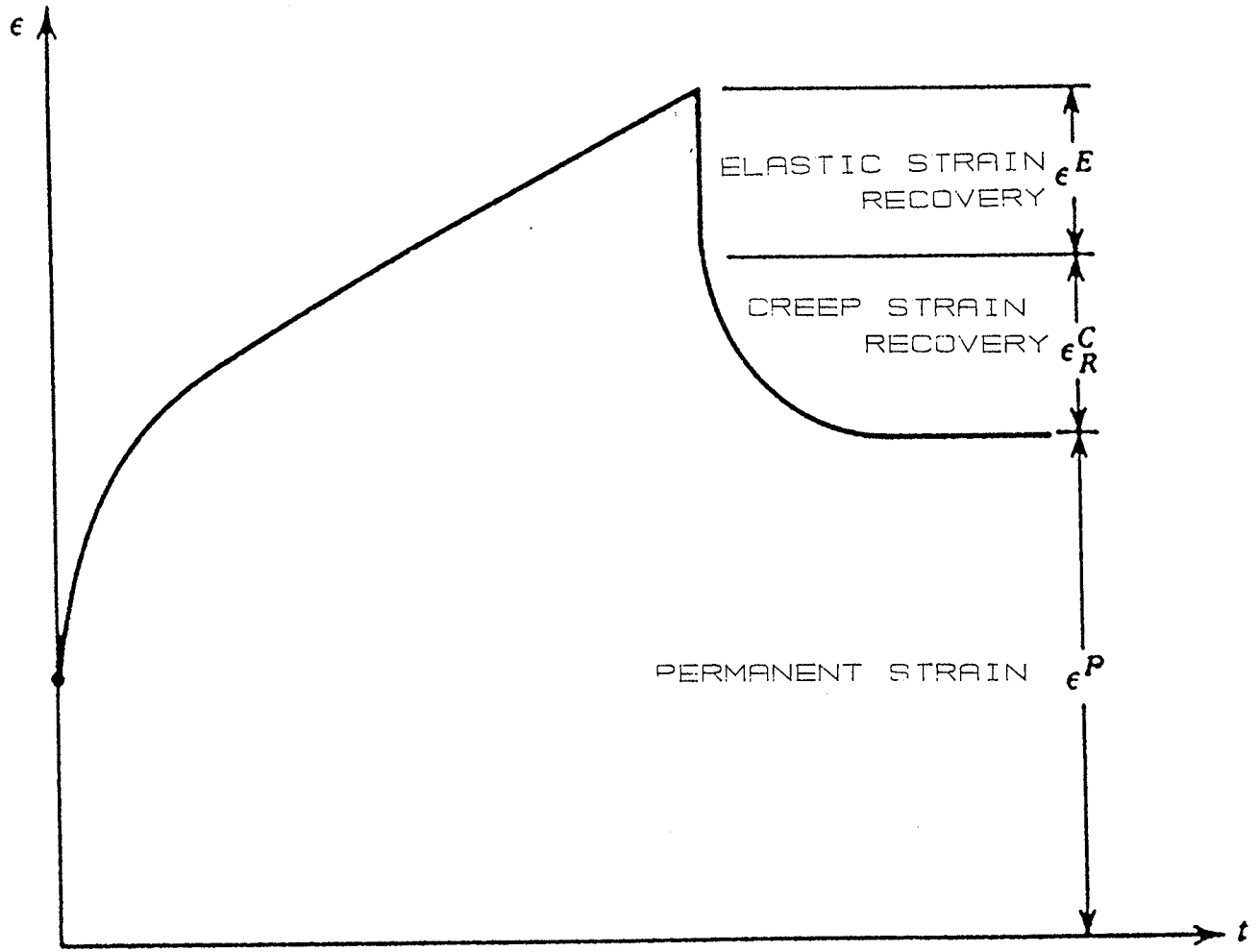

Figure 2.4 A typical creep recovery

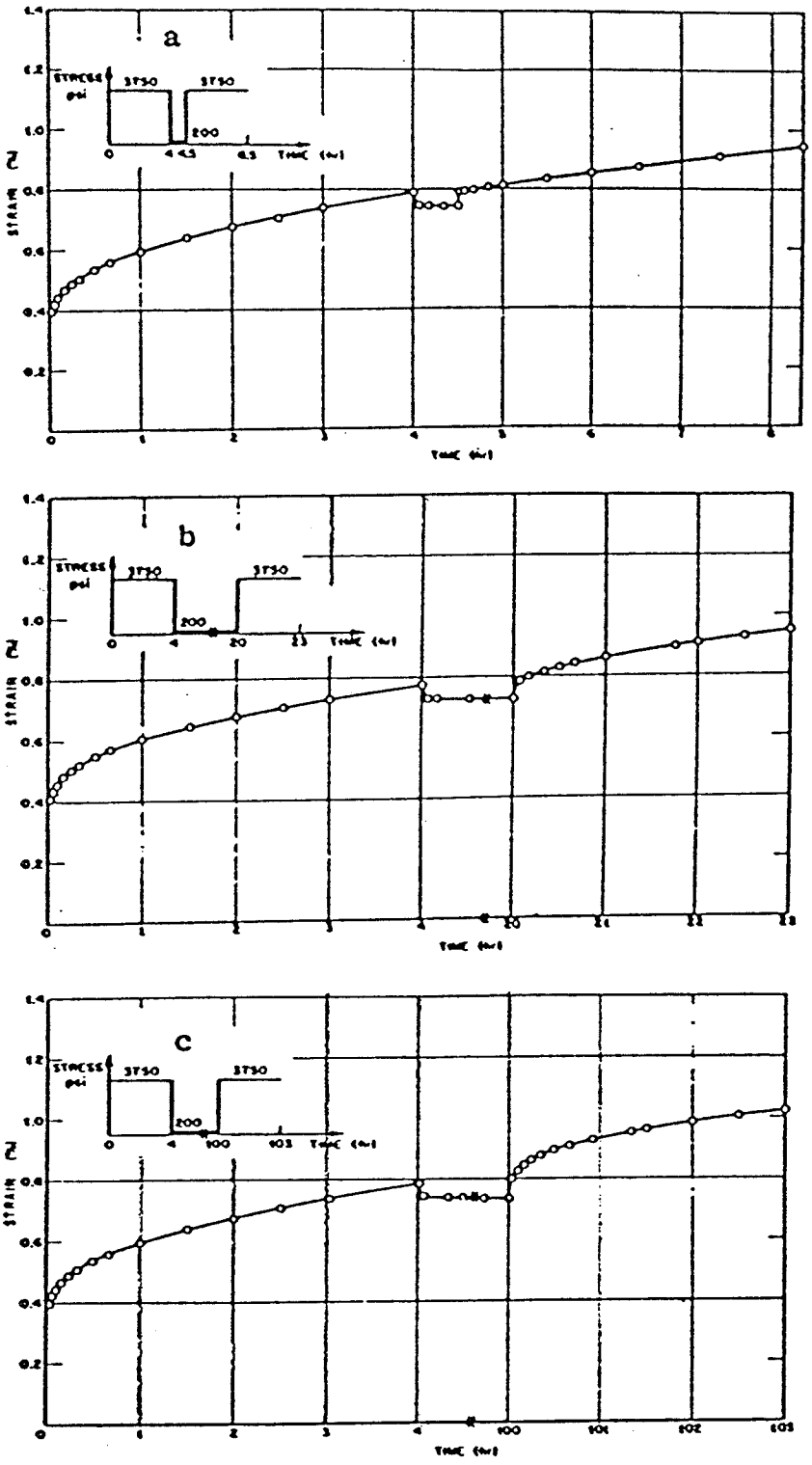

Figure 2.5 The influence of a rest period on the subsequent creep curve for 1100 aluminum at 300°F[5]. Rest periods: a = 0.5 hour, b = 16 hours, c = 96 hours

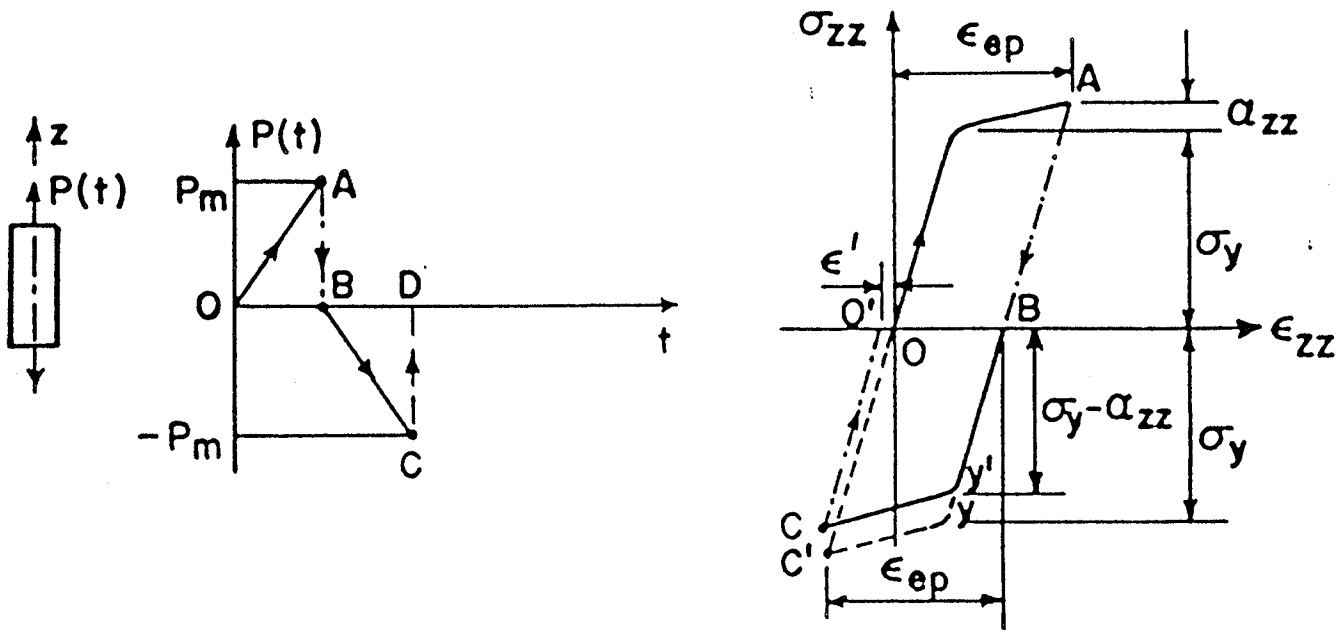

Figure 3.1 Paths for a uniaxially loaded bar under kinematic hardening plastic deformation

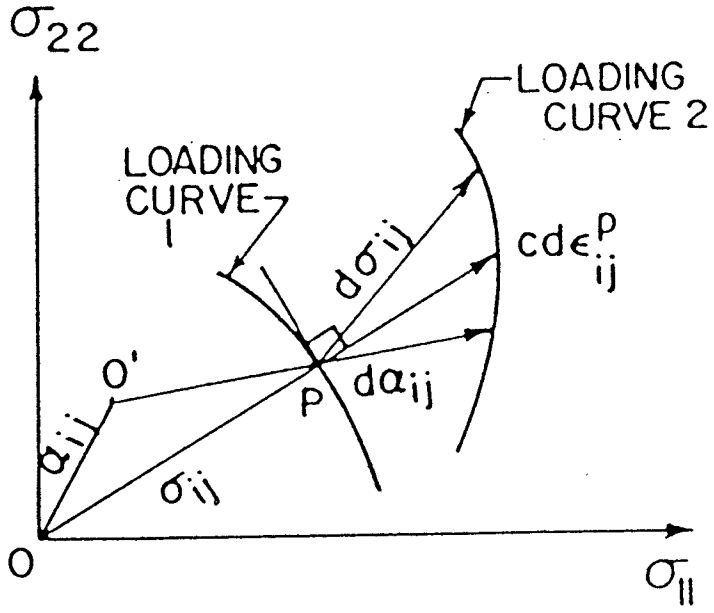

(a) Prager's original scheme

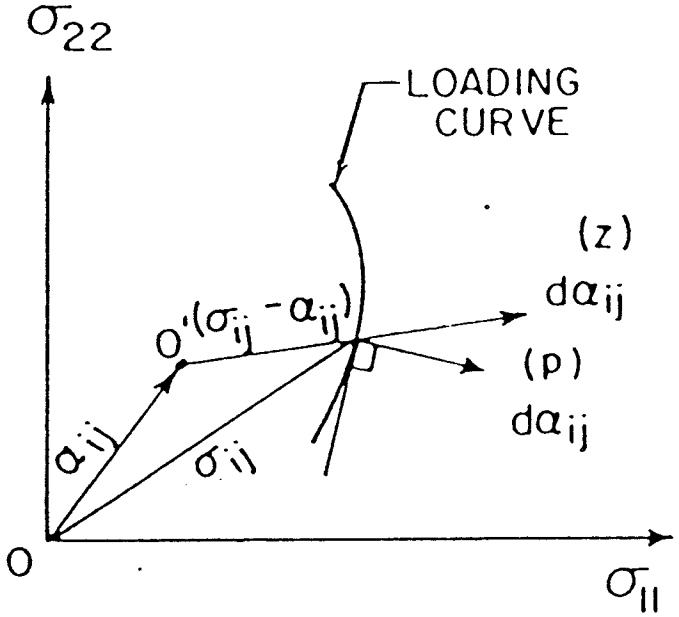

(b) Ziegler's modified scheme

Figure 3.2 Schematic representation of the Prager and Ziegler's hardening rules

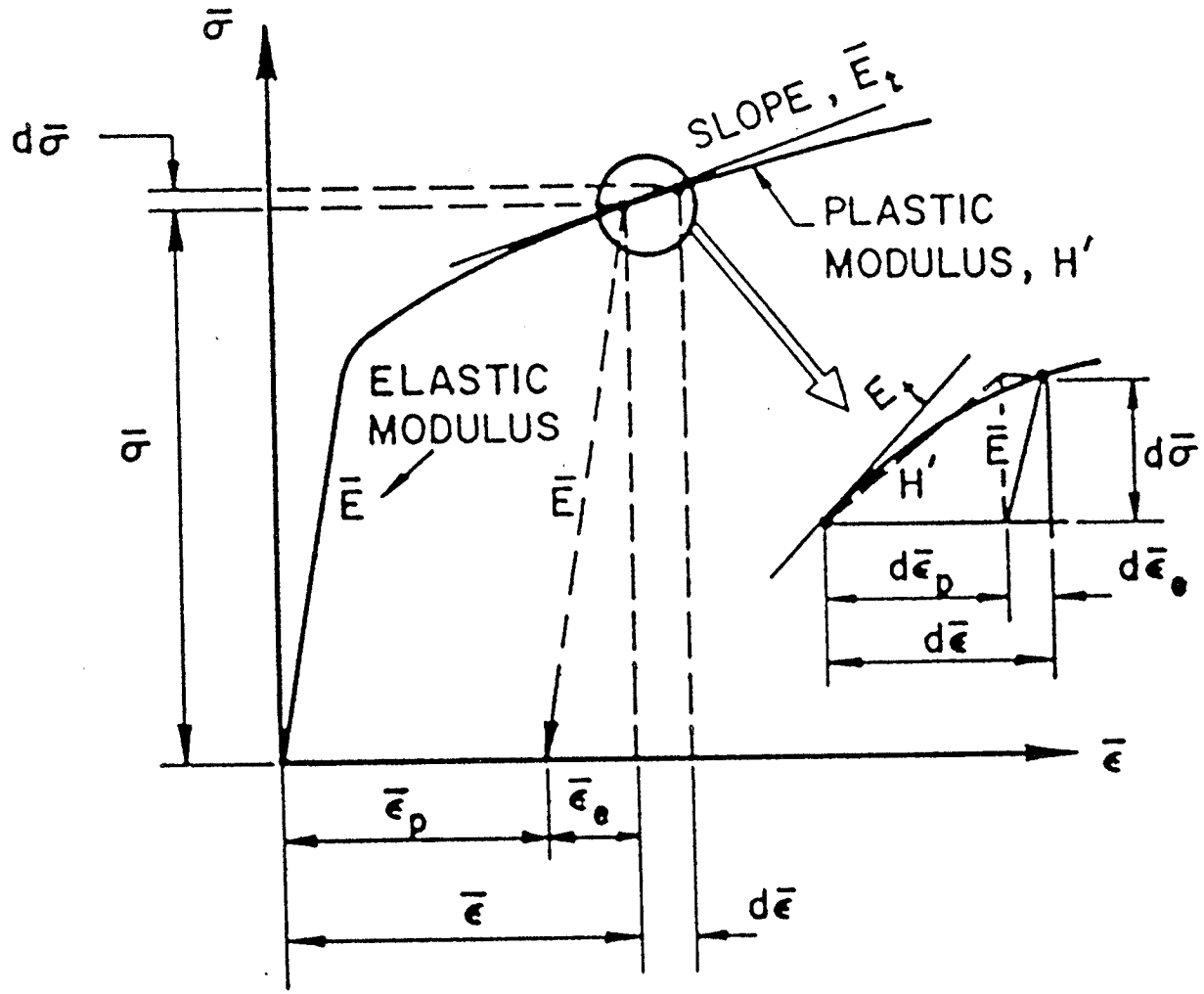

Figure 3.3 Graphic representation of material stiffness during elastic-plastic deformation

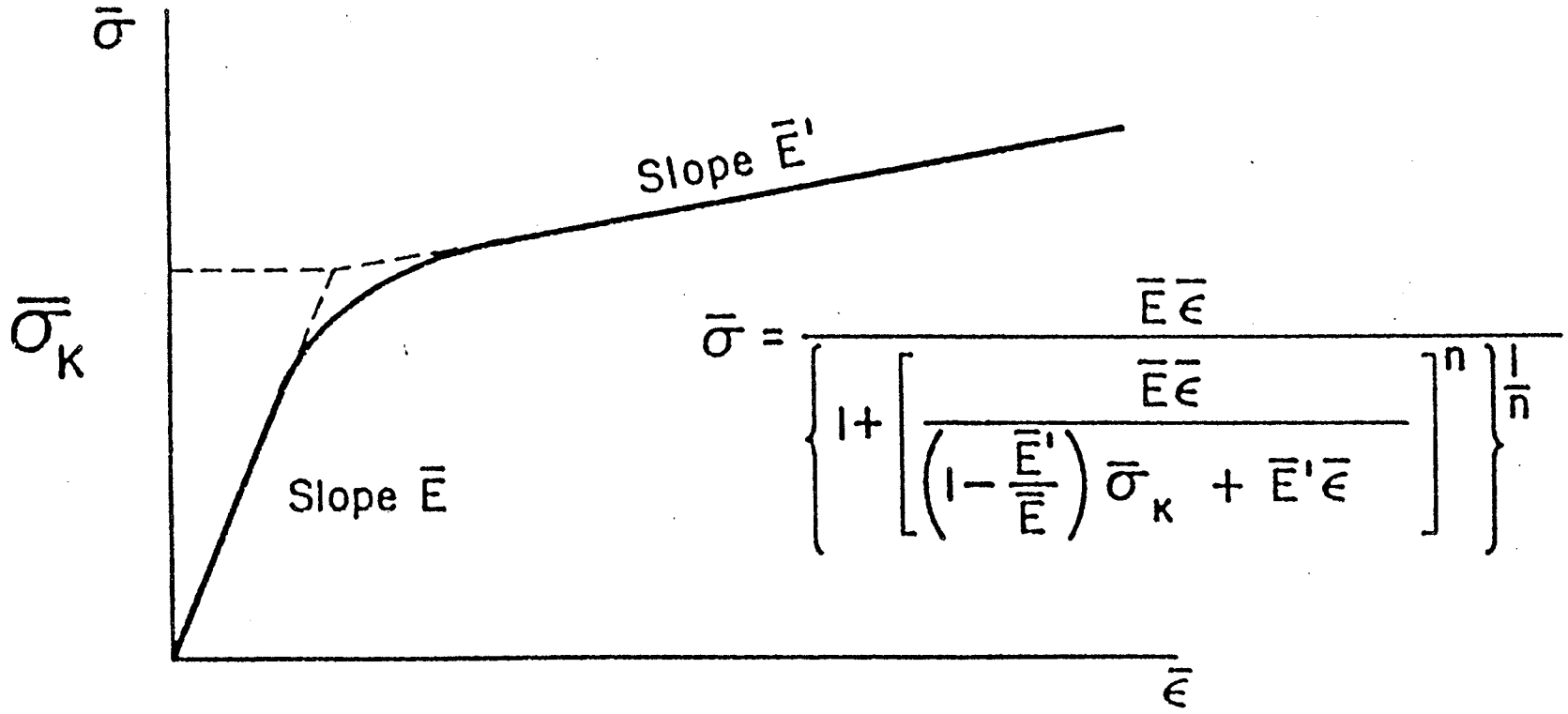

Figure 3.4 Polynomial approximation of stress-strain relation

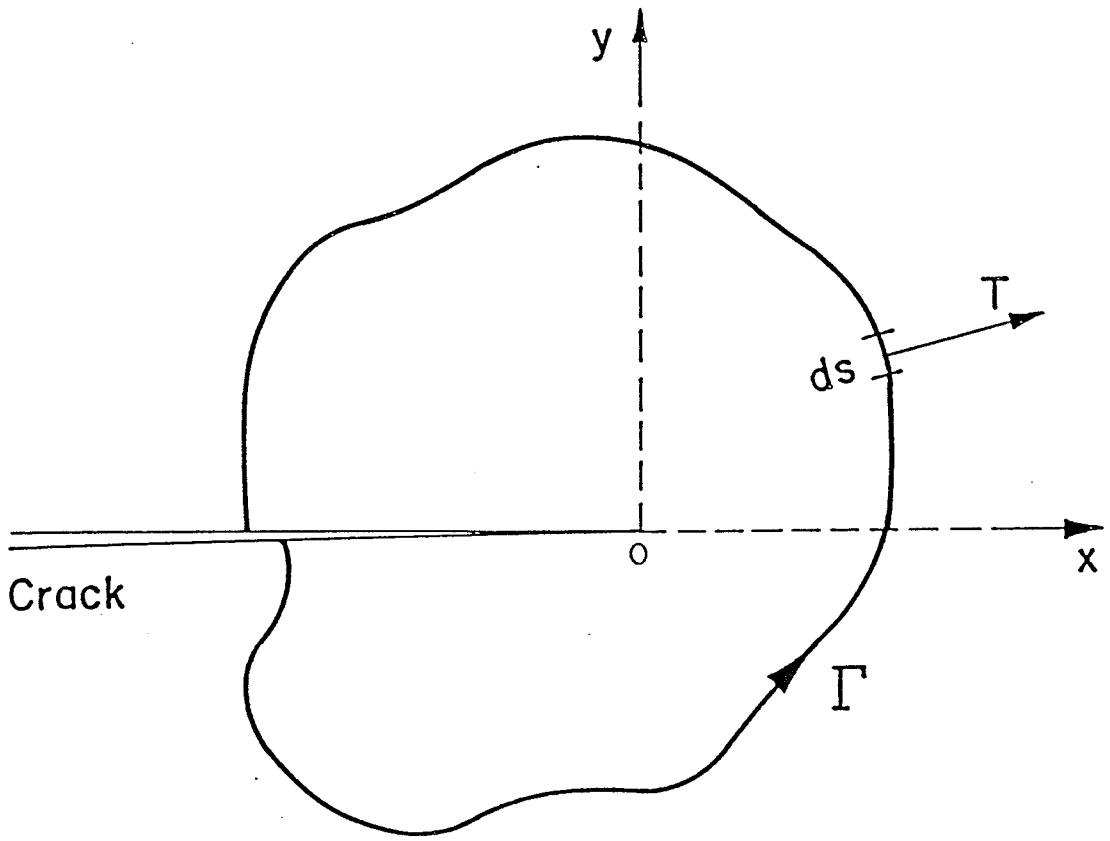

Figure 4.1 Path of integration for J-integral

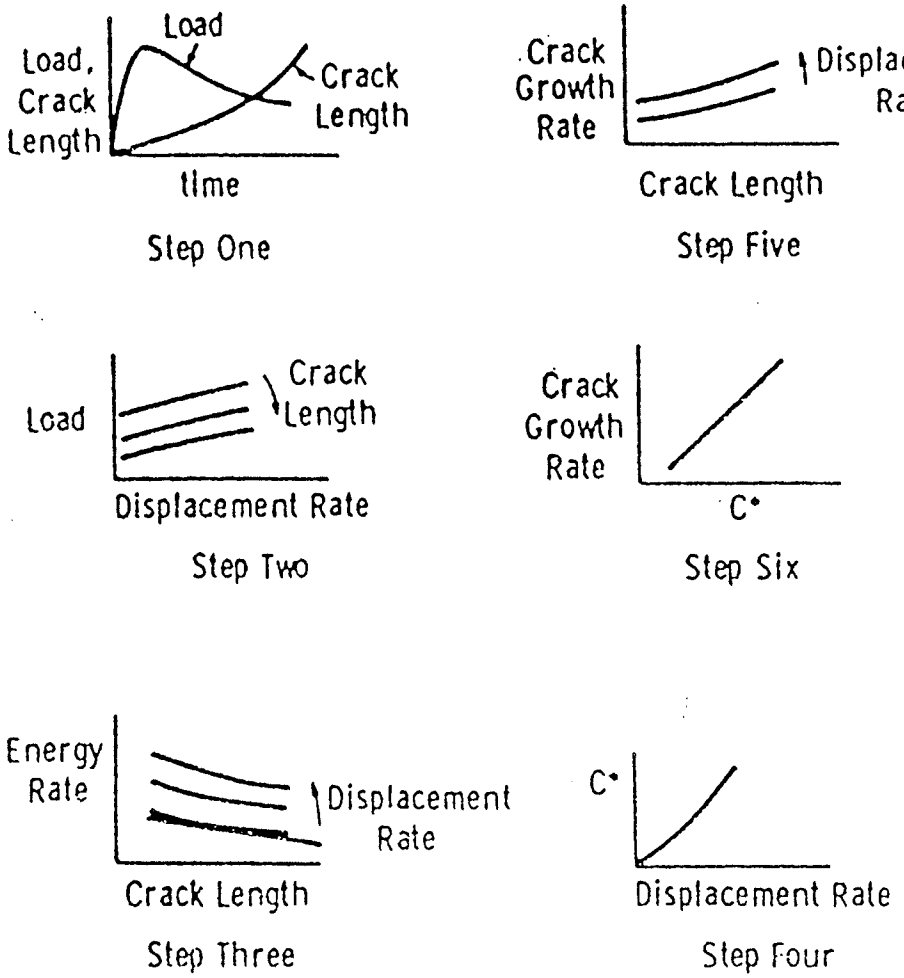

Figure 4.2 Data reduction scheme for the determination of C^*

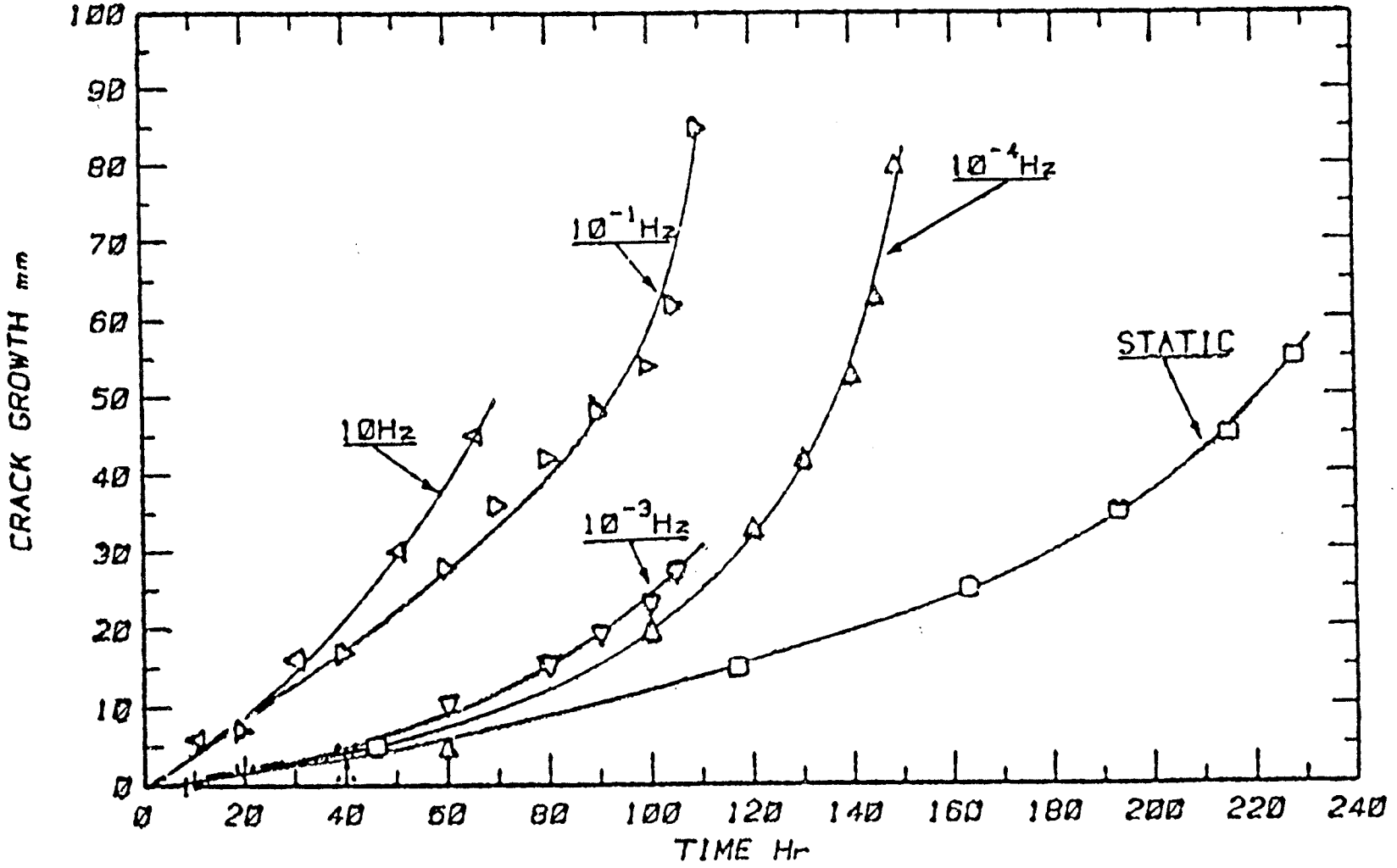

Figure 4.3 Effect of frequency on crack growth of 1/2 Cr Mo V steel at 565°C [90]

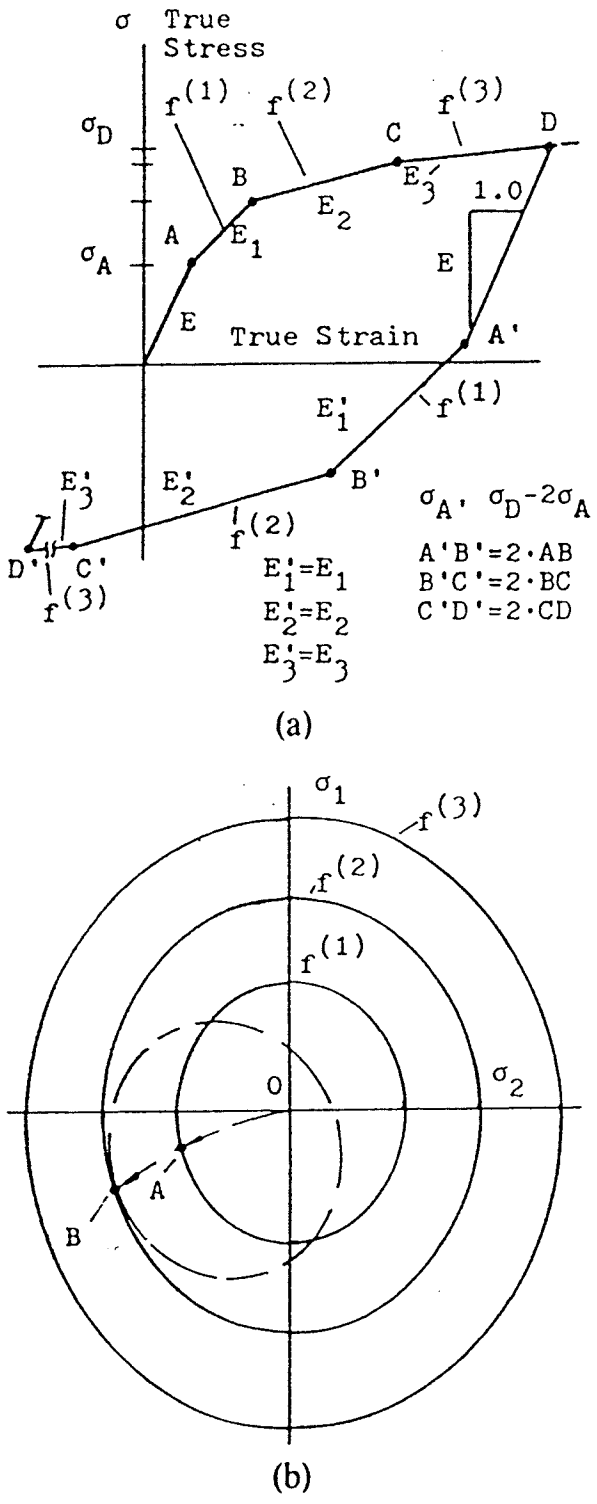

Figure 5.1 The relationship between the material uniaxial curve and the two dimensional stress field
(a) The material idealized uniaxial stress-strain curve
(b) Schematic representation of the yield surfaces at the initial condition and after translation of the first surface (dotted line)

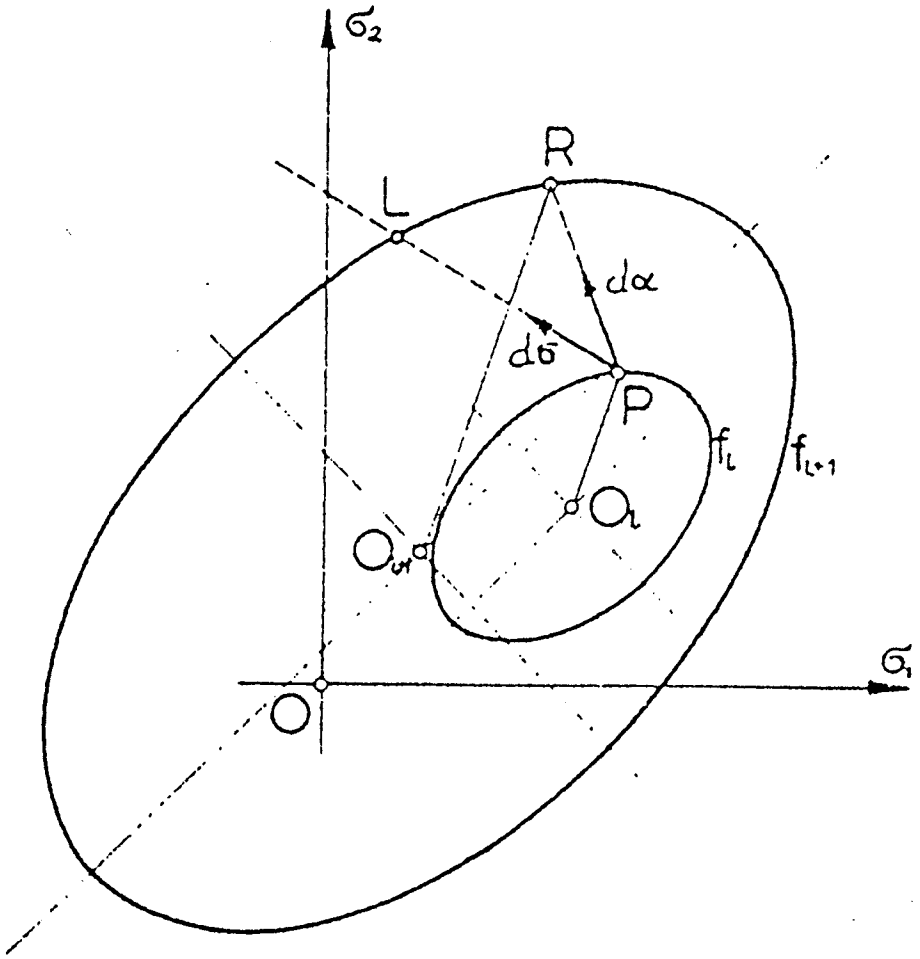

Figure 5.2 Schematic representation of the Mroz's hardening rule

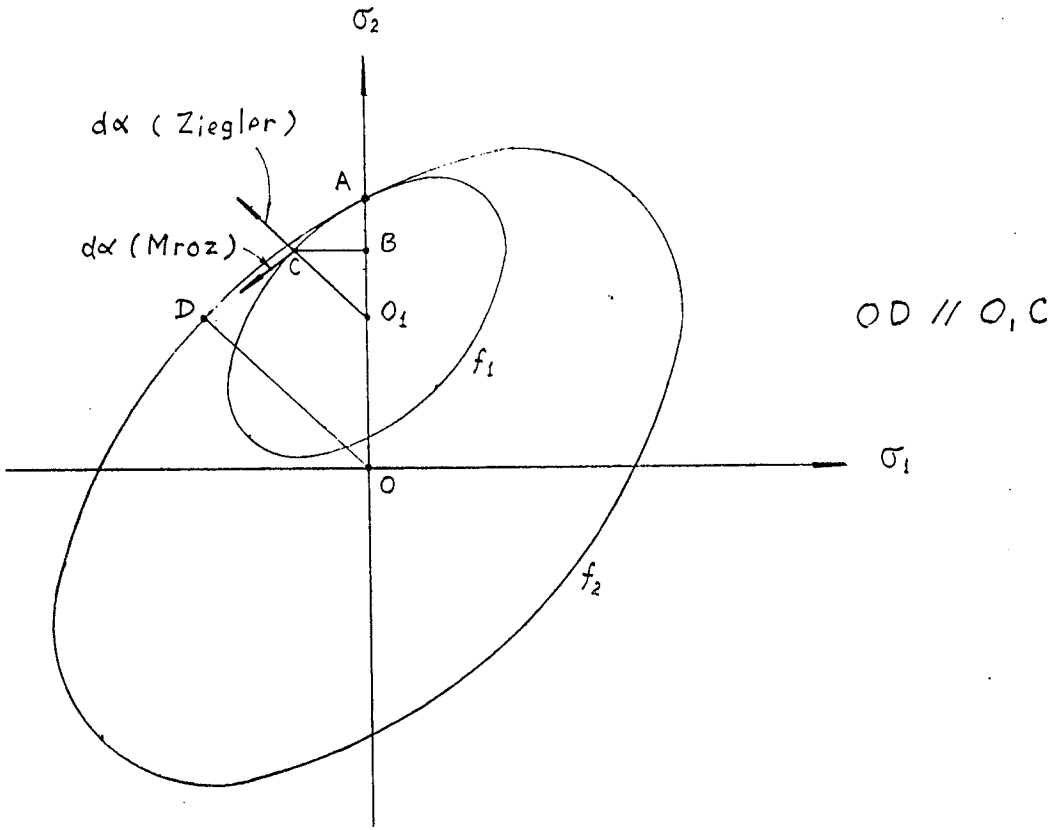

Figure 5.3 Ziegler's and Mroz's hardening rules for non-proportional loadings

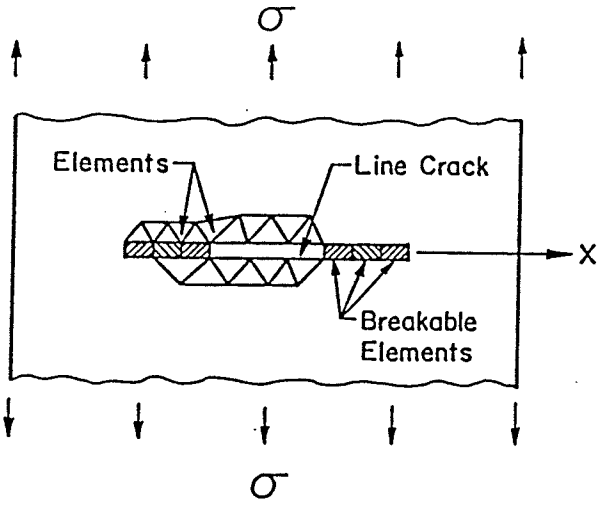

(a) Geometry of Breakable Elements

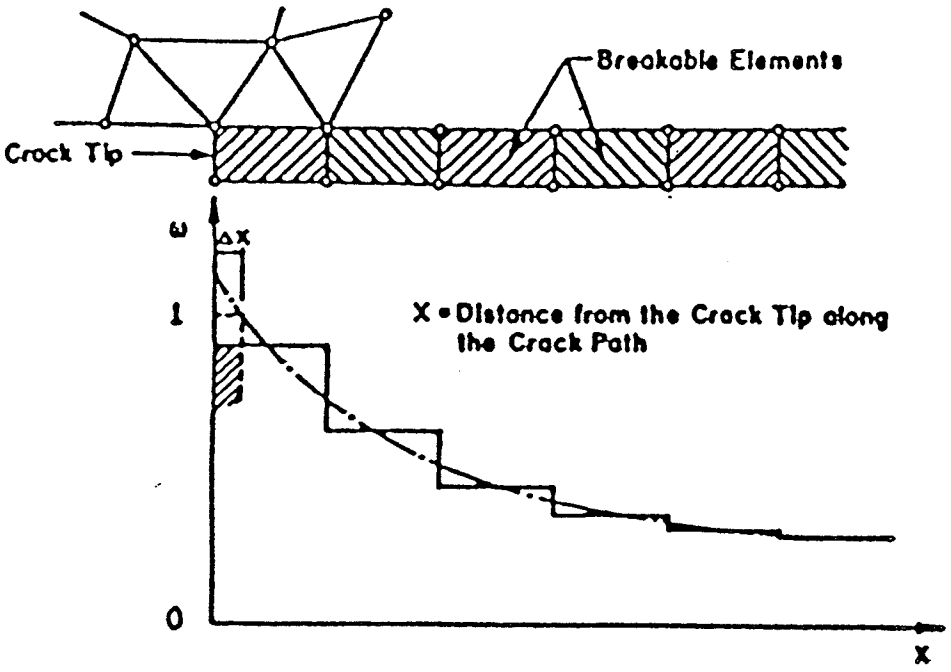

(b) Extrapolation of damage

Figure 5.4 The breakable elements

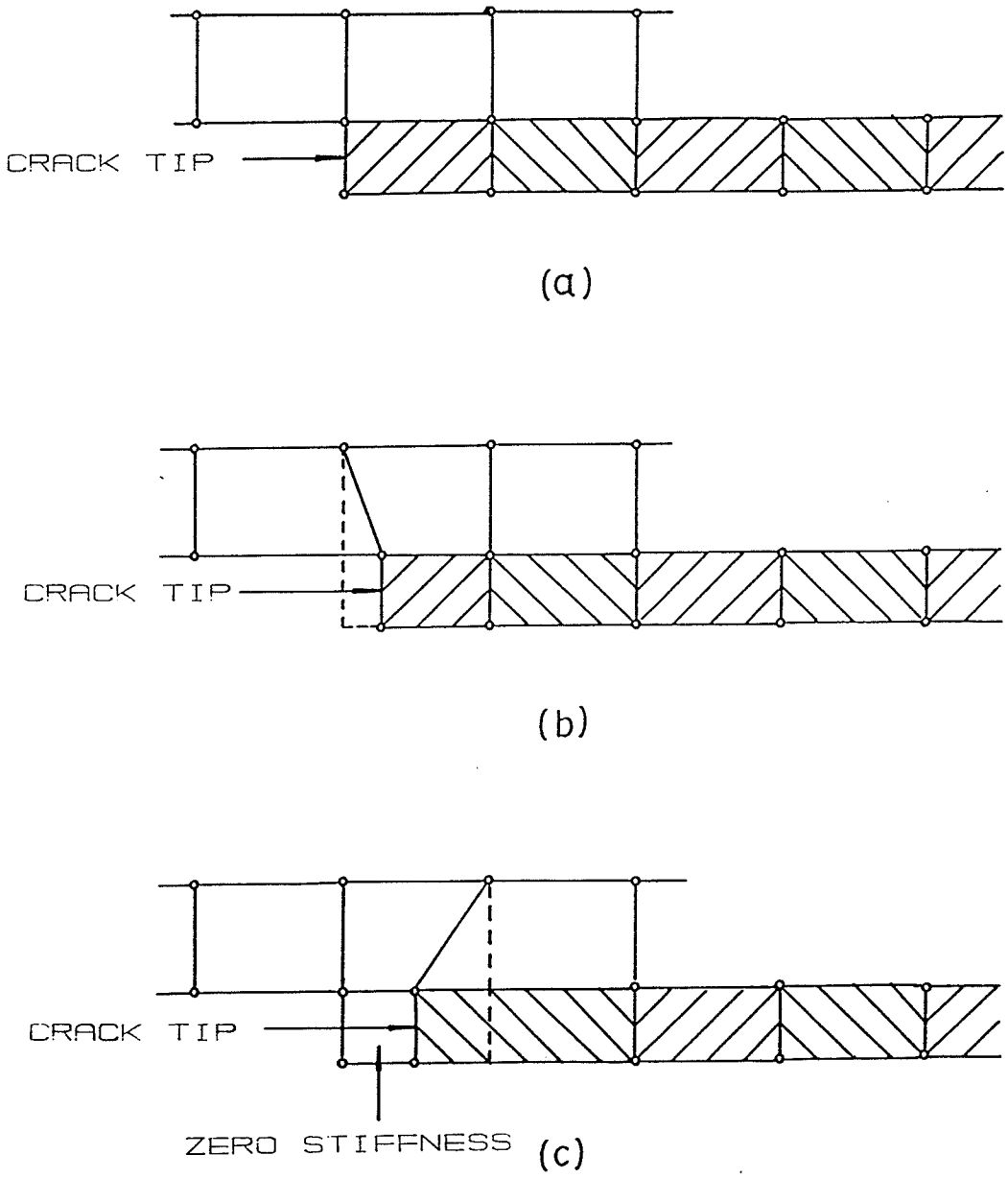

Figure 5.5 Numerical modeling of crack growth
(a) Initial crack
(b) Shifting of crack tip nodes
(c) Local remesh

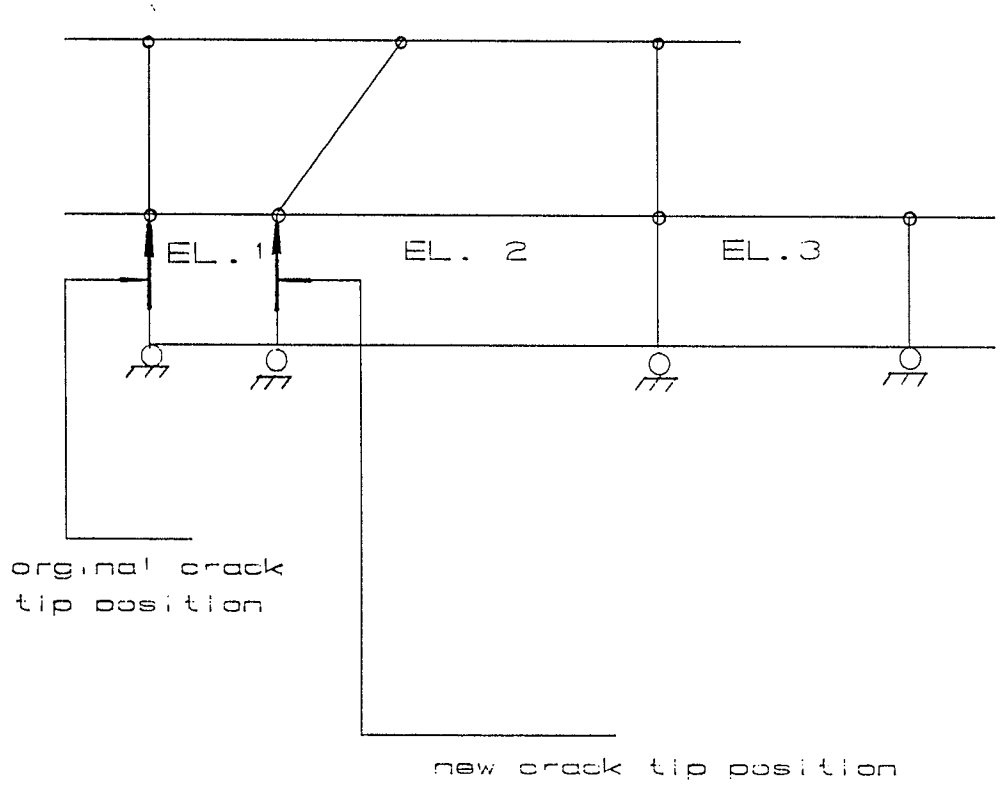

Figure 5.6 Application of nodal reaction force

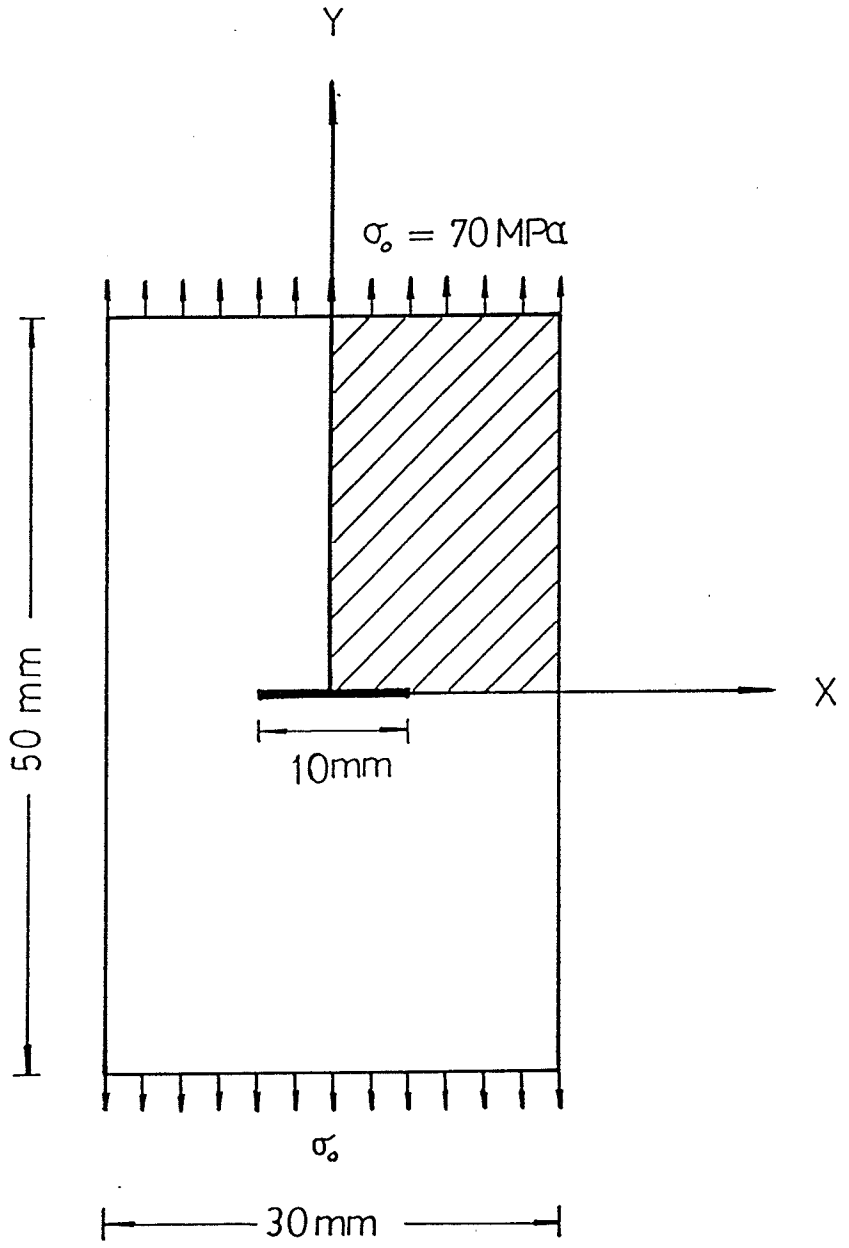

Figure 6.1 A centre cracked plate

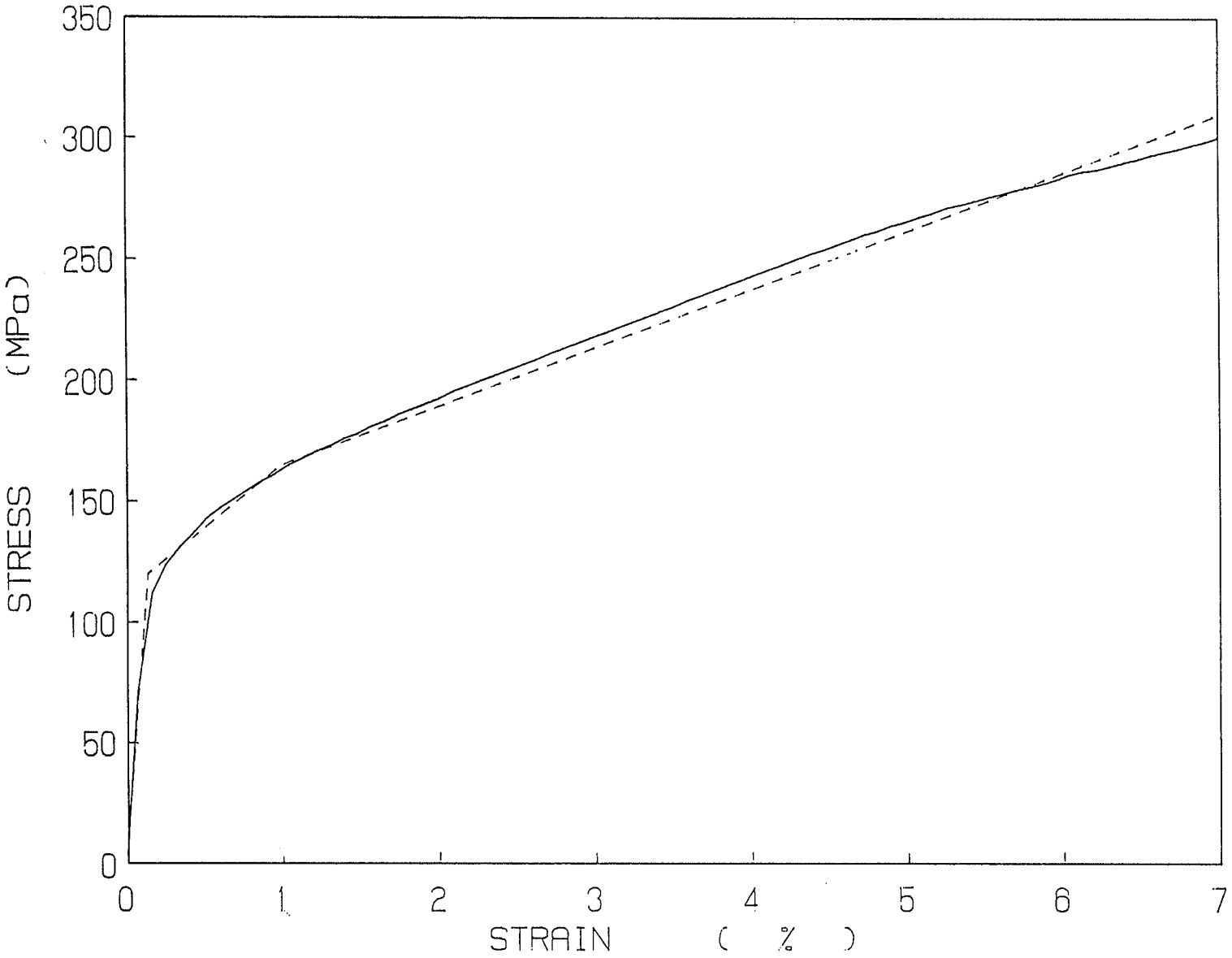

Figure 6.2 Uniaxial stress-strain curve for 316 SS at 650°C

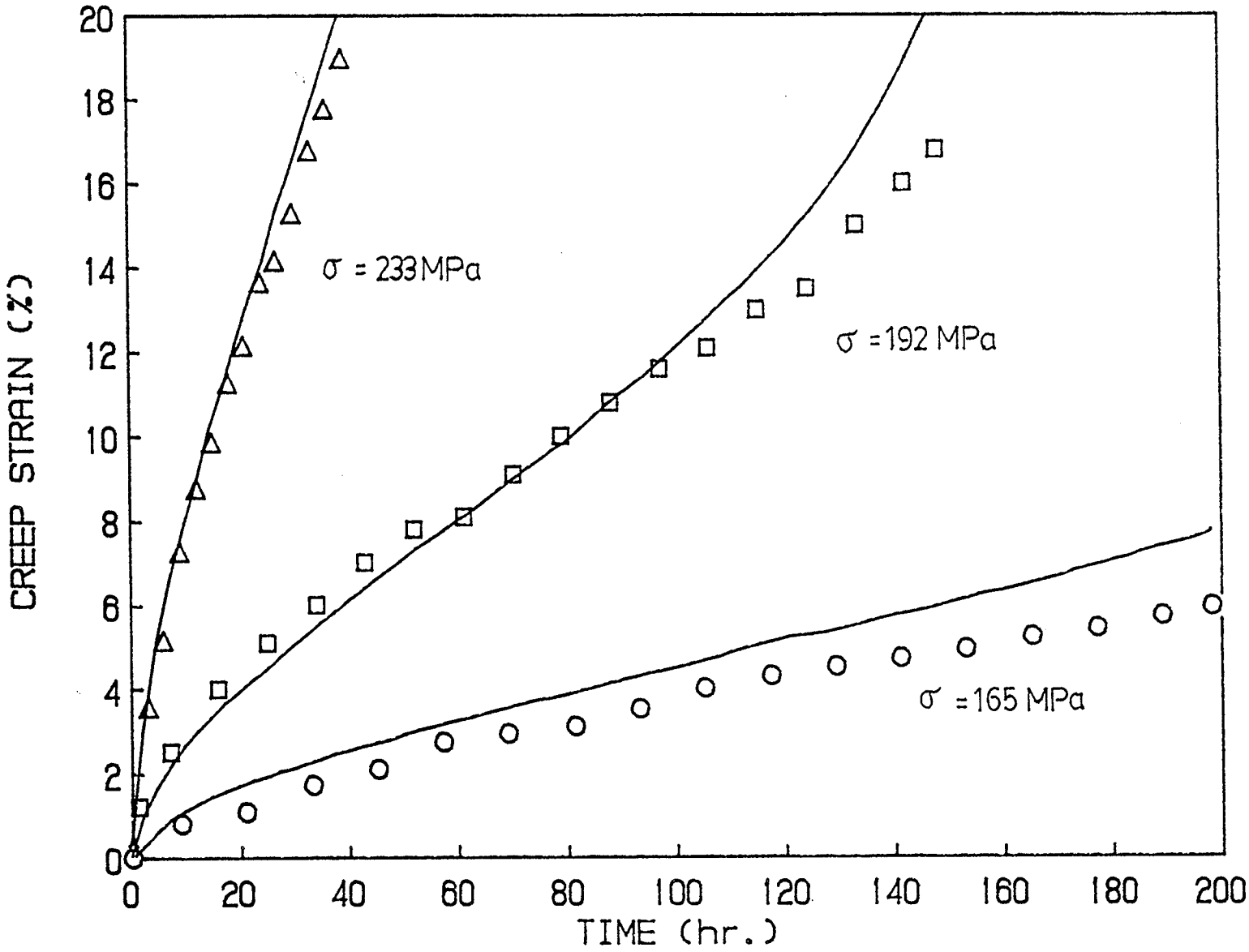

Figure 6.3 Uniaxial creep curves for 316 SS at 650°C

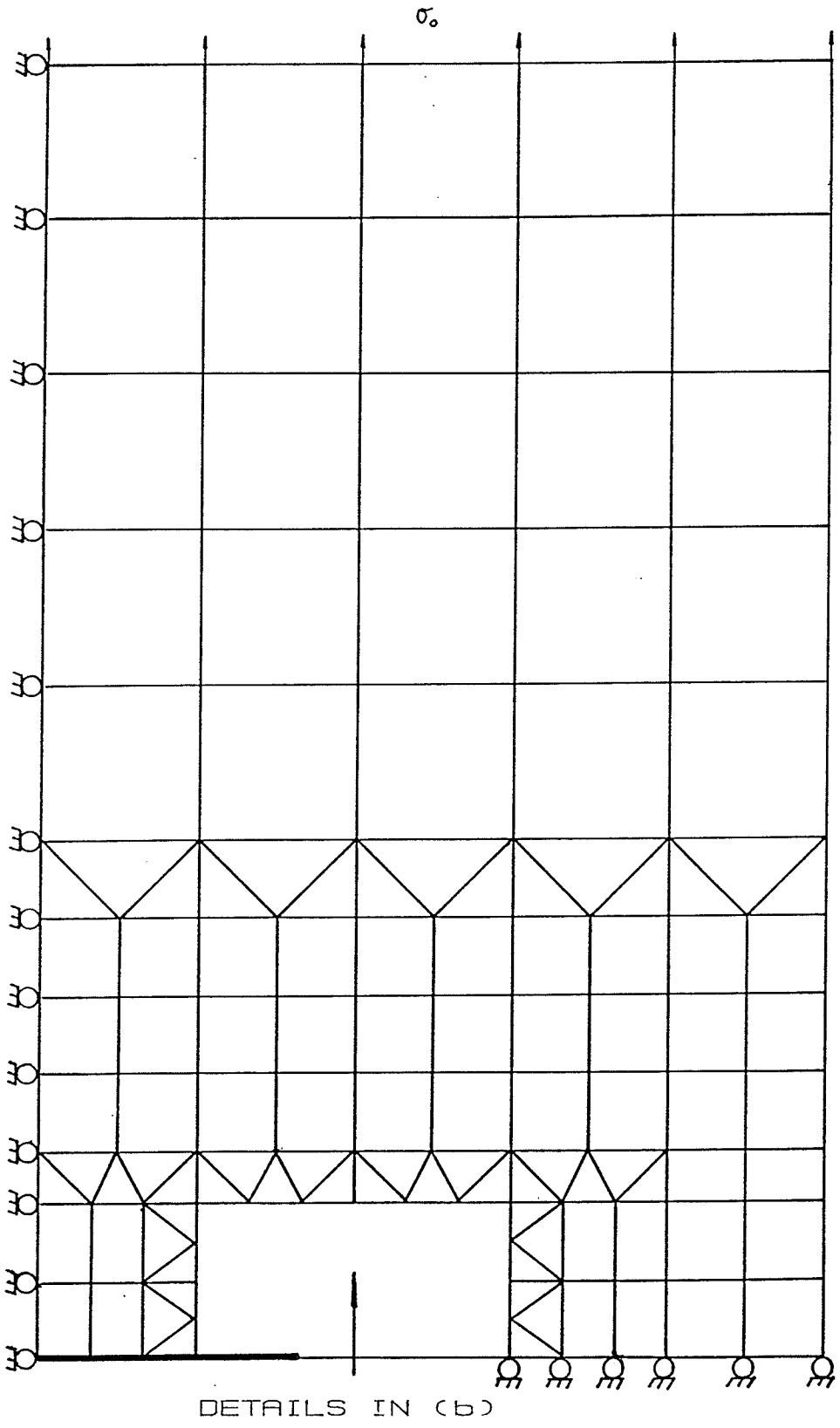

Figure 6.4(a) Finite element mesh: Overall view

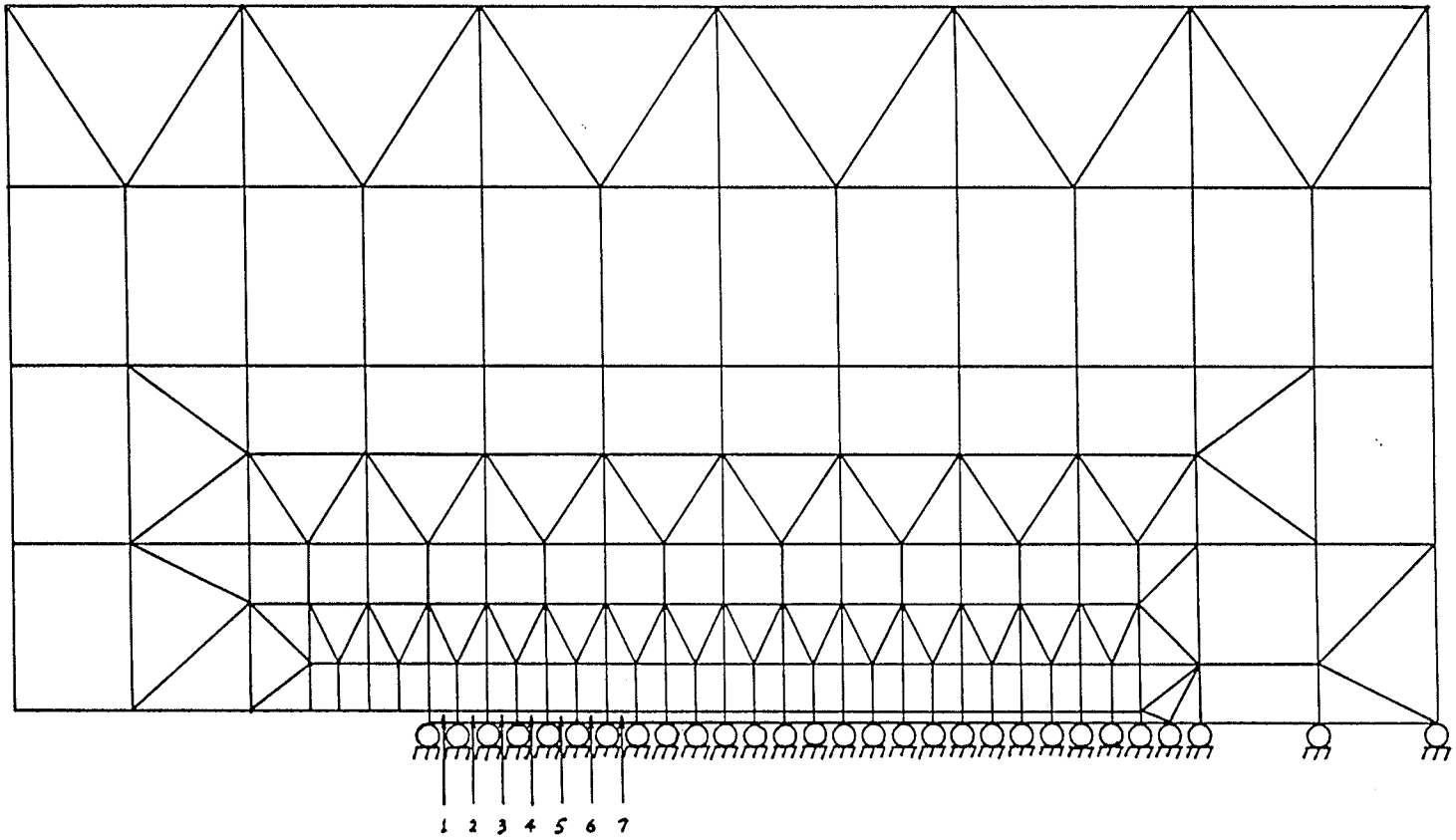

Figure 6.4(b) Finite element mesh: Crack tip region

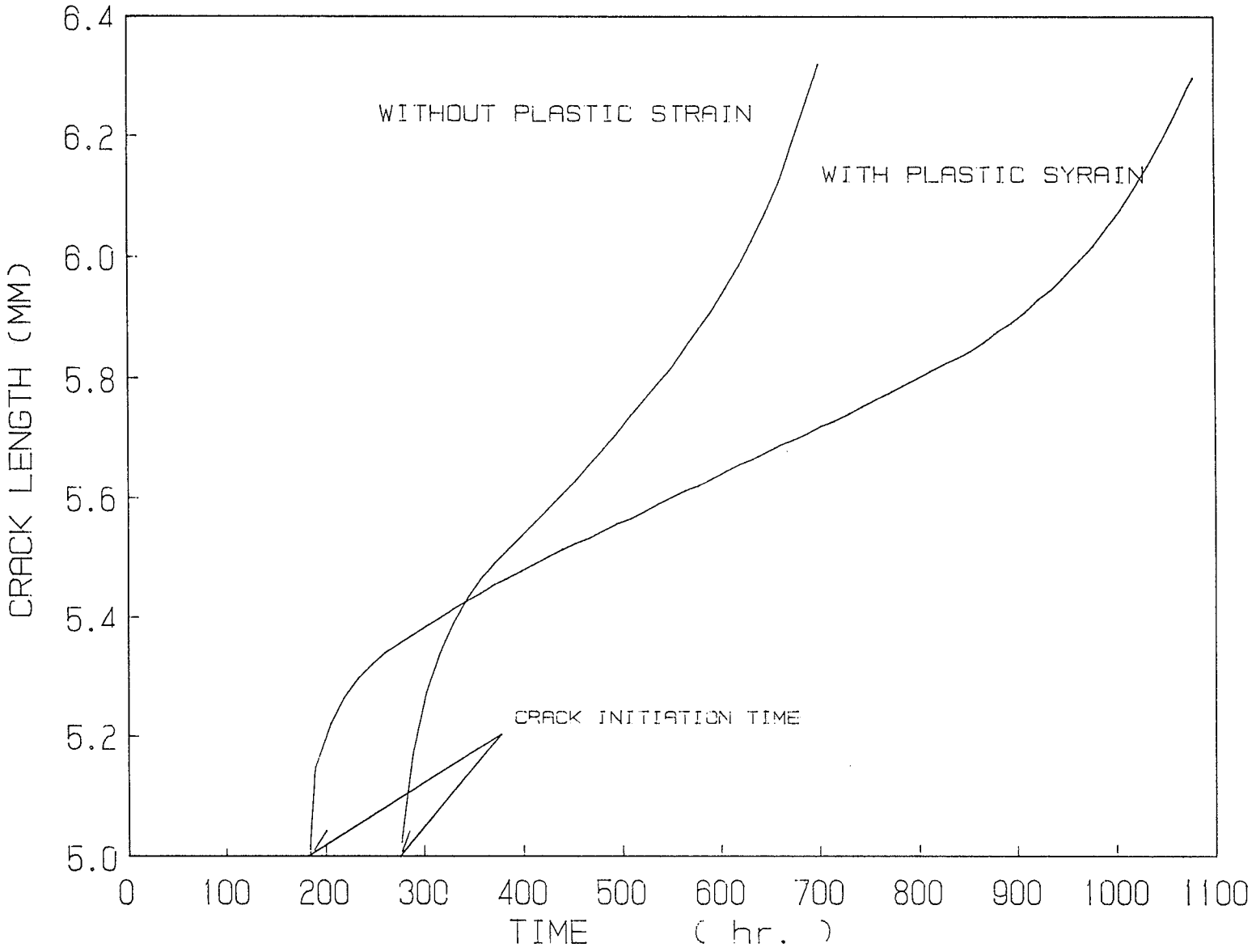

Figure 6.5 Crack growth vs. time in a panel under static loading

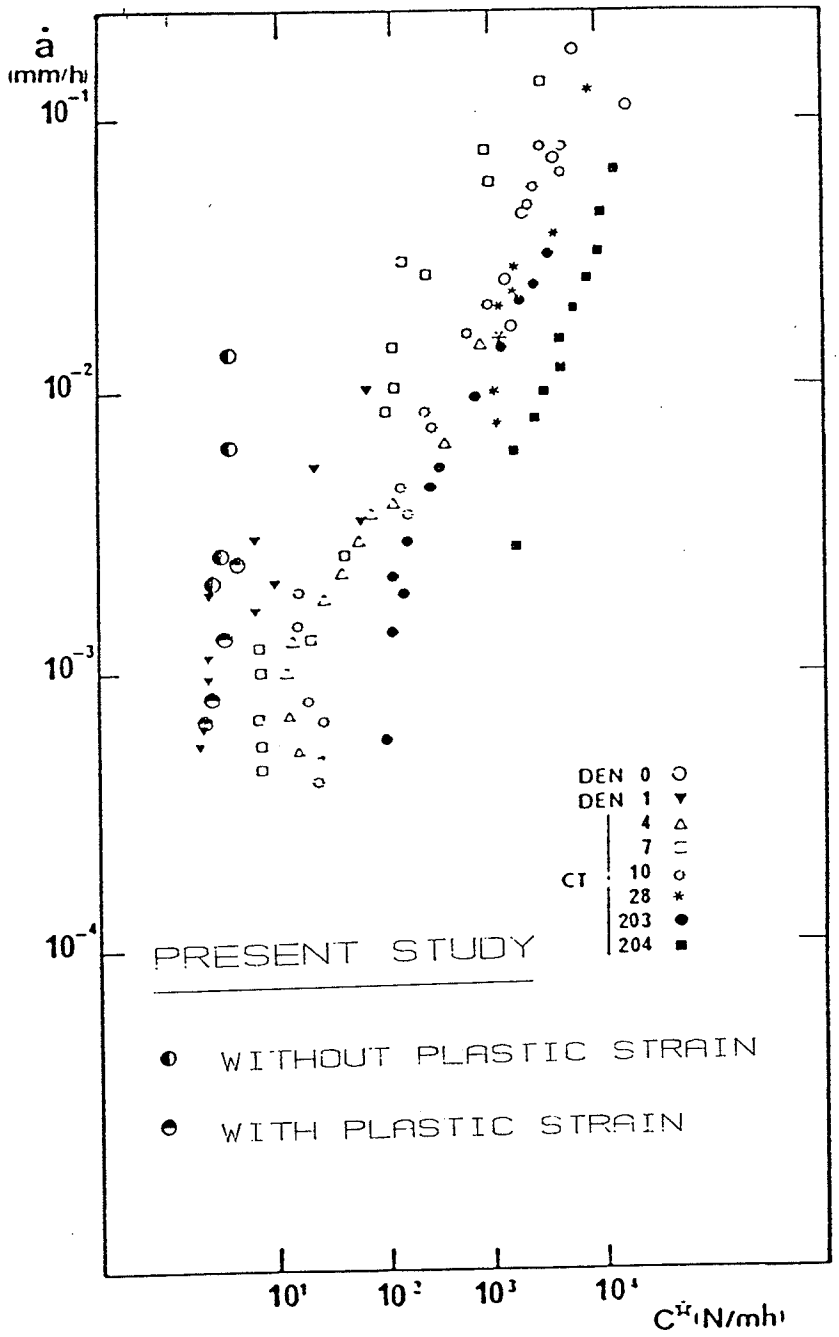

Figure 6.6 Comparison with Mass's experimental data[79]

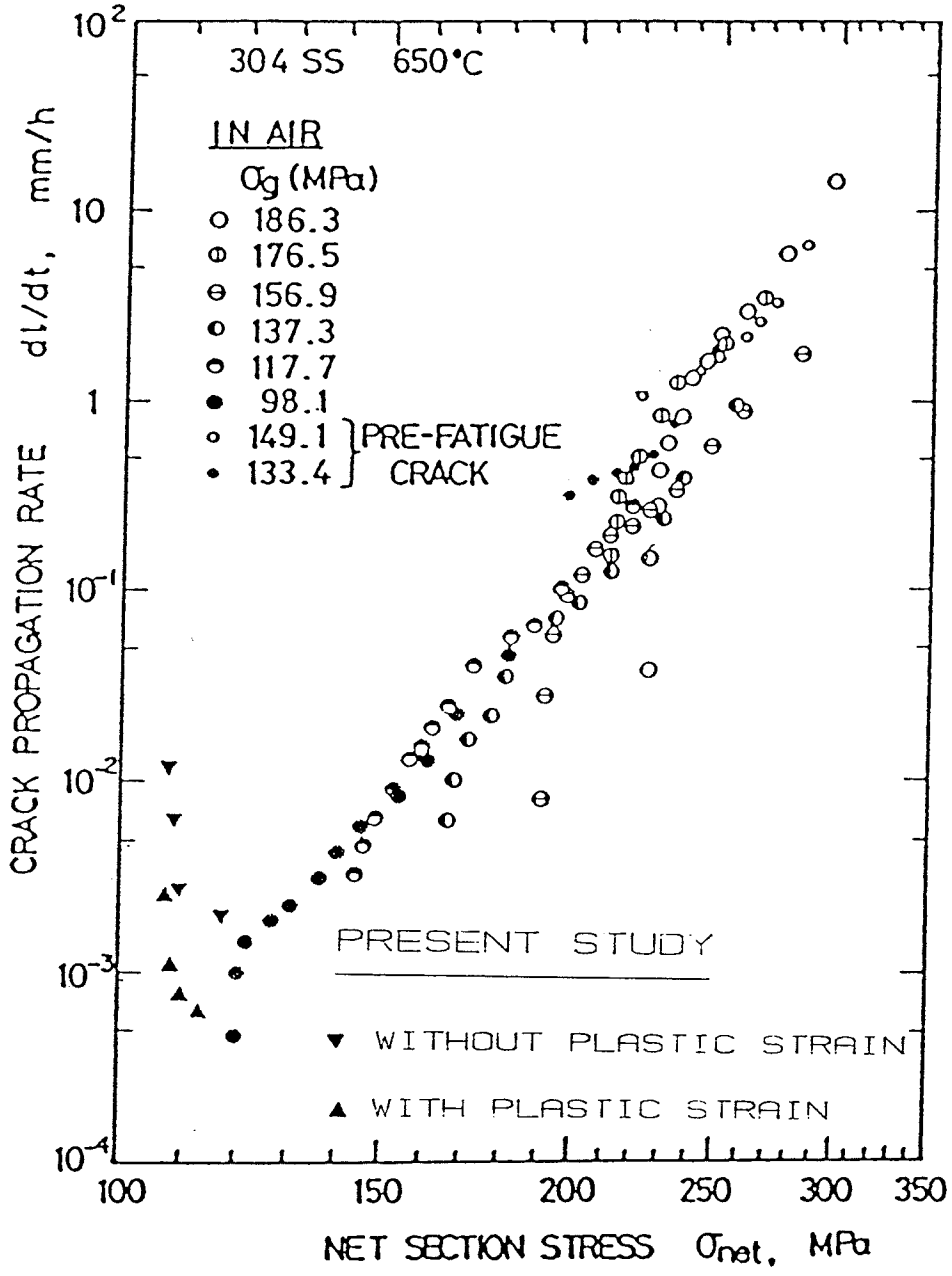

Figure 6.7 Comparison with Taira's experimental data[106]

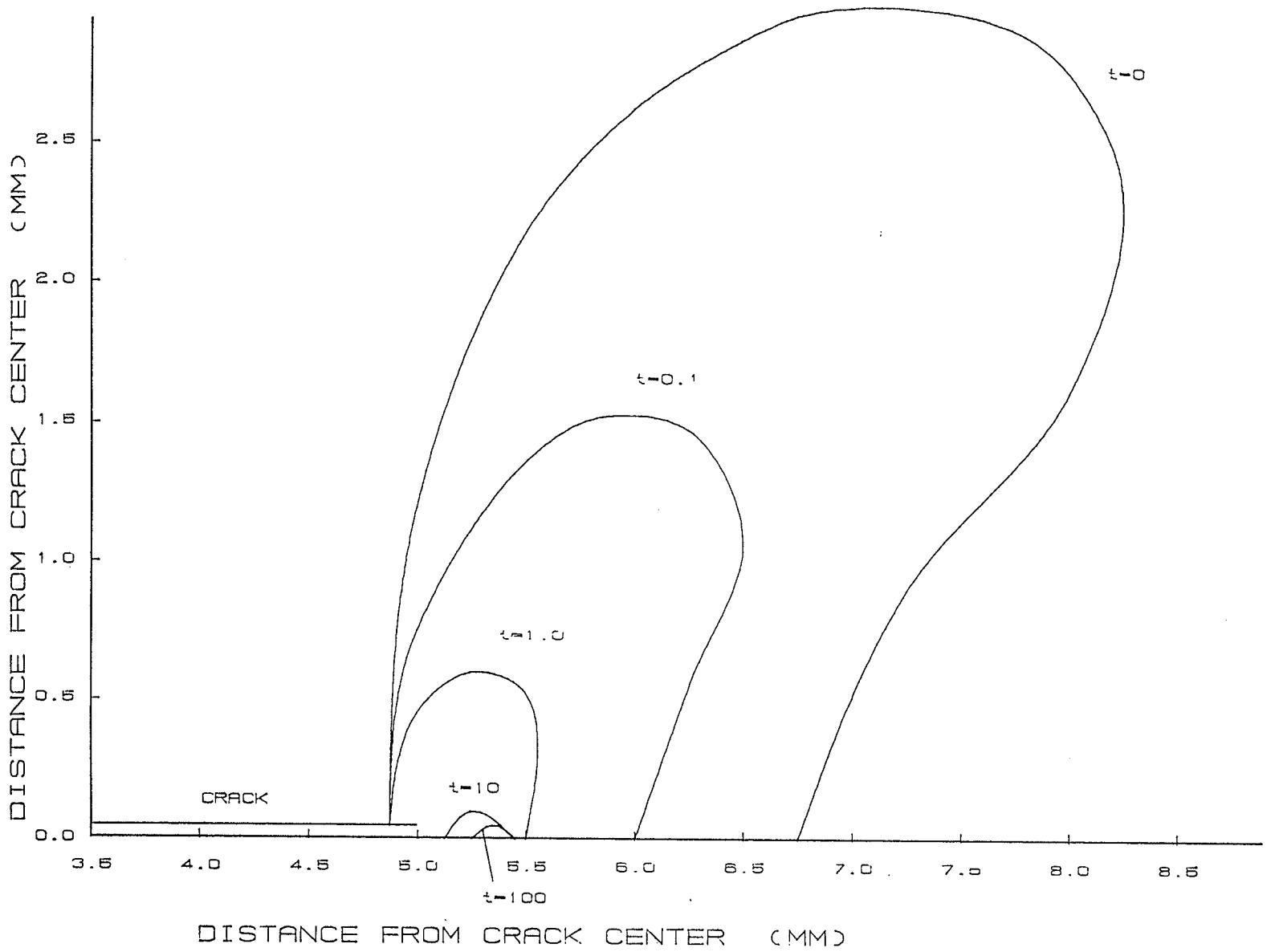

Figure 6.8 Variation of plastic zone

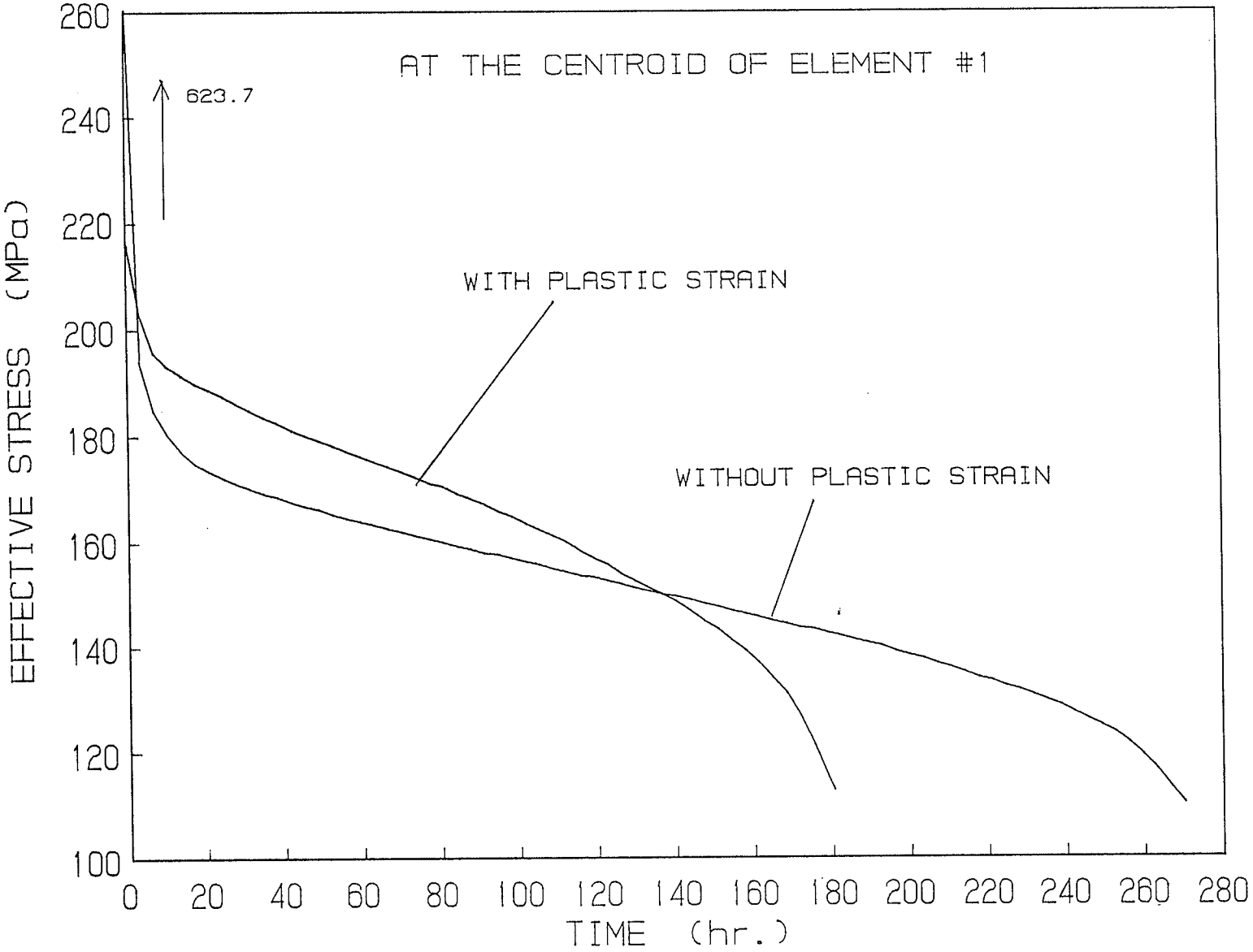

Figure 6.9 Variations of effective stress with time in crack tip element

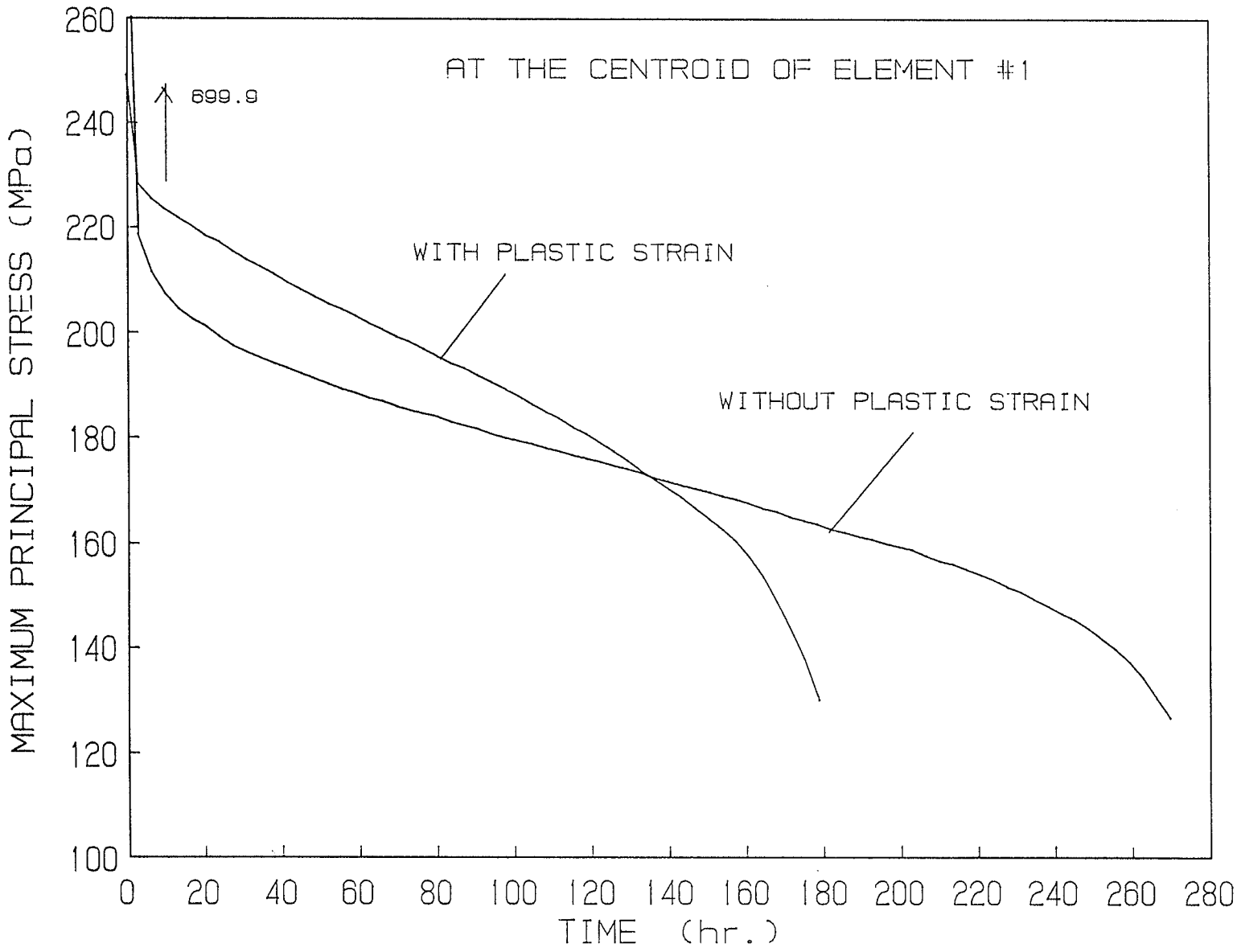

Figure 6.10 Variations of maximum principal stress with time in crack tip element

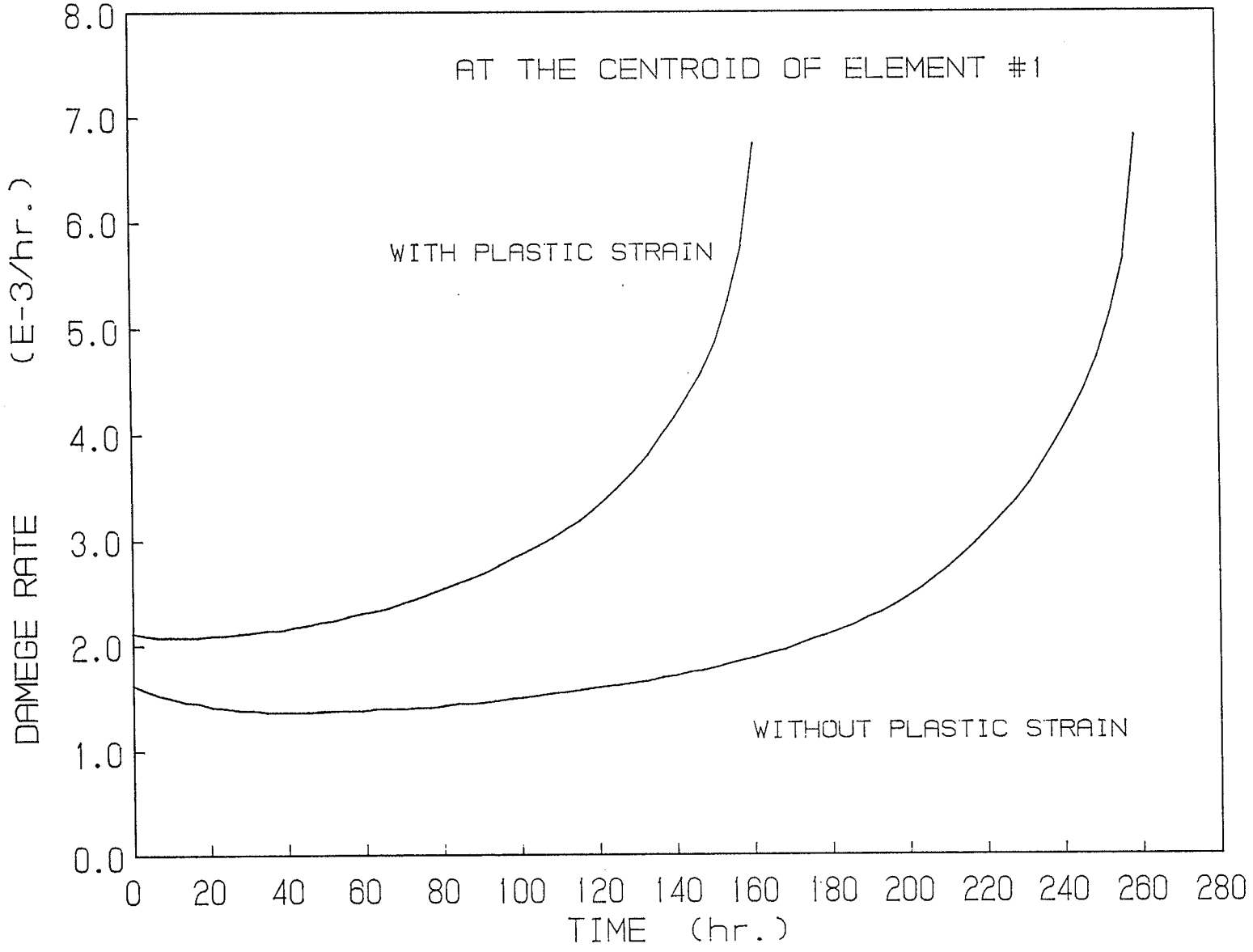

Figure 6.11 Variations of damage rate with time in crack tip element

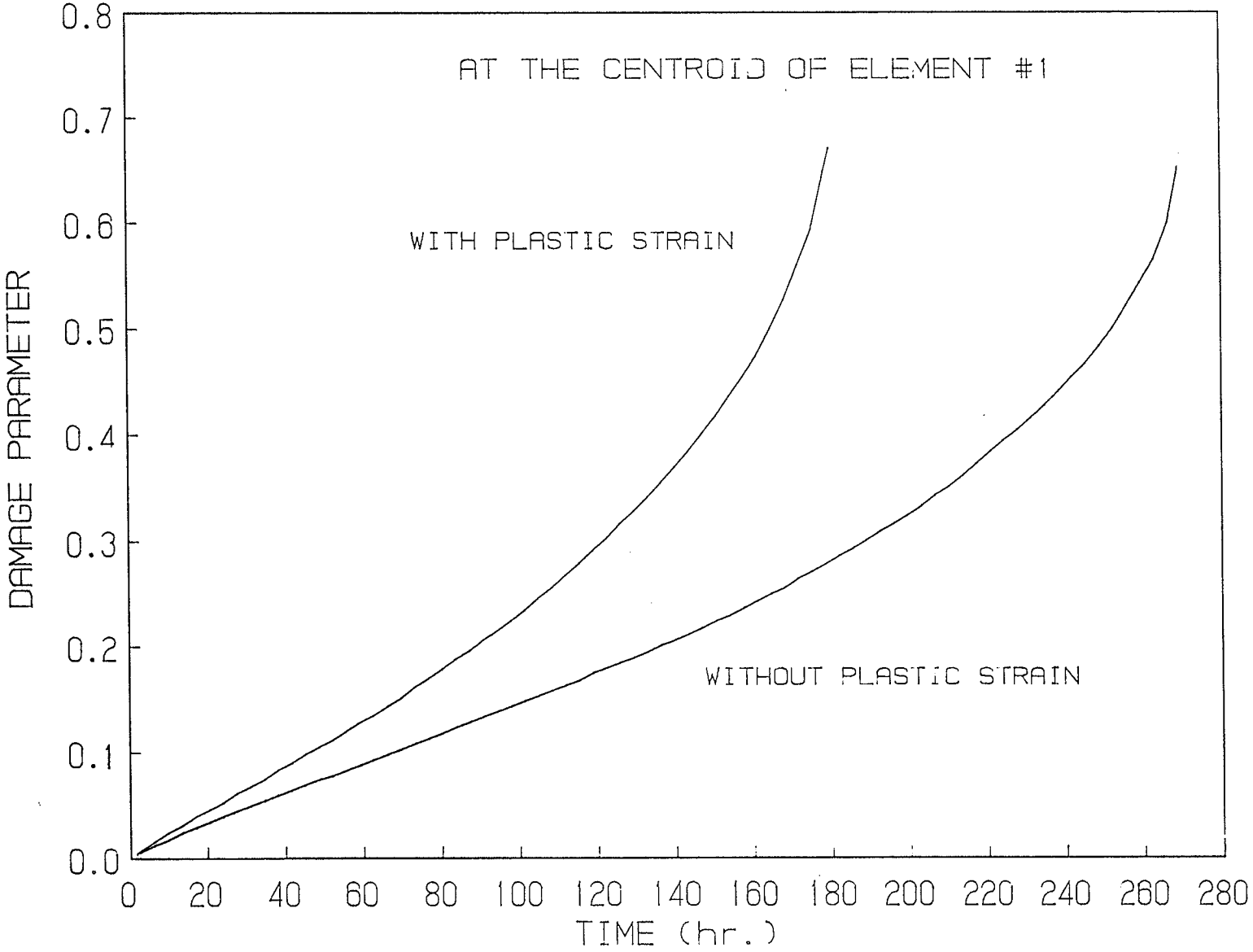

Figure 6.12 Damage evolutions in crack tip element

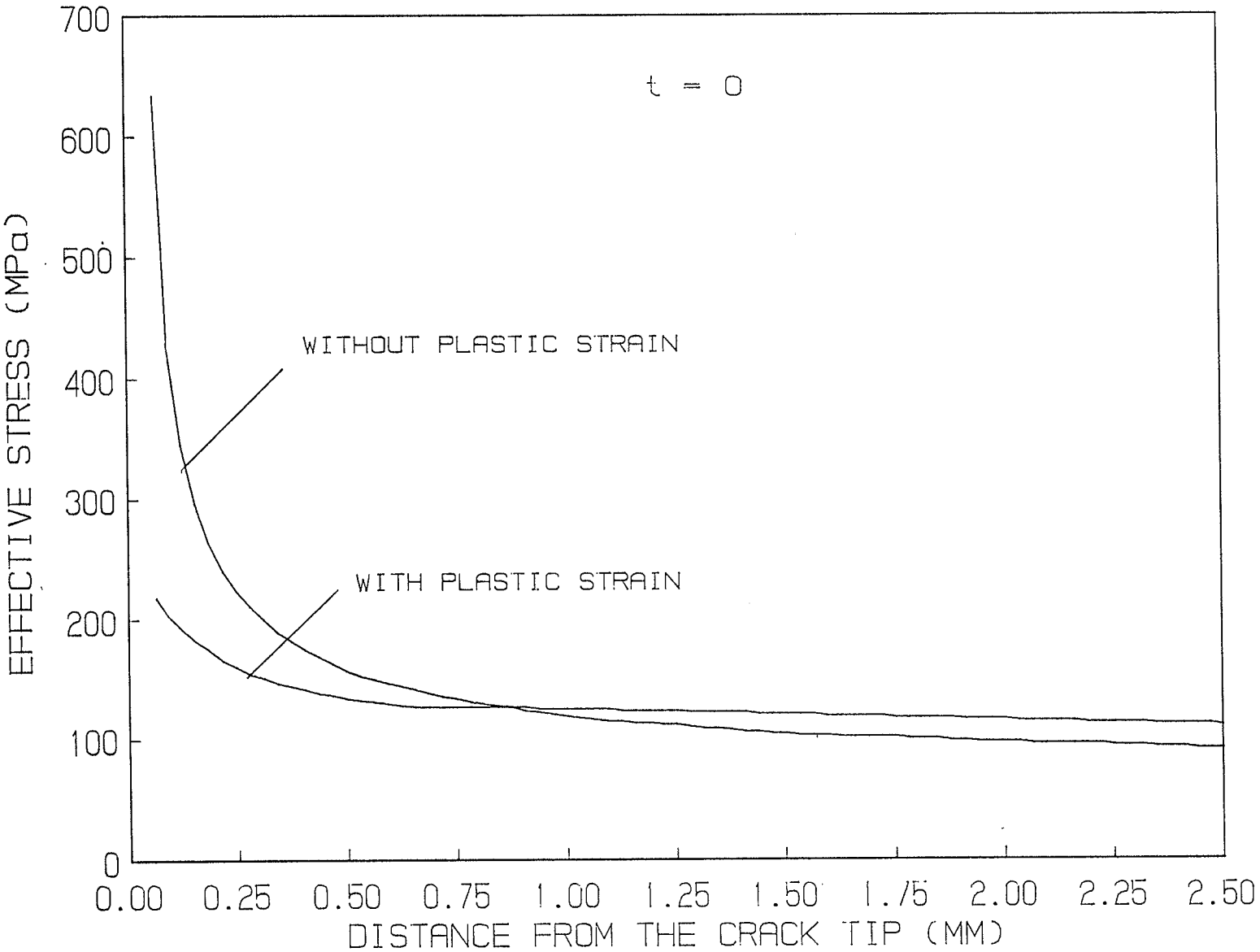

Figure 6.13 Distributions of effective stress ahead of crack tip at t = 0

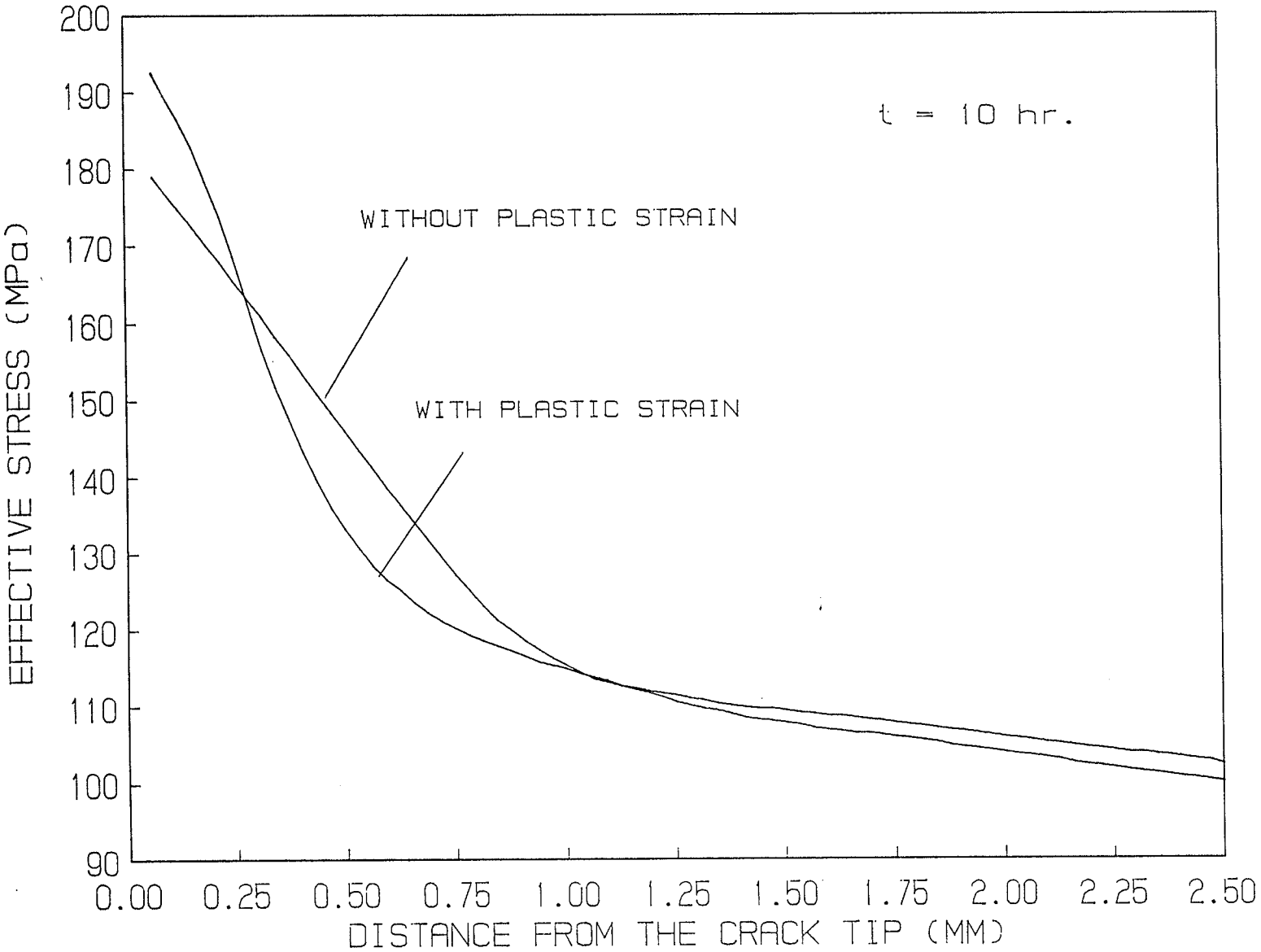

Figure 6.14 Distributions of effective stress ahead of crack tip at t = 10 hours

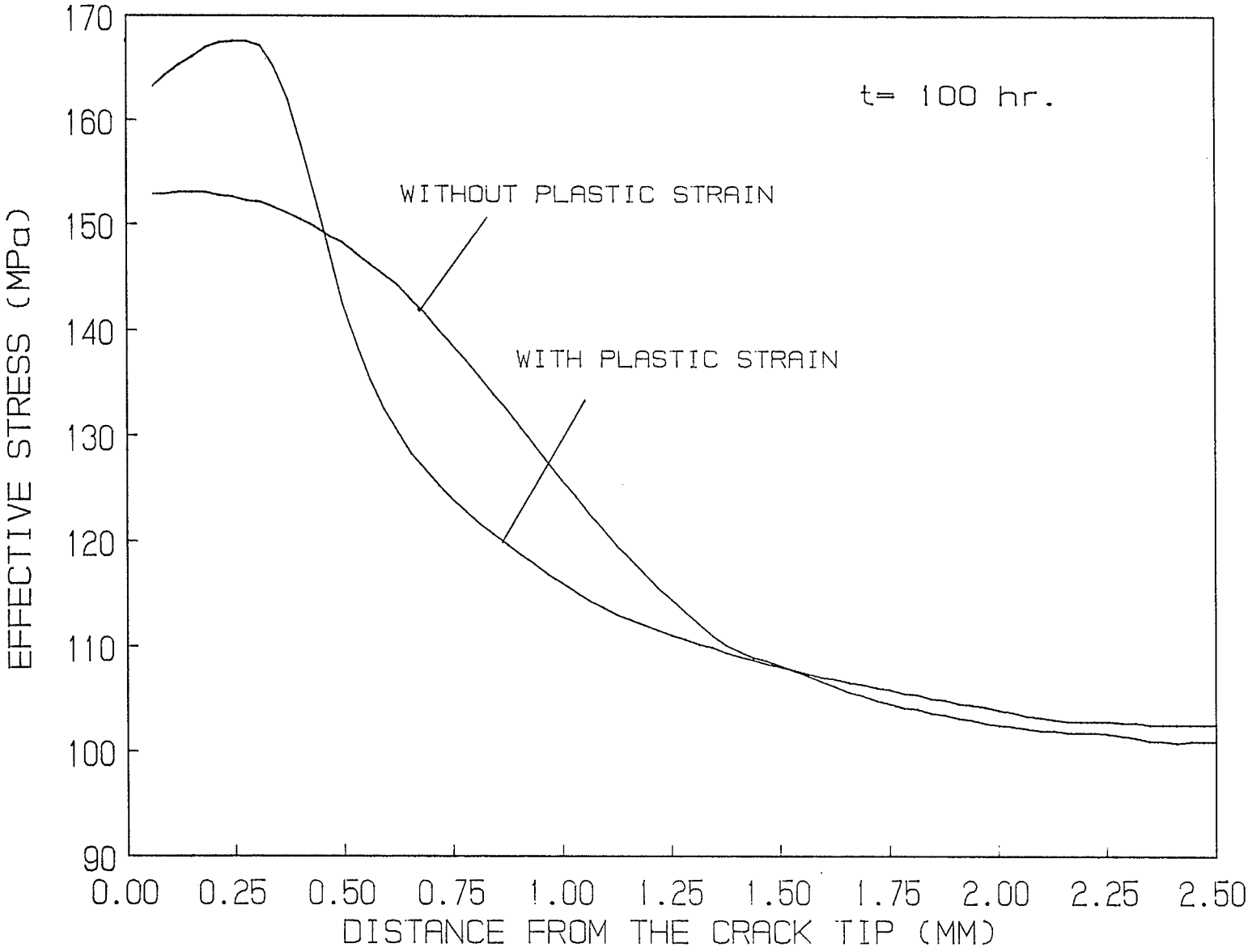

Figure 6.15 Distributions of effective stress ahead of crack tip at t = 100 hours

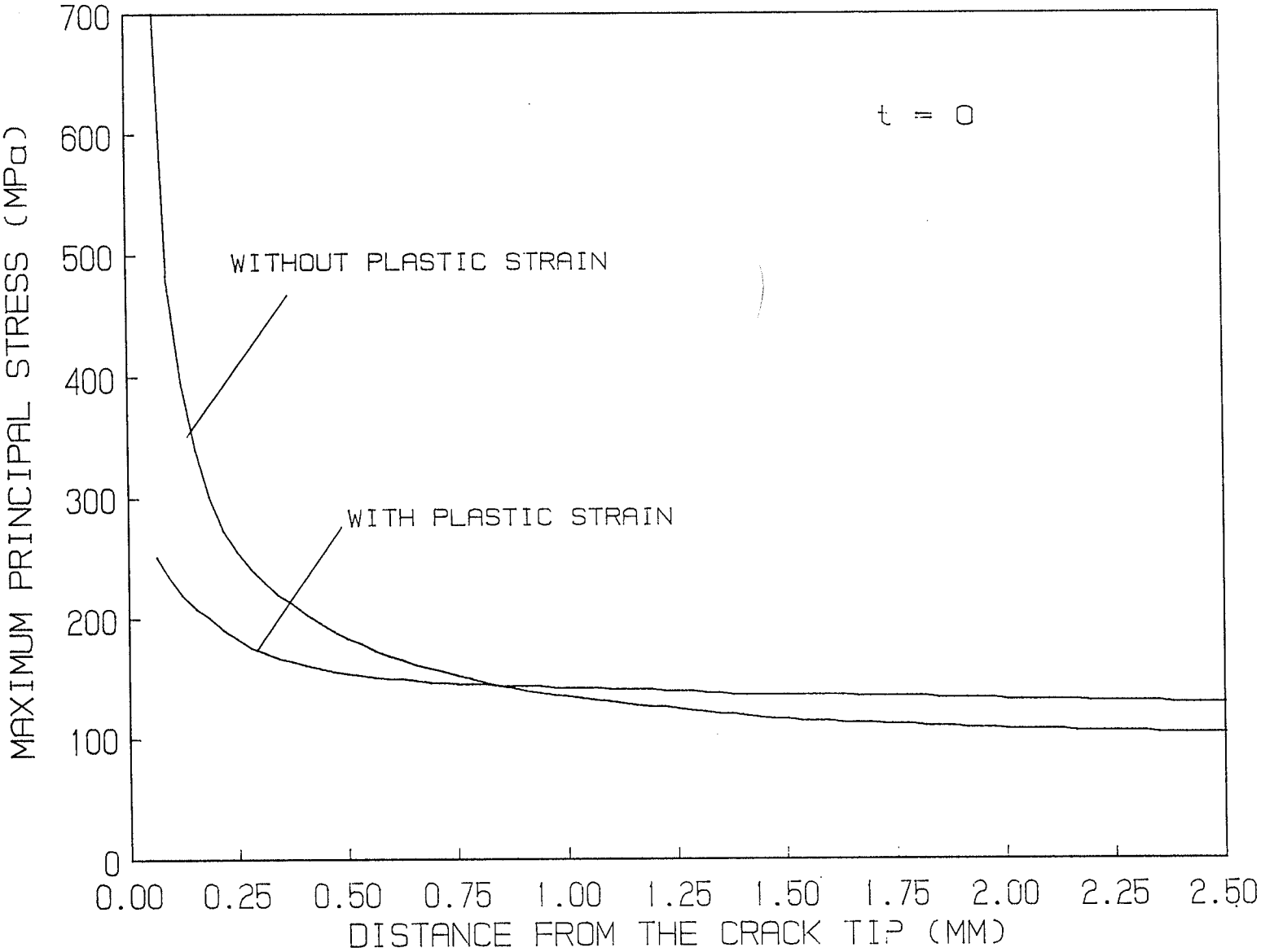

Figure 6.16 Distributions of maximum principal stress ahead of crack tip at t = 0

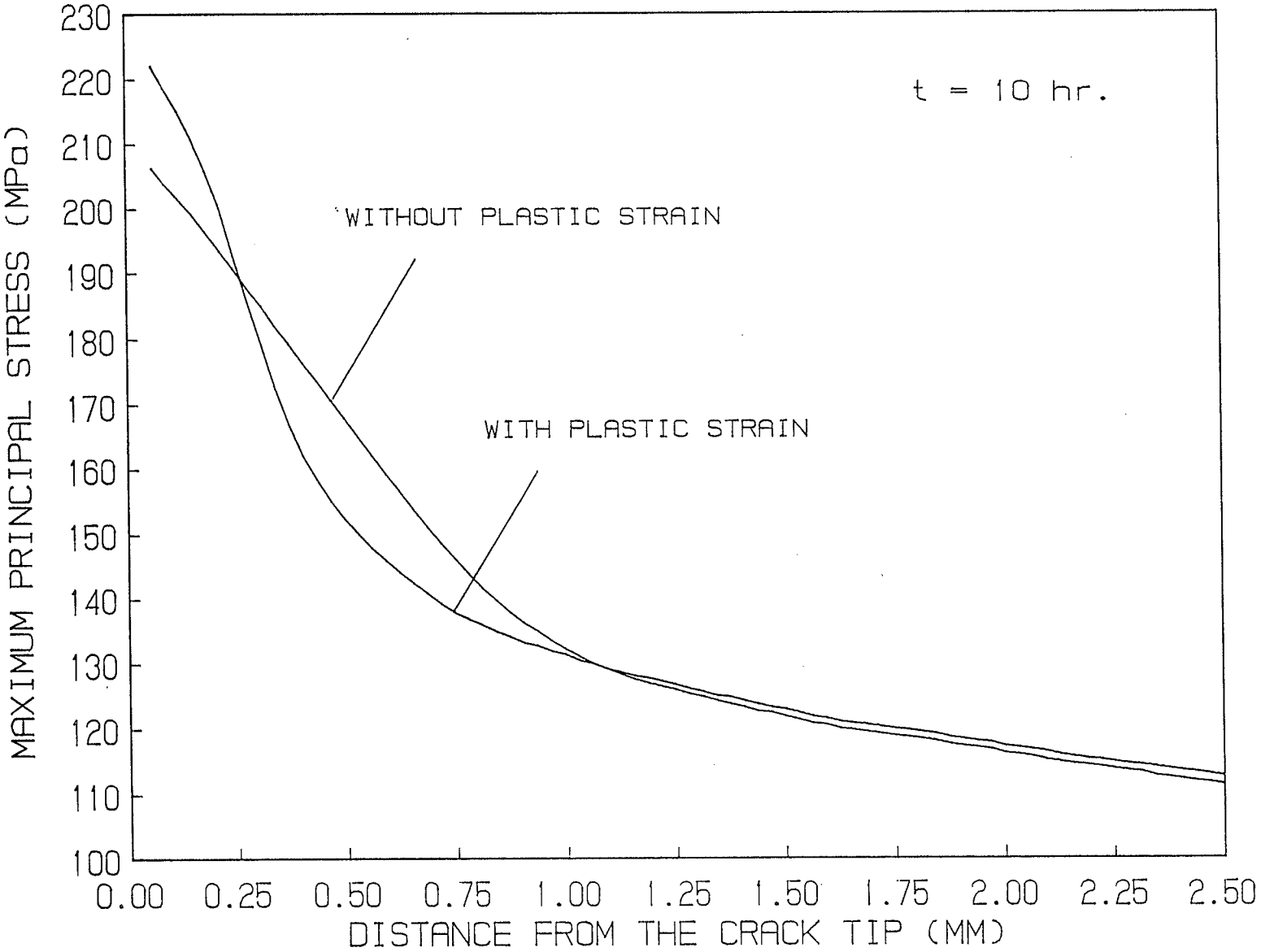

Figure 6.17 Distributions of maximum principal stress ahead of crack tip at t = 10 hours

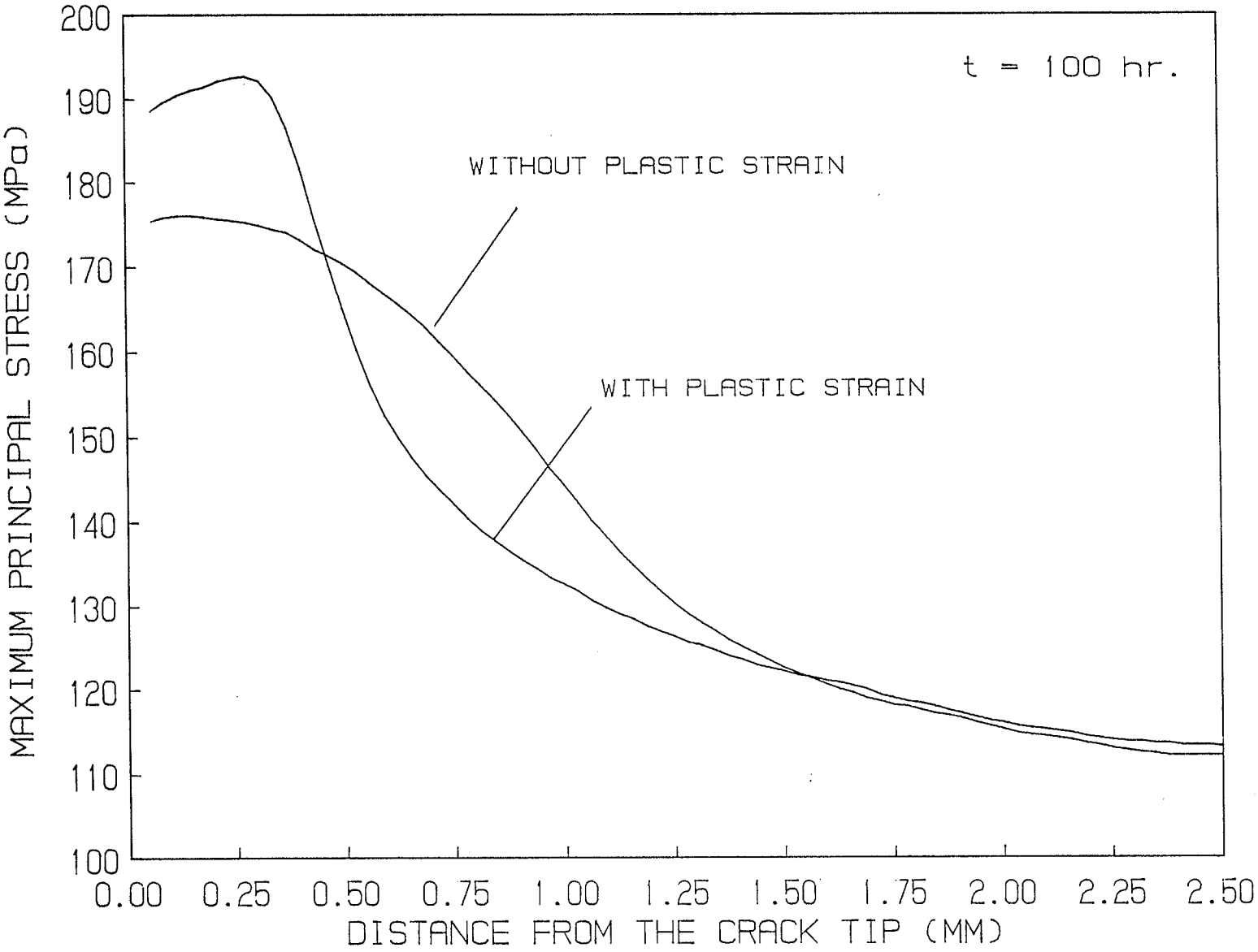

Figure 6.18 Distributions of maximum principal stress ahead of crack tip at t = 100 hours

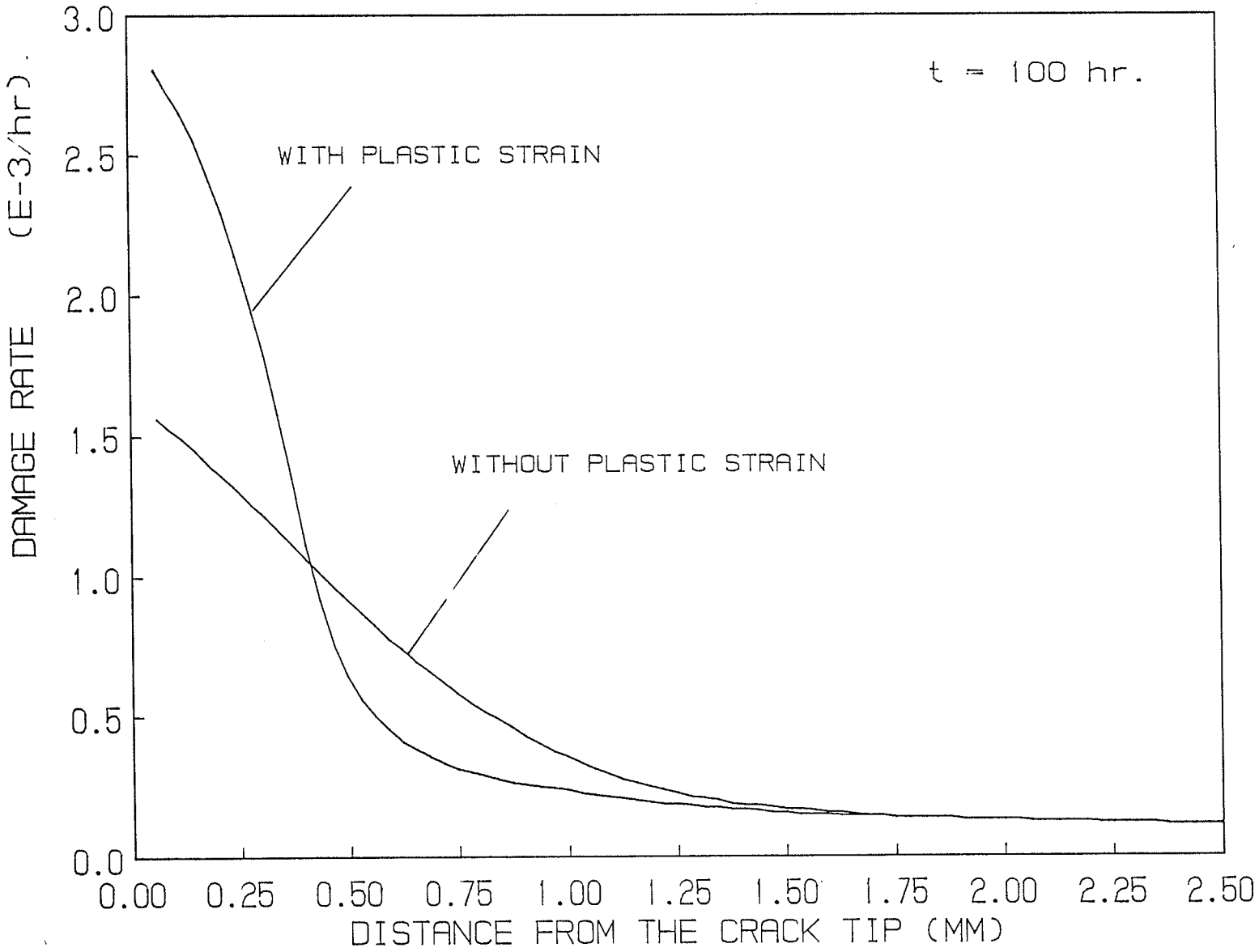

Figure 6.19 Distributions of damage rate ahead of crack tip at t = 100 hours

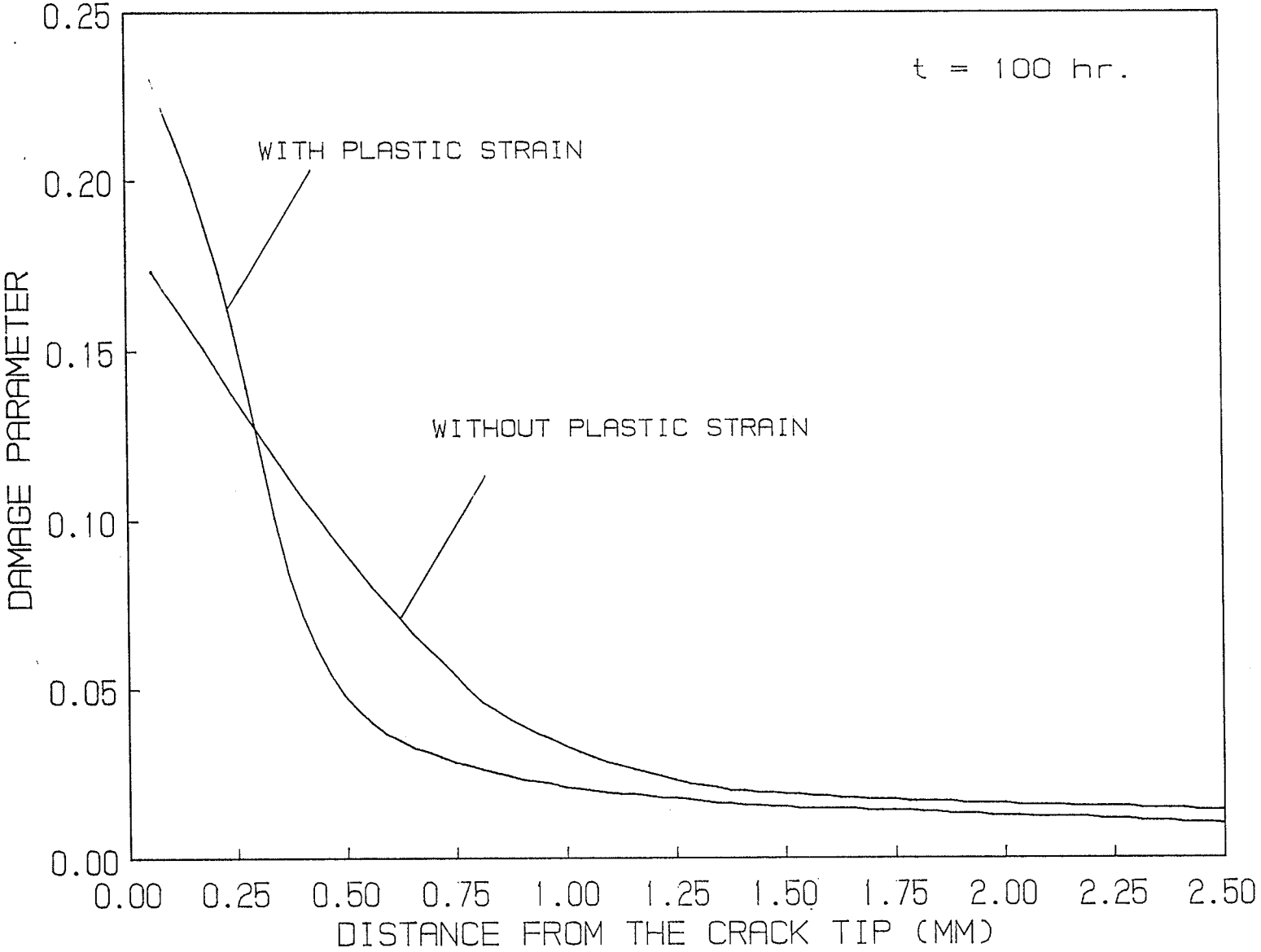

Figure 6.20 Damage distributions ahead of crack tip at t = 100 hours

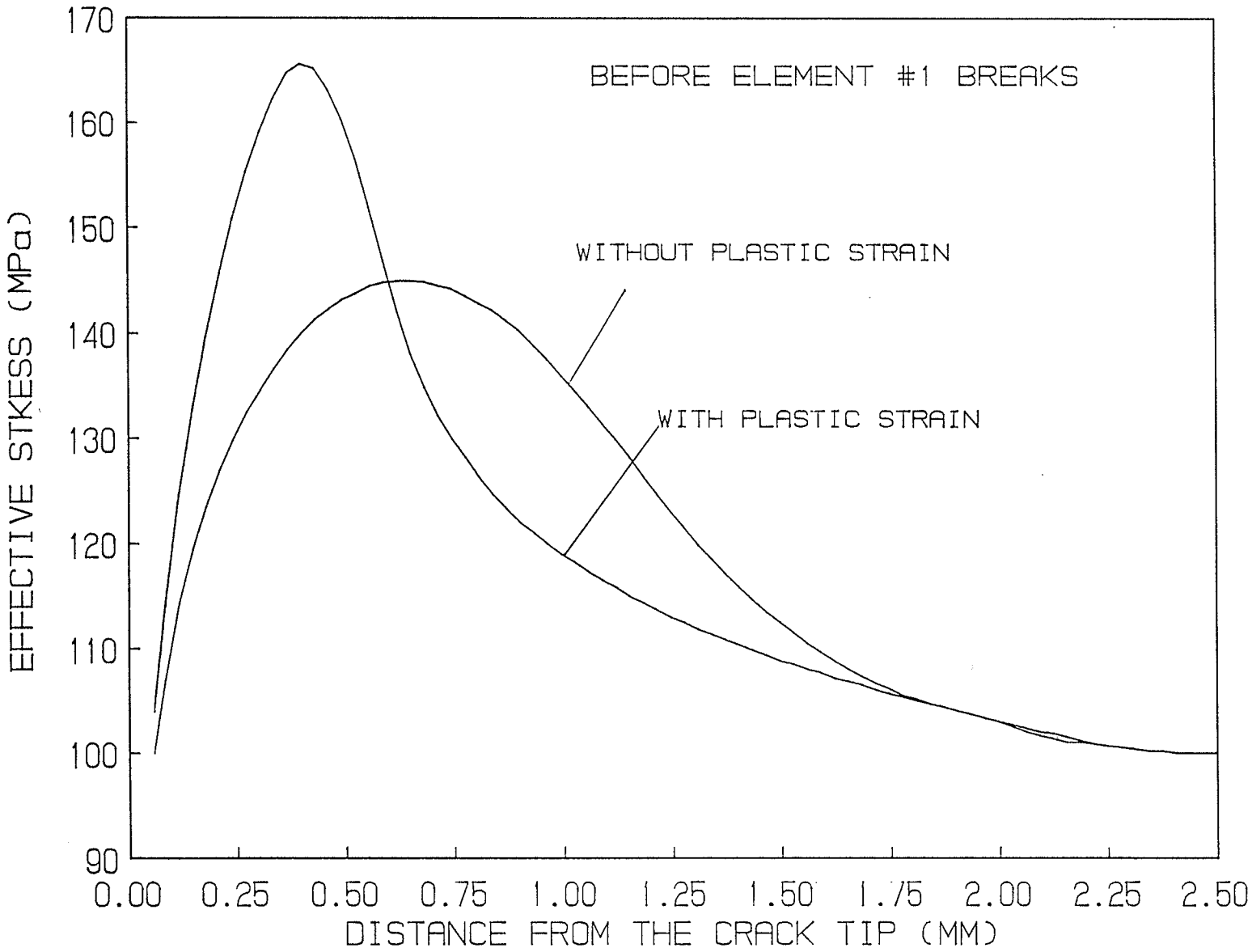

Figure 6.21 Distributions of effective stress ahead of crack tip before element #1 breaks

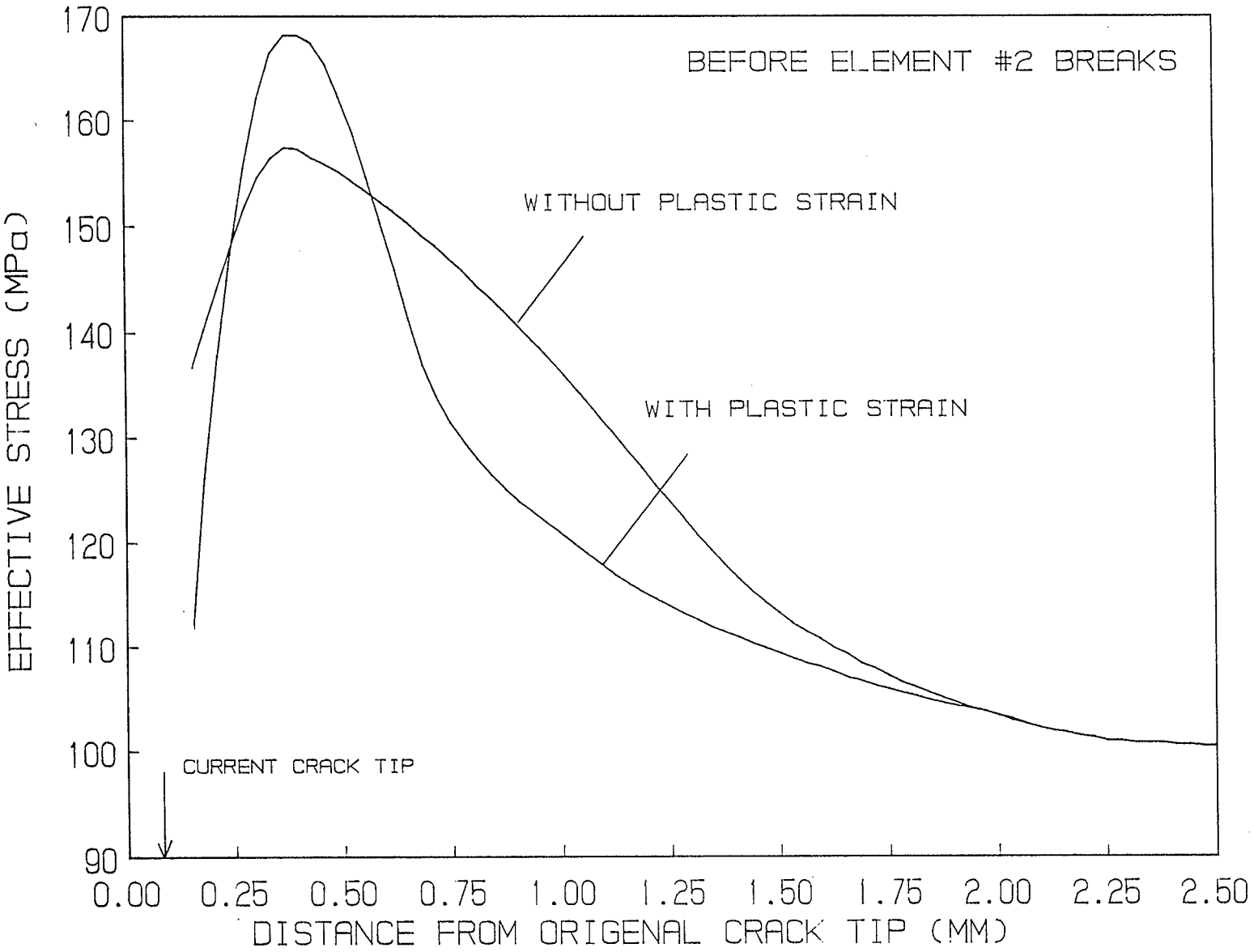

Figure 6.22 Distributions of effective stress ahead of crack tip before element #2 breaks

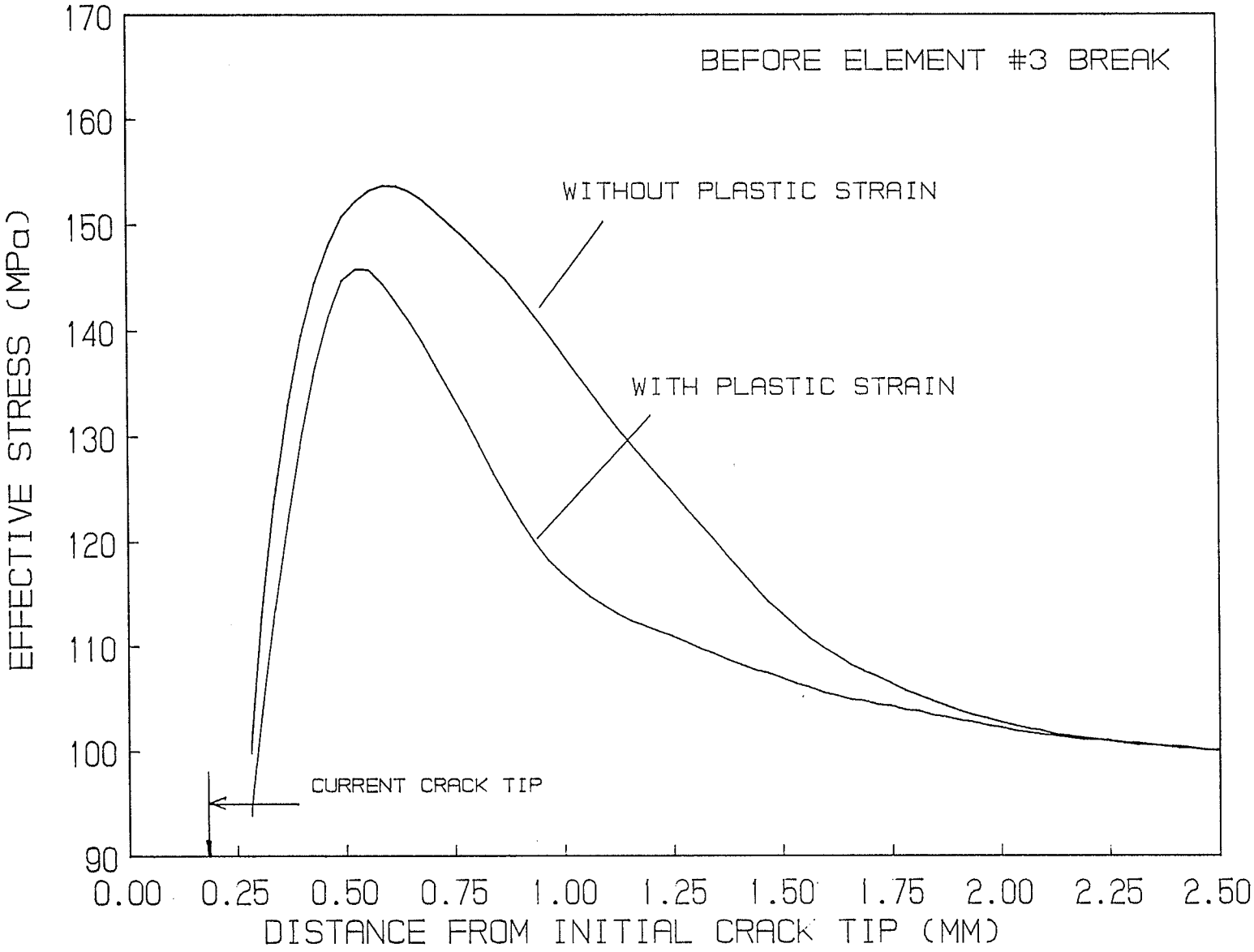

Figure 6.23 Distributions of effective stress ahead of crack tip before element #3 breaks

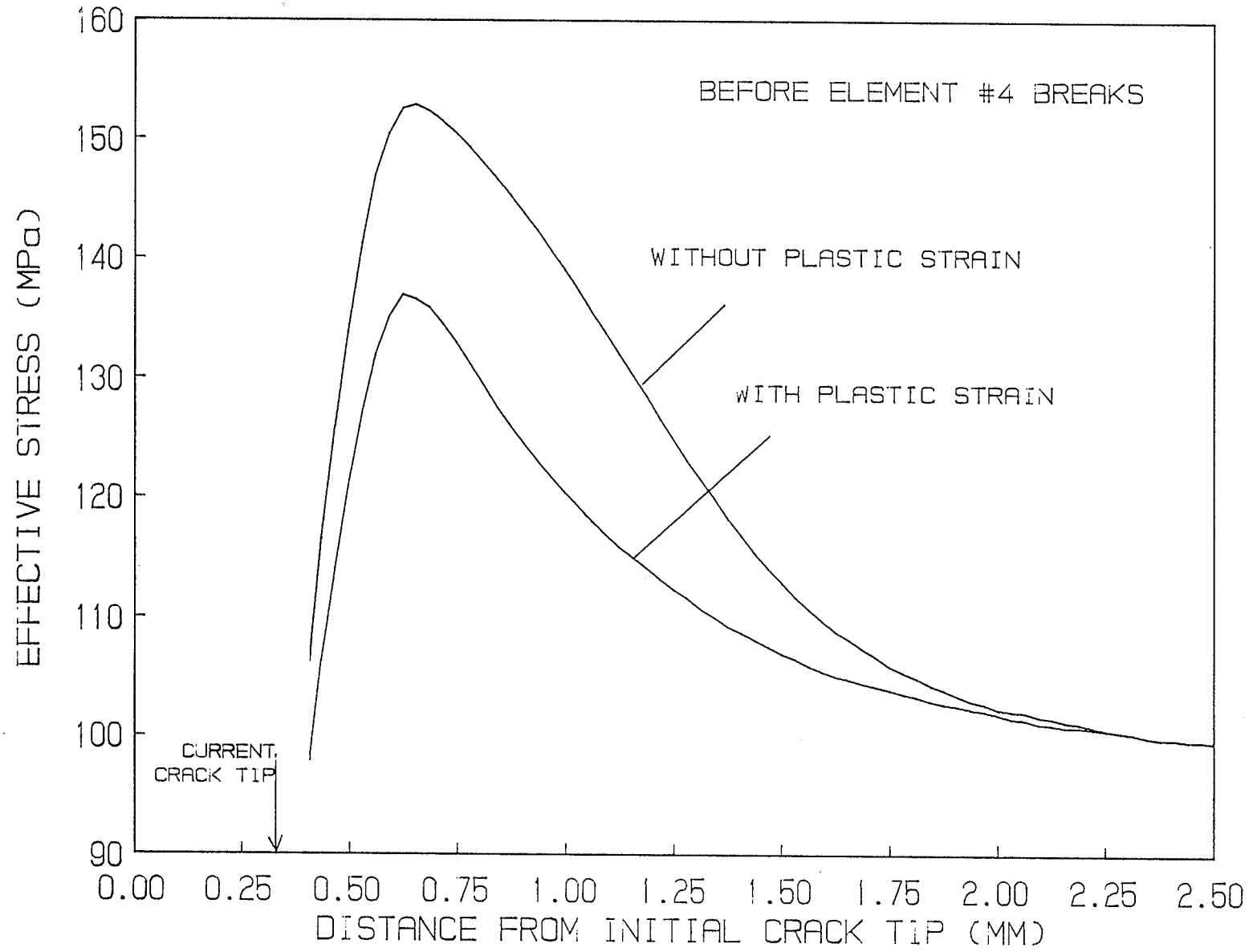

Figure 6.24 Distributions of effective stress ahead of crack tip before element #4 breaks

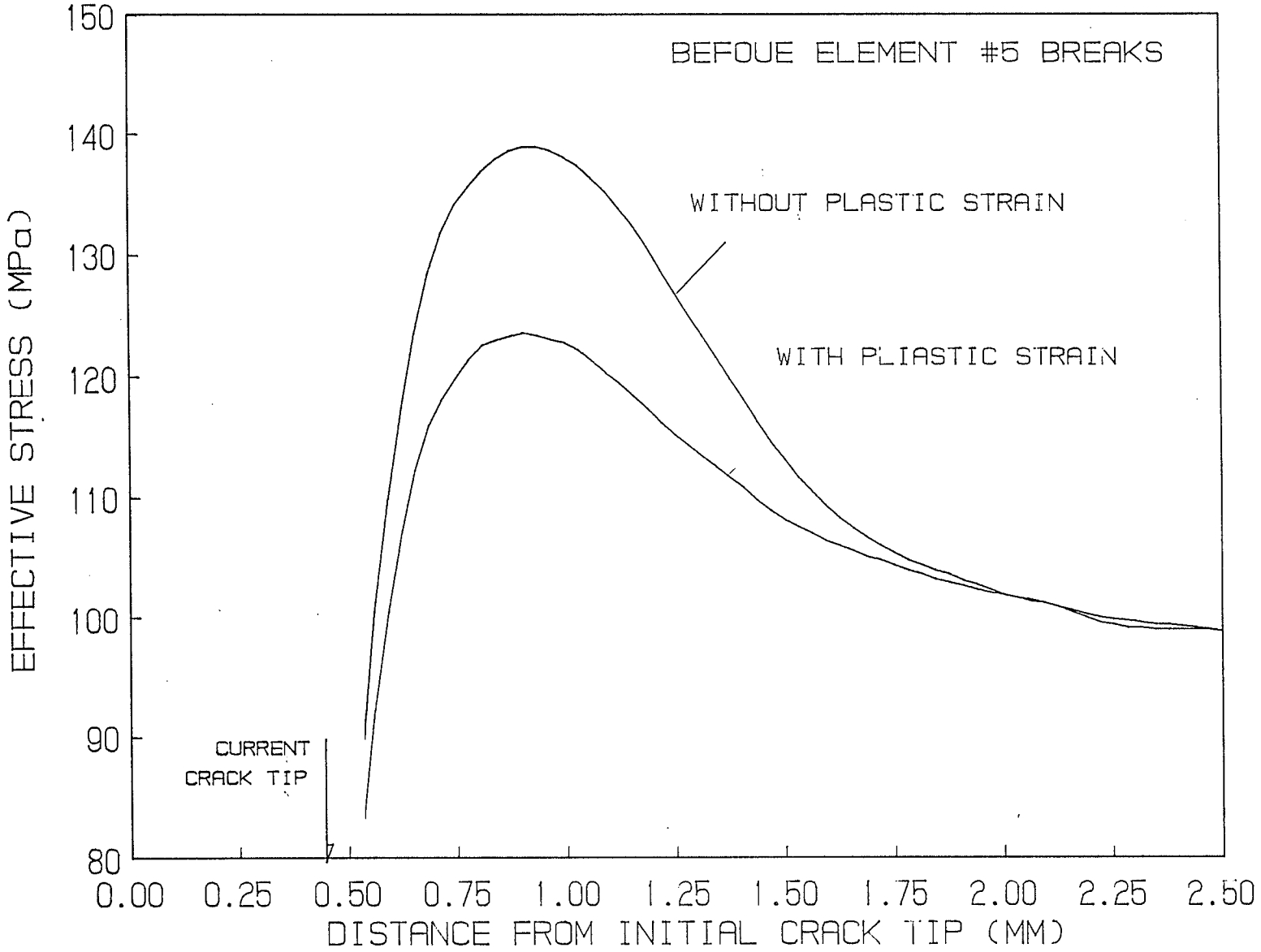

Figure 6.25 Distributions of effective stress ahead of crack tip before element #5 breaks

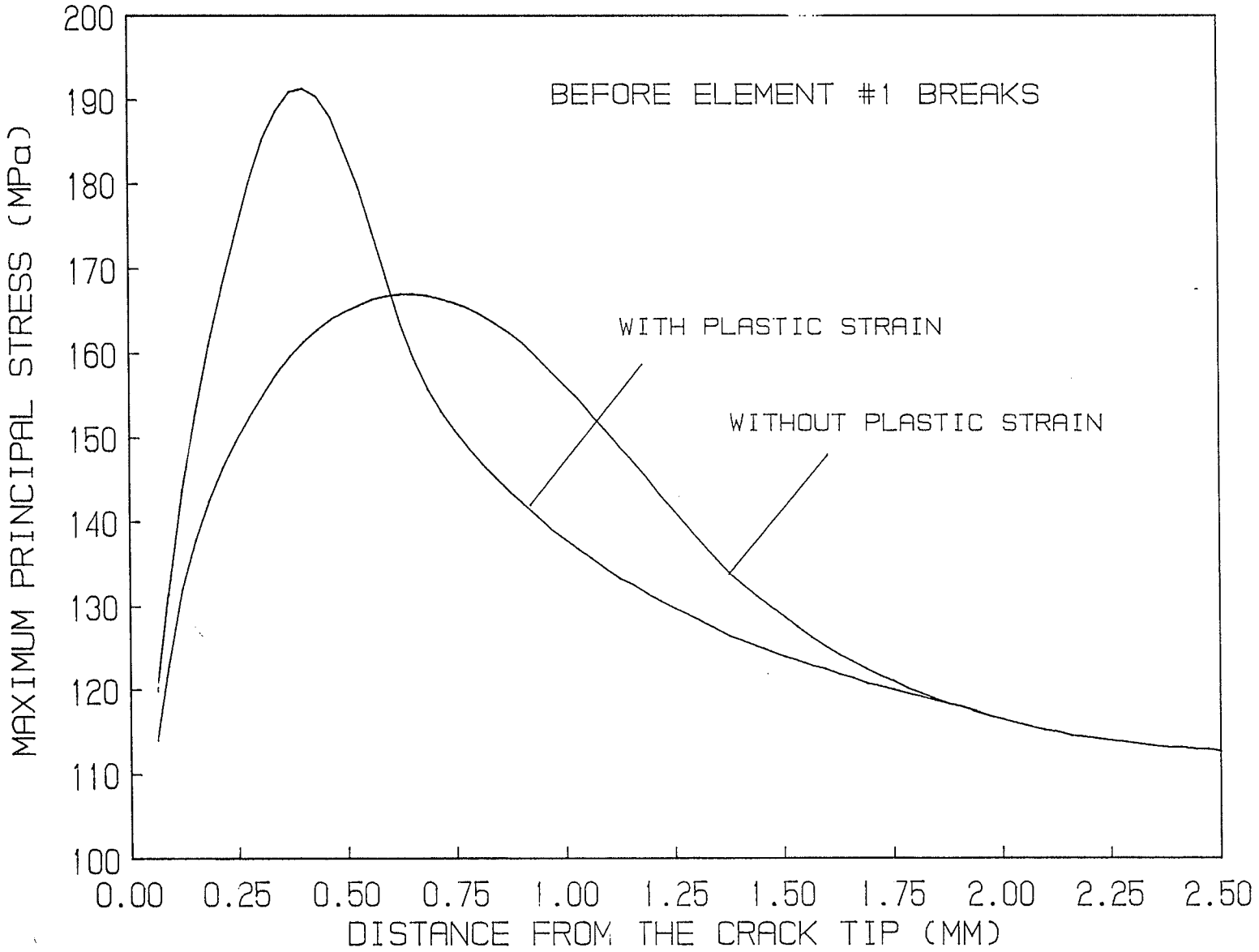

Figure 6.26 Distributions of maximum principal stress ahead of crack tip before element #1 breaks

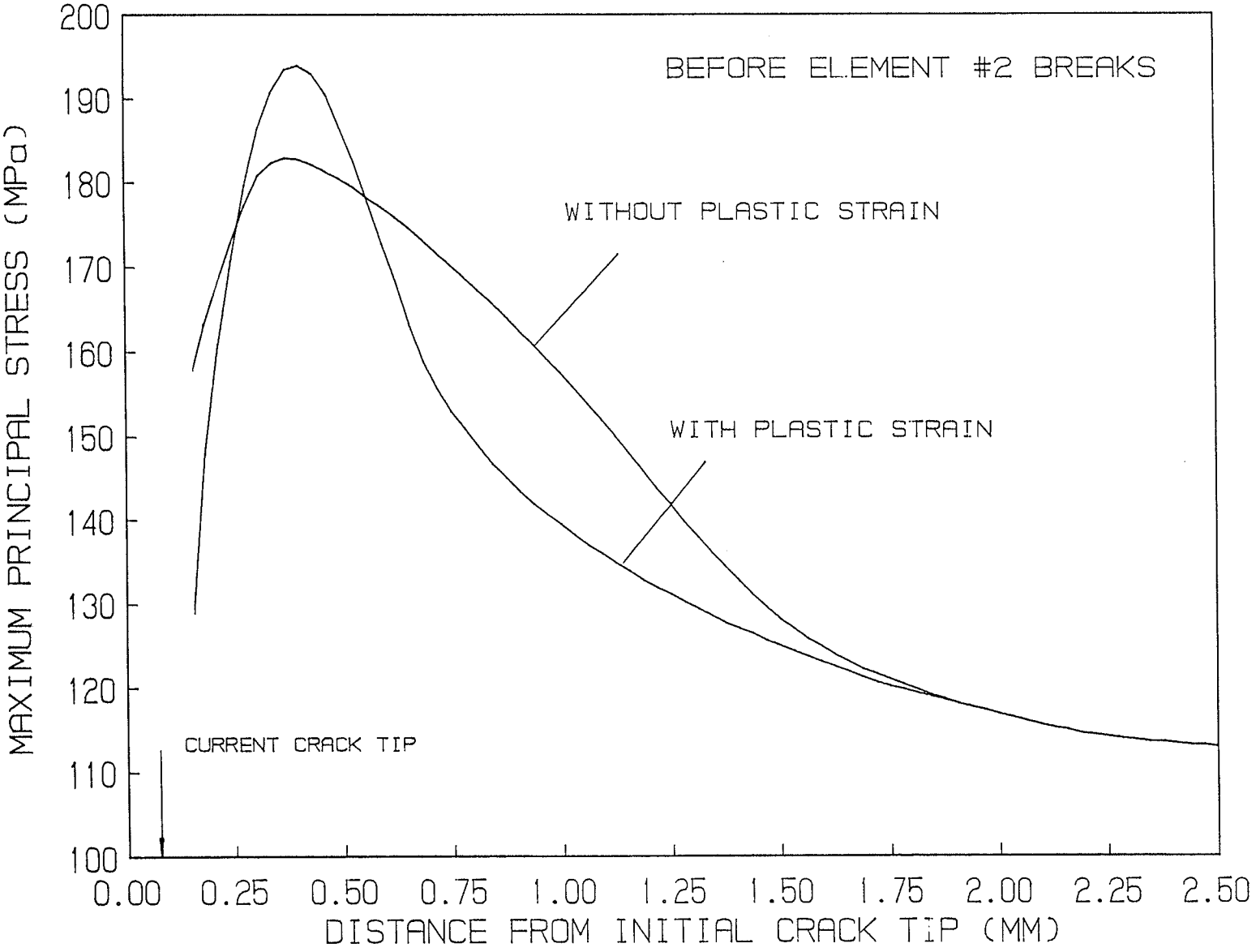

Figure 6.27 Distributions of maximum principal stress ahead of crack tip before element #2 breaks

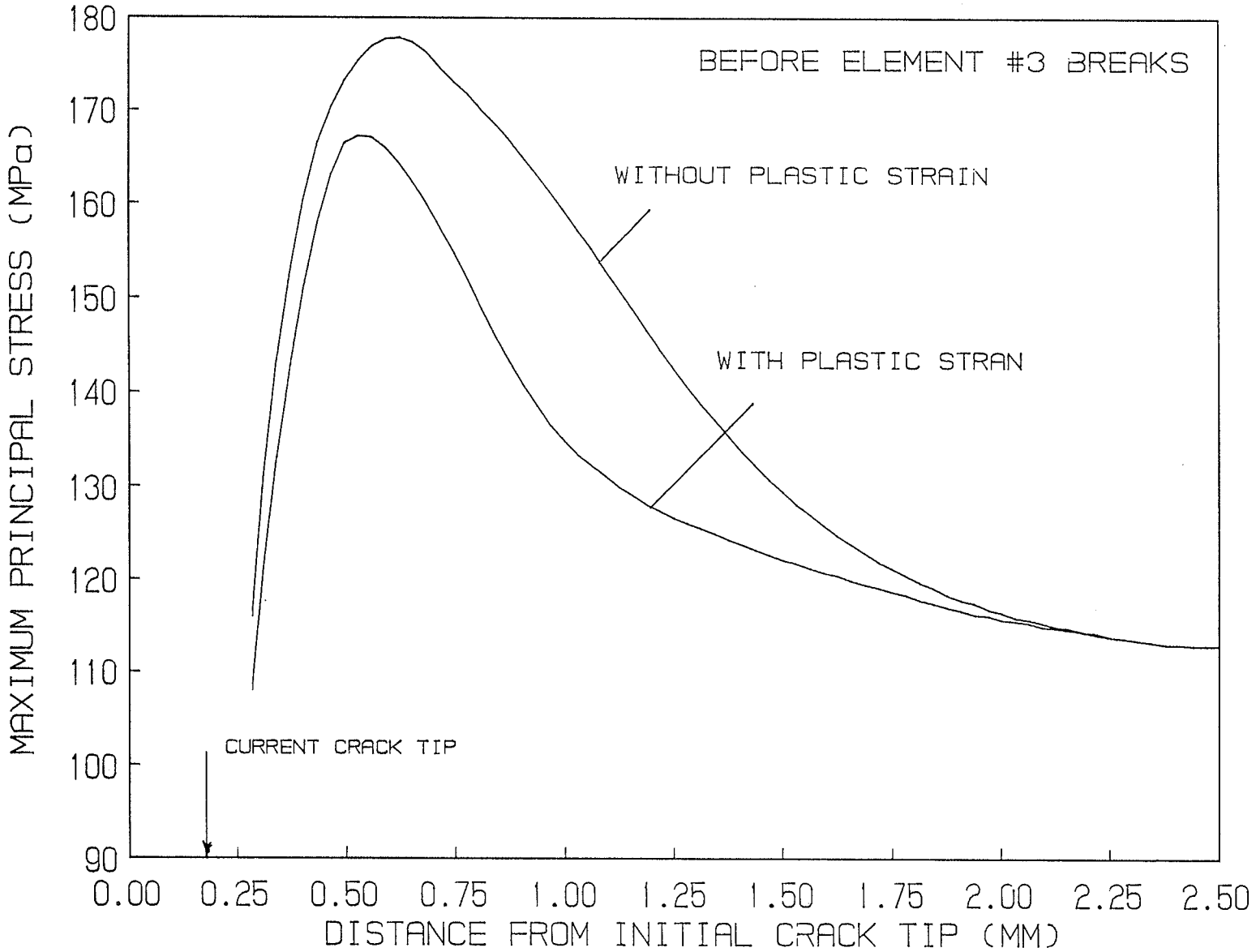

Figure 6.28 Distributions of maximum principal stress ahead of crack tip before element #3 breaks

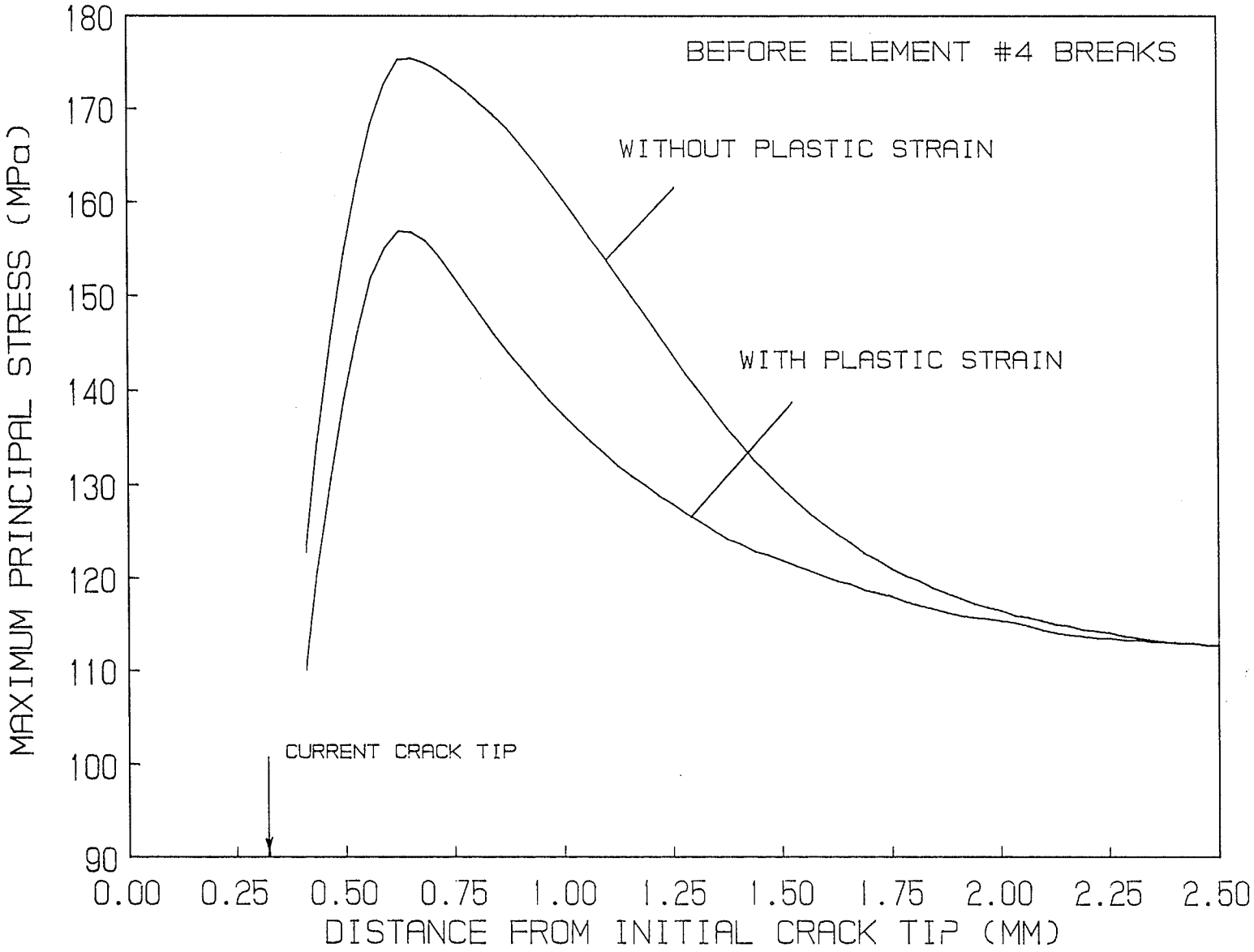

Figure 6.29 Distributions of maximum principal stress ahead of crack tip before element #4 breaks

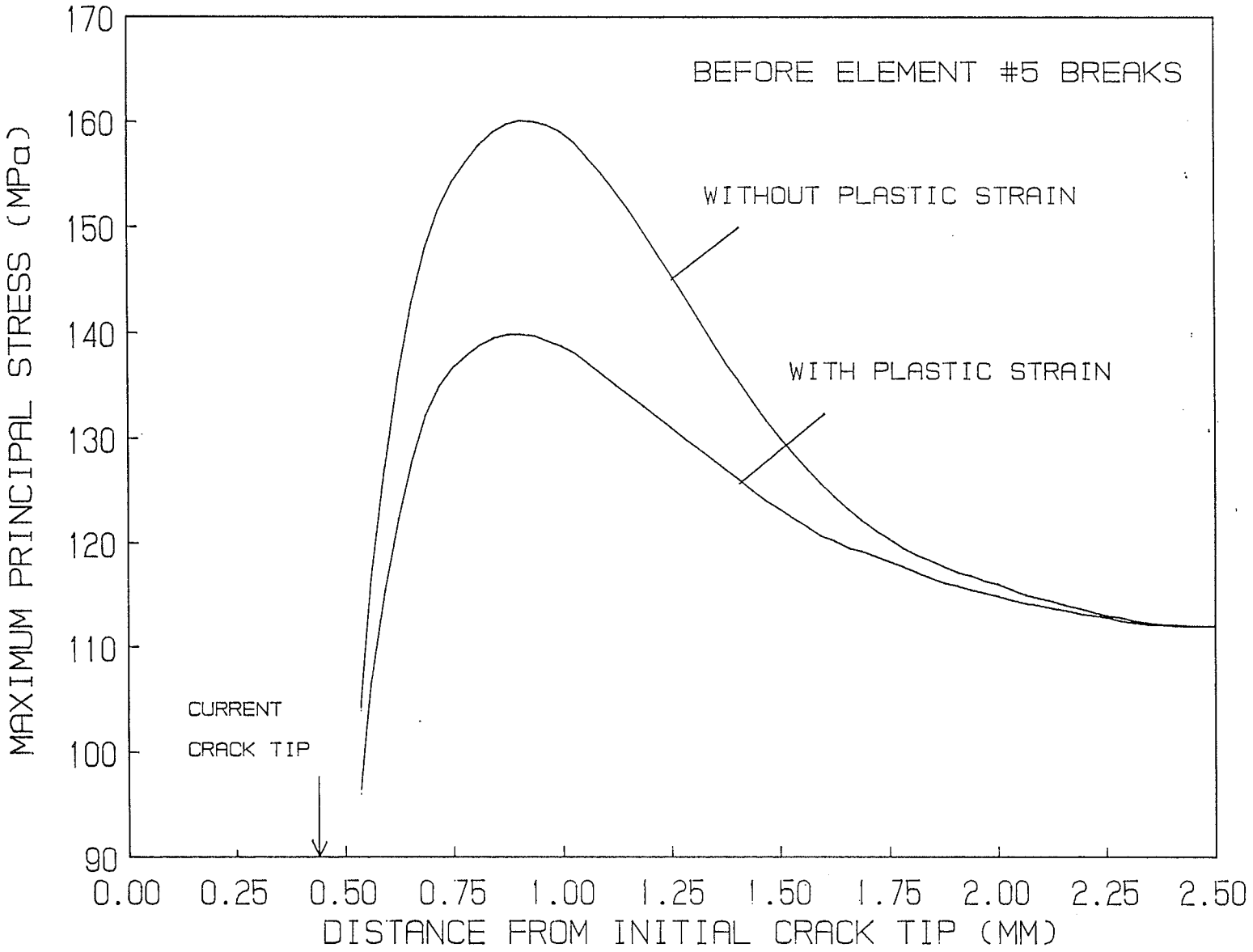

Figure 6.30 Distributions of maximum principal stress ahead of crack tip before element #5 breaks

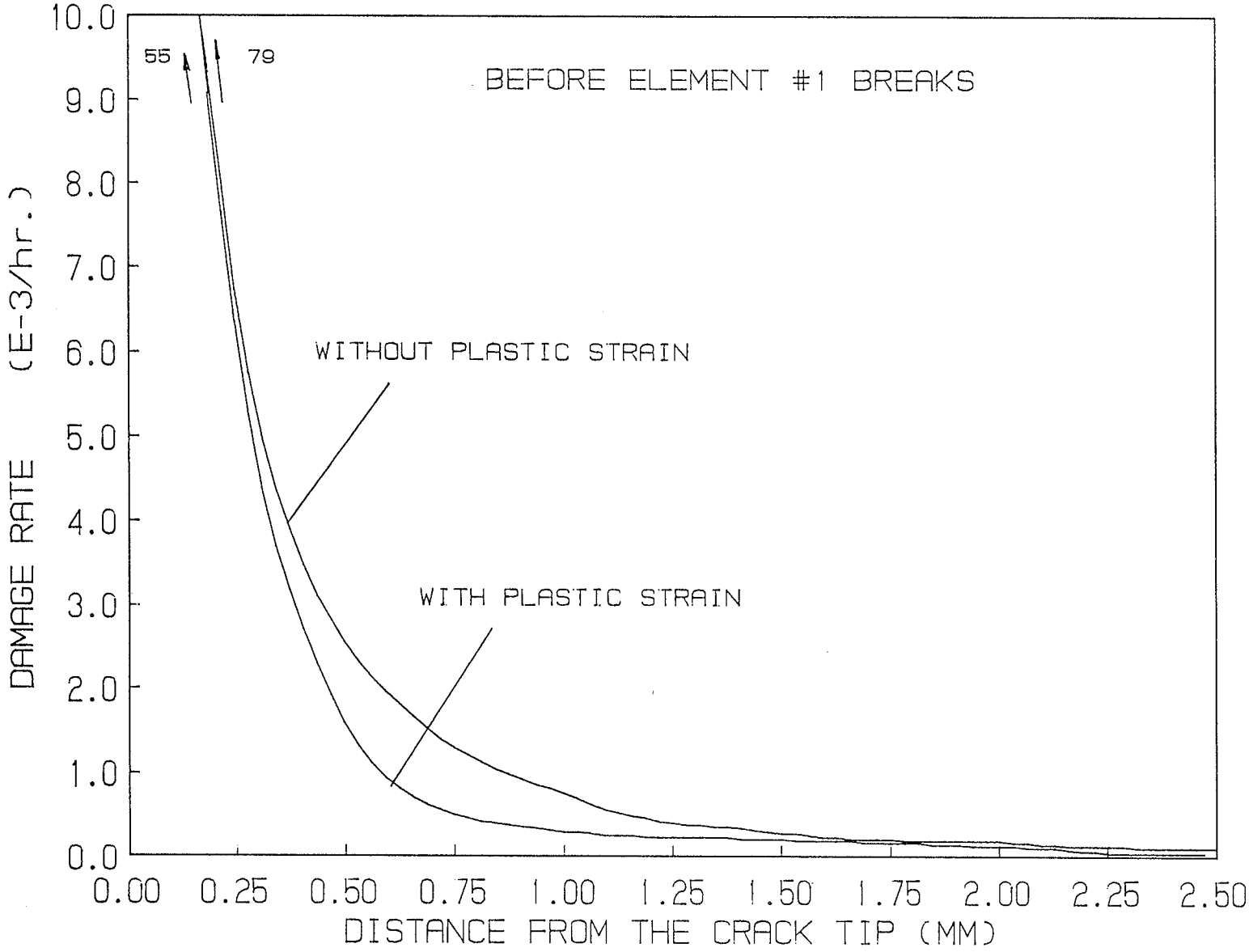

Figure 6.31 Distributions of damage rate ahead of crack tip before element #1 breaks

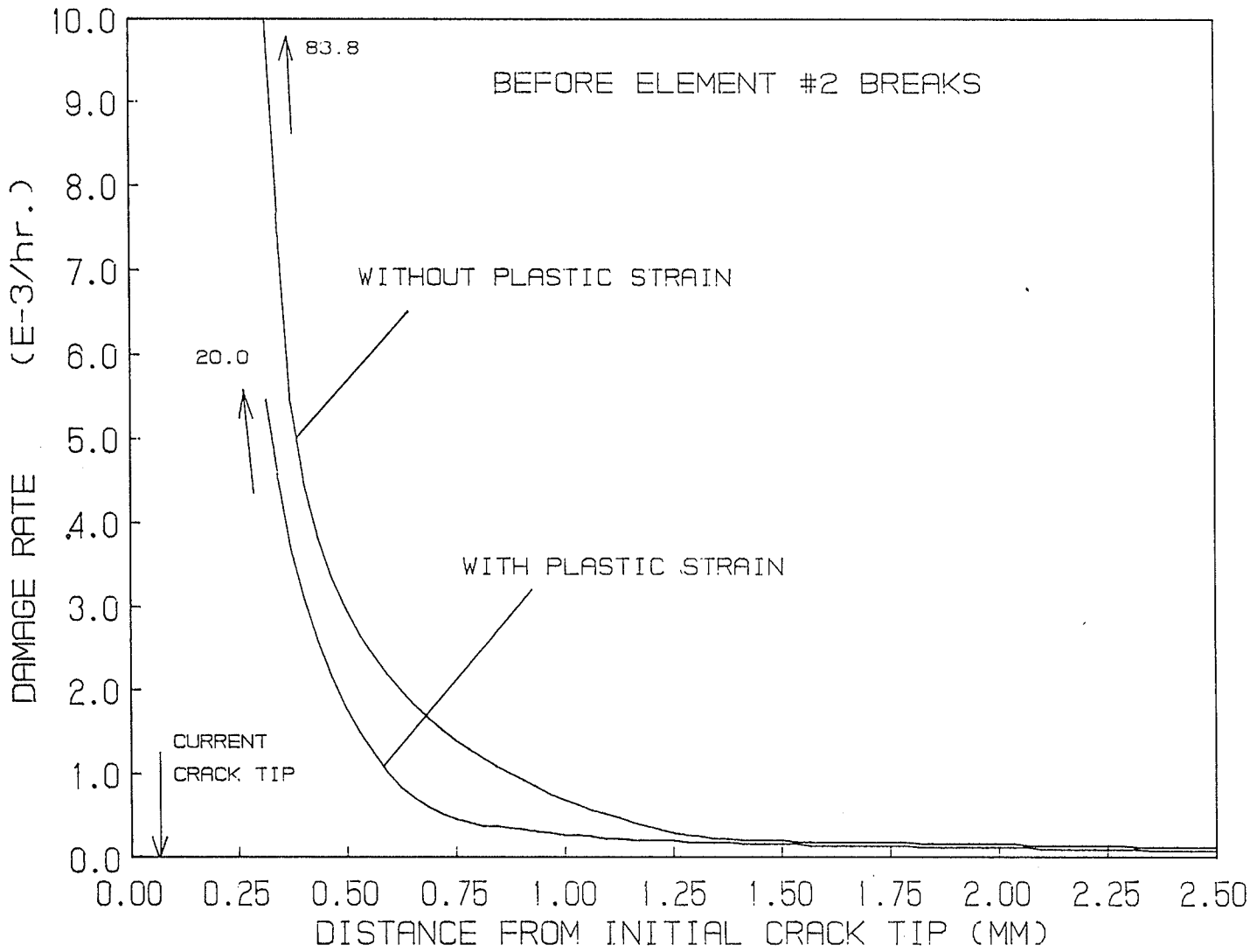

Figure 6.32 Distributions of damage rate ahead of crack tip before element #2 breaks

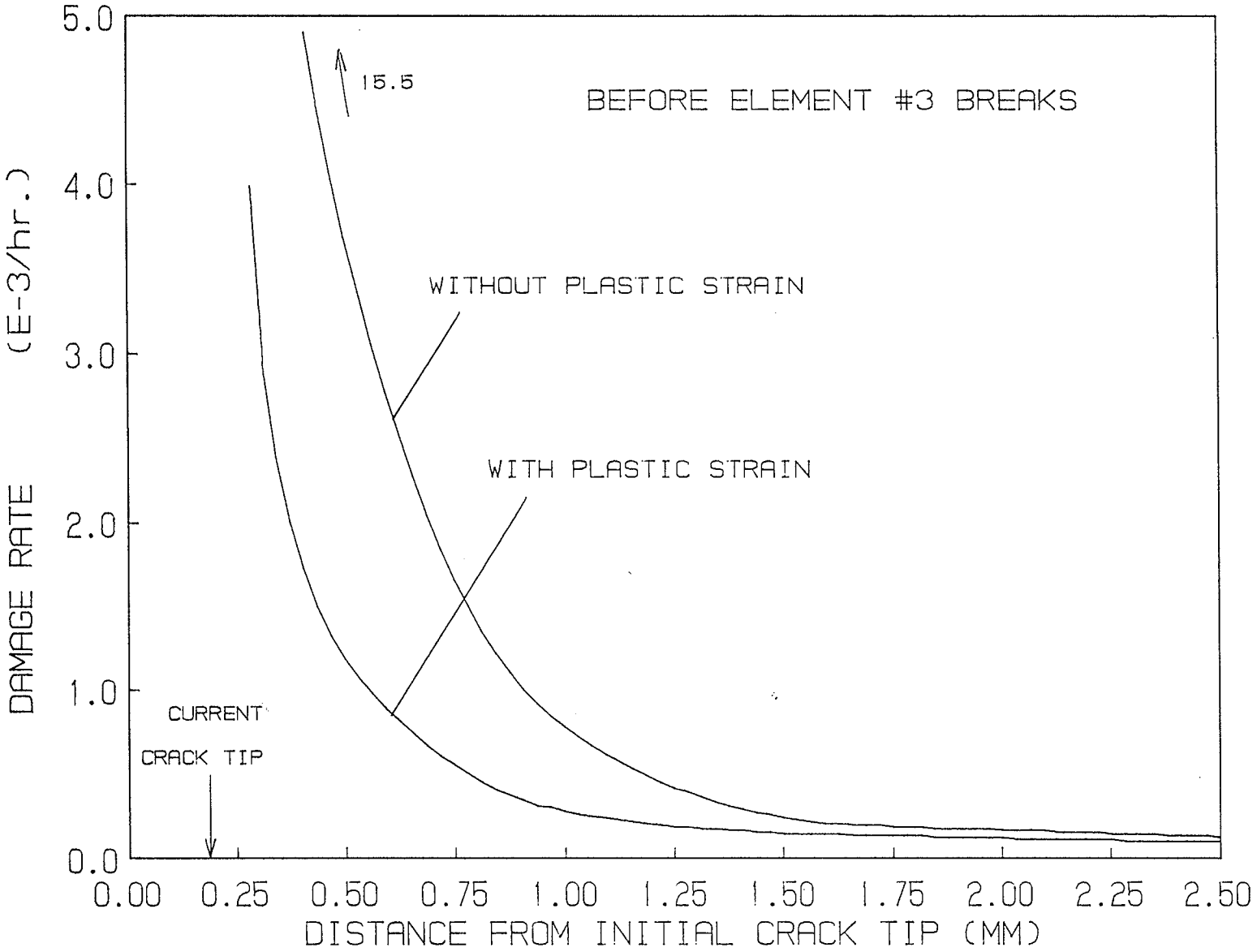

Figure 6.33 Distributions of damage rate ahead of crack tip before element #3 breaks

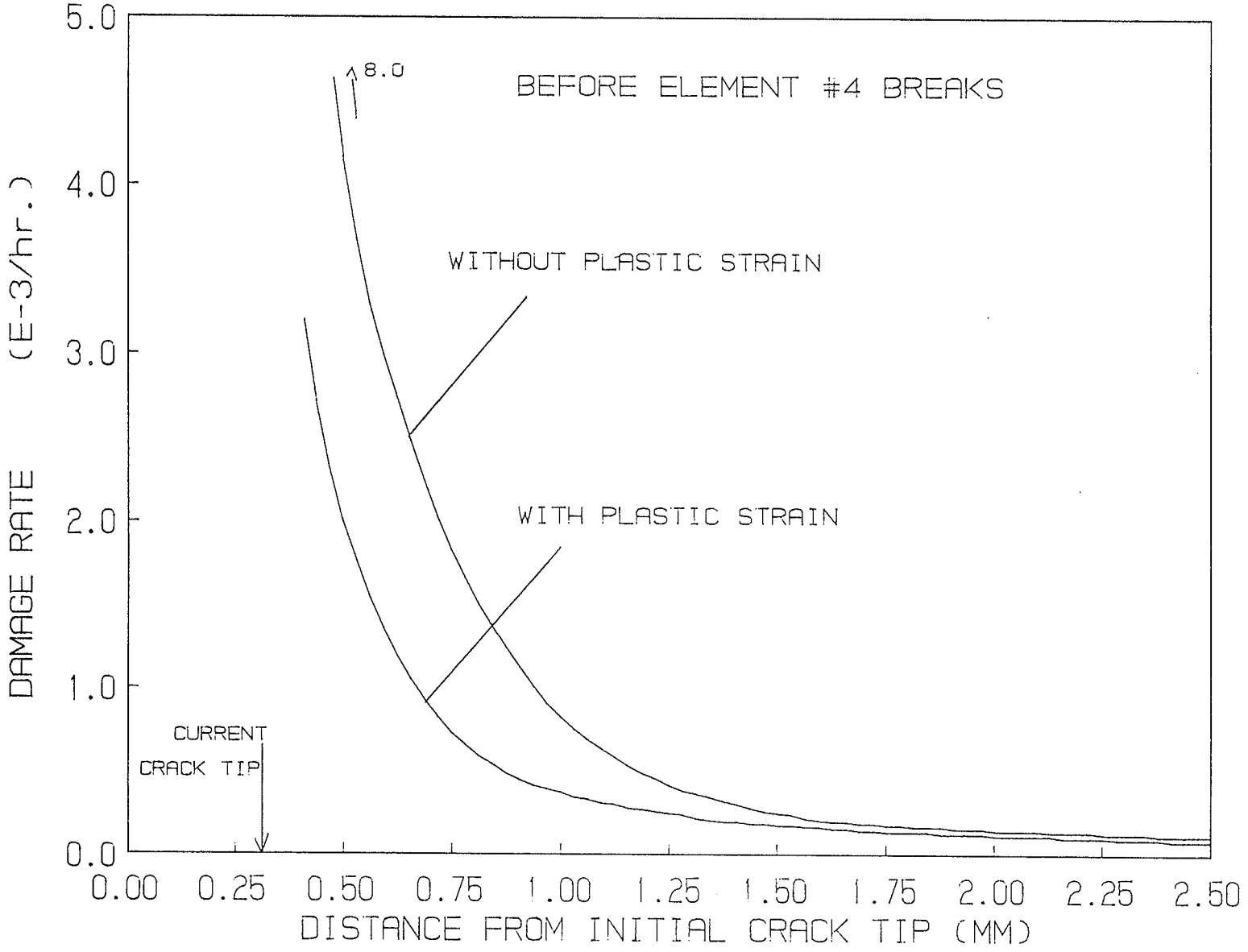

Figure 6.34 Distributions of damage rate ahead of crack tip before element #4 breaks

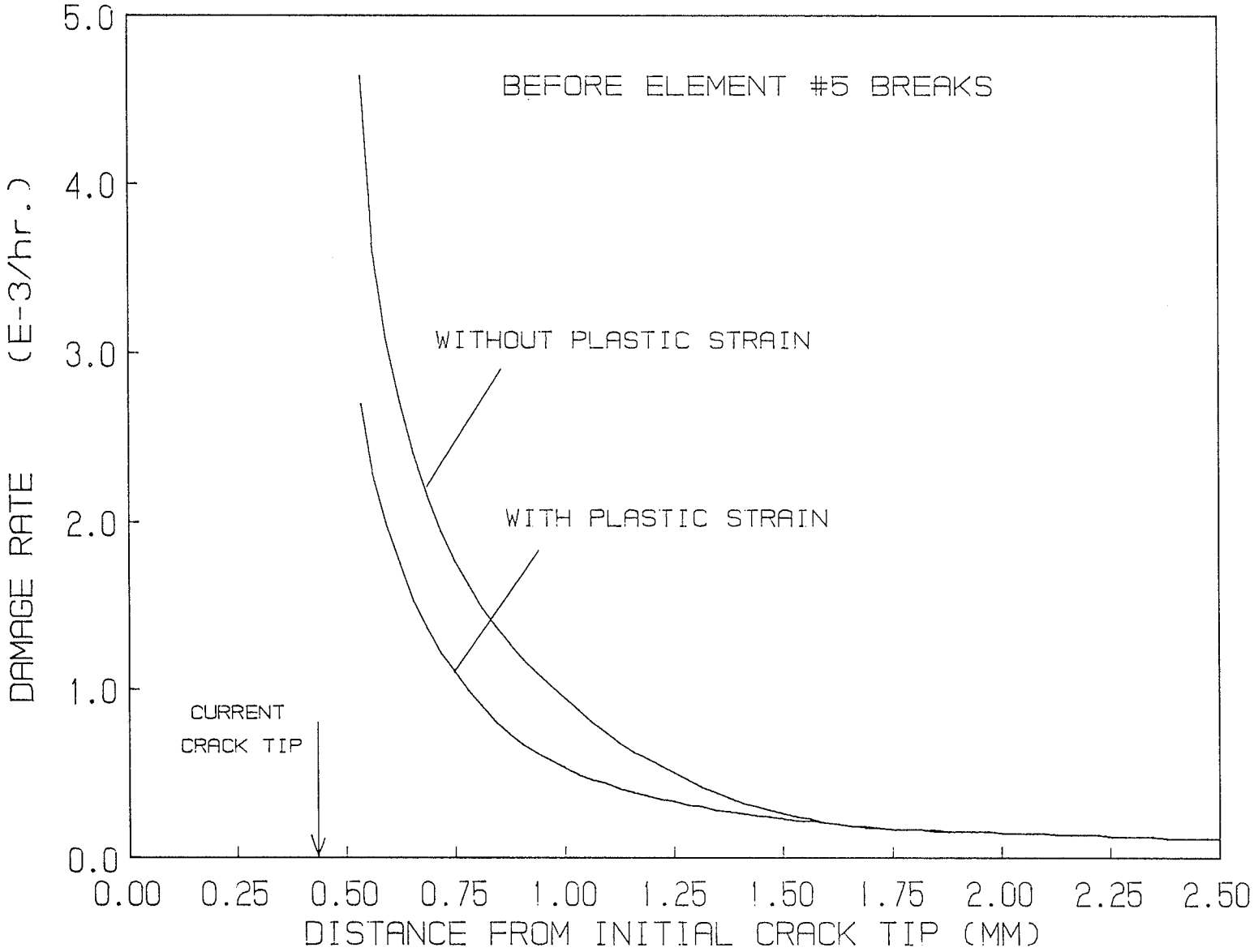

Figure 6.35 Distributions of damage rate ahead of crack tip before element #5 breaks

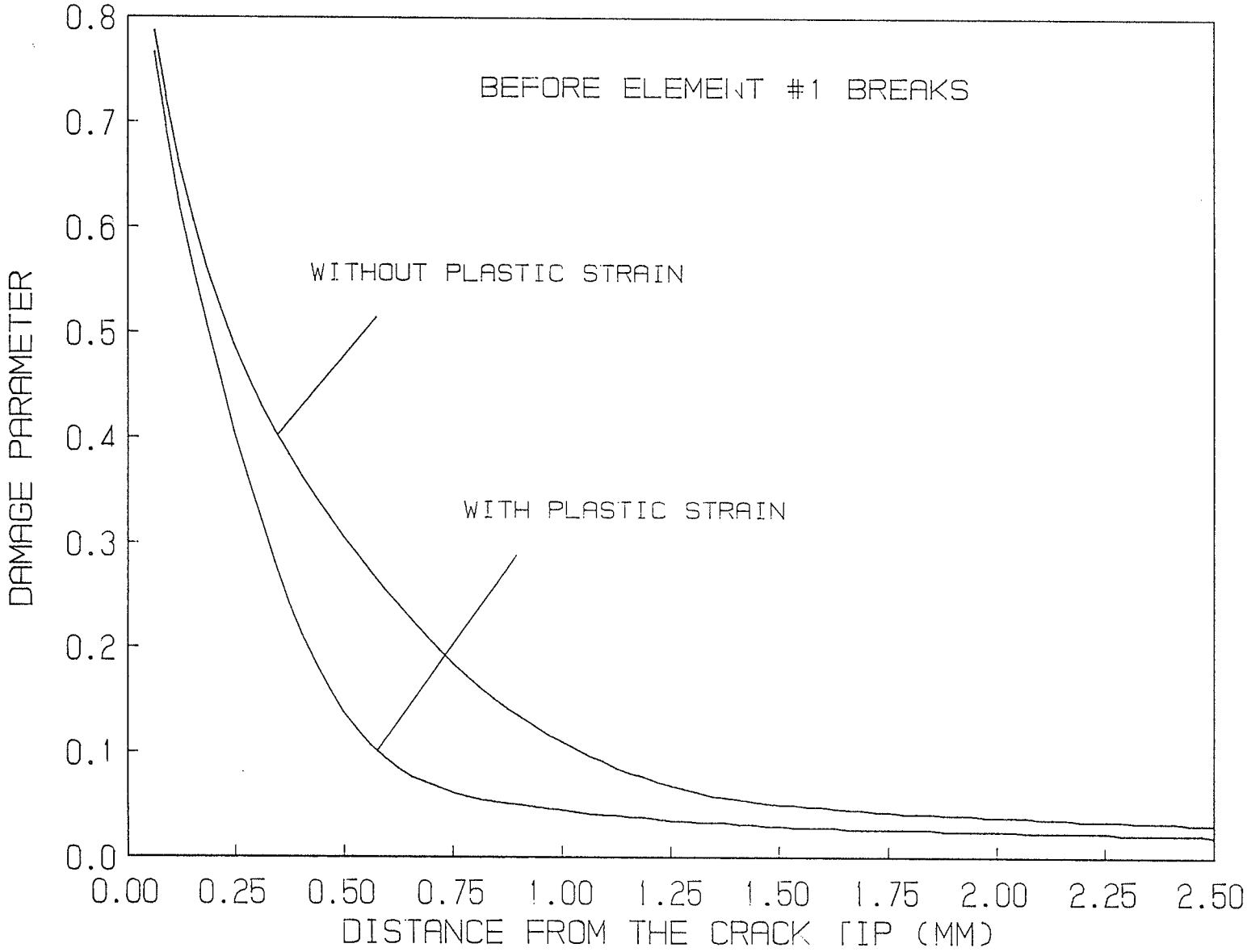

Figure 6.36 Damage distributions ahead of crack tip before element #1 breaks

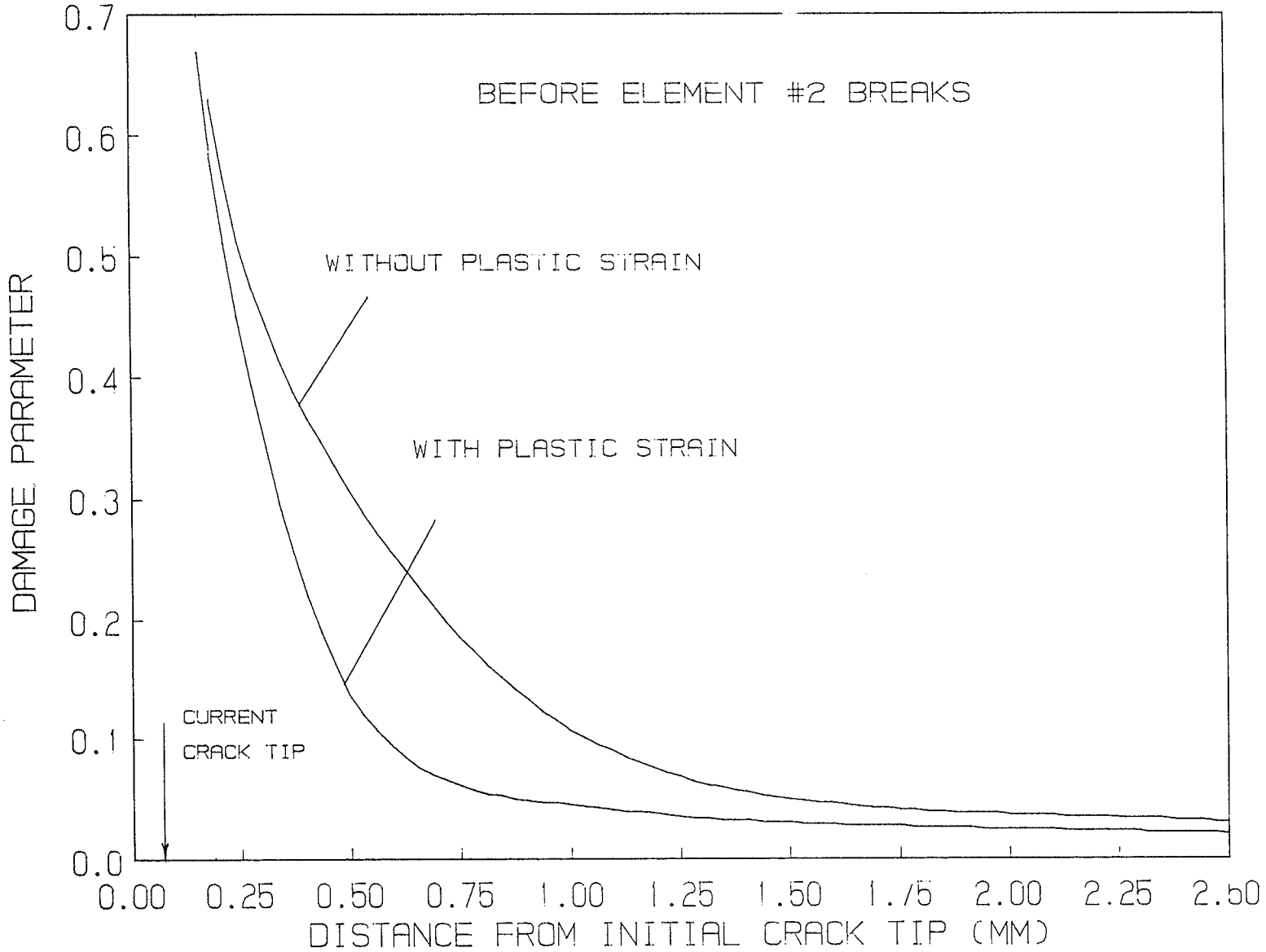

Figure 6.37 Damage distributions ahead of crack tip before element #2 breaks

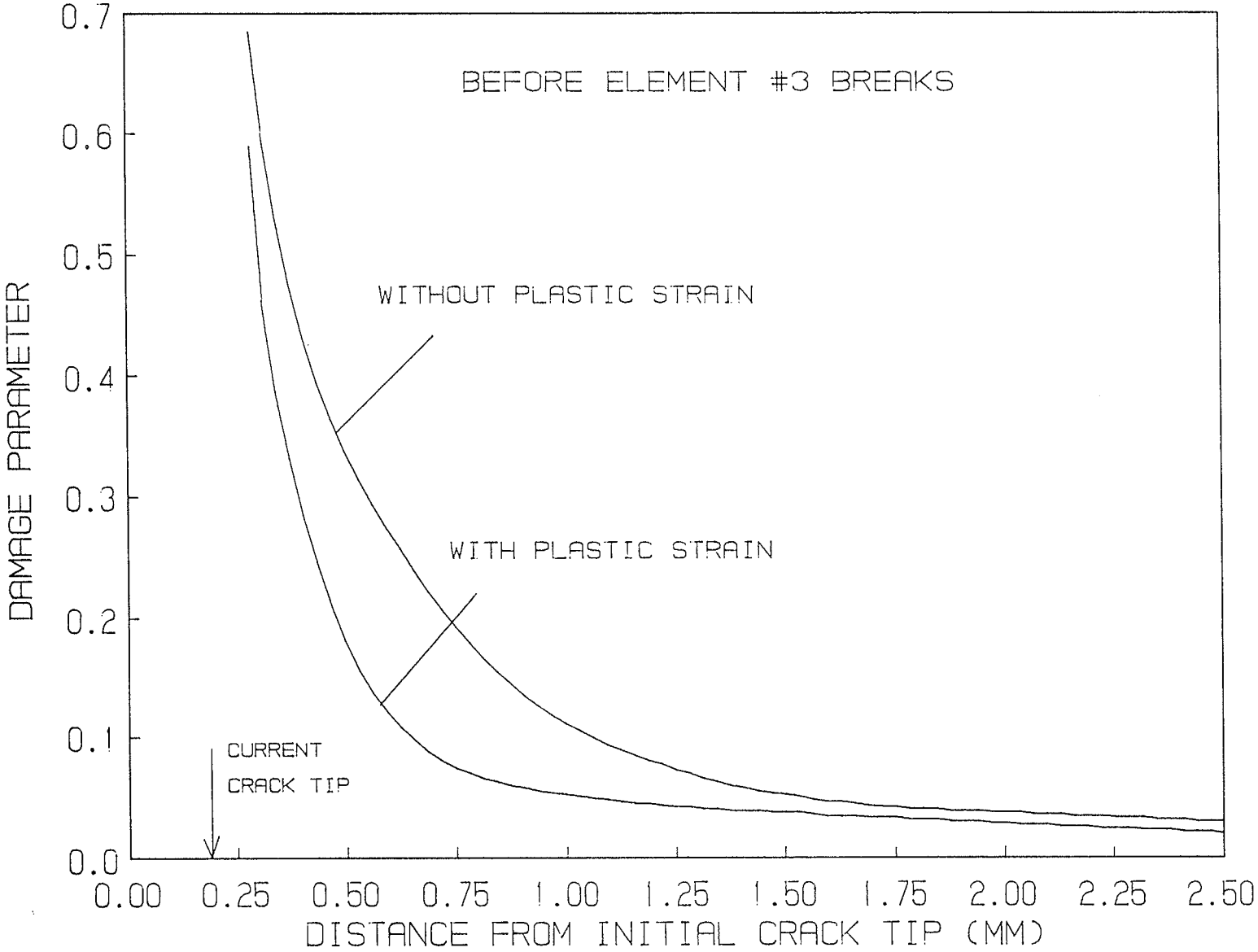

Figure 6.38 Damage distributions ahead of crack tip before element #3 breaks

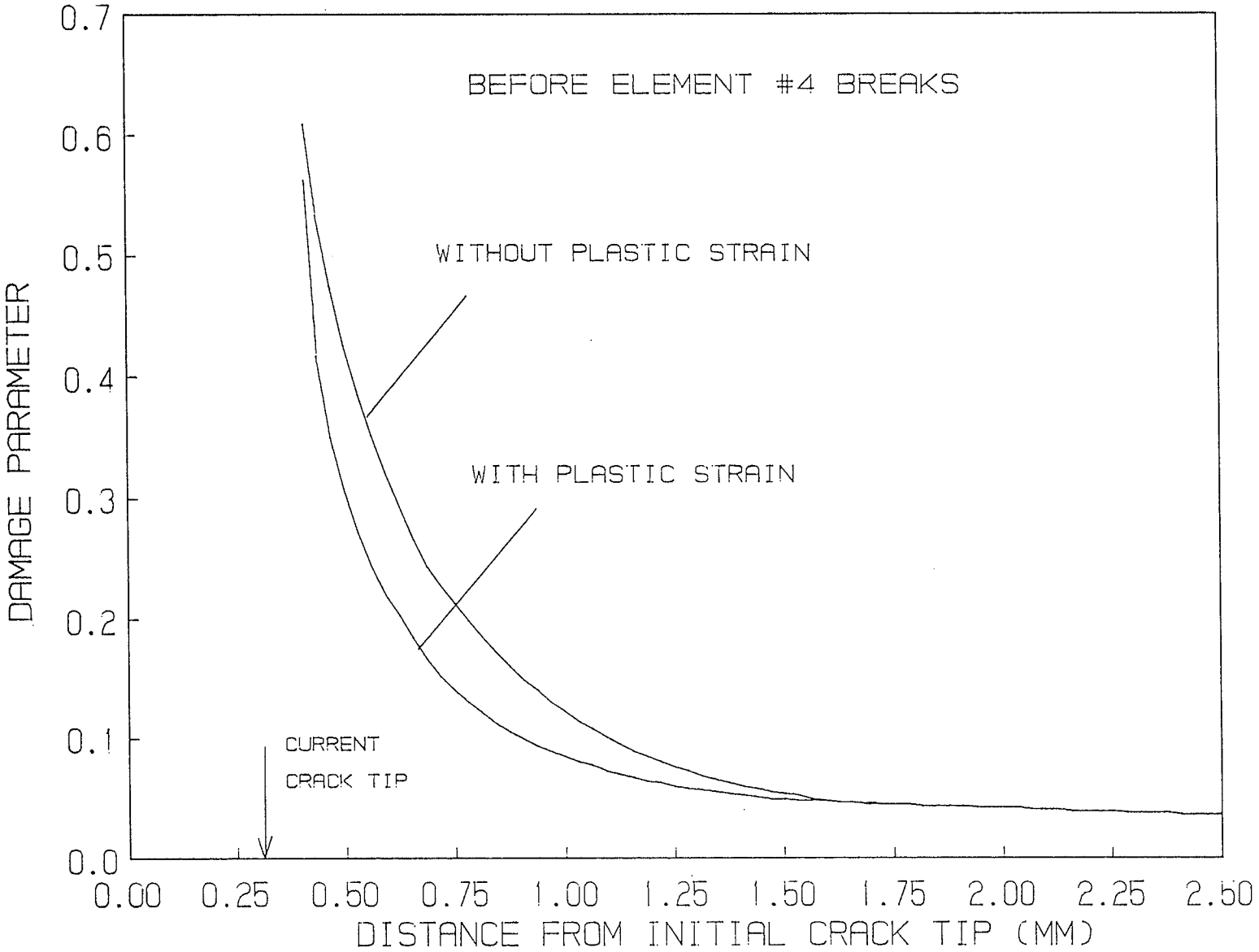

Figure 6.39 Damage distributions ahead of crack tip before element #4 breaks

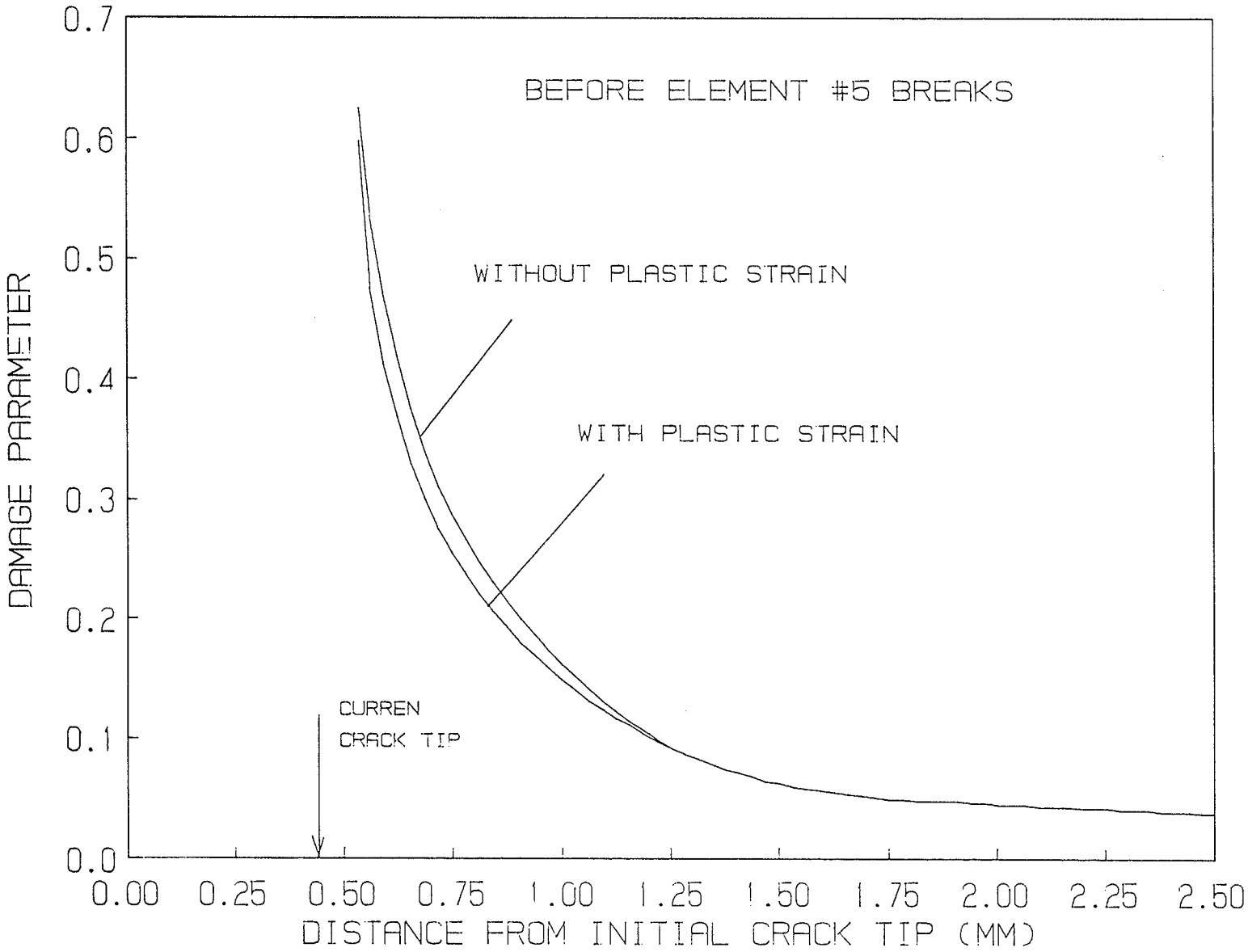

Figure 6.40 Damage distributions ahead of crack tip before element #5 breaks

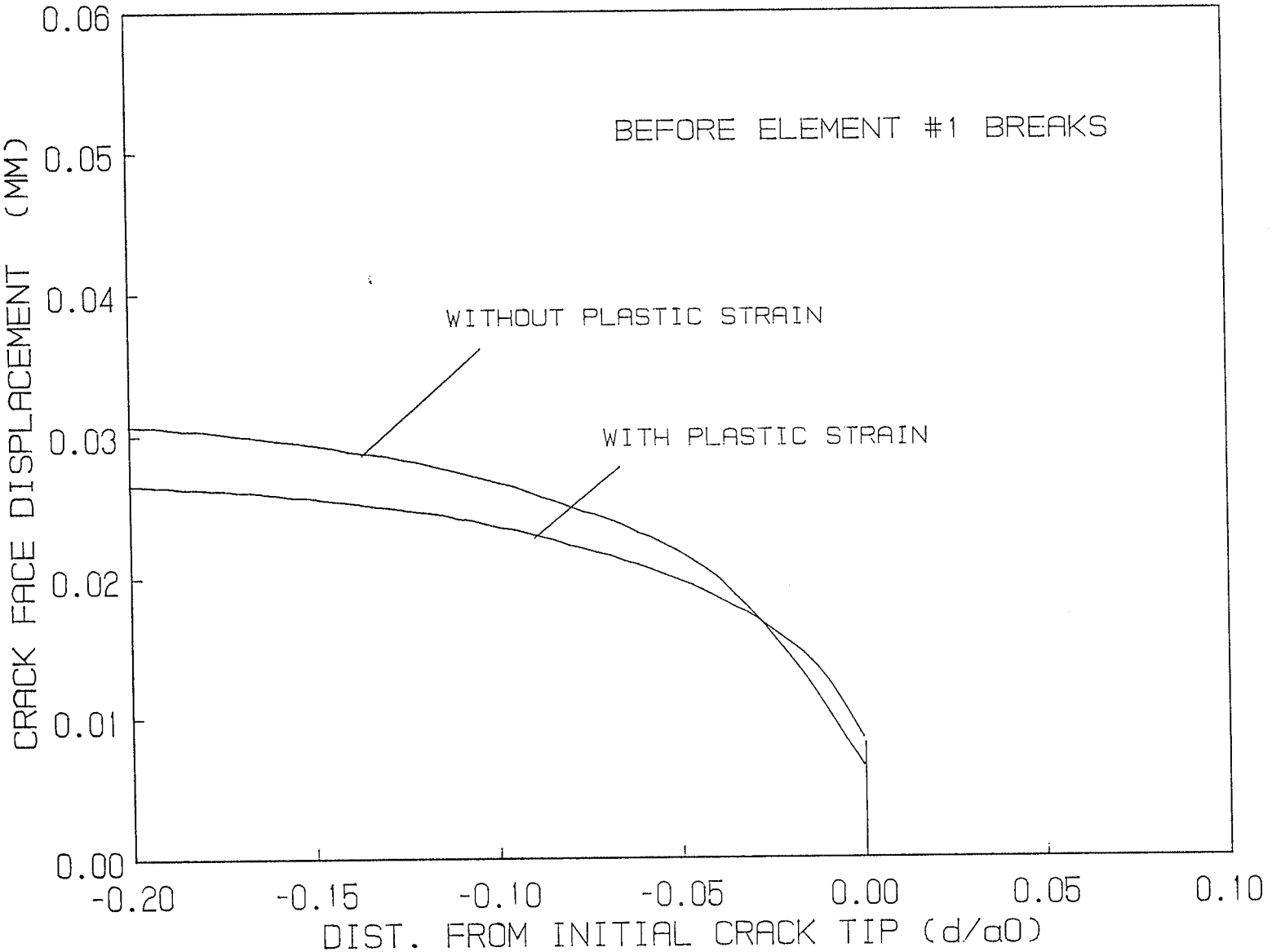

Figure 6.41 Crack profiles before element #1 breaks

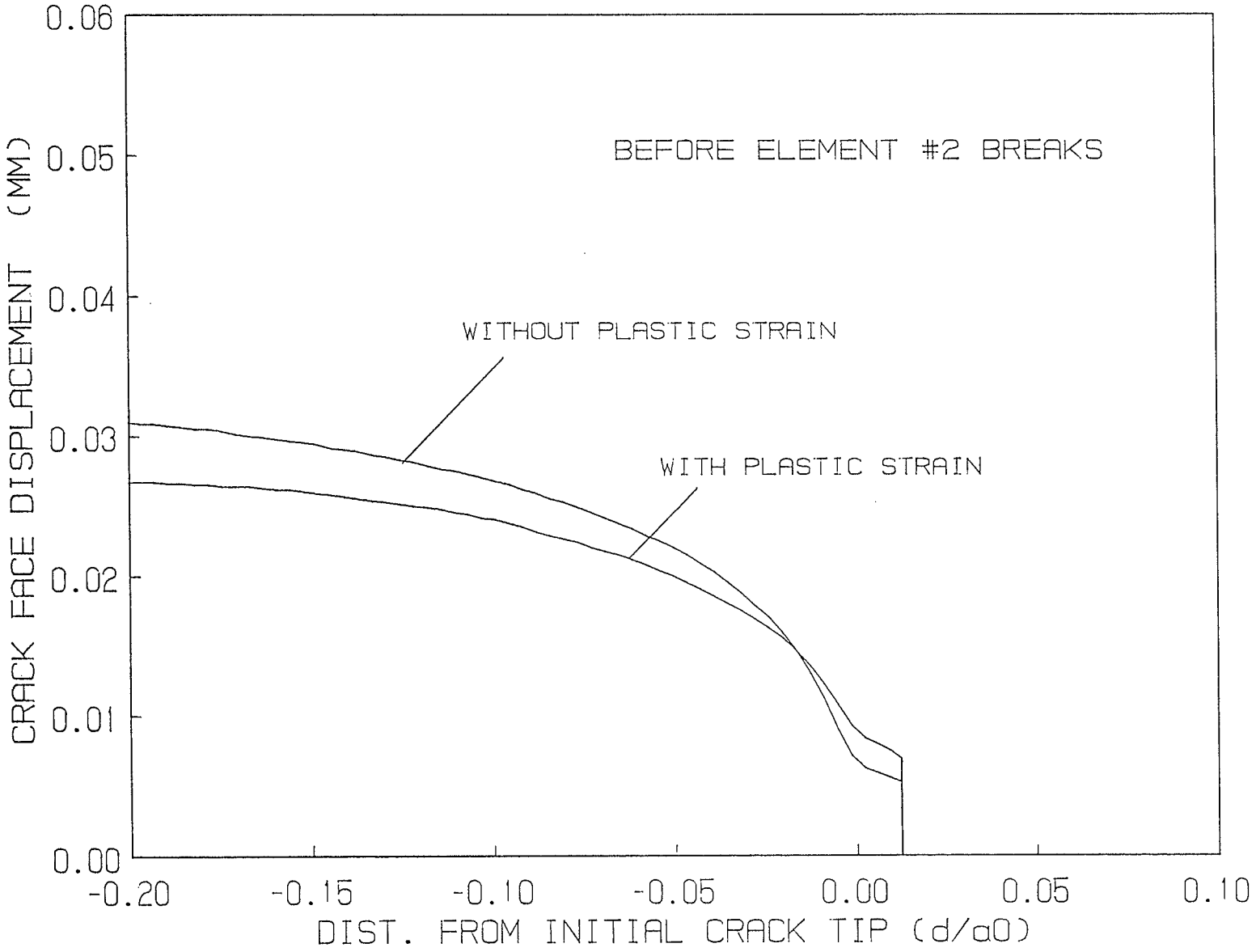

Figure 6.42 Crack profiles before element #2 breaks

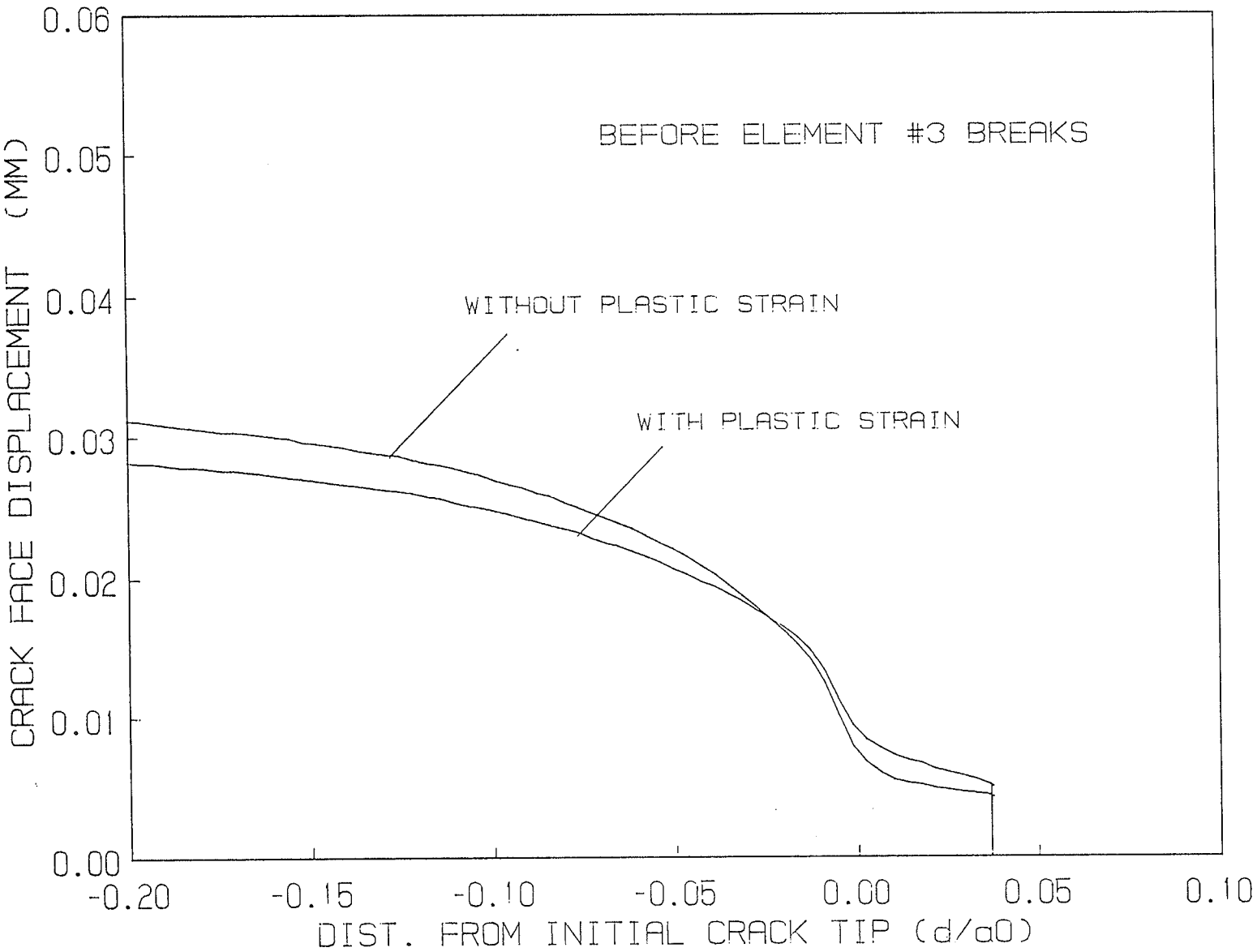

Figure 6.43 Crack profiles before element #3 breaks

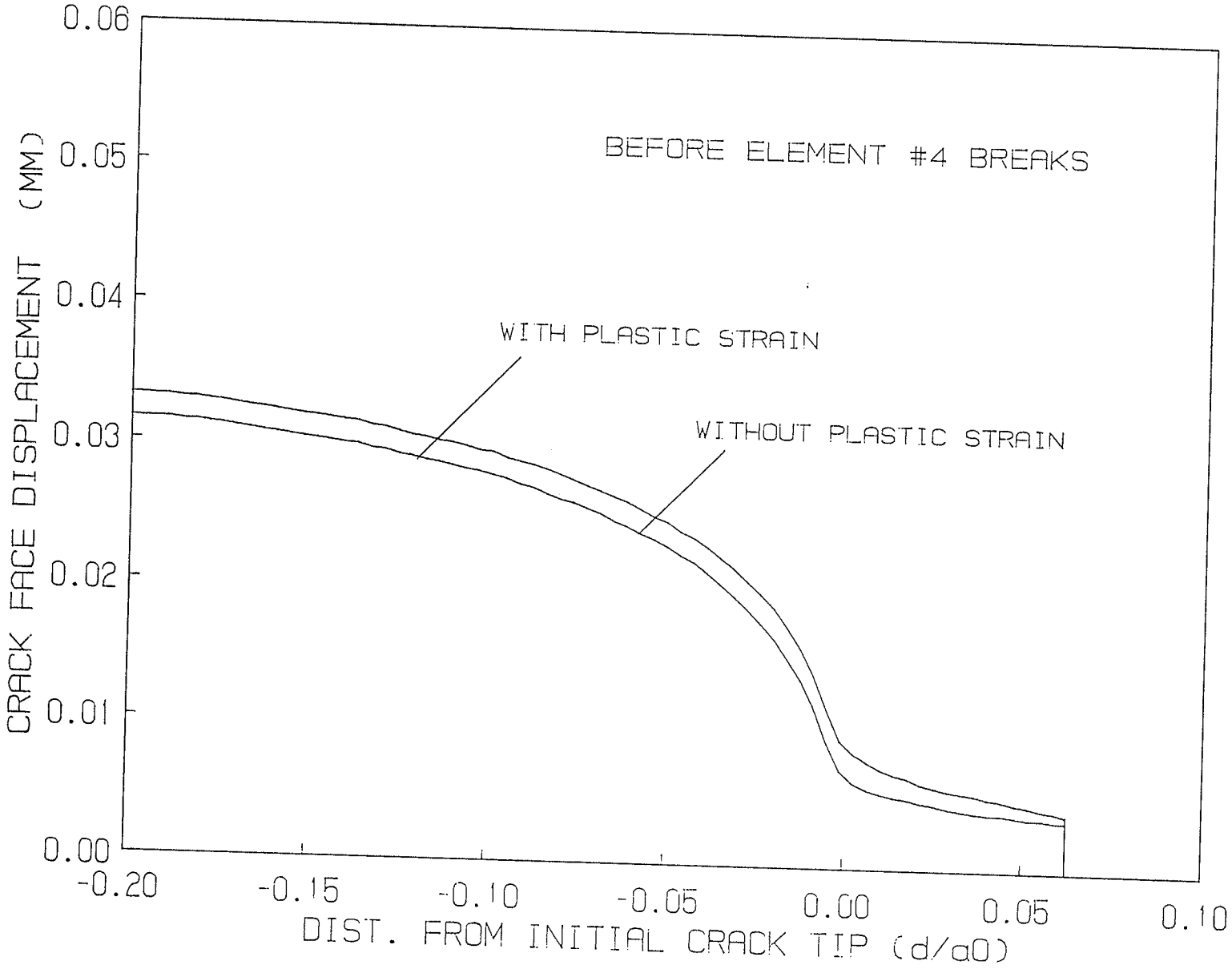

Figure 6.44 Crack profiles before element #4 breaks

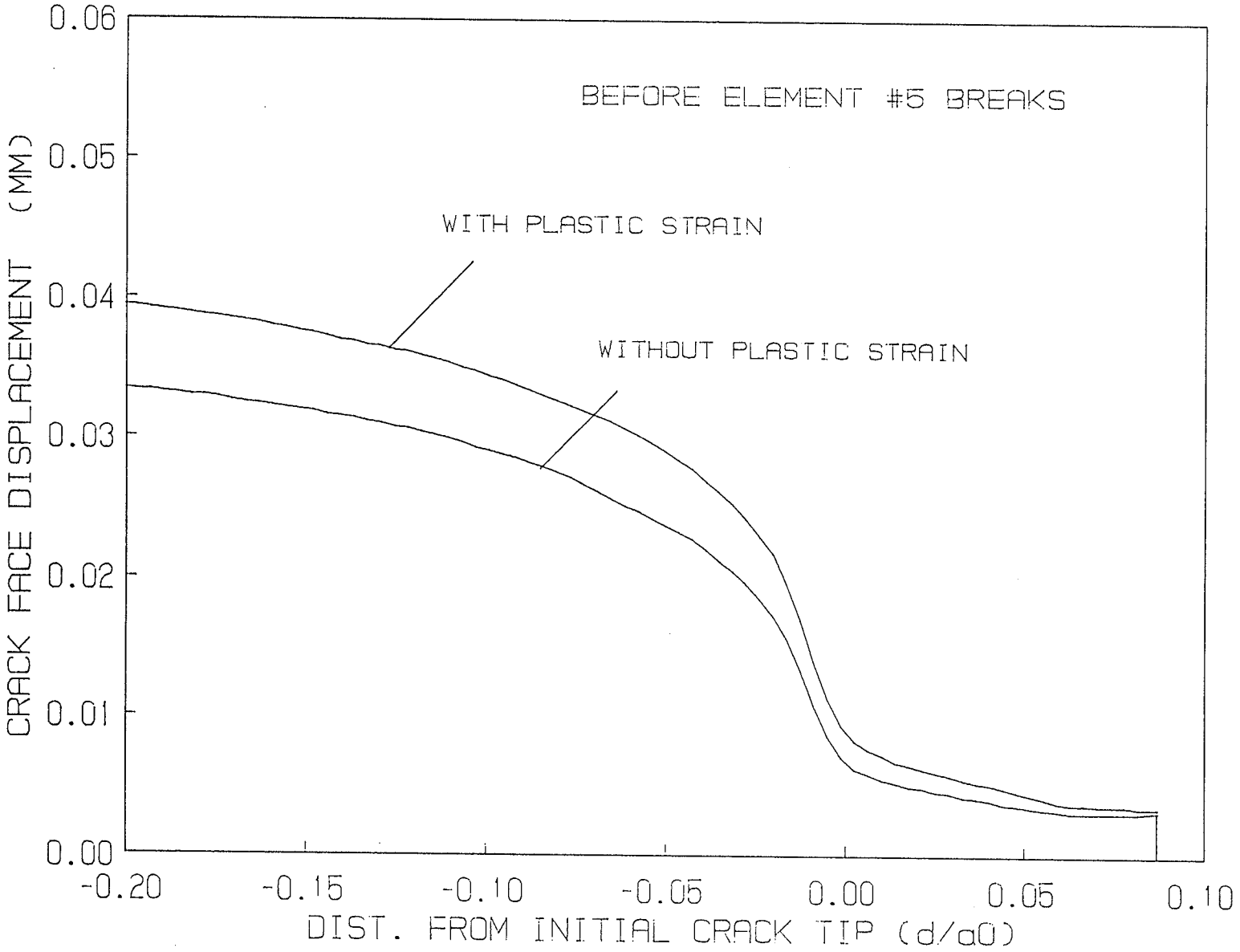

Figure 6.45 Crack profiles before element #5 breaks

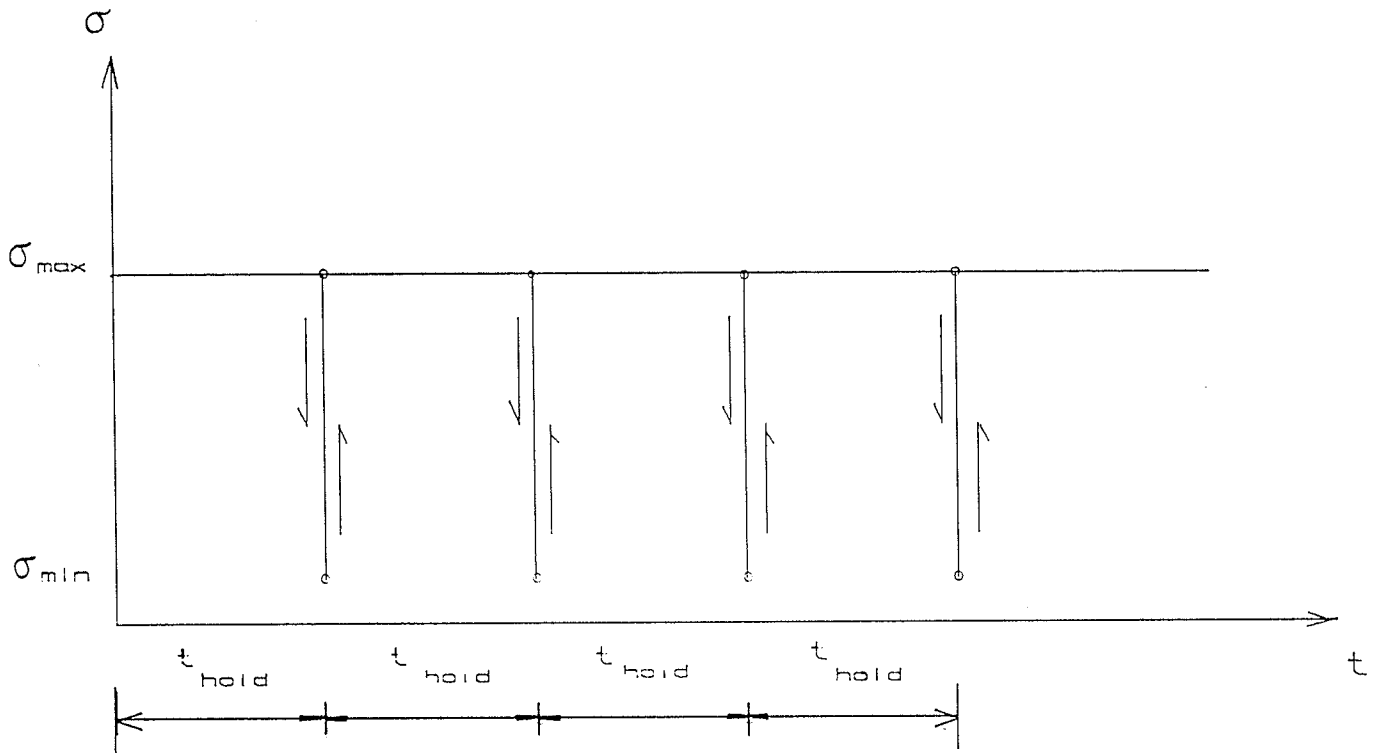

Figure 7.1 Repeated loading without rest period

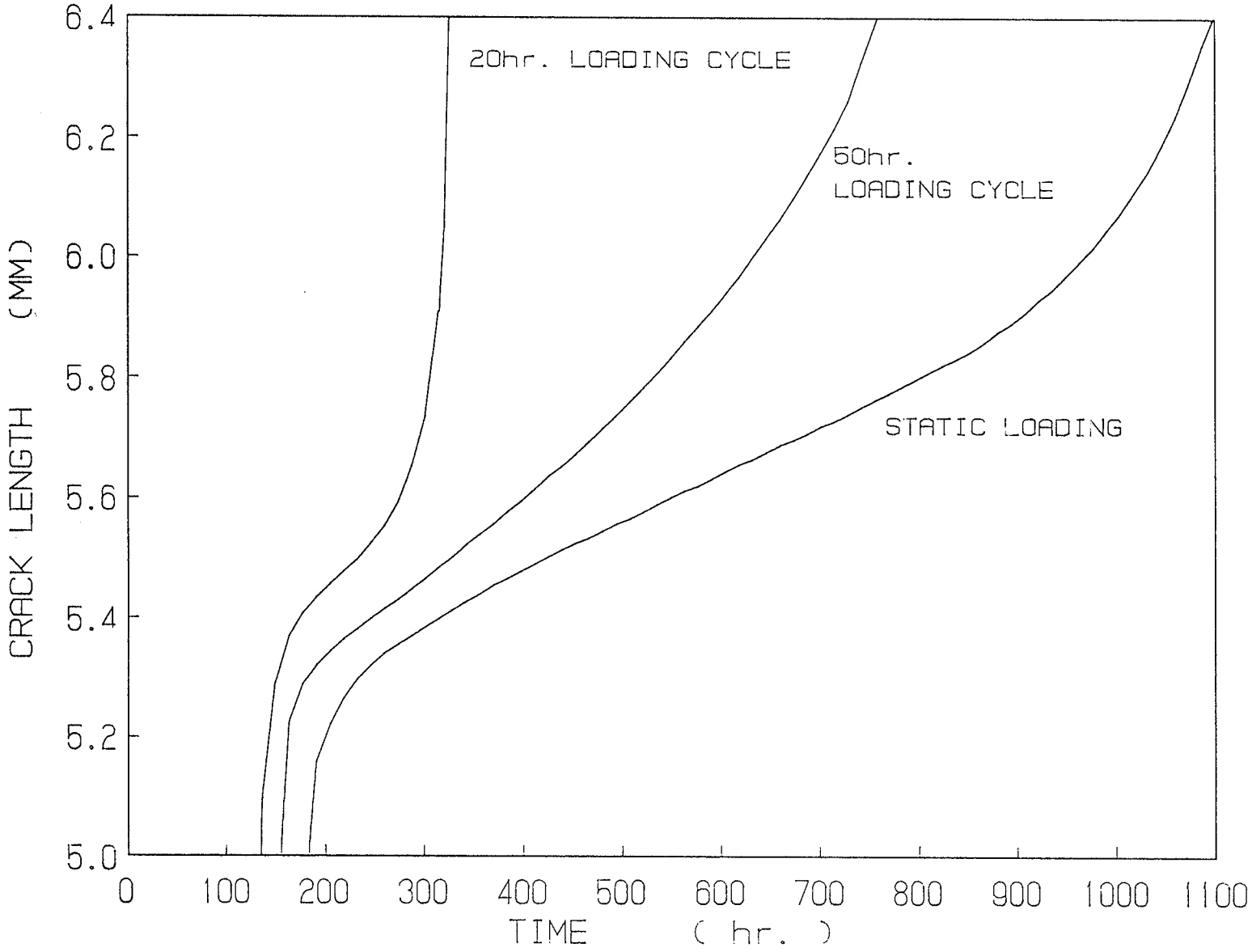

Figure 7.2 Crack growth vs. time

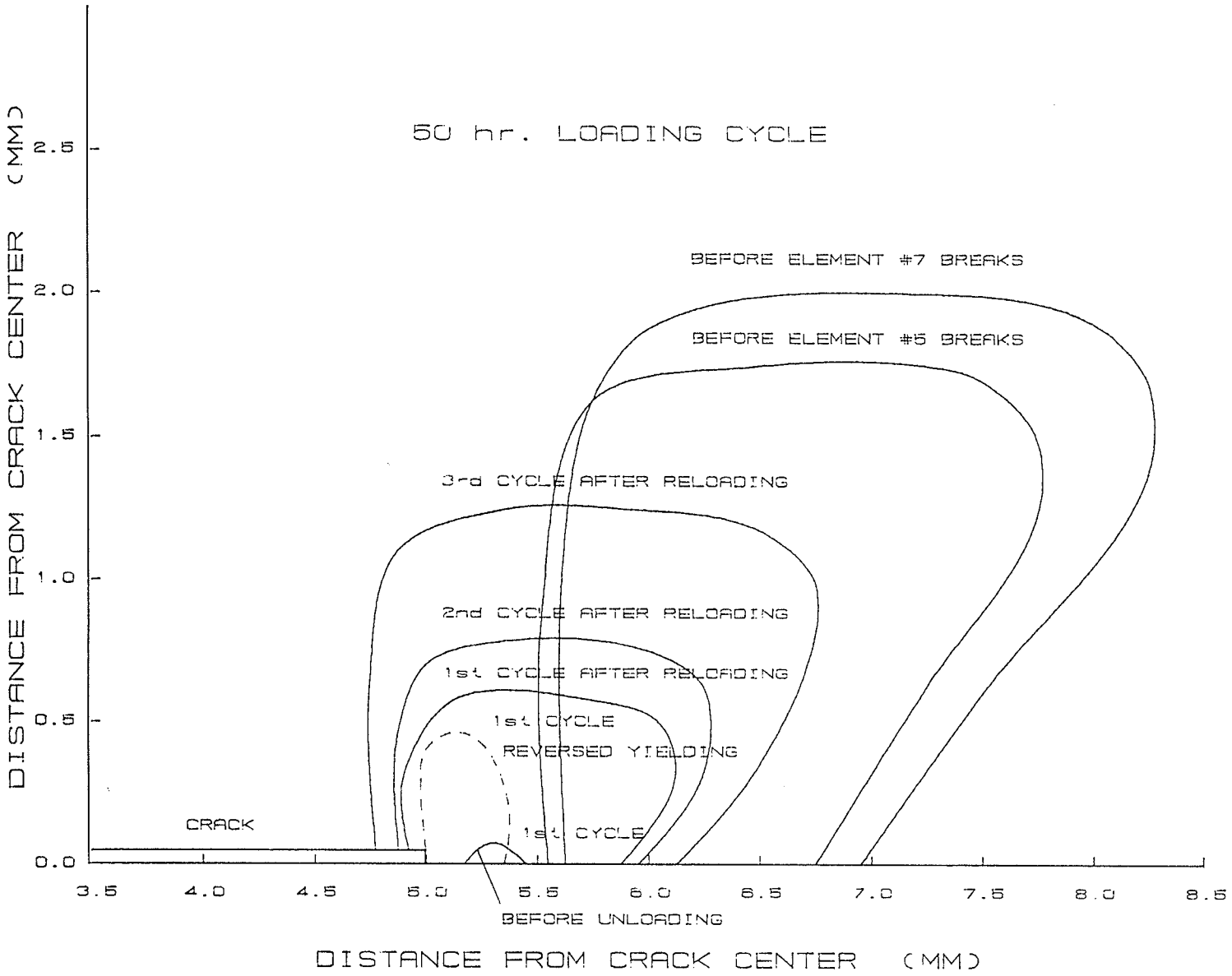

Figure 7.3 Variation of plastic zone in case 2

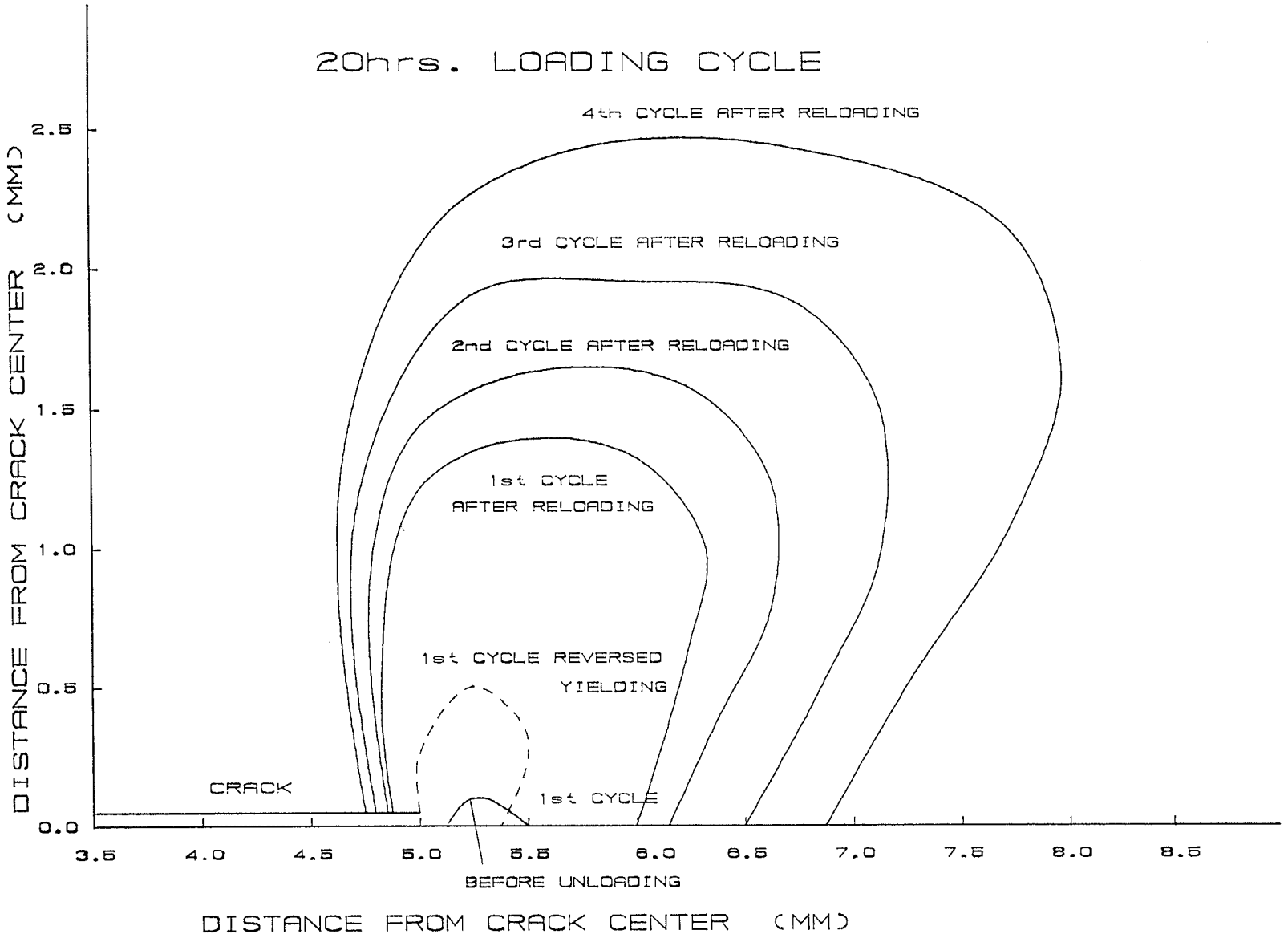

Figure 7.4 Variation of plastic zone before crack initiation in case 3

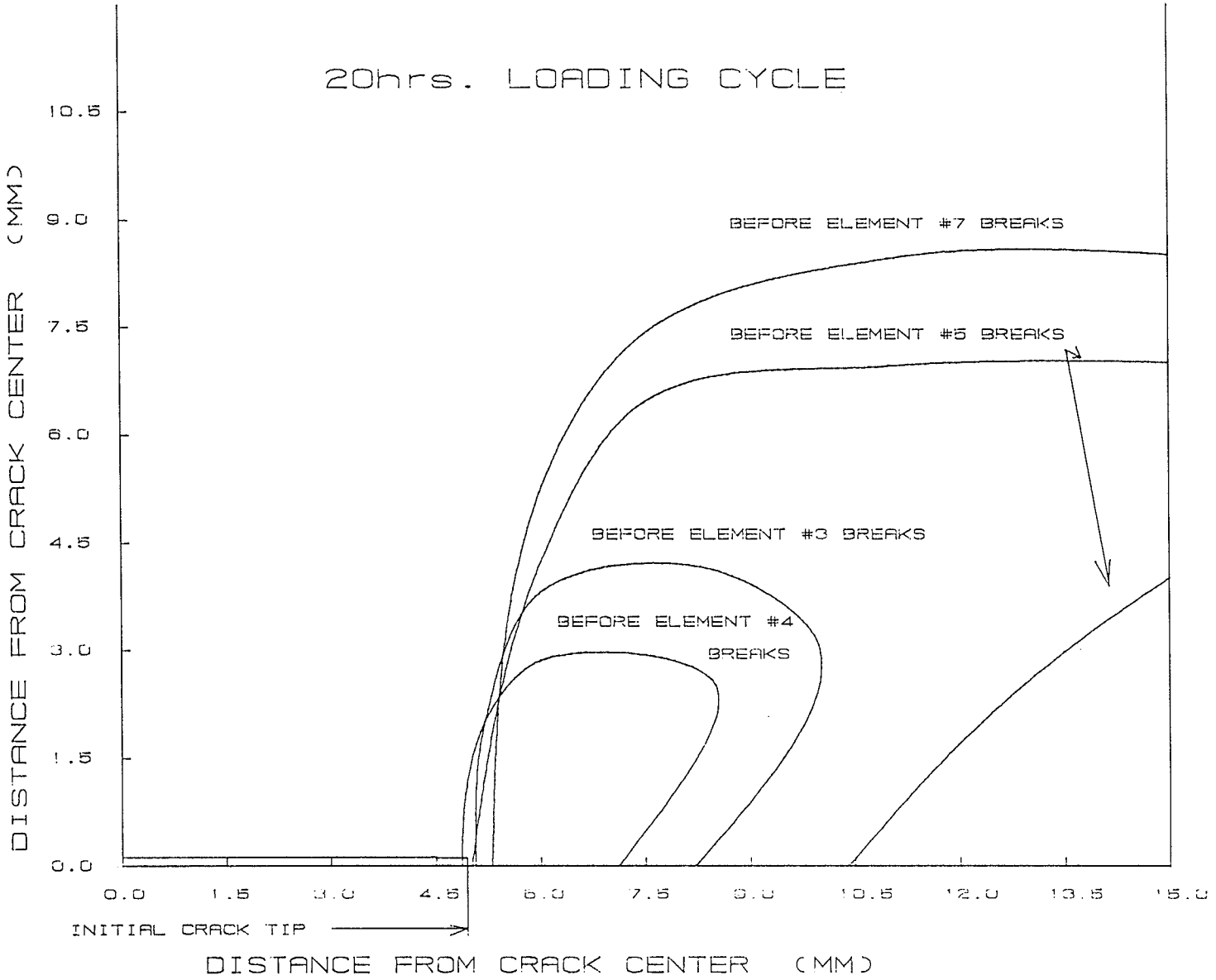

Figure 7.5 Variation of plastic zone during crack growth in case 3

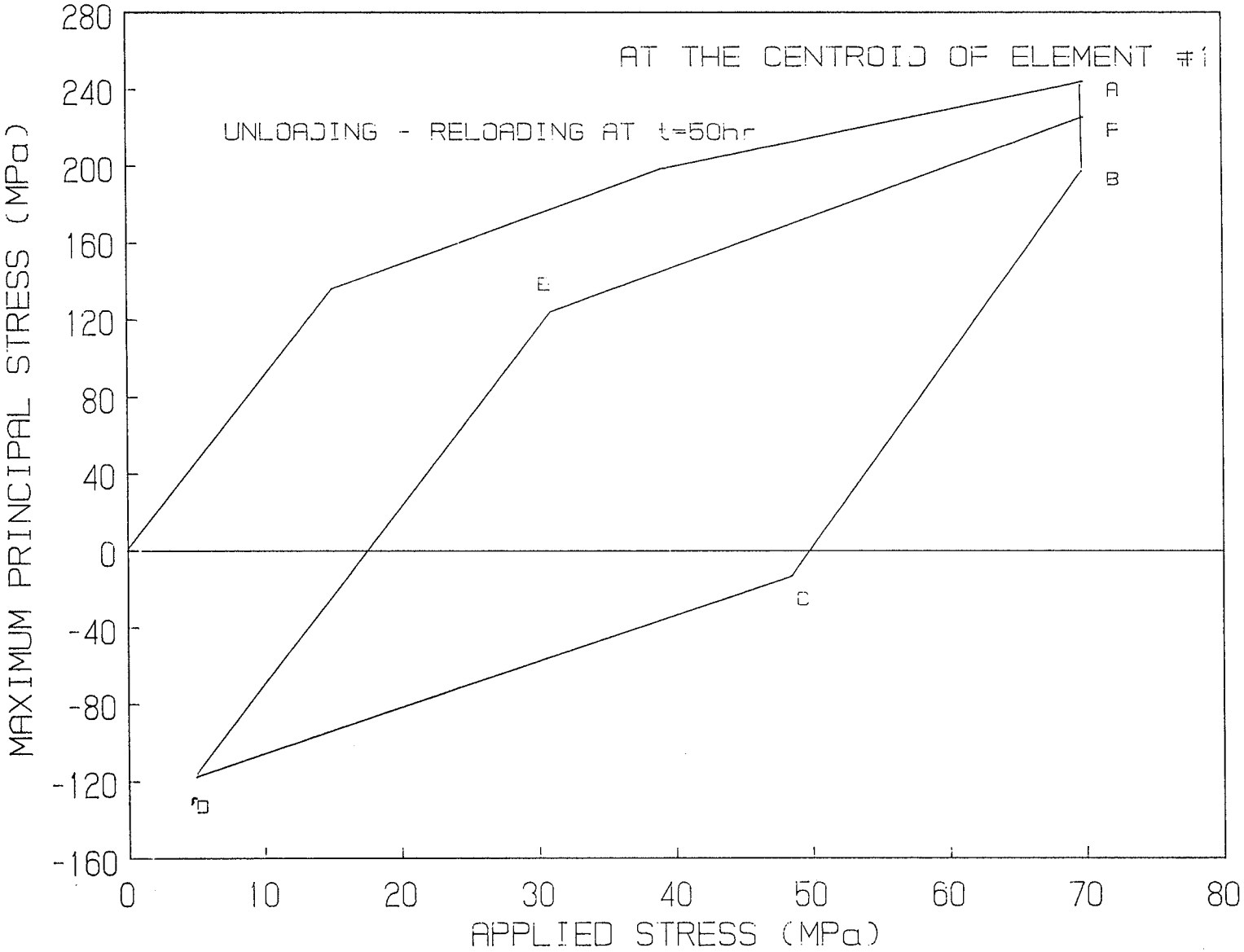

Figure 7.6 Variation of maximum principal stress in crack tip element in first load cycle in case 2

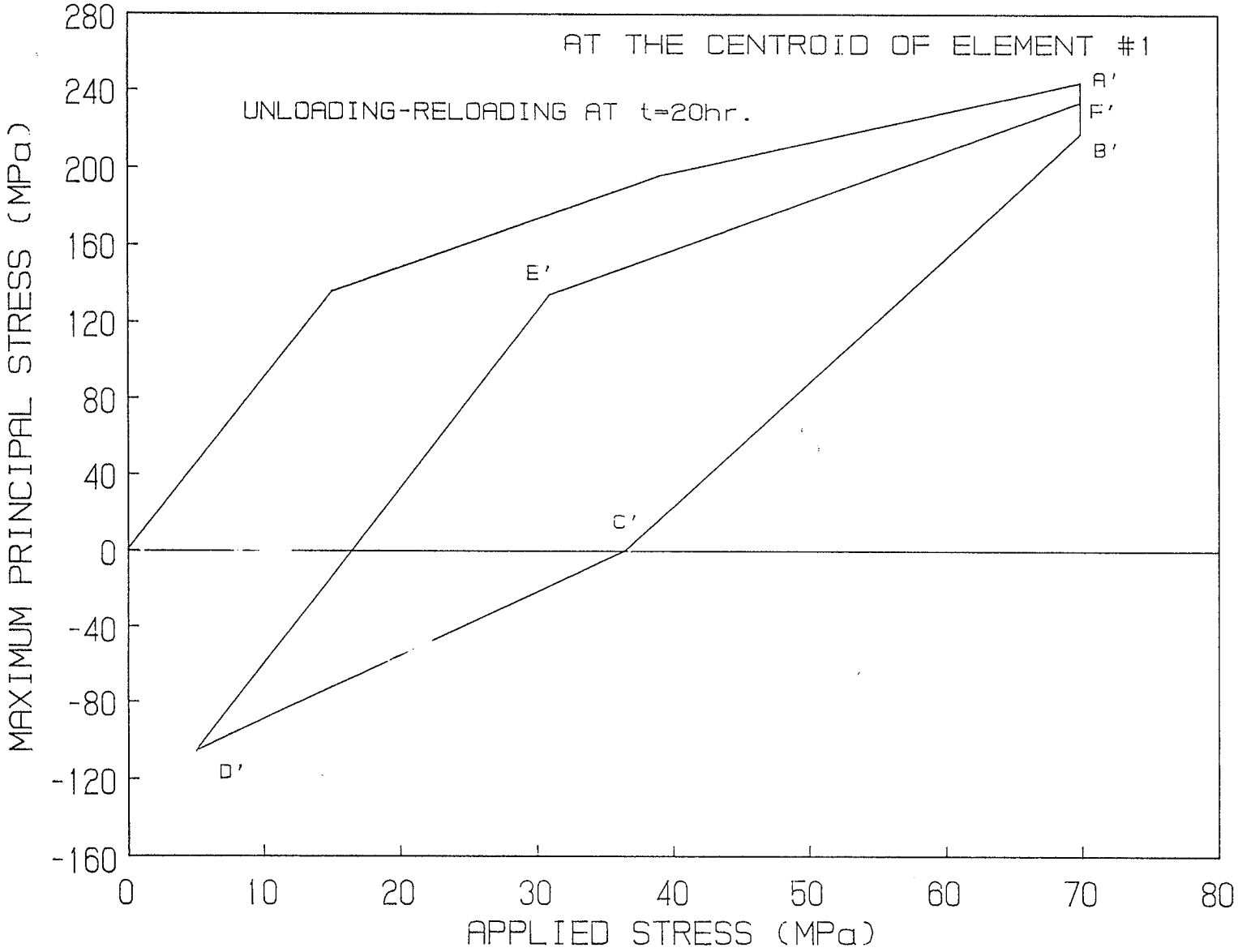

Figure 7.7 Variation of maximum principal stress in crack tip element in first load cycle in case 3

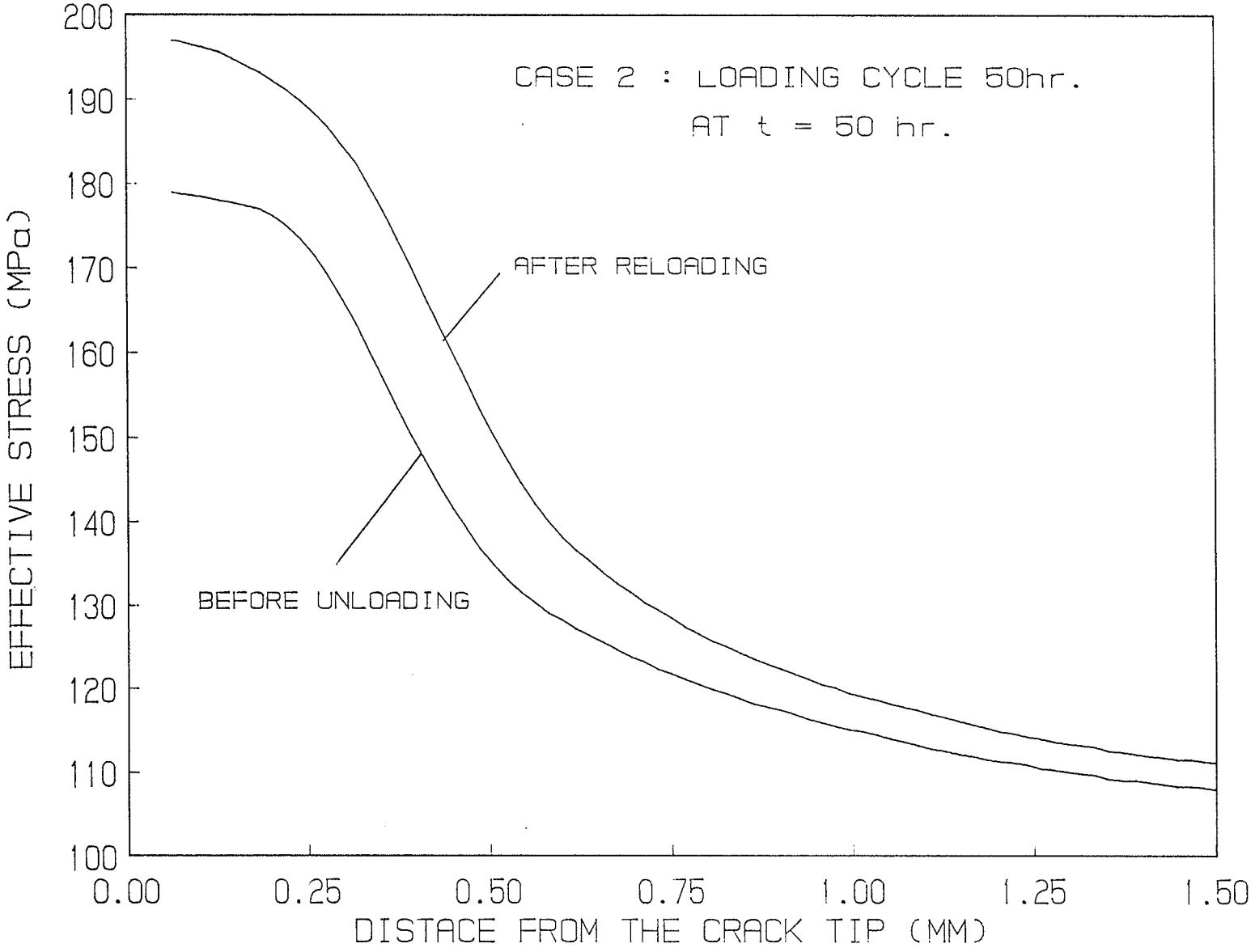

Figure 7.8 Increase of effective stress ahead of crack tip after unloading and reloading (case 2)

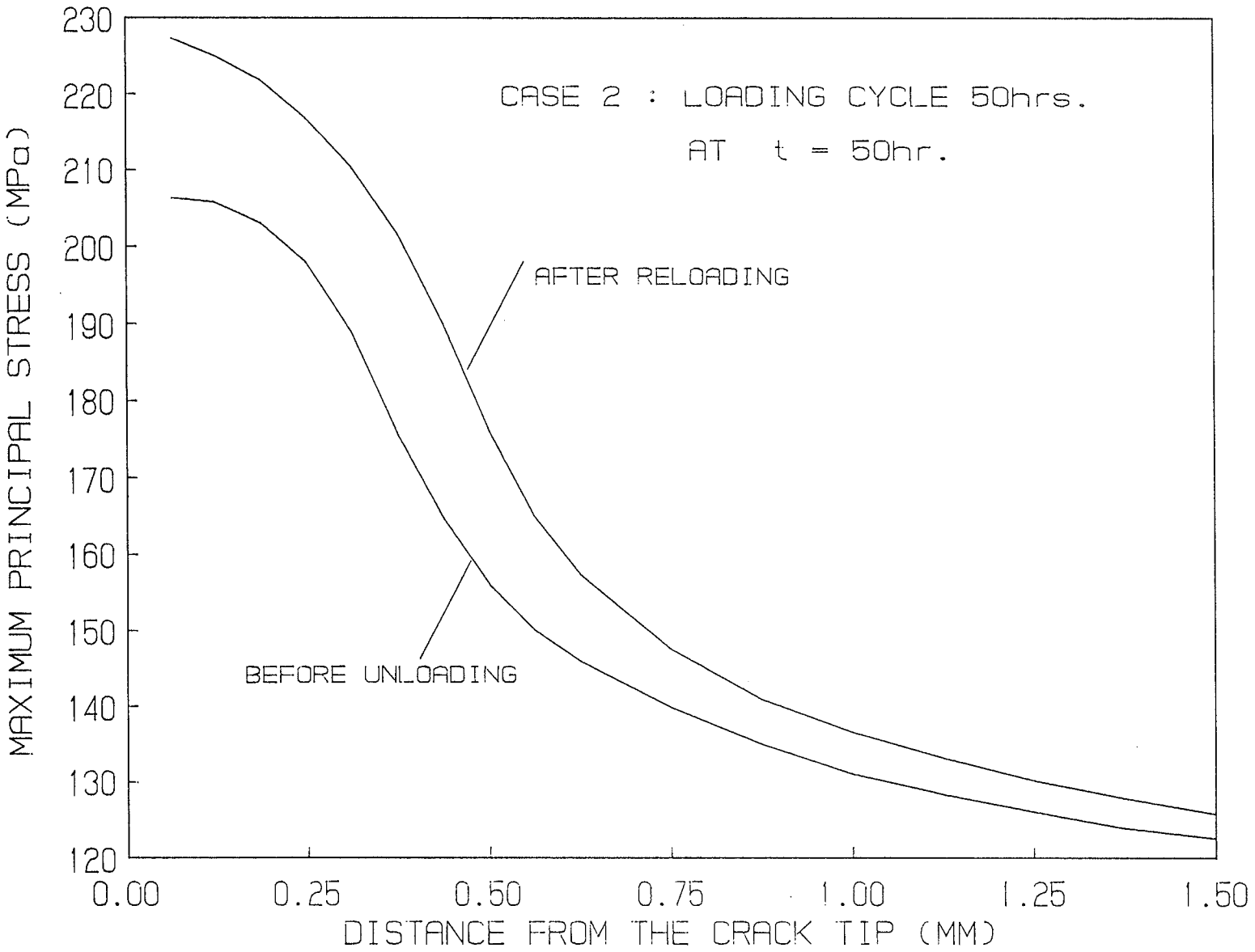

Figure 7.9 Increase of maximum principal stress ahead of crack tip after unloading and reloading (case 2)

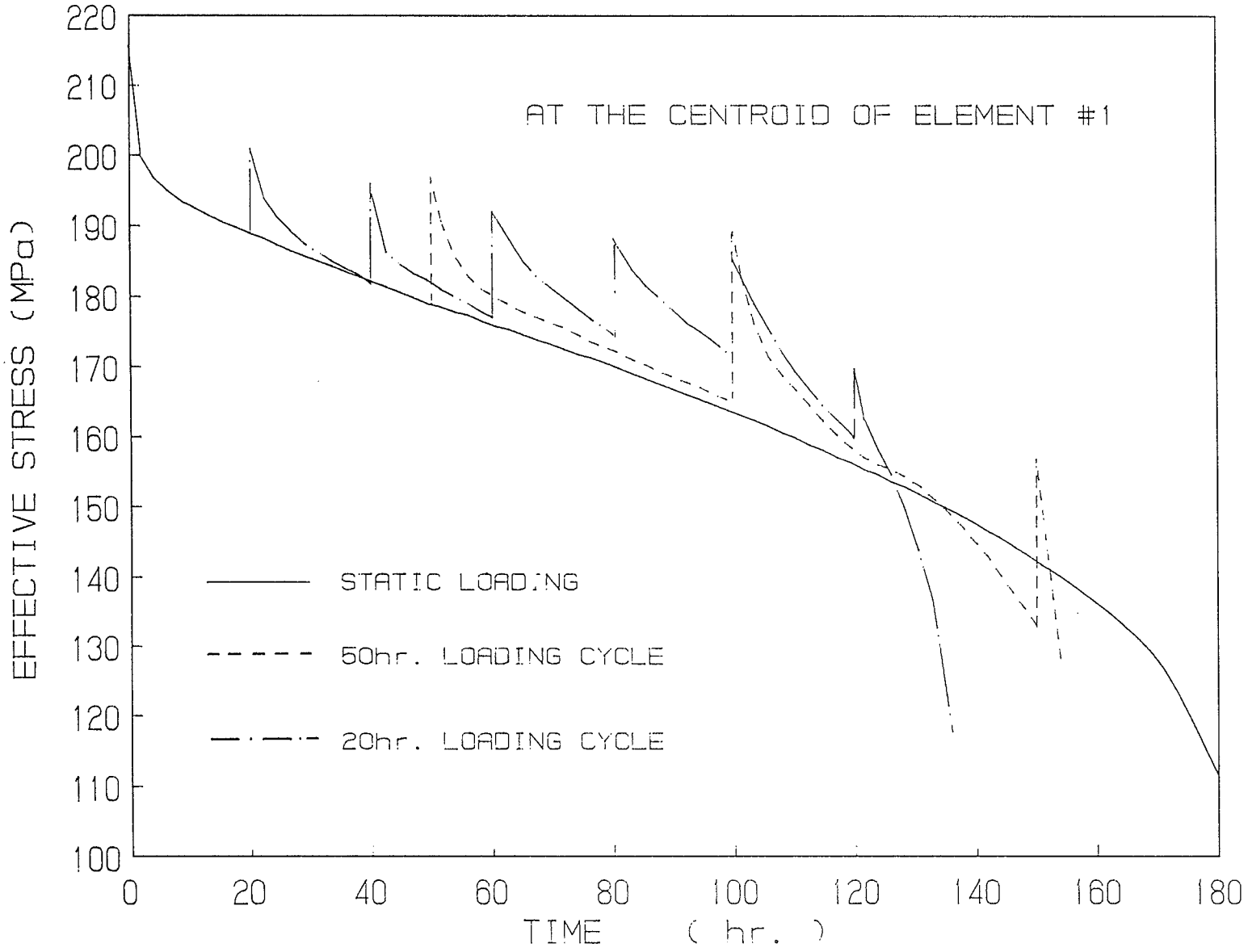

Figure 7.10 Variations of effective stress with time in crack tip element

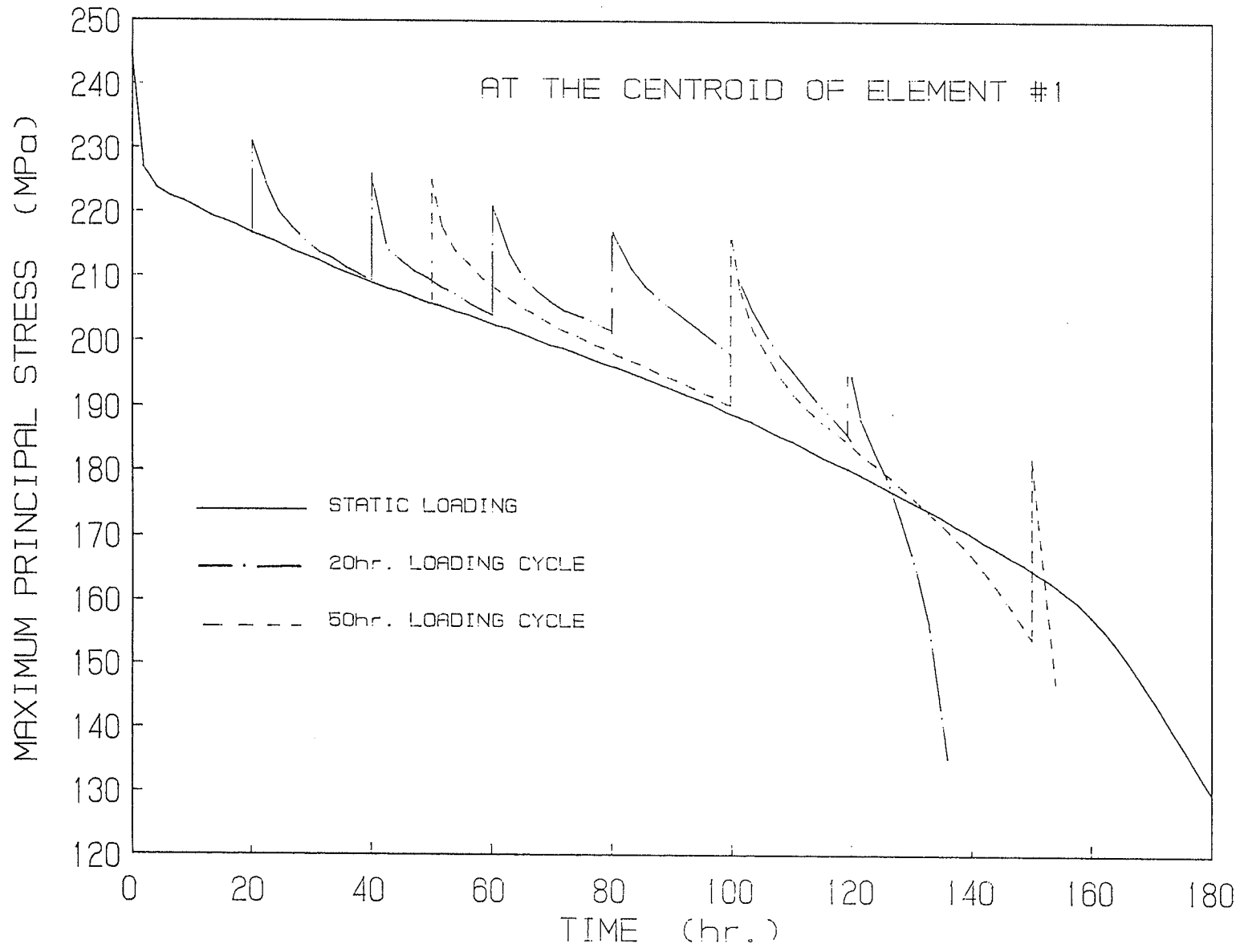

Figure 7.11 Variations of maximum principal stress with time in crack tip element

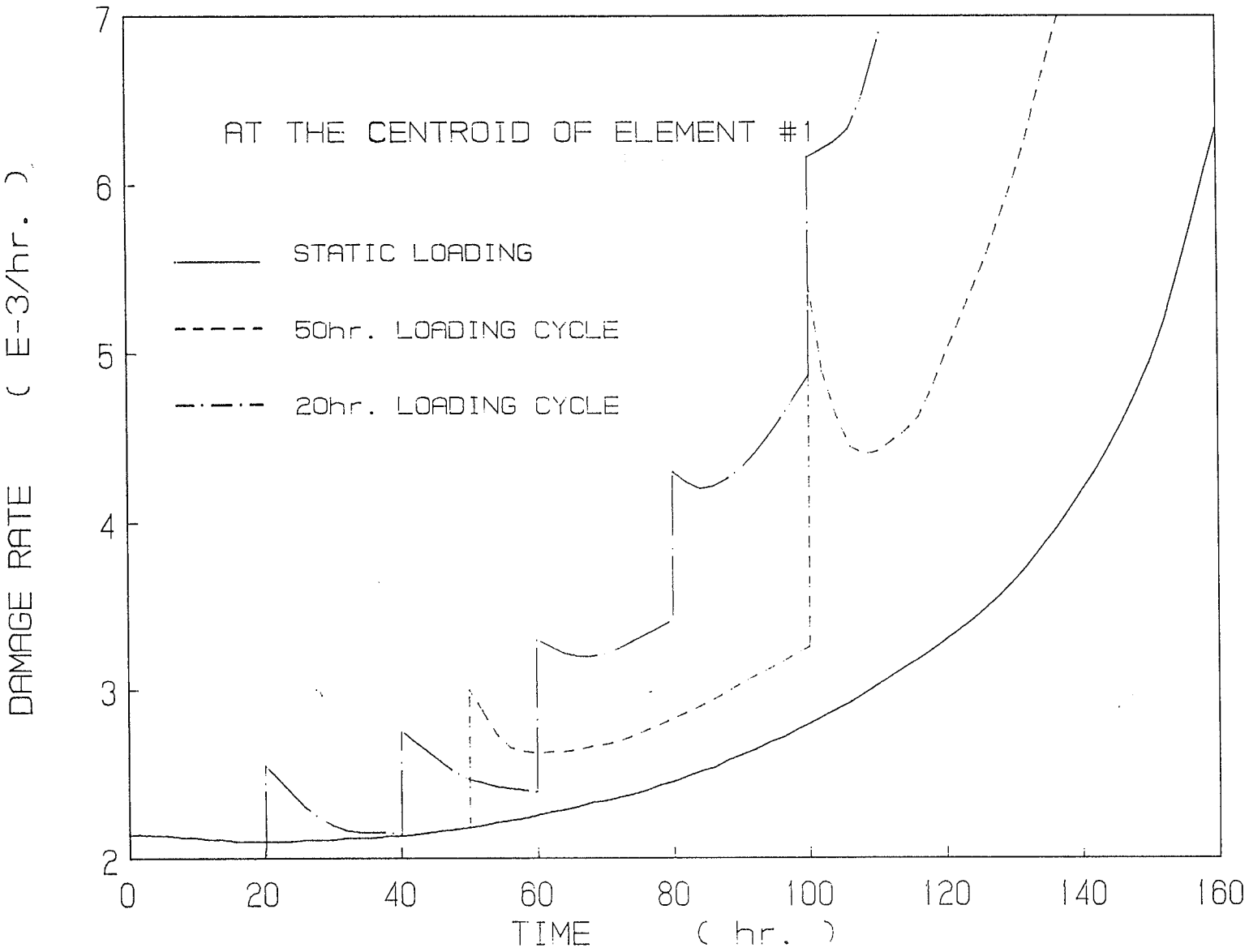

Figure 7.12 Variations of damage rate with time in crack tip element

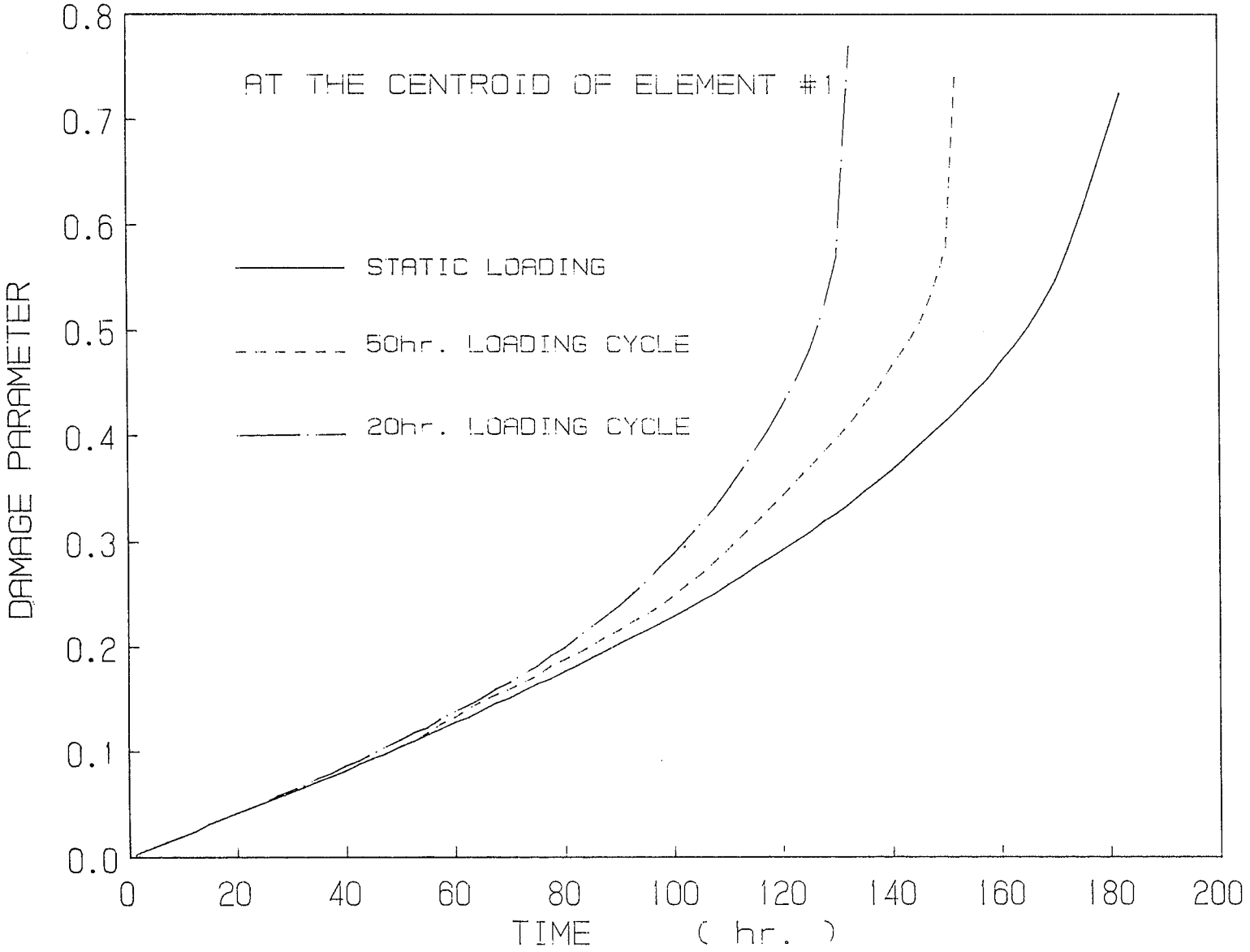

Figure 7.13 Damage evolutions in crack tip element

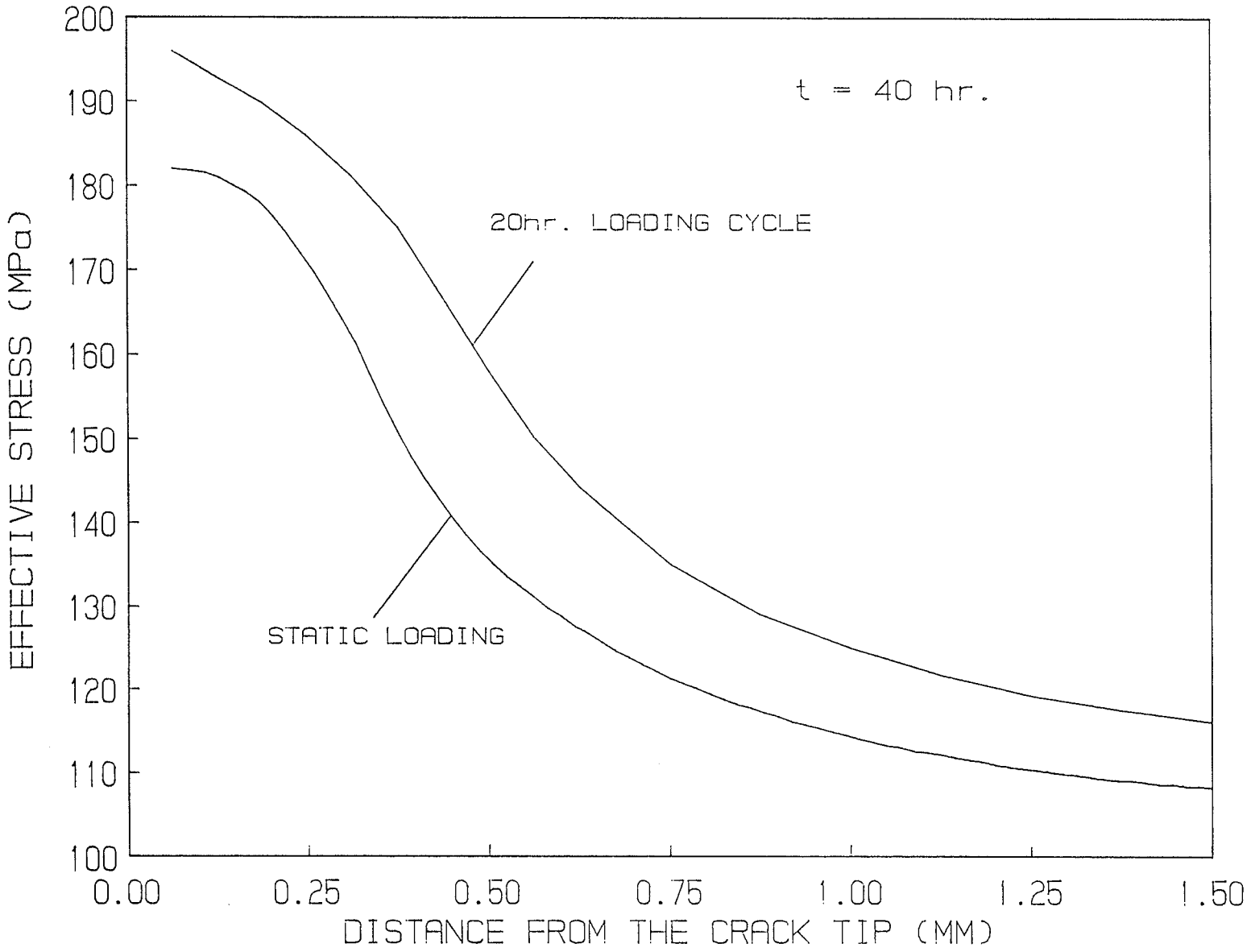

Figure 7.14 Distributions of effective stress ahead of crack tip at t = 40 hours

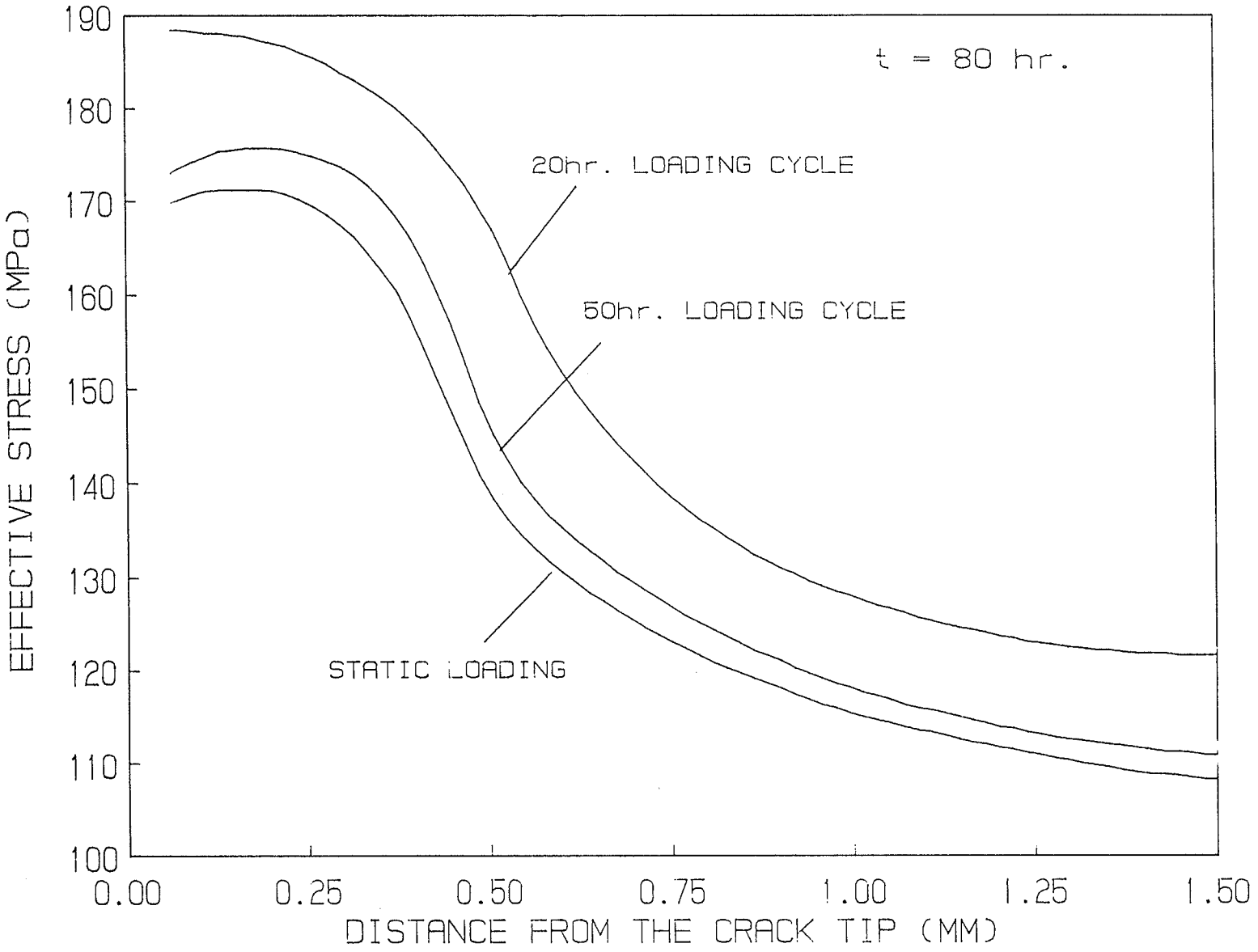

Figure 7.15 Distributions of effective stress ahead of crack tip at t = 80 hours

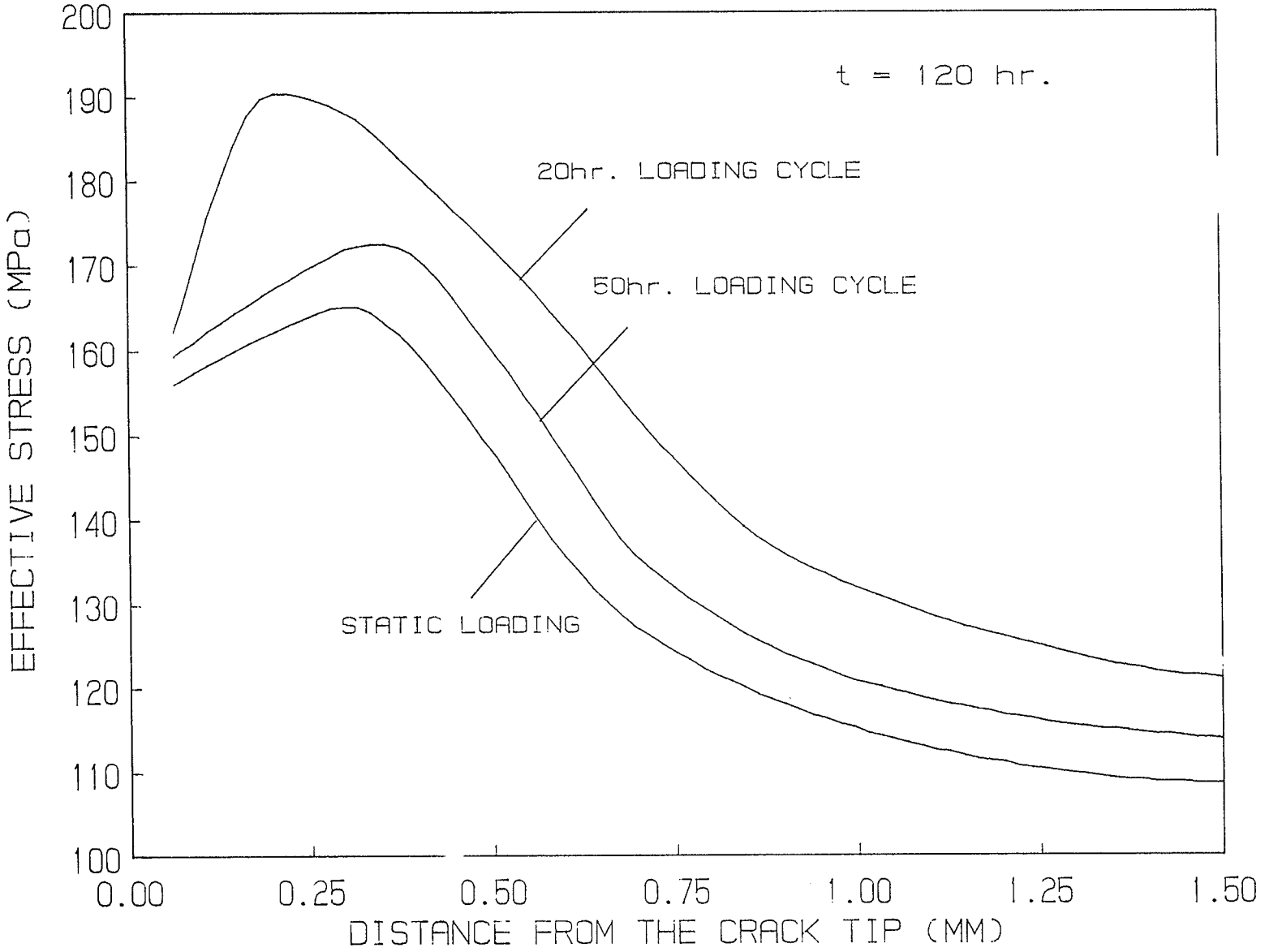

Figure 7.16 Distributions of effective stress ahead of crack tip at t = 120 hours

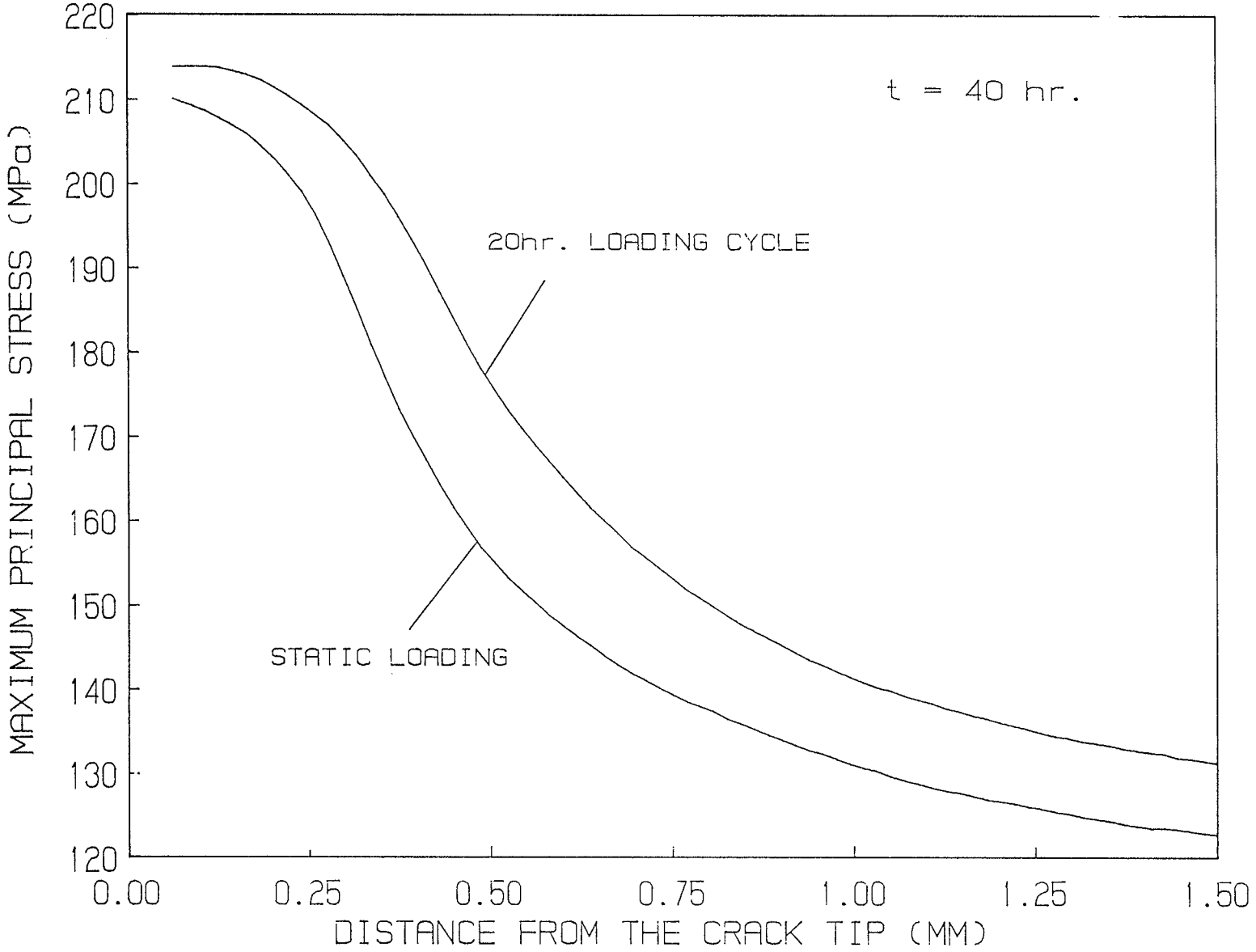

Figure 7.17 Distributions of maximum principal stress ahead of crack tip at t = 40 hours

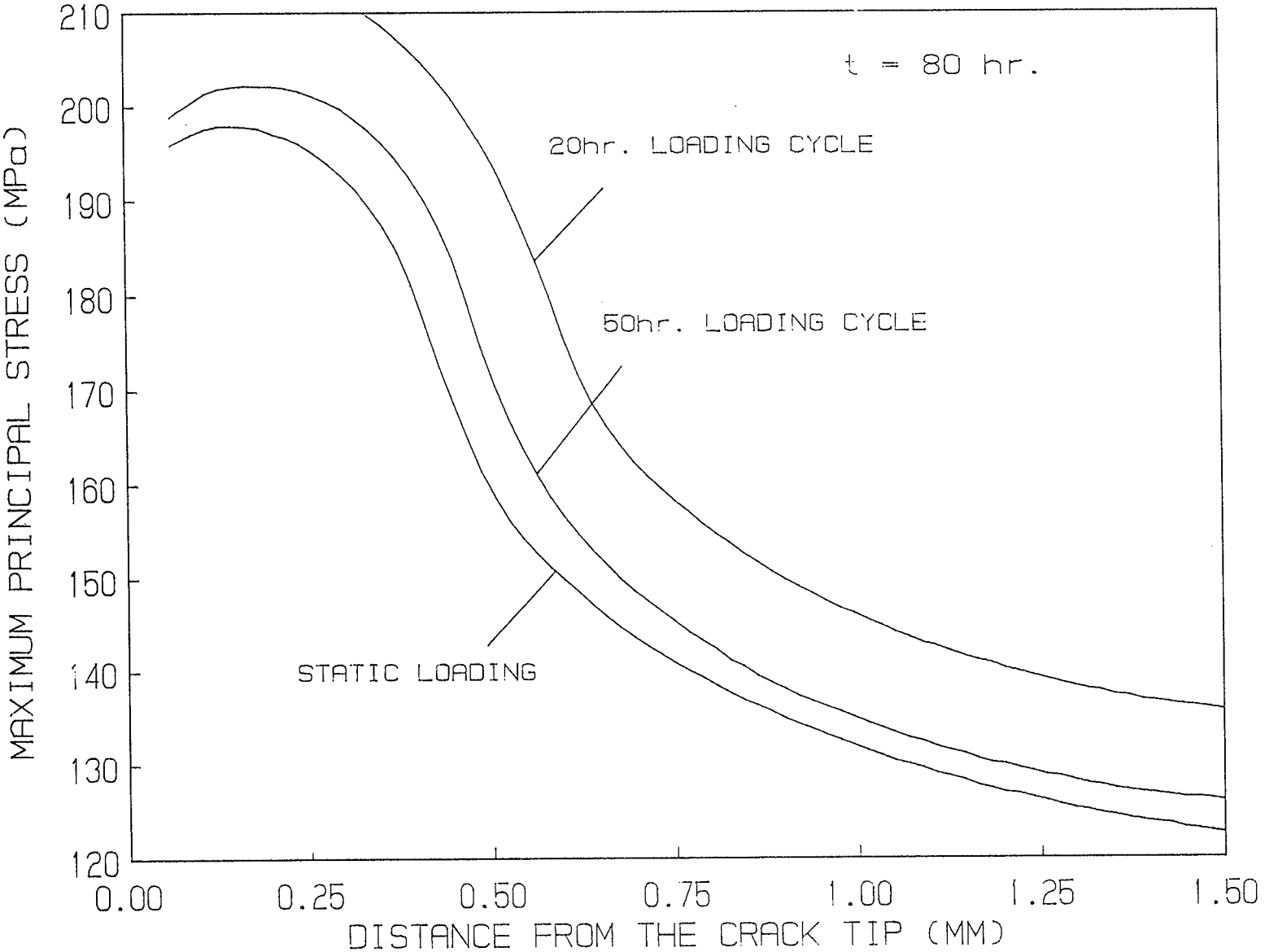

Figure 7.18 Distributions of maximum principal stress ahead of crack tip at t = 80 hours

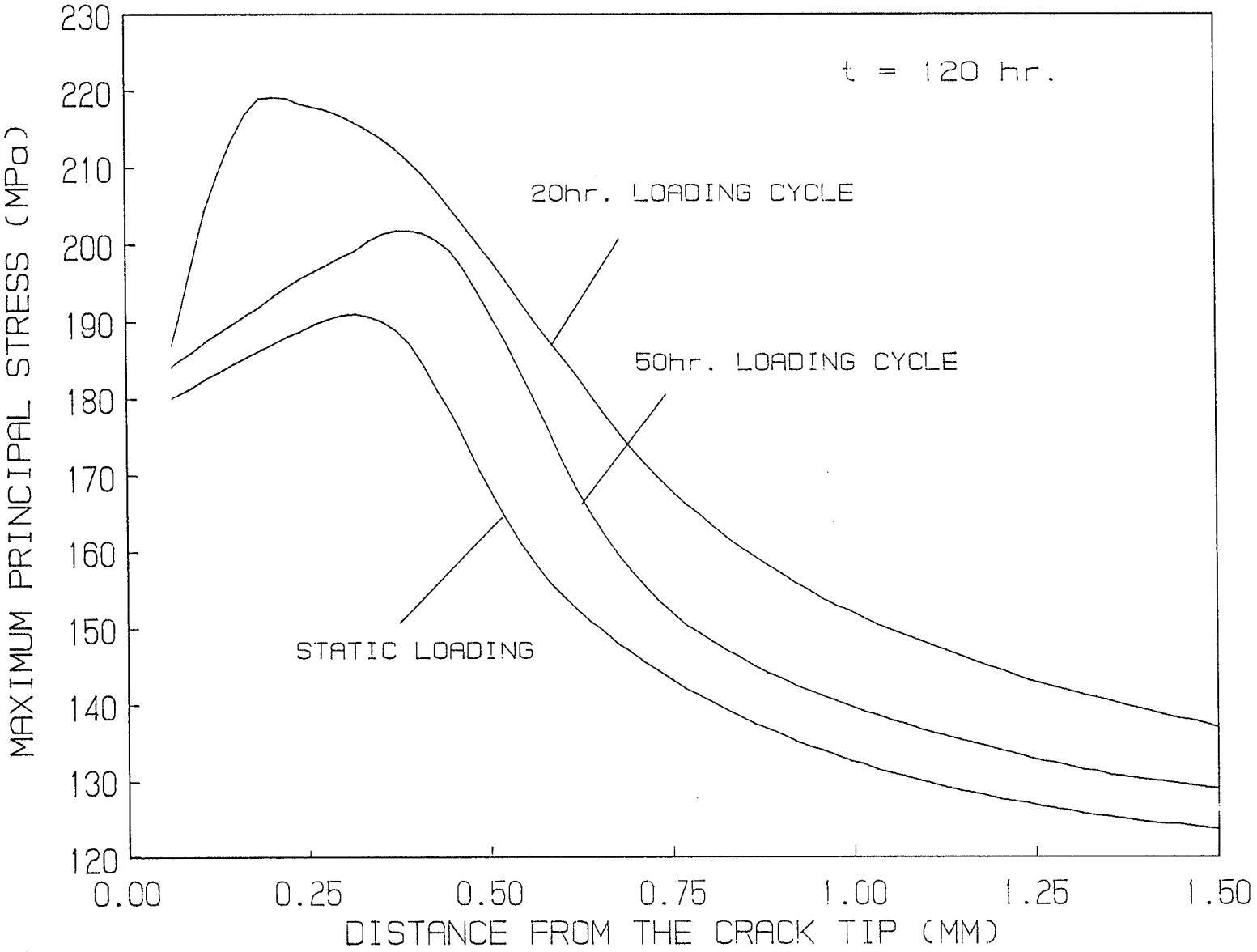

Figure 7.19 Distributions of maximum principal stress ahead of crack tip at t = 120 hours

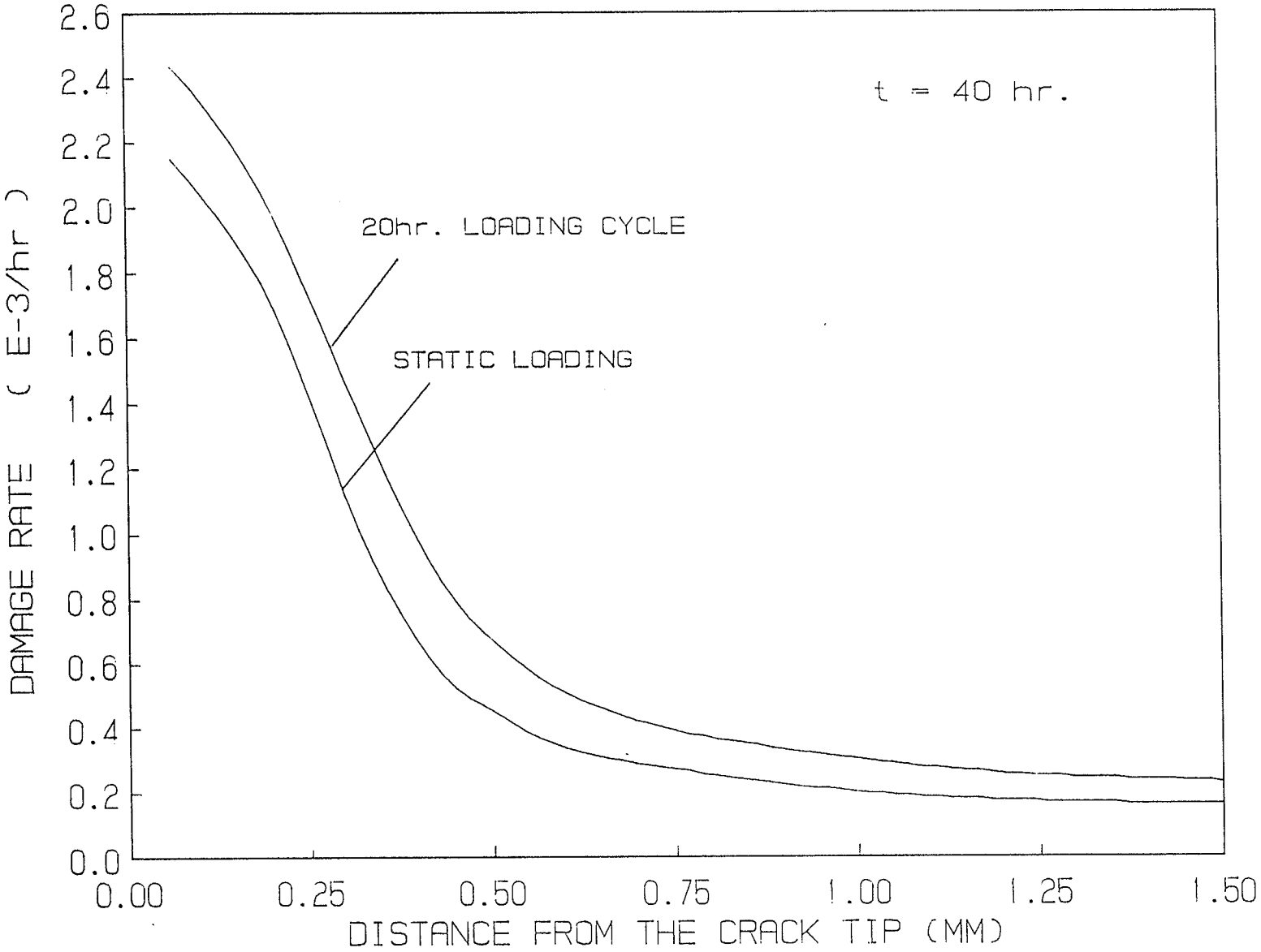

Figure 7.20 Distributions of damage rate ahead of crack tip at t = 40 hours

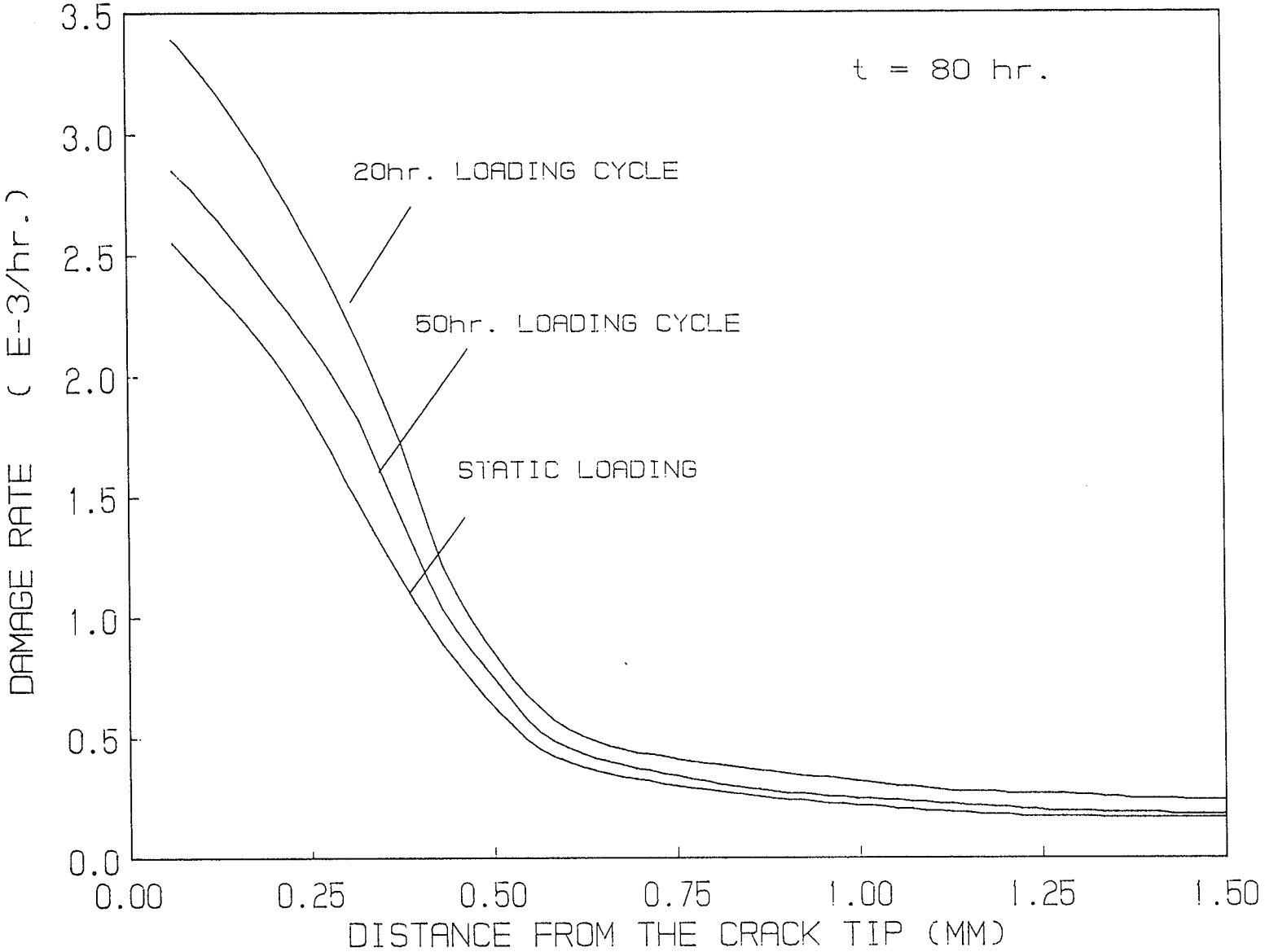

Figure 7.21 Distributions of damage rate ahead of crack tip at t = 80 hours

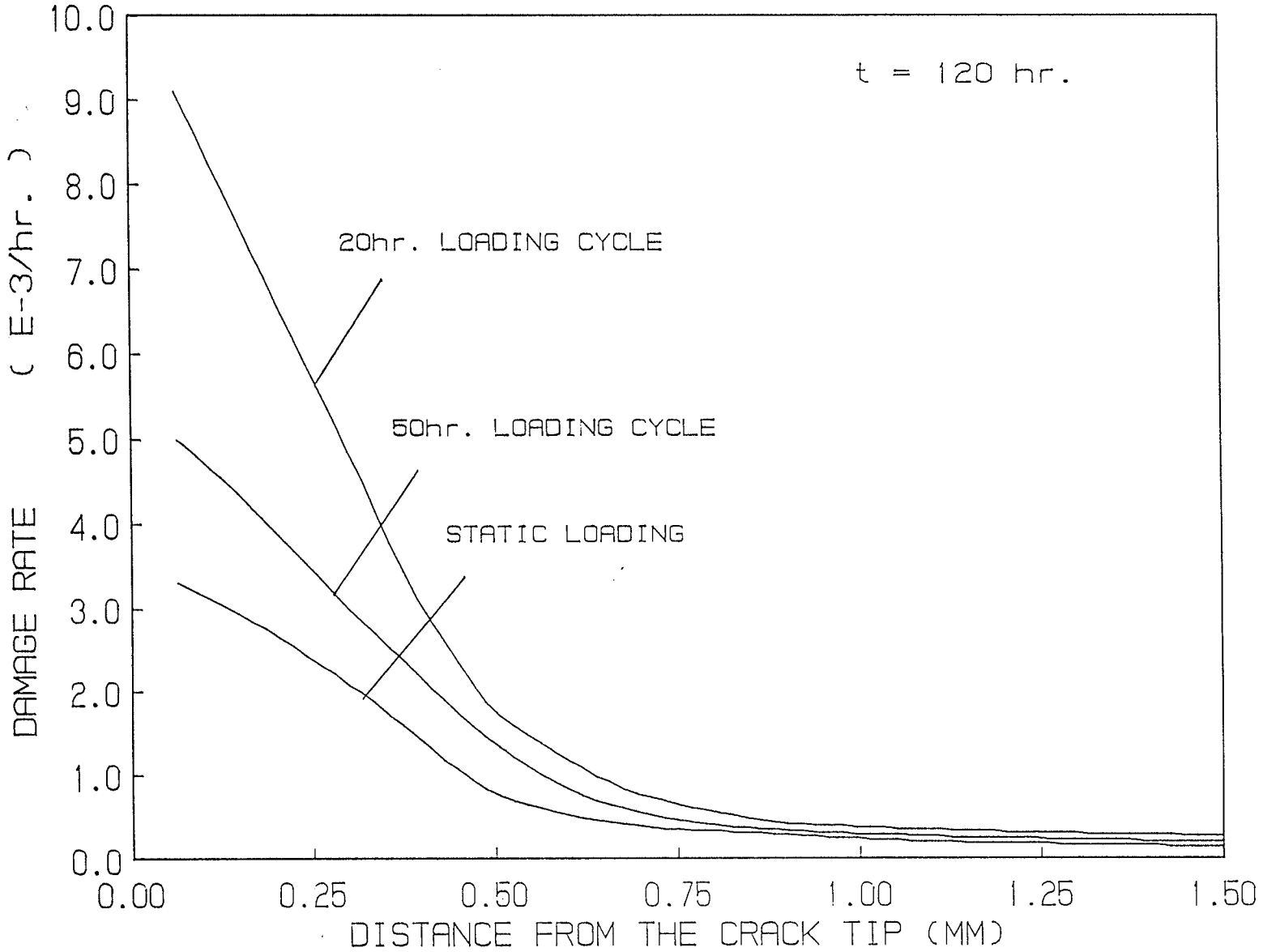

Figure 7.22 Distributions of damage rate ahead of crack tip at t = 120 hours

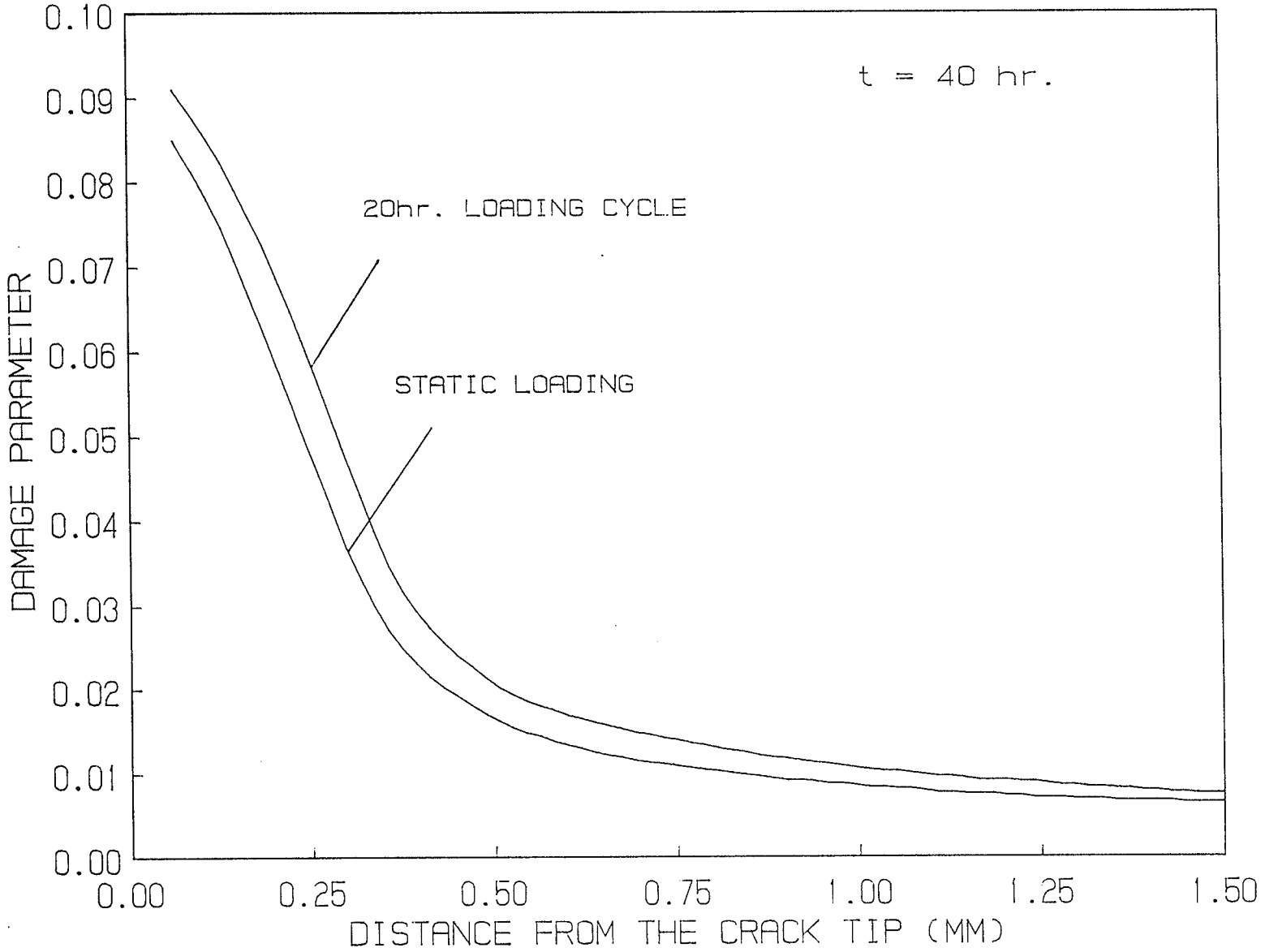

Figure 7.23 Damage distributions ahead of crack tip at t = 40 hours

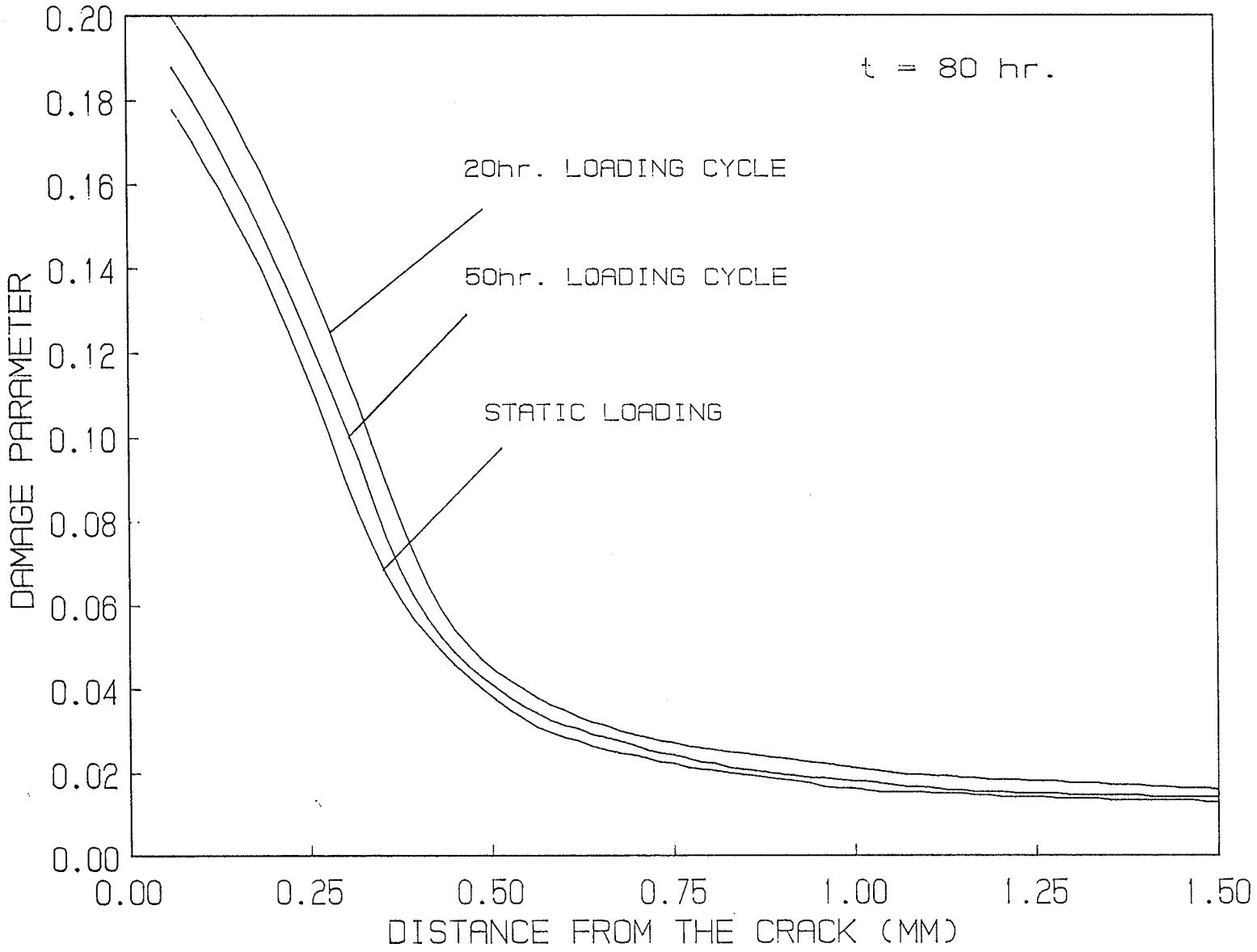

Figure 7.24 Damage distributions ahead of crack tip at t = 80 hours

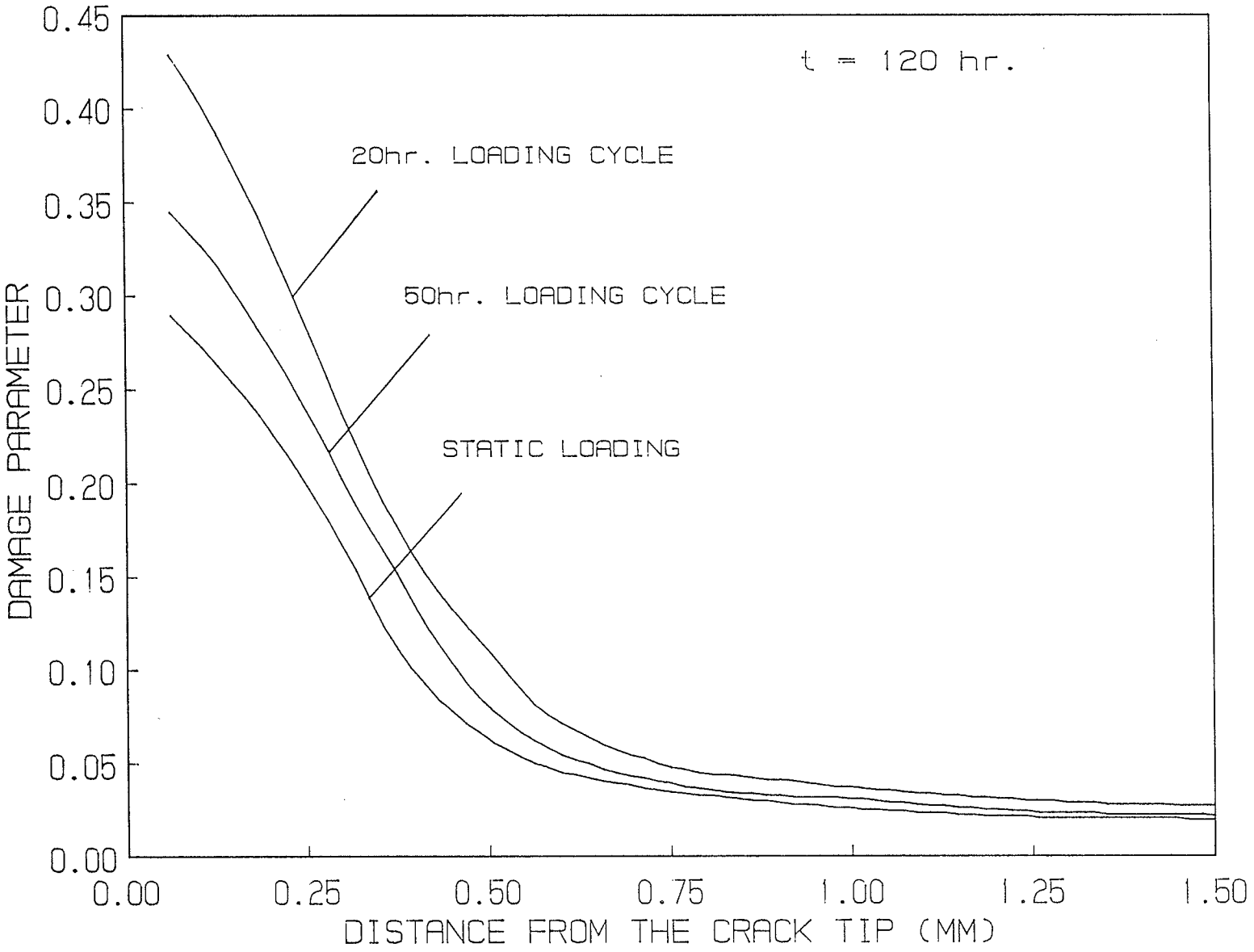

Figure 7.25 Damage distributions ahead of crack tip at t = 120 hours

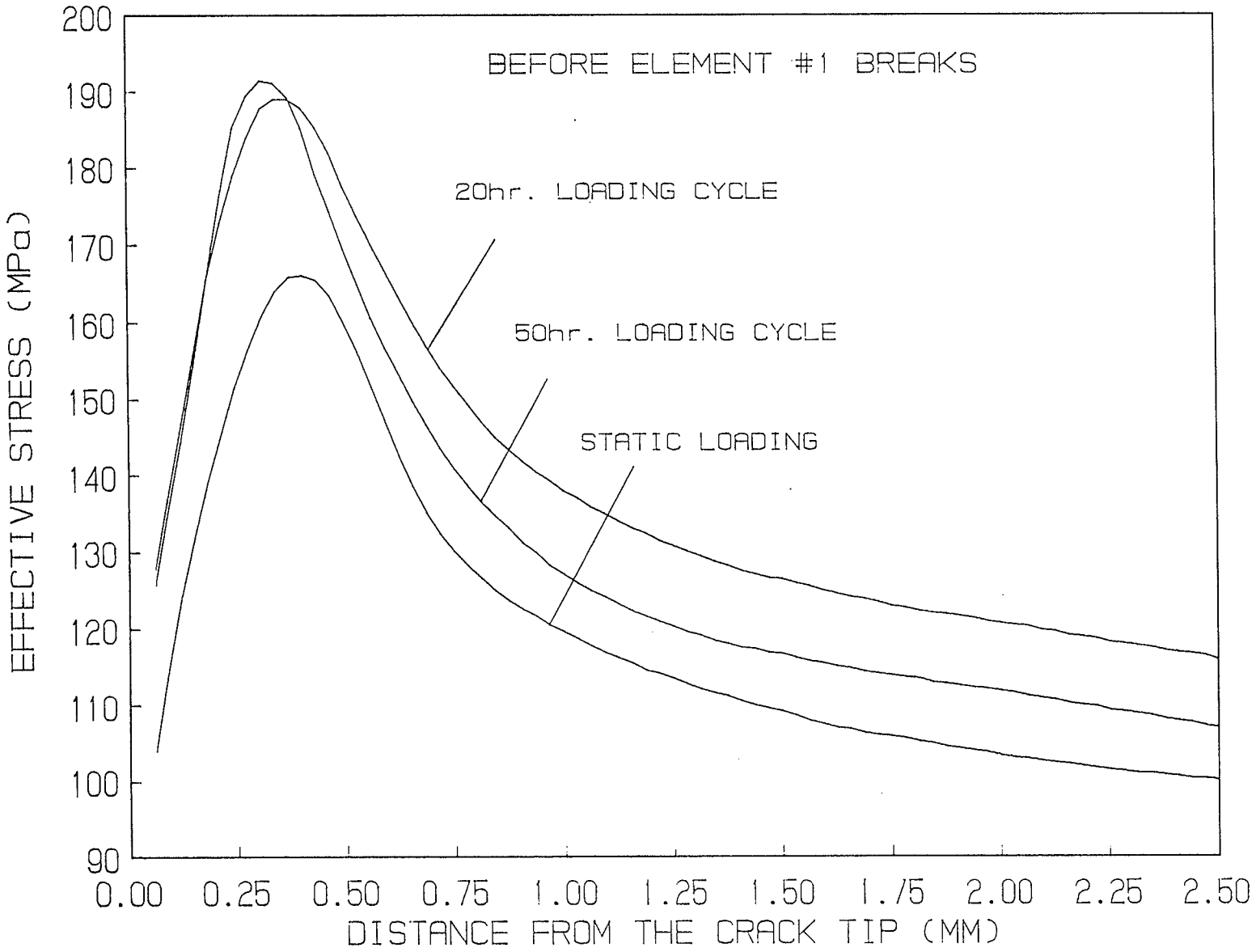

Figure 7.26 Distributions of effective stress ahead of crack tip before element #1 breaks

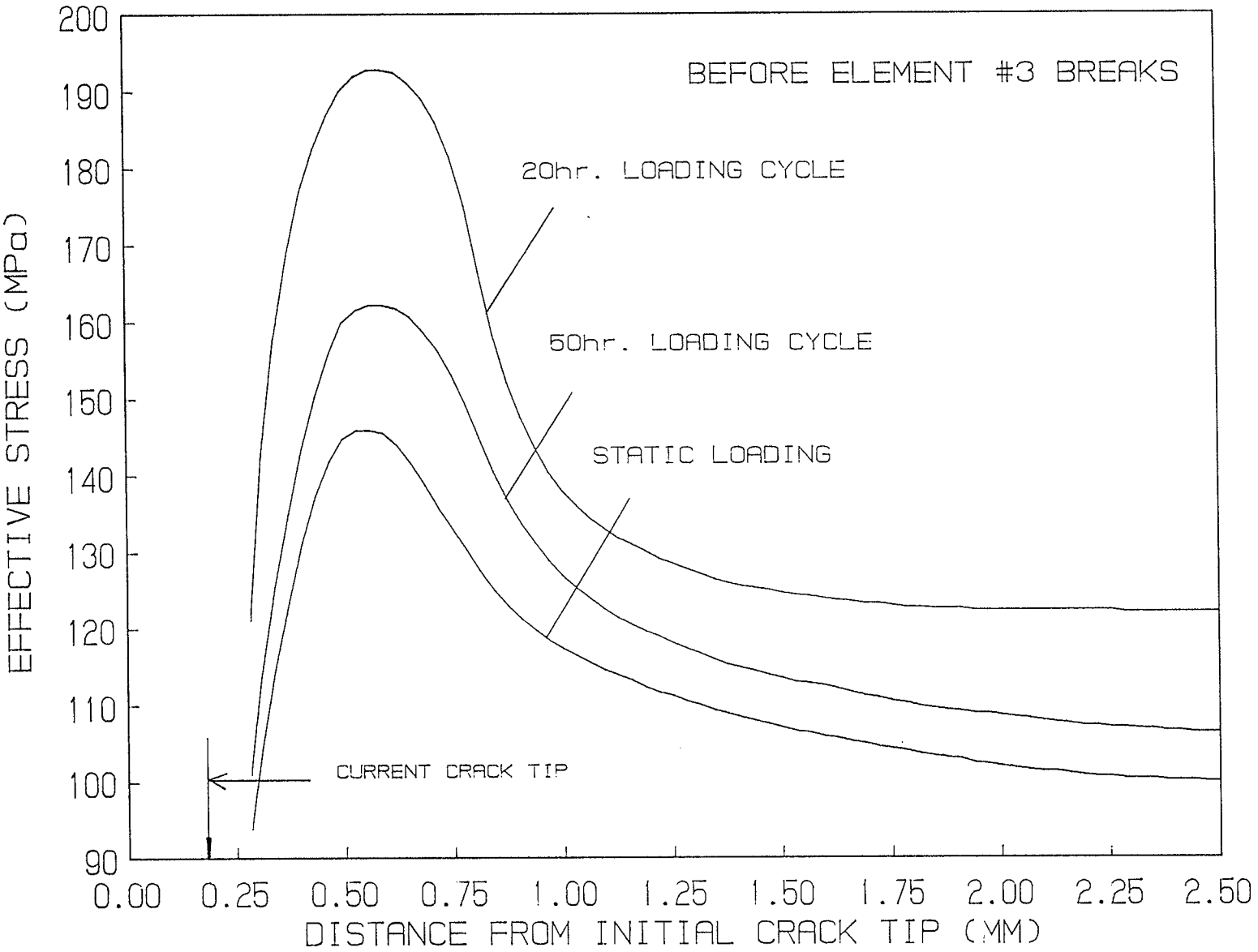

Figure 7.27 Distributions of effective stress ahead of crack tip before element #3 breaks

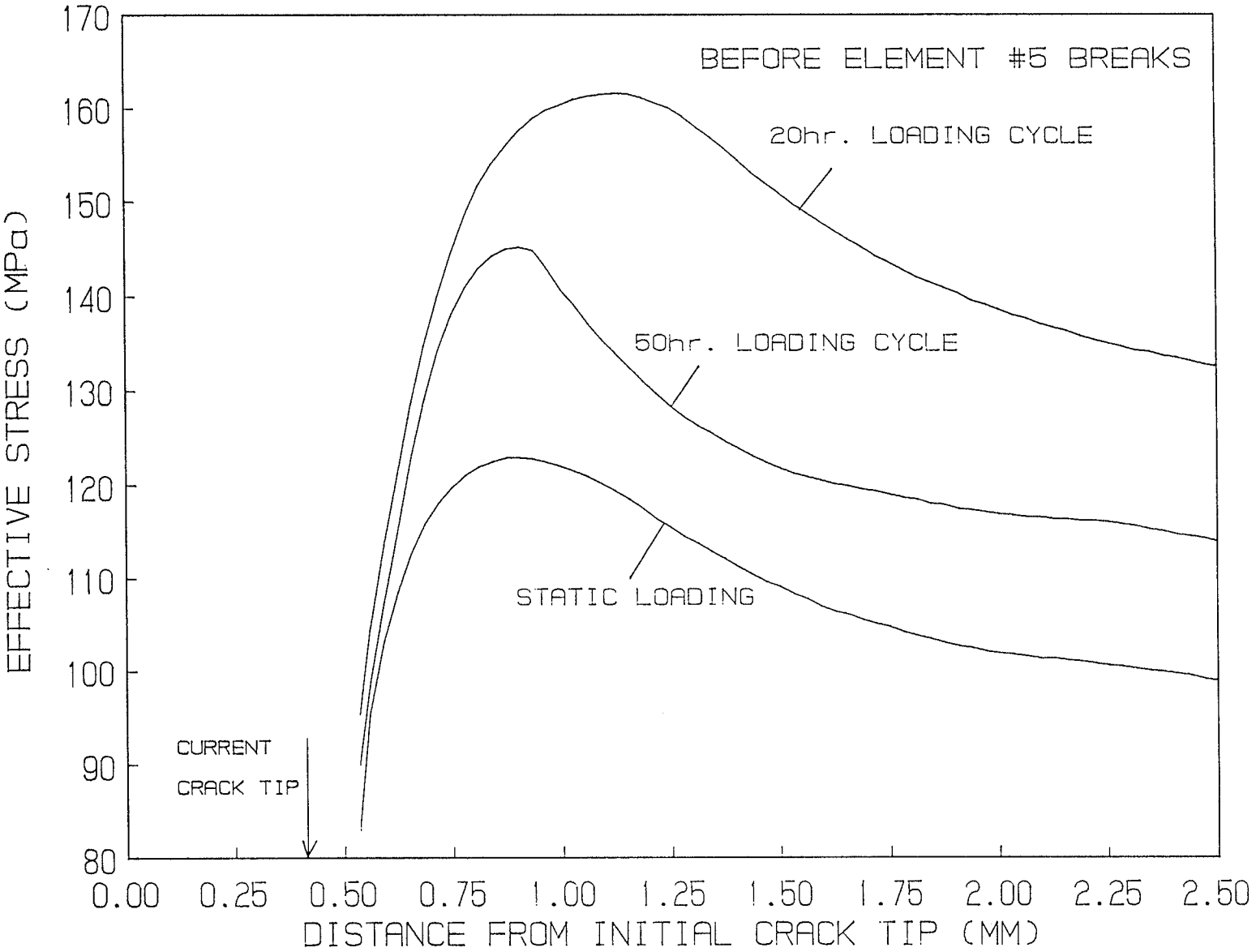

Figure 7.28 Distributions of effective stress ahead of crack tip before element #5 breaks

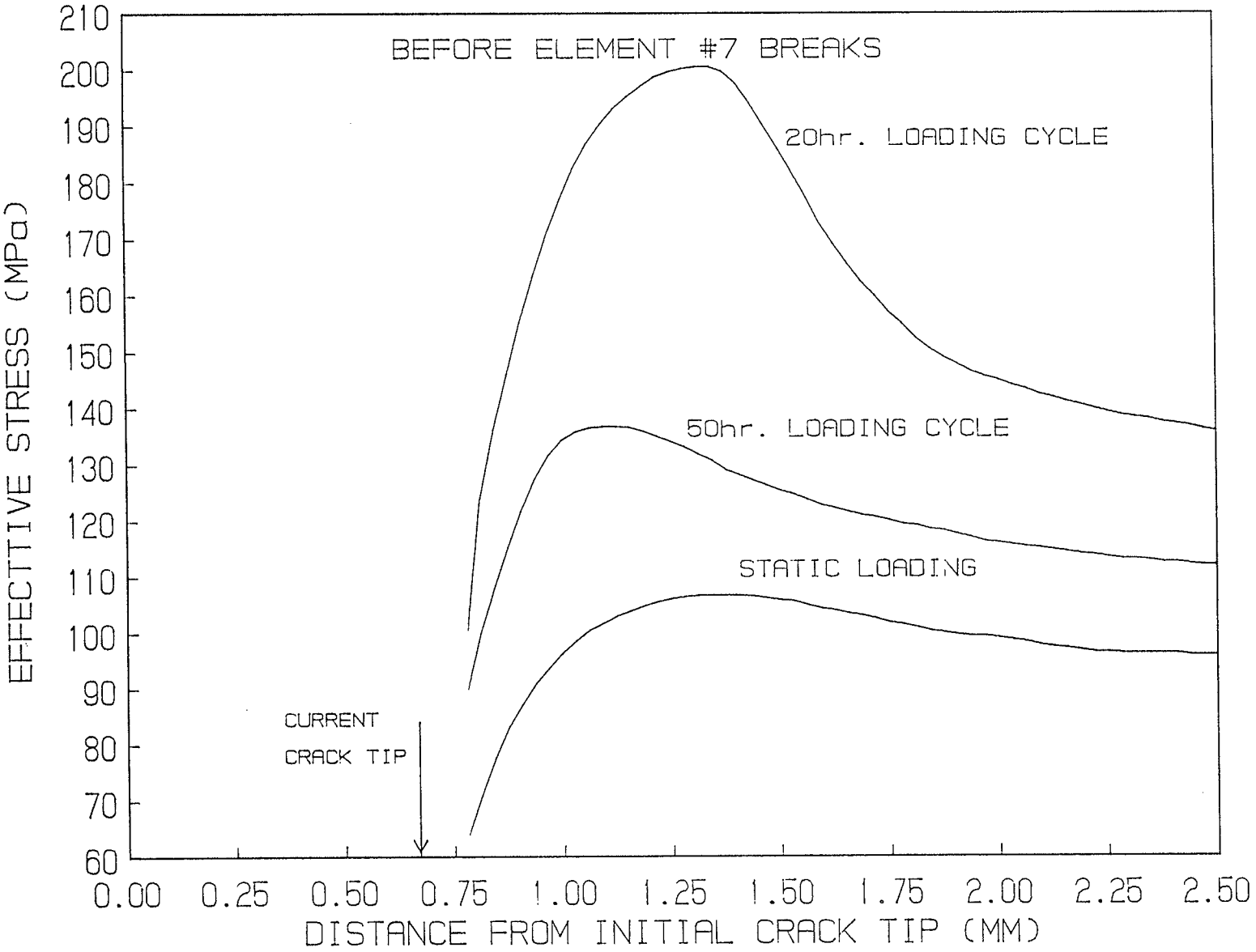

Figure 7.29 Distributions of effective stress ahead of crack tip before element #7 breaks

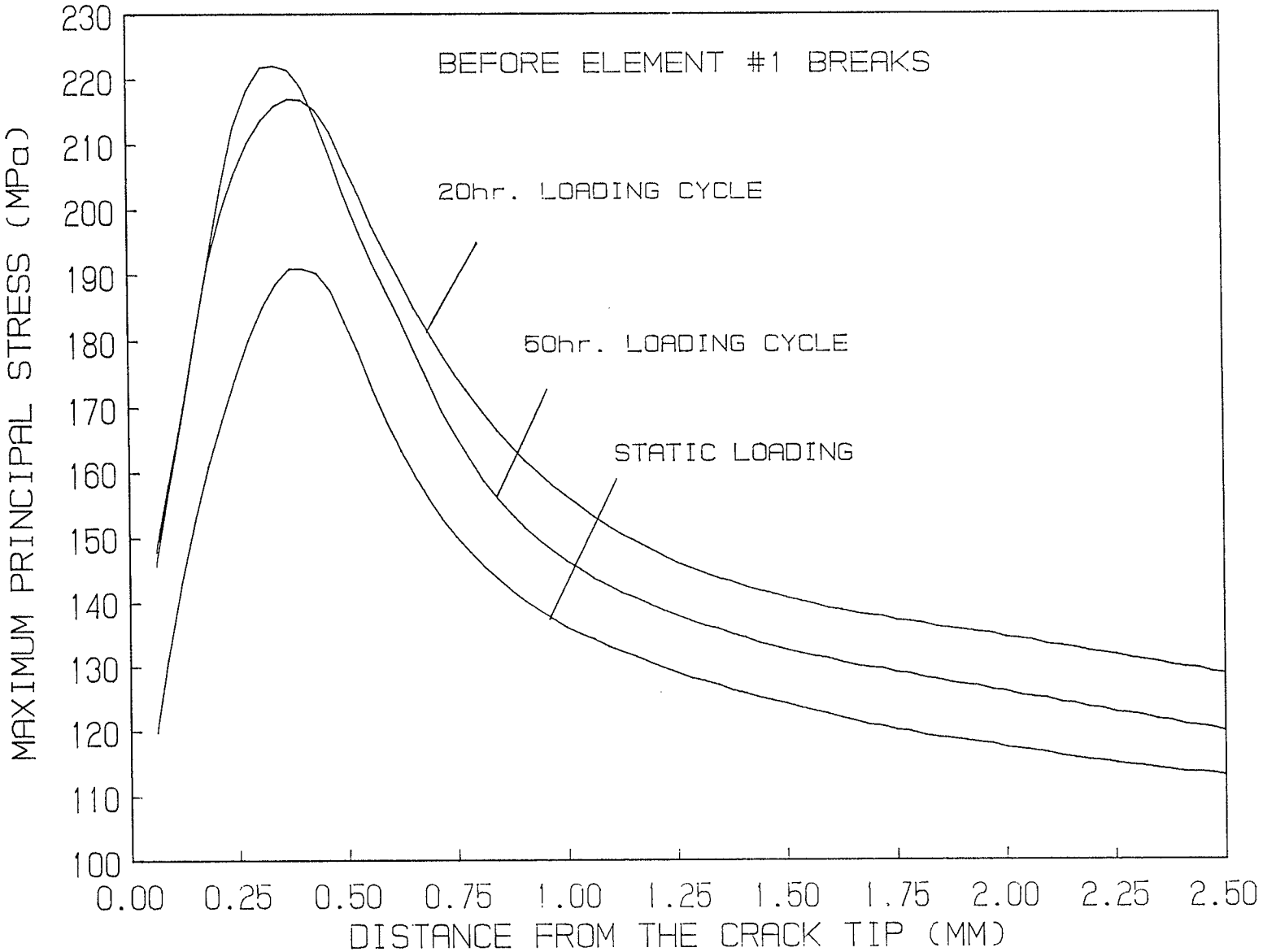

Figure 7.30 Distributions of maximum principal stress ahead of crack tip before element #1 breaks

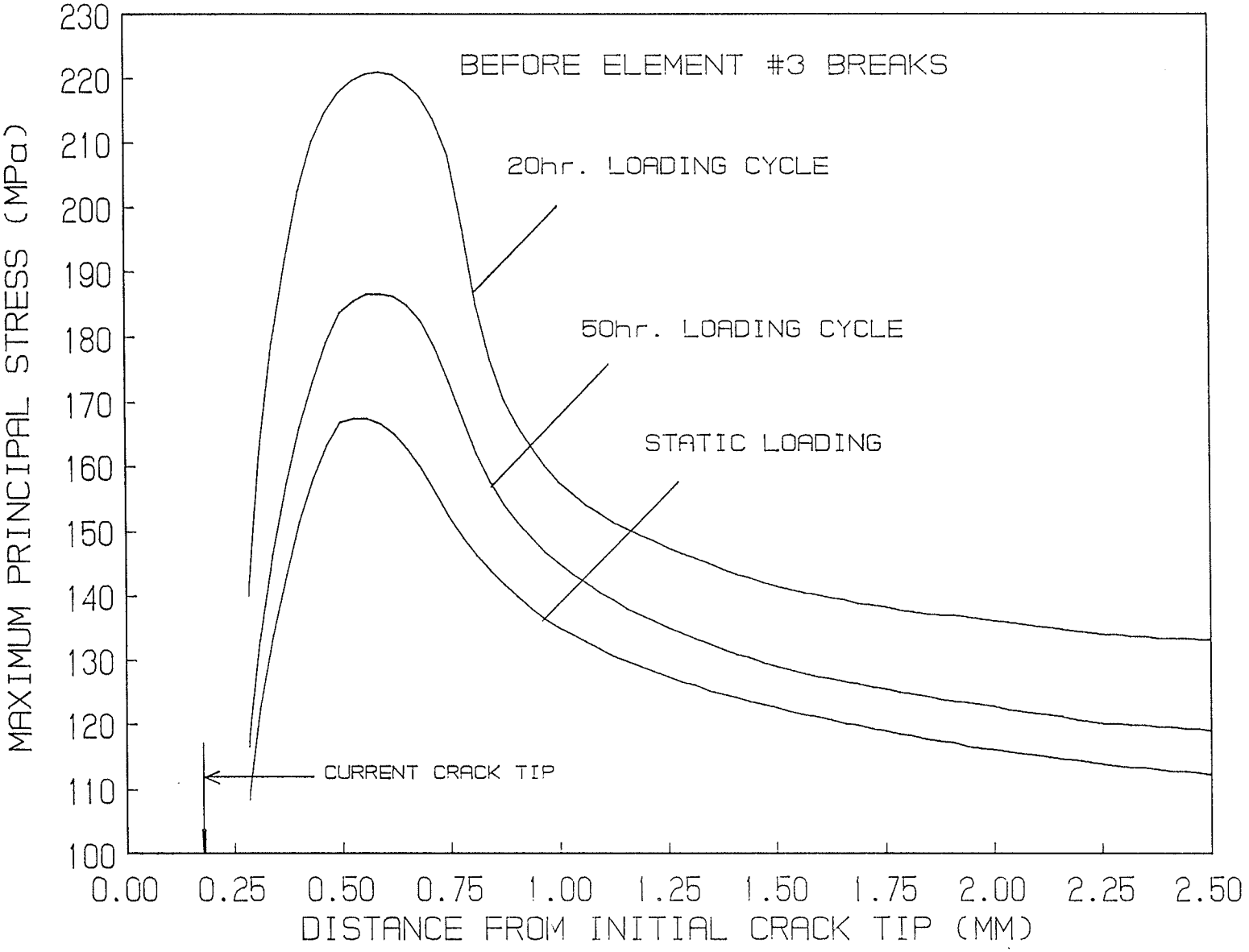

Figure 7.31 Distributions of maximum principal stress ahead of crack tip before element #3 breaks

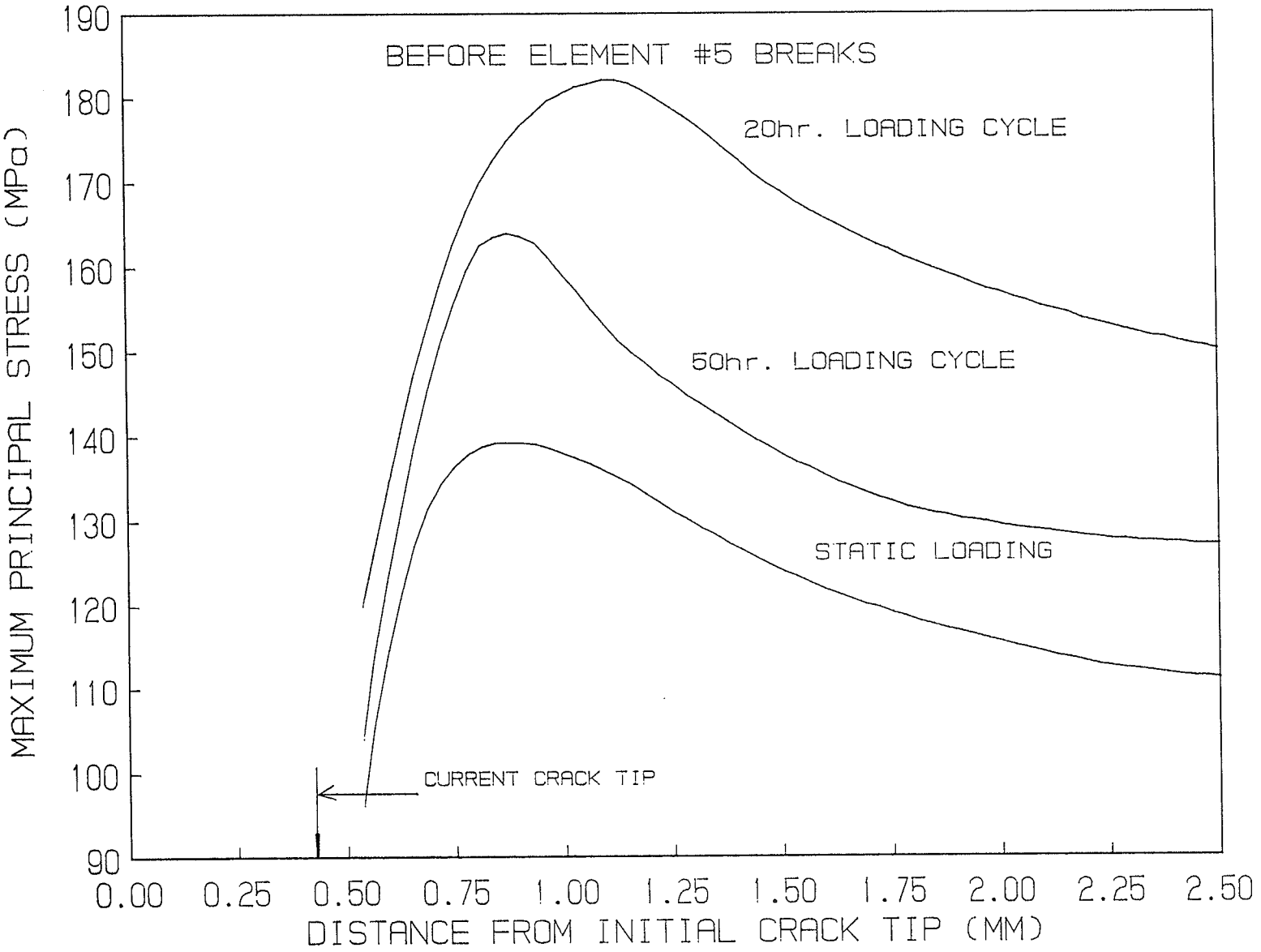

Figure 7.32 Distributions of maximum principal stress ahead of crack tip before element #5 breaks

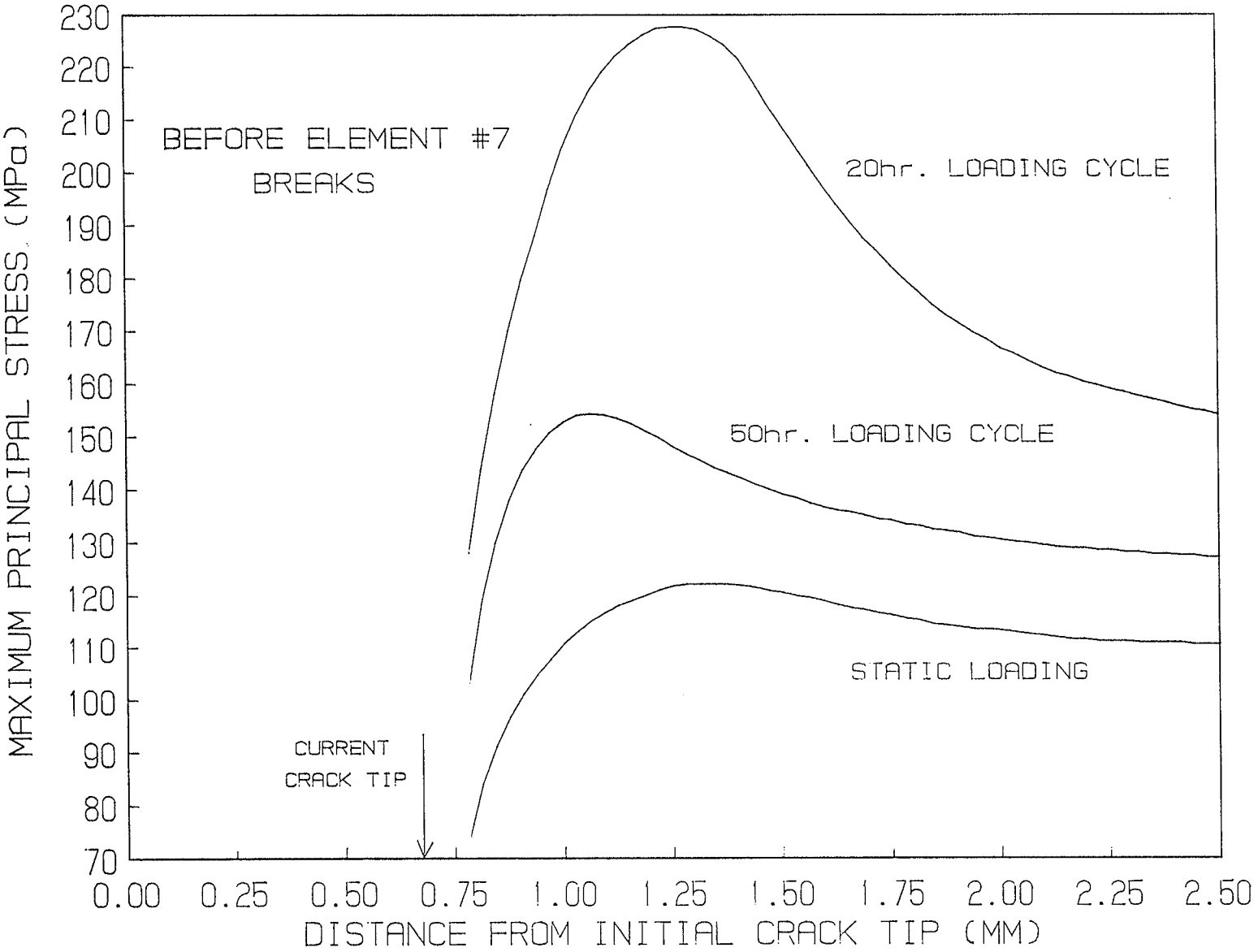

Figure 7.33 Distributions of maximum principal stress ahead of crack tip before element #7 breaks

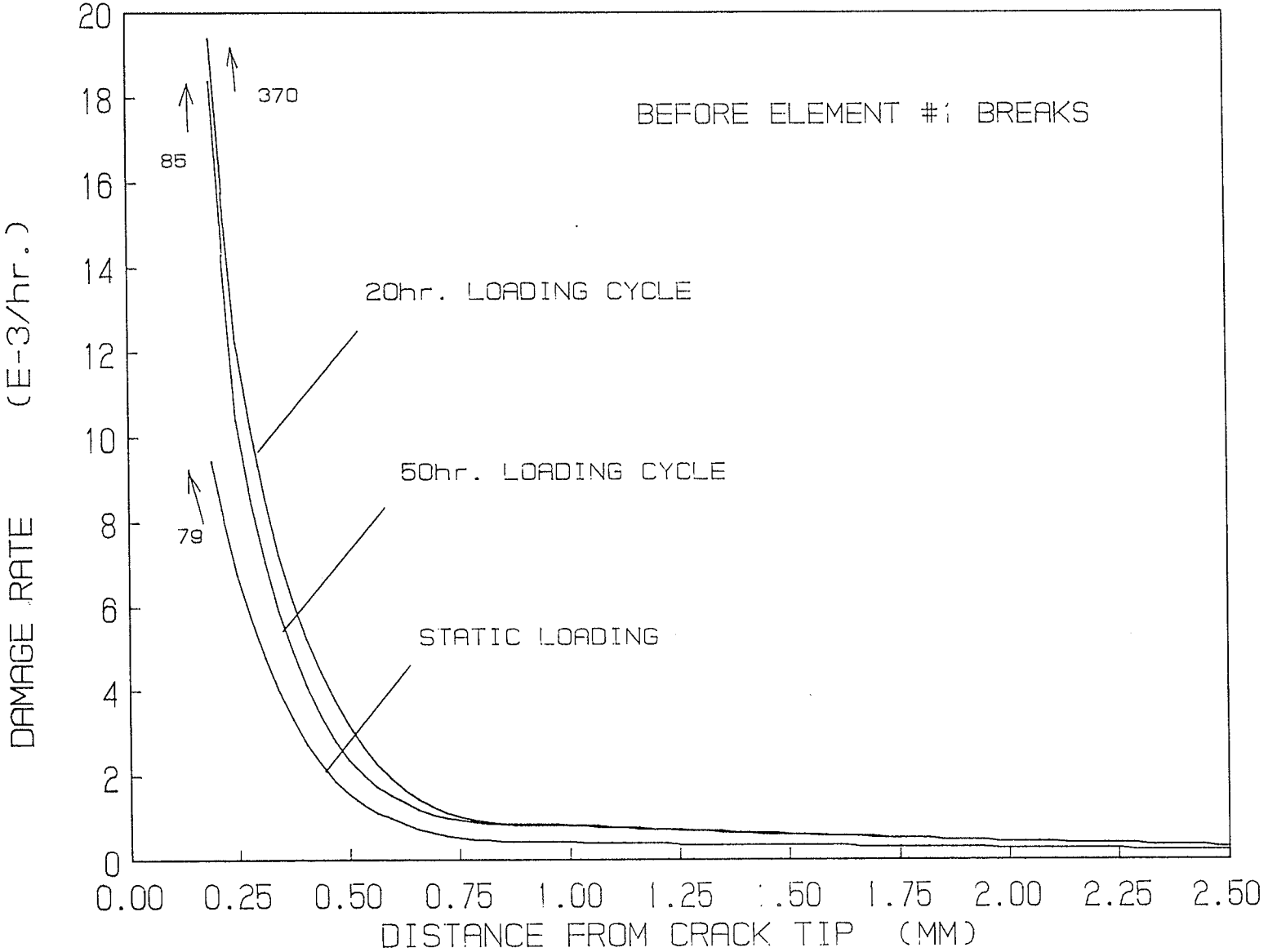

Figure 7.34 Distributions of damage rate ahead of crack tip before element #1 breaks

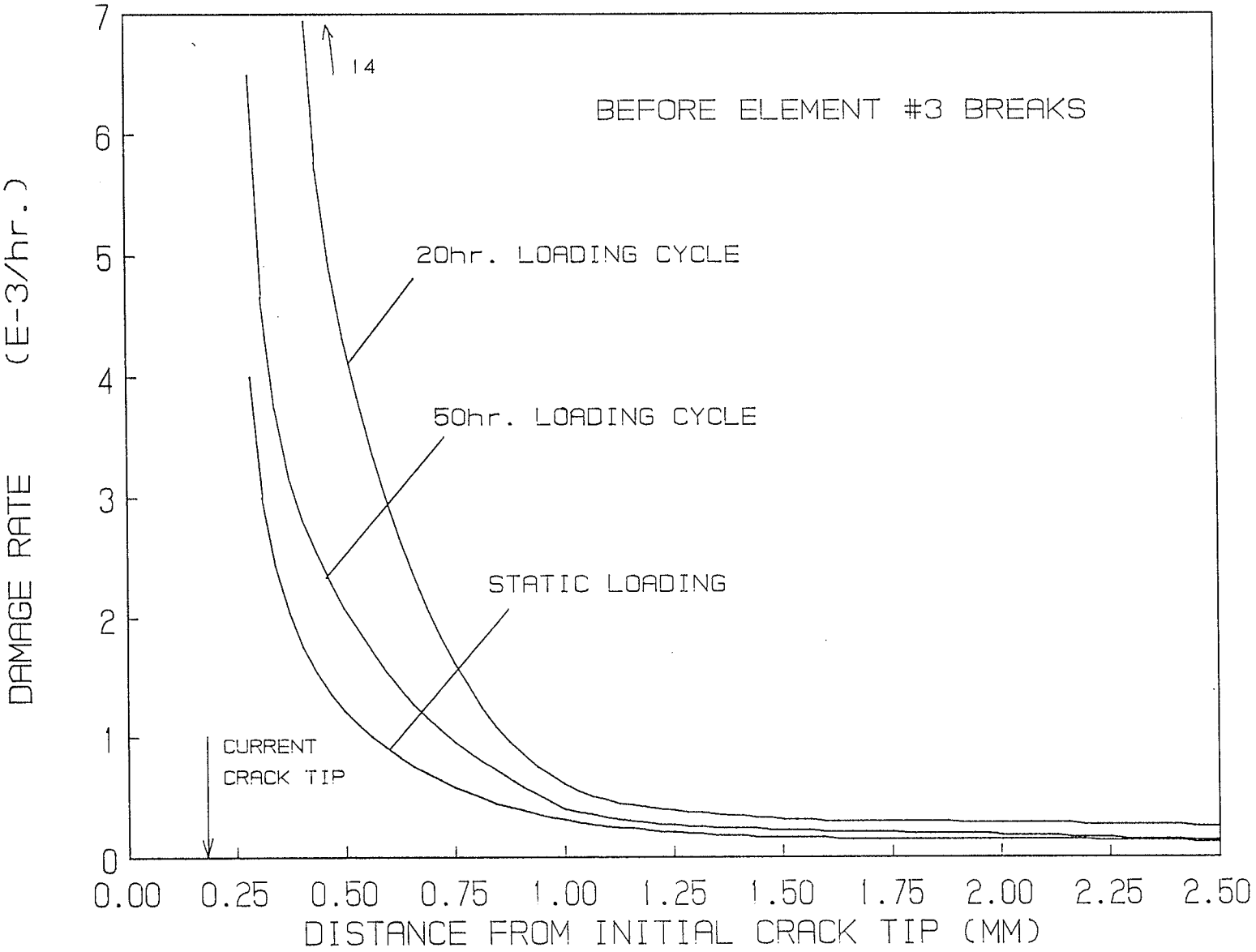

Figure 7.35 Distributions of damage rate ahead of crack tip before element #3 breaks

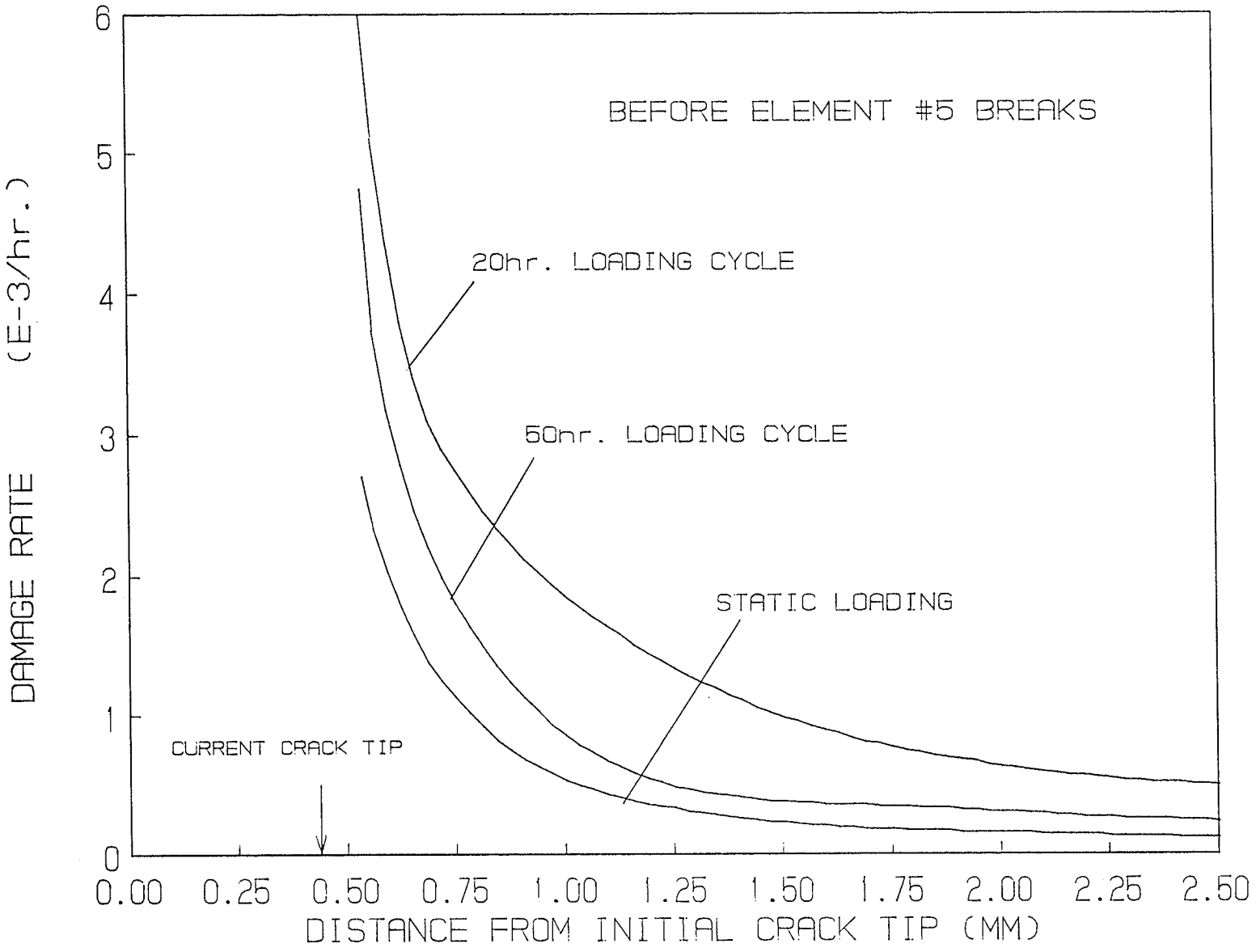

Figure 7.36 Distributions of damage rate ahead of crack tip before element #5 breaks

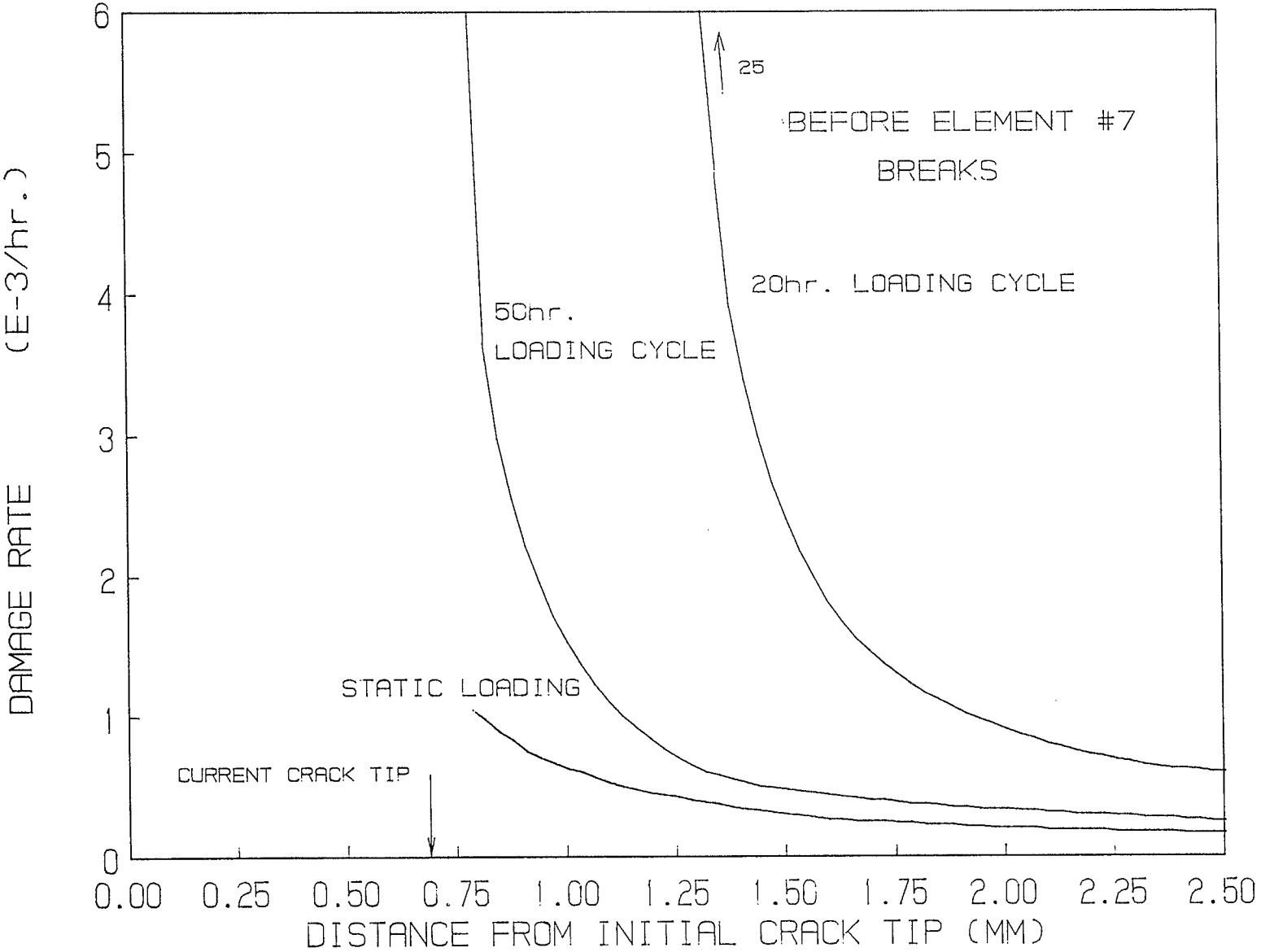

Figure 7.37 Distributions of damage rate ahead of crack tip before element #7 breaks

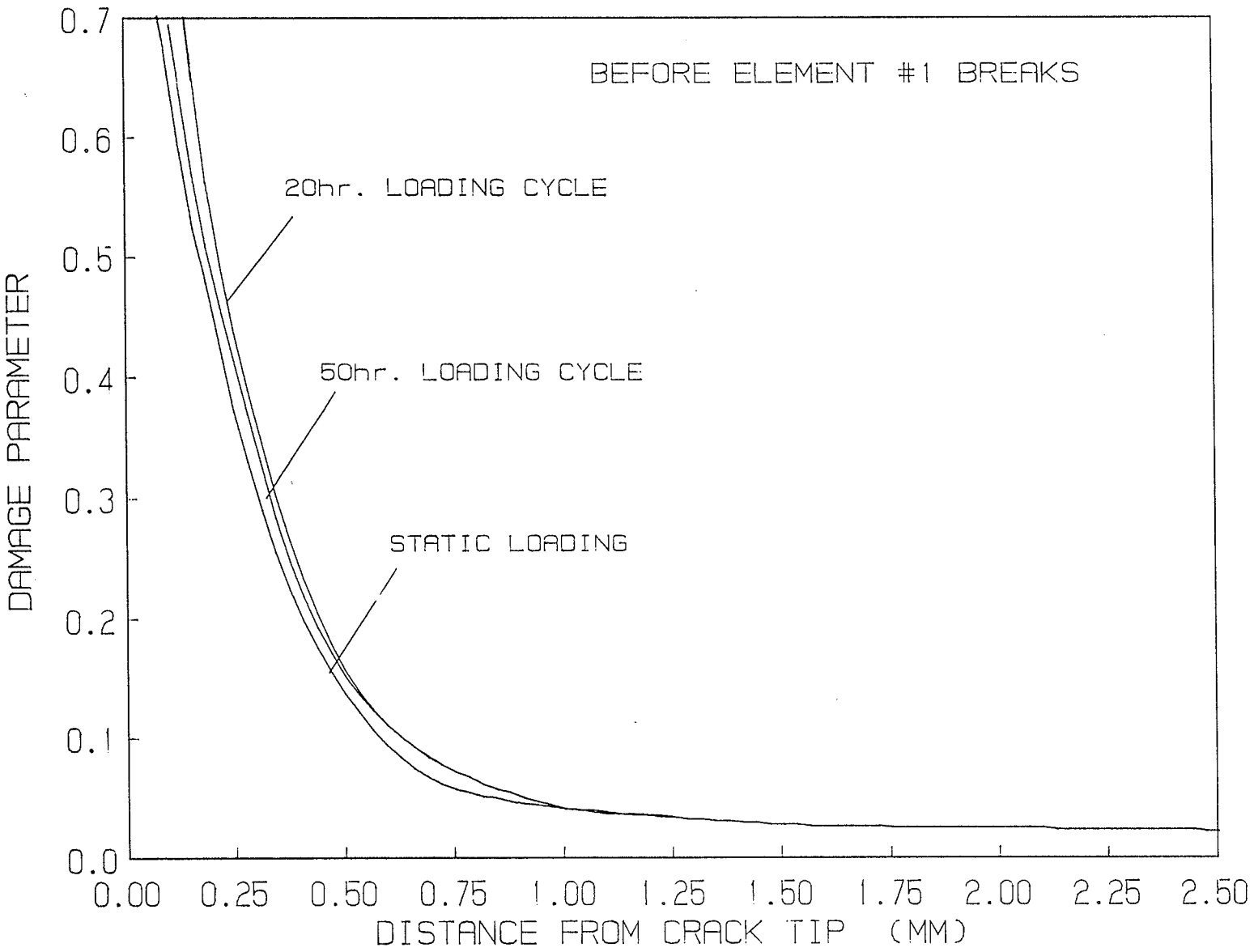

Figure 7.38 Damage distributions ahead of crack tip before element #1 breaks

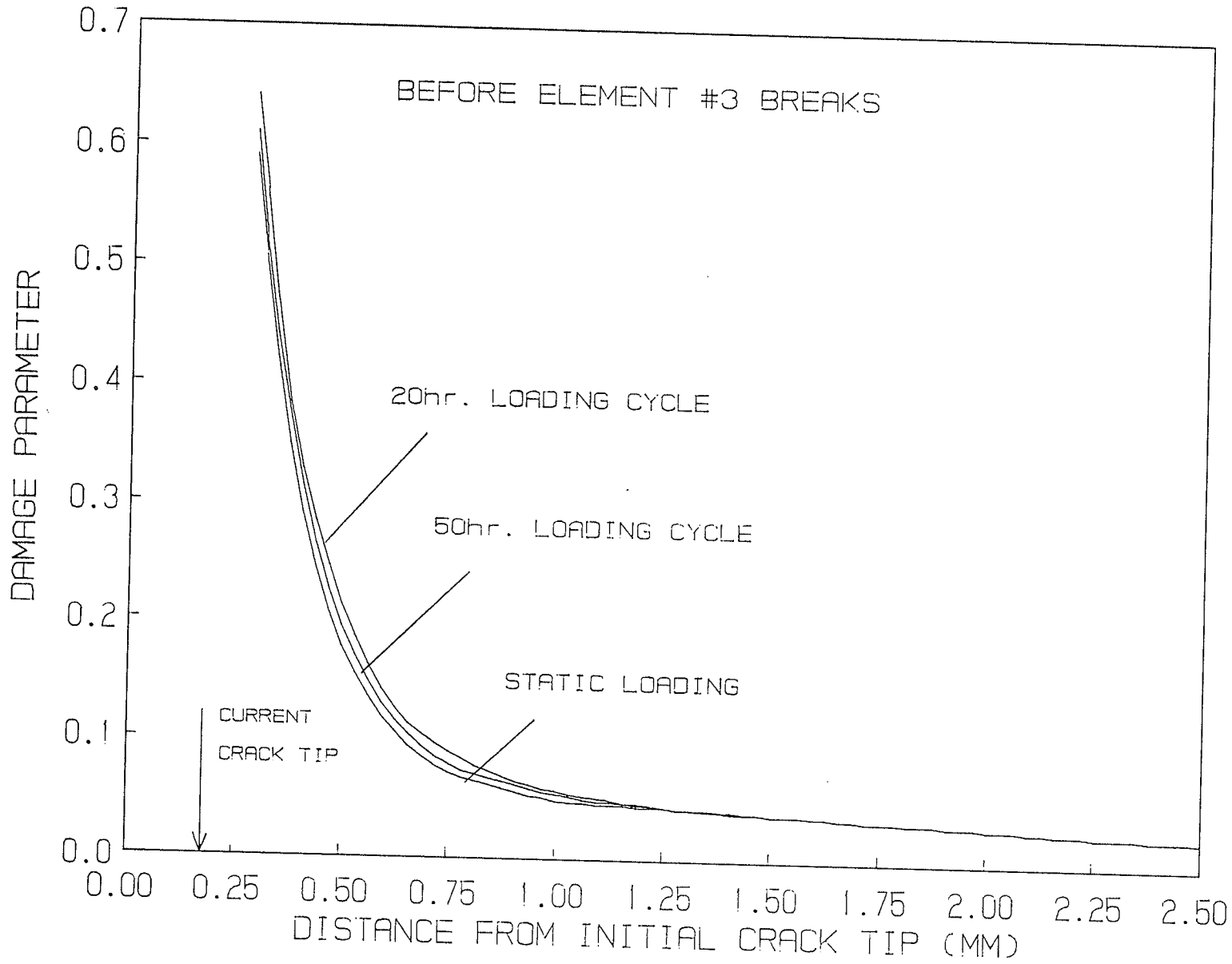

Figure 7.39 Damage distributions ahead of crack tip before element #3 breaks

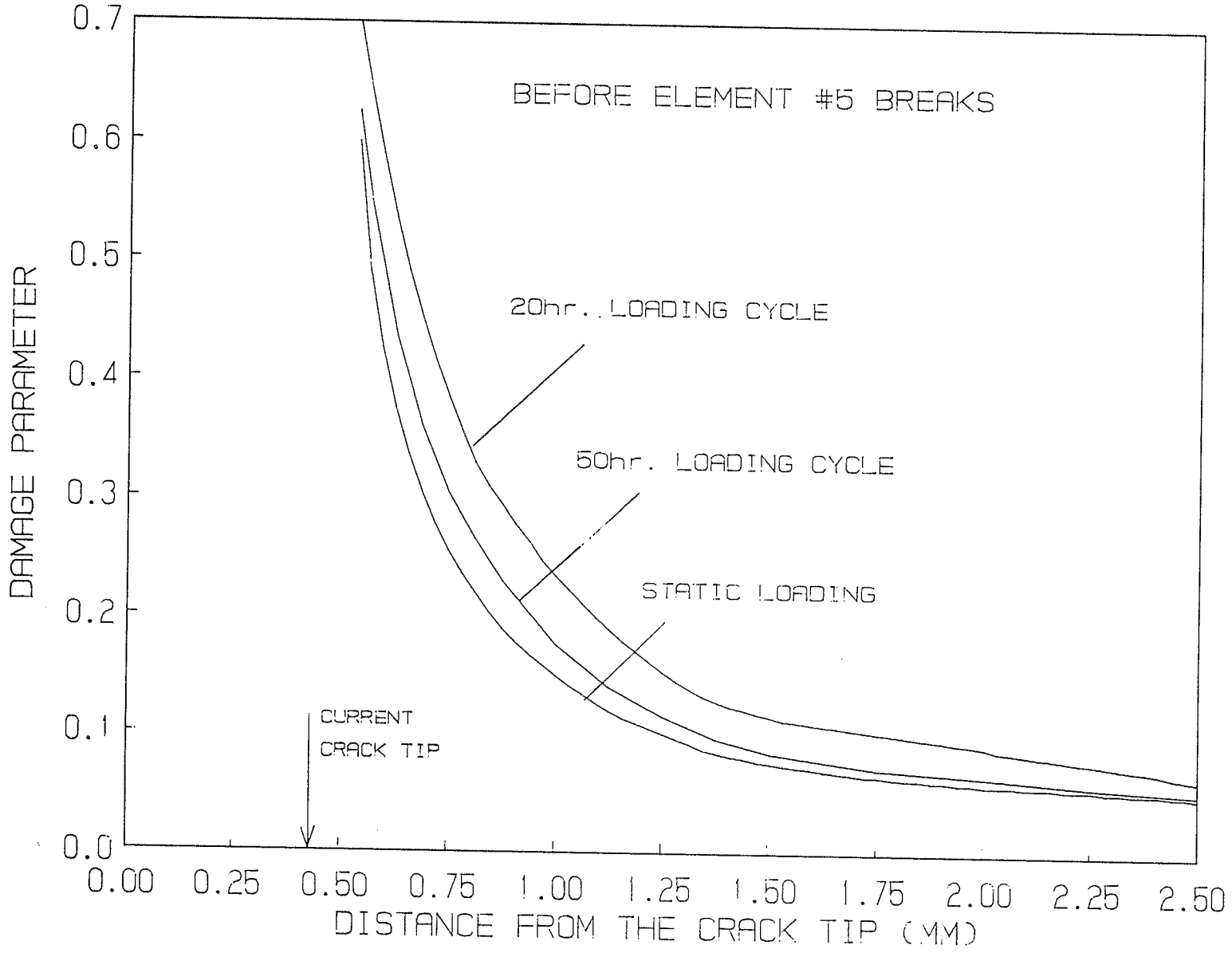

Figure 7.40 Damage distributions ahead of crack tip before element #5 breaks

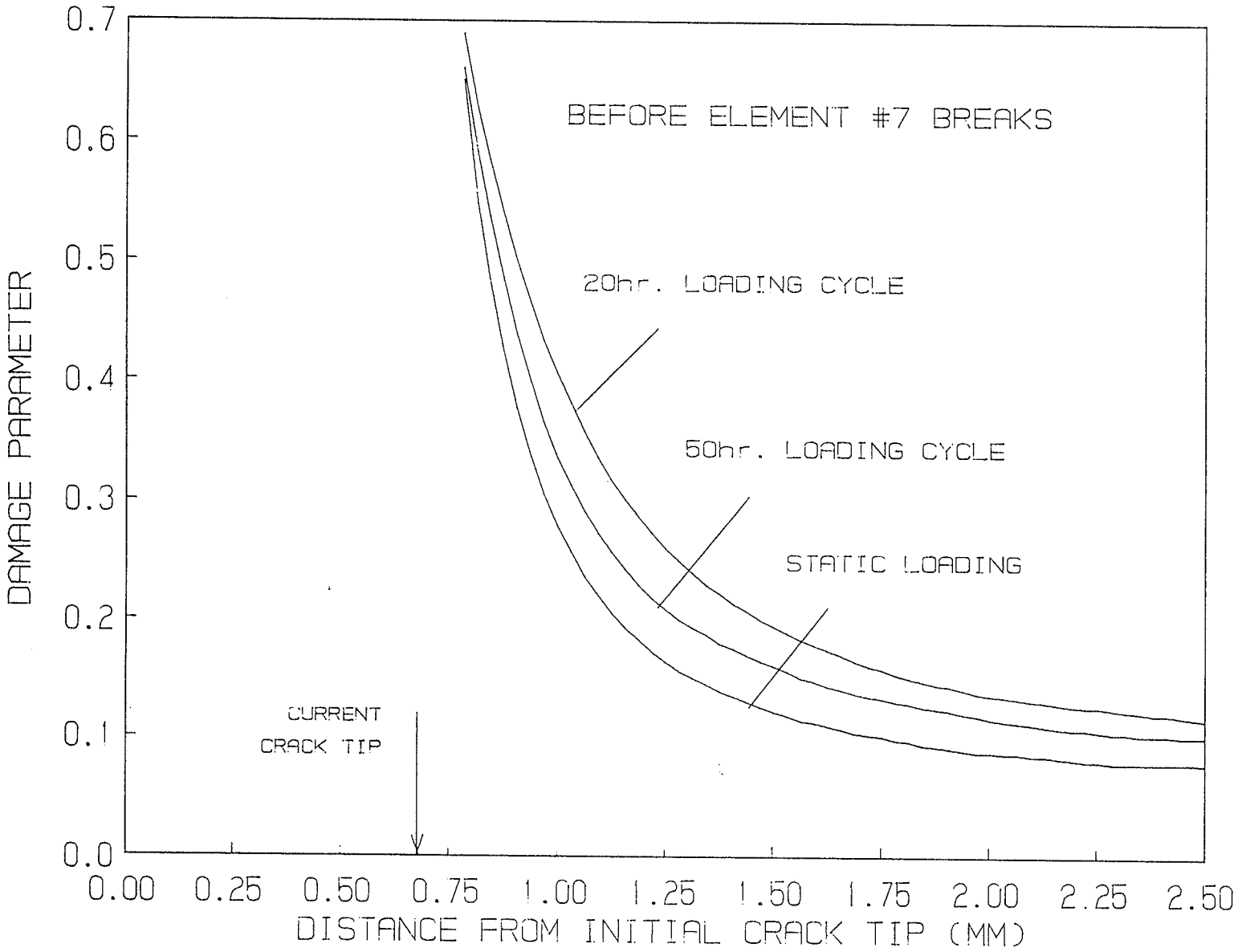

Figure 7.41 Damage distributions ahead of crack tip before element #7 breaks